Communauté
UNIVERSITÉ Grenoble Alpes

THÈSE

Pour obtenir le grade de

DOCTEUR DE LA COMMUNAUTÉ UNIVERSITÉ GRENOBLE ALPES

Spécialité : Physique pour les Sciences du Vivant

Arrêté ministériel : 25 mai 2016

Présentée par

Robin DELHOM

Thèse dirigée par **Giovanna FRAGNETO** et
codirigée par **Hanna WACKLIN**
préparée au sein du **Laboratoire Institut LAUE LANGEVIN**
dans **l'École Doctorale Physique**

Isolement et caractérisation structurale de lipides naturels deutérés et d'acides gras issus de micro-organismes

Isolation and structural characterization of natural deuterated lipids and oils from microorganisms

Thèse soutenue publiquement le **20 décembre 2017**,
devant le jury composé de :

Madame JAYNE LAWRENCE
PROFESSEUR, UNIVERSITE DE MANCHESTER - ROYAUME-UNI, Rapporteur
Monsieur THIERRY CHARITAT
PROFESSEUR, UNIVERSITE STRASBOURG, Rapporteur

Madame CHRISTELLE BRETON
PROFESSEUR, UNIVERSITE GRENOBLE ALPES, Examinateur et Présidente du Jury

Madame LAURA CANTU
PROFESSEUR, UNIVERSITE DE MILAN - ITALIE, Examinateur

Madame KAREN EDLER
PROFESSEUR, UNIVERSITE DE BATH - GRANDE-BRETAGNE, Examinateur

« Frères humains, laissez-moi vous raconter comment ça s'est passé. On n'est pas votre frère, rétorquerez-vous, et on ne veut pas le savoir. […] Ça risque d'être un peu long, après tout il s'est passé beaucoup de choses, mais si ça se trouve vous n'êtes pas trop pressés, avec un peu de chance vous avez le temps. »

***Les Bienveillantes* (2006) - Jonathan Littell**

ACKNOWLEDGEMENTS

Looking back in time, I can say that the past three years have been particularly rich and in so many aspects that go far beyond the thesis work itself. Many possibilities, many languages, many travels, many experiments, and many persons were brought to me by this multidisciplinary, international and challenging PhD project. Thus, before anyone else, and because the work presented here would not have been possible otherwise, I deeply thank Giovanna Fragneto and Hanna Wacklin. My sincere gratitude goes indistinctly to both of them as they succeeded to take care of me, my questions, my well-being and both my personal and professional development. They perfectly organized and orchestrated together to supervise me and the PhD project. I am glad that I found such working environment and conditions. I also thank ILL and ESS for reaching an agreement to fund this PhD together.

I should also thank Valérie Laux and Michael Haertlein from the D-Lab (ILL) for the valuable deuteration materials prepared as well as Juliette Jouhet from CEA and her help in the lipid analysis. Richard Campbell, Bruno Demé, Viviana Cristiglio, Philip Gutfreund and Andrew Nelson for the access and use of the large structures instruments and useful discussions.

There is a strong Italian community that I should also thank. Iniziando con Sandro Sonnino e Laura Cantù per avermi aperto, sia la foresterìa che i laboratori loro. Grazie. Grazie a la Ciampa, Laura Mauri e Yuri Pomè per avermi accettato e fatto spazio nel laboratorio con loro a Milano Due. Non dimenticherò nemmeno tutti gli altri di LITA, Davide, Giulia, Martino, Domitilla e Maura per i loro sorrisi oltre tutto e anche Giovanni, Lucas, Simone o Dario con chi il calcetto e le serate al birrificio avranno completato la mia integrazione italica. Fino all'ILL anche, e Tumminino che ringrazio particolarmente della sua amicizia, ma anche Marco e Yuri Gerelli o Alessandra con chi spero rimarrò in contatto.

There is also Wolfgang Knecht, Katarina Koruza, Anna Leung and Zoe Fisher that I want to thank for their help, company and nice discussions, whether I was or not in Sweden, and their implication in the work performed between LP3 and ESS, in a very nice working environment; Tack så mycket!

I obviously finish by thanking my family and friends. I thank Aljosa, Dominik, Elodie and I could go on like this for a long time. So thanks you all of you who participated and have been involved directly or indirectly to my PhD. Merci à tous! Merci à Laz, Gaff, Charles, Kiki, Am, Popo, Binou pour m'avoir donné envie de rester à Grenoble. Merci à vous mes parents, mes deux frères, à toi belle-soeur et à mon petit neveu pour ses sourires, très importants dans la dernière ligne droite. Merci à tous mes amis, grenoblois mais pas uniquement, qui m'ont soutenus, m'ont vu aller et venir mais sont toujours restés présents.

Et pour finir, bien sûr, merci à toi - grazie a te.

TABLE OF CONTENTS

ABBREVIATIONS

AFM : Atomic Force Microscopy
ANSTO : Australian Nuclear Science and Technology Organization
AmB : Amphotericin B
ATP : Adenosine Triphosphate
BMGY : Buffered glycerol complex medium
BSM : Bacterial Standard Medium
Chol : Cholesterol
CL : Cardiolipin
CM3 : Contrast Match 3 (SLD = 3 10^{-6} $Å^{-2}$)
CM4 : Contrast Match 4 (SLD = 4 10^{-6} $Å^{-2}$)
CMSi : Contrast Match Silicon
CoA : Coenzyme A
d- : Deuterated
D-Lab : Deuteration Laboratory of ILL
DMSO: Dimethyl sulfoxide
DNA : Deoxyribonucleic acid
Erg : Ergosterol
EtOH : Ethanol
FAME : Fatty Acid Methyl Ester
FID : Flame Ionization Detector
FIGARO : Fluid Interfaces Grazing Angles ReflectOmeter
FTIR : Fourier Transform Infra Red
GC : Gas Chromatography
GUV : Giant Unilamellar Vesicles
HEPES : 2-[4-(2-hydroxyethyl)piperazin-1-yl]ethanesulfonic acid
HPLC : High Performance Liquid Chromatography
ILL : Institut Laue-Langevin
LAMP : Large Array Manipulation Program
MeOH: Methanol
NMR : Nuclear Magnetic Resonance
NR : Neutron Reflectometry
OD : Optical Density

PA : Phosphatidic acid

PC : Phosphatidylcholine

PE : Phosphatidylethanolamine

PEEK : Polyether Ether Ketone

PG : Phosphatidylglycerol

PI : Phosphatidylinositol

PL : Phospholipid(s)

PO : 1-palmitoyl-2-oleyl

Polar : Phospholipid mixture extracted from *P. pastoris*

POPC : 1-palmitoyl-2-oleyl-sn-glycero-3-phosphatidylcholine

PS : Phosphatidylserine

QCM-D : Quartz Crystal Microbalance with Dissipation monitoring

RH : Relative Humidity

RNAi : Ribonucleic Acid Interference

SLB : Supported Lipid Bilayer

SLD : Scattering Length Density

SM : Sphingomyelin

TLC : Thin Layer Chromatography

UV : Ultraviolet

YNB : Yeast Nitrogen Base

1. INTRODUCTION

1.1. Membranes and lipids

Every entity is defined by its boundaries, or its outline. Life is not an exception as each living cell, independently of its origin, is defined by the barrier that surrounds it : the cell membrane. This limit, separating the inside from the outside of life's building blocks is not just a passive barrier but it actively participates in many molecular interactions and processes that occur at its surface [1-5]. The characteristics of cell membranes have been investigated since the discovery of the cell in 1665 and James Hook's invention of the microscope [6]. The lipid nature of cell membranes was first hypothesized by Overton in 1895 [7], but the phospholipid bilayer structure consisting of two layers of phospholipids, shown by E. Gorter and F. Grendel in 1925 [8] and their work on red blood cells, was a breakthrough leading to the concept of the Fluid Mosaic model expressed by Singer and Nicolson in 1972 [9]. Figure 1.1 illustrates the concept of the fluid mosaic membrane.

A

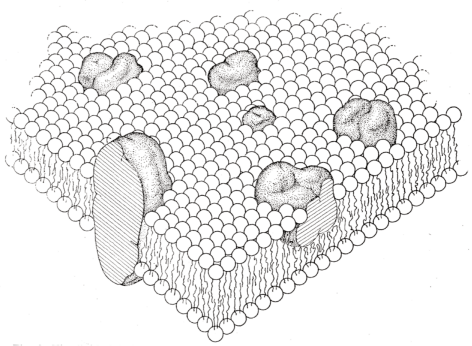

B

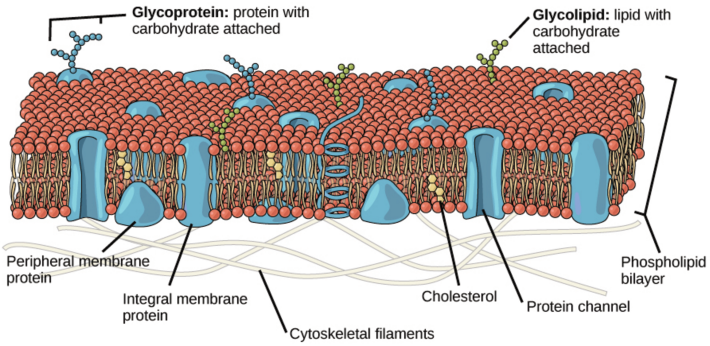

Figure 1.1 : *Fluid mosaic membrane illustrations. A : Singer–Nicolson original representation (1972) [9], B : Current depiction [10].*

The term 'mosaic' refers to the heterogeneous structure of the membrane composed of many molecules of different nature including lipids, proteins, complex sugars among others. The term 'fluid' is a dynamic concept, referring to the liquid-like state of the membrane in which the molecules can freely move laterally. Lipids can diffuse, rotate and translocate from one leaflet to the other, a process known as flip-flop [11]. The model postulates that the membrane is a two dimensional liquid, in which proteins are incorporated. Lipids are thus an inert medium in which proteins perform all functions associated with the membrane. This is still the most accepted theory even though many developments have been added to it [12, 13], among which some question the passive nature of the lipid constituents [14-16].

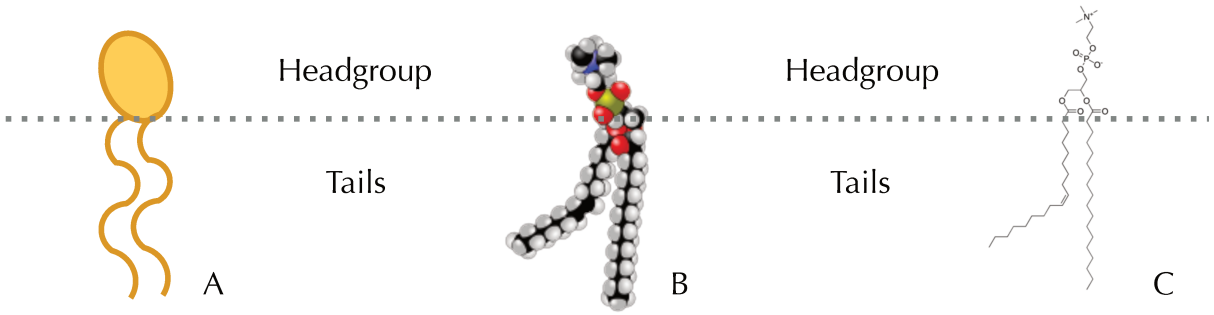

Figure 1.2 : *Representations of phospholipids. A = Schematic representation, B = Atomistic ball-and-stick model and C = Condensed chemical formula (Image source B & C : Wikipedia).*

Different types of amphipathic molecules are generally found in the lipid content of the cell membrane : phospholipids, constituents of the larger group of glycerolipids, but also glycolipids, sphingolipids and sterols. All amphipathic lipids possess a hydrophilic headgroup and one or two hydrophobic hydrocarbon chains also called lipid tail(s) (see figure 1.2). The lipid class is determined by the chemical nature of its headgroup (see figure 1.3), while both the class and the hydrocarbon chains define a specific molecular species. The hydrocarbon chains, derived from fatty acids, can vary in length, with generally only even number of carbons, consequence of to their biosynthesis [17]. A fatty acid chain may also have one or more unsaturations, i.e., double bonds, typically in well defined positions, in *cis* conformation.

For glycerophospholipids (commonly named phospholipids or PL), the fatty acids are connected to the phosphate side of the headgroup by a glycerol backbone and by a sphingosine for sphingolipids. Glycolipids are phospholipid- or sphingolipid-like molecules with sugars as headgroups. These can be attached directly to a phosphate group, but are, more often, directly linked via a glycerol or a sphingosine backbone to the hydrocarbon chains. Other more complex lipids such as cardiolipin (CL or bis-PG) exist, and correspond to the condensation of two phospholipids linked by a central glycerol molecule, as depicted in figure 1.3. We note also that free fatty acids and triglycerides, tri-substituted glycerols, can also be found in biological membranes.

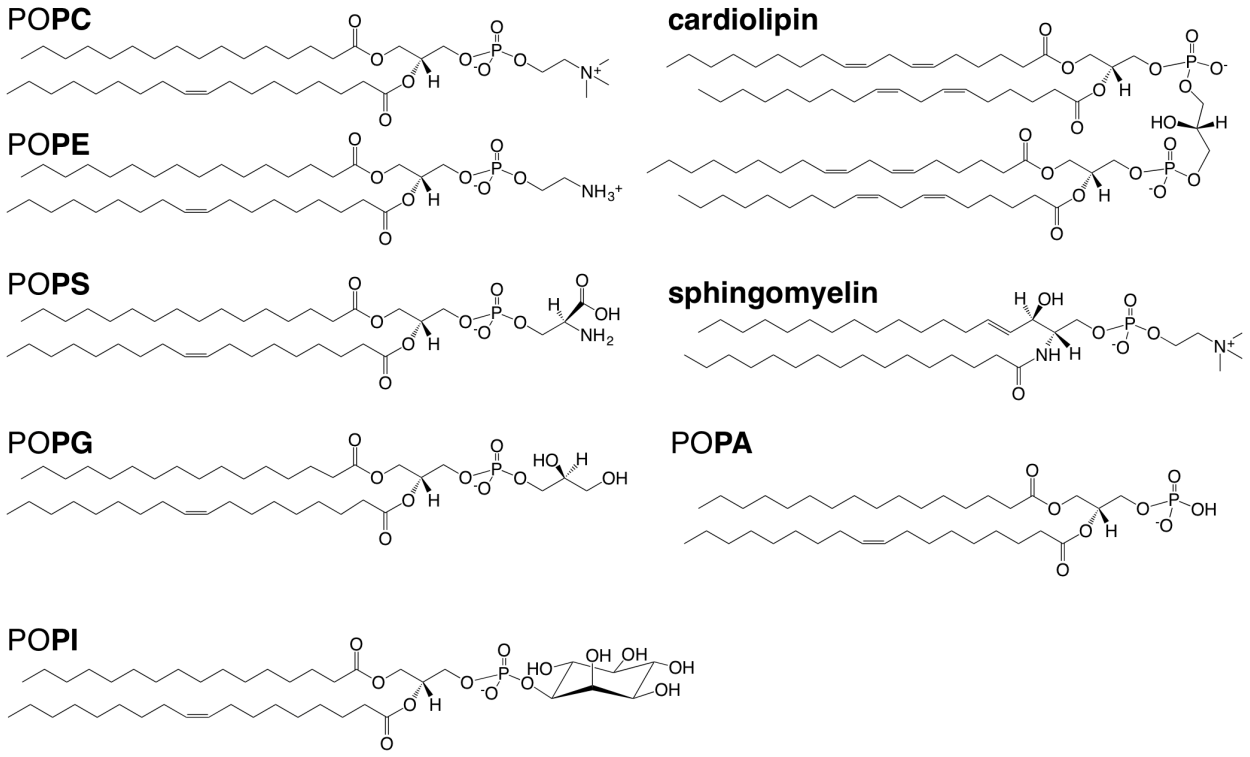

Figure 1.3 : *Main classes of phospholipids found in membranes. Illustrations from [18]. PO stands for 1-palmitoyl-2-oleoyl, the branch fatty acids chosen as a representative example. PC stands for phosphatidylcholine , PE for phosphatidylethanolamine, PS phosphatidylserine, PG phosphatidylglycerol, PI phosphatidylinositol and PA for phosphatidic acid.*

Sterols, mostly in the form of cholesterol for mammalians cells, ergosterol in fungi and ß-sitosterol in plants, are found in most eukaryotic cell membranes. Their shape is based on the steroid ring structure with a hydrocarbon chain and a small hydroxyl group, conferring them some amphipathic character (figure 1.4). Besides its molecular structure, being different from other lipid constituents of membranes, cholesterol is not only a very important molecule in our metabolism [19, 20] but it is thought to be prevalent in our evolution [21-23]. The biophysical effect of sterols on lipid bilayers has been extensively investigated, notably with the aim to prove the existence of so-called lipid rafts [24]. Indeed, sterols have ordering and condensing properties in lipid membranes [25]. Cholesterol orders the lipid acyl chains and induces a decrease in the area per molecule, know as condensing effect. Thus, this can lead to a lateral inhomogeneity in the distribution of specific lipids and proteins in dynamic domains, commonly named lipid rafts. Their existence and role in physiological conditions is still debated [26].

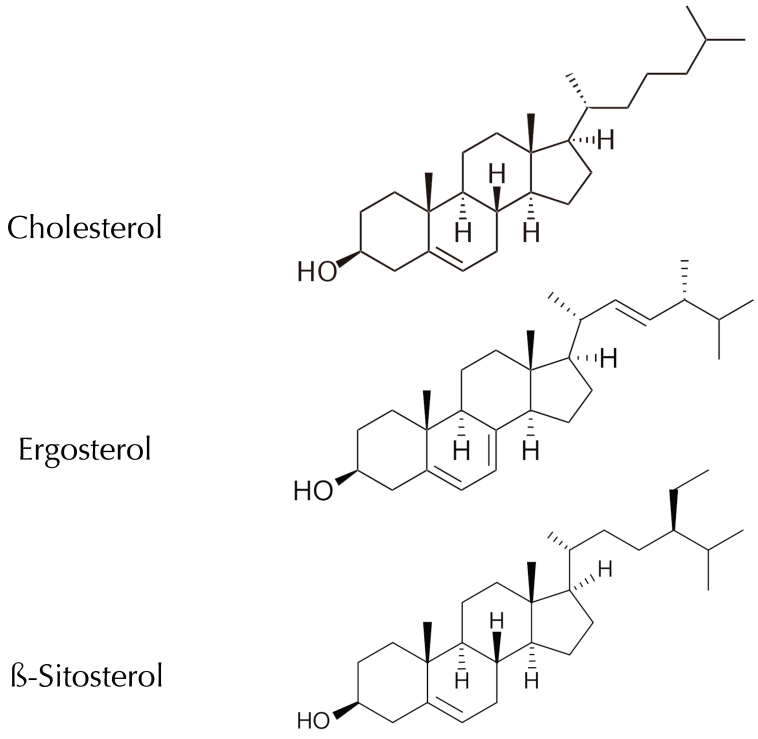

Figure 1.4 : *Structure of the principal sterols of eukaryotic organisms.*

The diversity of lipid molecular species in cell membranes is tremendous. And membranes are even more complex when taking into account the presence of proteins

and interactions with the surrounding, such as with the cytoskeleton in physiological systems. In addition, the composition and properties of a membrane are also dependent on their biological origin and functions [27]. Studying all the different membranes as a unique, similar entity is thus unsound. Nevertheless, the complexity of cell membranes often makes it difficult to investigate the contribution of each of the individual constituents involved in a given biological mechanism. This is the reason why model membranes, simplified versions of natural systems, mimicking them to some extent, have been developed and used in various biophysical techniques.

When working with lipids, different model systems can be investigated. Historically, lipid monolayers at the air/water interface, where the amphipathic molecules arrange themselves at the interface, were used as a model for half biological membranes. Relatively easy to handle, the structure of this system is probed mostly with X-Ray and neutron reflectometry and diffraction [28, 29] but also with ellipsometry, FTIR spectroscopy or Brewster Angle Microscopy [30, 31]. The main interest resides in the phase behavior of the (phospho)lipids. In general, for a given temperature and by compression of a monolayer, it will exhibit phase transitions from a gaseous phase into a liquid-expanded state to a liquid-condensed one to finally a gel phase. This behavior cares with the hydrocarbon chain length and unsaturations, similarly ti the effect on phase transition temperatures, as well as with the specific interaction with other molecules, such as sterols [32]. Liposomes, or giant unilamellar vesicles (GUV), are a versatile model system, presenting an inner aqueous compartment, mainly probed by microscopy and fluorescence techniques [33] for the investigation of the lipid phase behavior and membrane processes such as pore formation, membrane fusions or cell adhesion [33-35]. Liposomes present the drawback to have a relatively low stability in time. On the contrary, the supported lipid bilayer (SLB) system [36], a single flat lipid bilayer deposited onto a solid surface, is robust and mainly probed by Atomic Force Microscopy (AFM), Quartz Crystal Microbalance (QCM), X-Ray and neutron reflectivity [37-40]. SLBs can be formed by the Langmuir-Blodgett method [41], micelle deposition mediated by surfactants [42], vesicle fusion [43], or solvent exchange [44]. This system is suitable to observe proteins and molecular interactions with both lipid headgroups and hydrocarbon region as well as changes in the bilayer structure. Another system, oriented multilamellar stacks can be investigated via diffraction techniques, but are less amenable to *in-situ* interaction studies.

Concerning neutron scattering techniques and particularly neutron reflectometry (NR), it is worth noting that most of the work performed on lipids found in literature has been focused on using synthetic lipid systems [45-48]. If the problems arising from the complexity of natural mixtures, such as production, compositional analysis, sample depositions issues and intricate data treatment can be overcome, every observation and information gathered, as it relates to a more physiological system, is of great interest.

1.2. Deuteration

In a neutron scattering experiment, each element and isotope will interact with neutrons with a specific strength. By specifically substituting hydrogens with deuterium, its first isotope, it is then possible to enhance the power of neutron as a probe (the full concept of contrast variation is detailed in chapter 2.2.1). Deuteration, the production of molecules where hydrogens are replaced by deuterium, thus becomes fundamental for soft condensed matter studies as life science molecules usually present a large number of hydrogens. It is possible to deuterate a molecule either synthetically or biologically. Both present advantages and drawbacks. Concerning lipids, synthetic chemistry allows to produce specific and chemically pure deuterated molecules [49], but the technique is mainly limited by the complexity of syntheses required for building up (poly)unsaturated lipids. Biological deuteration implies adaptation of a suitable microorganism to growth in heavy water and subsequent extraction of the lipids, a process that leads to complex lipid mixtures [50] that can be challenging to separate. The deuteration can impact both the growth of a microorganism in a perdeuterated medium, i.e., fully deuterated, and the composition of its constituent membranes in a manner which is still not well understood [51, 52]. Furthermore, deuterated molecules can show isotopic effects in their physical and chemical behavior. Chemically, the carbon-deuterium bond is shorter and stronger than the carbon-hydrogen one. This characteristic is mainly used for NMR and Infra Red spectroscopy [53]. Kinetics processes are also impacted by the isotopic substitution [54]. Concerning lipids, the main physical effect is related to the modification of the gel-fluid phase transition of a given molecular species. A perdeuterated hydrocarbon chain has a lower phase-transition, usually around 4°C below the corresponding hydrogenous one [55, 56]. It has also been shown that the isotopic nature of the surrounding solvent, either light

water H_2O or heavy water D_2O, used in vesicle suspensions can impact the organization of the phospholipids [57].

1.3. Yeasts

Yeasts are members of the eukaryotic organisms called fungi, separated from the other life kingdoms of plants and animals. Most of its representatives are unicellular microorganisms that use organic compounds as source of energy: they are chemoorganotrophs, and do not need light in order to grow. They can grow in both aerobic and anaerobic conditions and were used by humans historically for fermentation of sugars and alcohol production such as in bread baking and beer brewing [58]. Nowadays, with the rise of biotechnologies, yeasts are employed for many other applications from pharmaceuticals to energy [59, 60].

Our interest in yeasts in this work is two-fold. On one side, there is a biotechnological research interest. It has been shown that the methylotrophic yeast *Pichia pastoris* can be adapted to grow in perdeuterated media and hence used as the source of perdeuterated lipids [50]. The yeast cell machinery allows accessing a large diversity of lipids including non-commercially available polyunsaturated phospholipids. Indeed, the composition of the lipids extracted from biomass relates to physiological conditions. In consequence the mixture obtained can be used as a model to mimic fungal systems. Also, by adapting other microorganisms to deuterium all compounds and model membranes can be obtained in principle [61] including those of potential interest to medical research. This connects to our second interest, health oriented.

While every year, millions of people suffer invasive life-threatening fungal infections, the number of available anti-fungal agents is not only limited, but their use is often restrained due to toxicity, resistance concerns and/or low bioavailability [62]. Furthermore, the mechanisms of action of such drugs are not always fully understood and use of a representative membrane of pathogenic yeasts could help improving our understanding of these mechanisms.

Related to the well studied deleterious yeast *Candida albicans*, *Candida glabrata* became a main cause of mucosal and systemic infections during the last decades [63].

A major limitation to the study of this microorganism is the difficulty to achieve gene deletions [64]. Some essential genes cannot be deleted and the deletion of others, impacting several phenotypes at the same time, renders it difficult to understand the gene function. To overcome these gene deletion limitations, RNA interference (RNAi) tools have been developed at Lund University [65, 66]. These tools do avoid some of the limitations expressed before, regulating gene expression rather than simply switching it on or off. A gene can be kept down-regulated or over expressed depending on the needs of the experimenter and the use of dedicated libraries allows to cover the whole genome. This new tool can be exploited to understand the triptych relationship between the changes in membrane lipid composition, drug resistance and changes in gene expression of a poorly understood pathogenic yeast. Also, the comparison of the lipid composition of more or less virulent yeasts and their membranes can provide insights into the key parameters of the activity of a given drug and their resistance mechanism.

1.4. Amphotericin B

Among all the clinically used anti fungal molecules, there is an outstanding one because of its broad spectrum of activity, its efficiency, durability and the relative low mycological resistances induced over time. As a matter of fact, the polyene macrolide Amphotericin B, abbreviated AmB, is used as last resort for life-threatening systemic fungal infections. Discovered in 1955 by Oura et al., and presented in Antibiotics Annual, the molecule is synthesized by a bacterium [67]. The ring structure is composed by a hydrophilic side, where the several polar substituents point, and a hydrophobic one, displaying seven conjugated *E* double bonds (see figure 1.5). The amphipathic property is enhanced by the presence of the amino sugar, D-mycosamine.

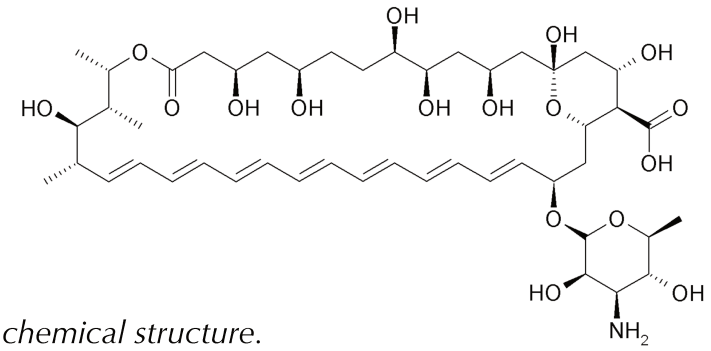

Figure 1.5 : *AmB chemical structure.*

It is important to note that the formulation of the drug evolved over the past 60 years, principally to lower the nephrotoxicity and side effects caused by the antibiotic [68]. The use of colloidal suspensions and lipid-based formulations allowed to lower the nephrotoxicity and enhanced the efficiency of the drug [69] without clear evidences of the reason of such behavior.

Amphotericin B is thought to gain its fungicidal properties by interacting preferentially with ergosterol, the fungal sterol, and less so with cholesterol, the mammalian one [70, 71]. Besides its favorable affinity with ergosterol [72, 73] and its use over decades, the mechanism of action of this antimycotic molecule remains unclear. However, among the extensive literature available over a large period of time, it is possible to recount the evolution of views in few axis.

For many years, the aqueous pore formation induced by AmB was the prevalent hypothesis towards fungal toxicity as studies using many different techniques such as electrochemistry, fluorescence & UV spectroscopy [74-76] or NMR [77] abounded in this direction. AmB would bind preferentially to the ergosterol and form aqueous pores into the fungal membrane, leading to cell death. But contradictory [78] and additional results were also obtained [79, 80] suggesting that the interaction with ergosterol and AmB cytotoxicity was not dependent on direct permeabilization of the membrane. Recently, the hypothesis of the sterol sponge model, where the AmB forms extramembraneous aggregates extracting the ergosterol from the bilayers, emerged [5]. The removal and sequestration of the ergosterol impact the structure of the membrane and interfere with the biological processes associated to it [81]. These are thought to be the basis of the fungicidal properties of the drug. Evidence for this hypothesis along with the impact of lipid polyunsaturation towards AmB-ergosterol interaction were recently obtained by neutron reflectometry [16].

Nevertheless, the hypothesis has not yet been confronted to the mechanism of AmB in cholesterol containing membranes and the reason of the host cell cytotoxicity is still poorly understood.

1.5. Objectives of this work

Biophysical techniques are nowadays largely employed to address health-related issues as well as to sustain the development of the knowledge necessary for a better understanding of the surrounding world. Deuteration is of paramount importance if one wants to take advantage of neutron scattering techniques as the contrast variation method (see chapter 2.2.1) allows to overcome the phase problem inherent to all scattering techniques while selective deuteration allows to highlight parts of the investigated system. But neutron-related lipid science is limited by the number and complexity of commercially available deuterated phospholipids. The development of efficient deuteration and lipid production methods is thus of major importance. Biodeuteration allows access to a large diversity of lipid molecules within reasonable resources. The recovered lipid mixtures are representative of the associated microorganisms and can be used as relevant model membranes for many biophysical studies among which drug, protein and/or nanoparticle interactions studies.

Following the work performed by former ILL PhD student Alexis de Ghellinck [82], who first succeeded with his collaborators to prepare both hydrogenous and deuterated planar lipid bilayers from yeast lipid total extracts and study by neutron reflectometry their interaction with AmB, it appeared interesting to pursue more investigations. The isotope effect and its modulation, the deuteration of pathogenic microorganisms, the development of a reliable deposition process for such natural mixtures, the structural characterization of the corresponding bilayers, the quantification of the AmB mechanism and the molecular process leading to its toxicity effect as well as the impact of the lipid components on AmB action are the main questions addressed by the present thesis.

2. EXPERIMENTAL TECHNIQUES

2.1. Quartz Crystal Microbalance with Dissipation monitoring (QCM-D)

Before being able to structurally characterize supported lipid bilayers with neutrons, it is usually necessary to determine the conditions for good bilayer deposition onto the supporting surface. The Quartz Crystal Microbalance (QCM) is a very sensitive device that allows to probe small changes of the order of a few nanograms in the adsorbed mass as a function of time. This is achieved by monitoring the changes in the resonance frequency of a quartz crystal when material is absorbed at its surface. The chip necessary for such measurements is a piezoelectric thin quartz crystal, with electrodes on both sides, which will resonate when subjected to an electric field. With an alternating current, an acoustic wave is created and propagated onto the crystal which makes it possible to measure the orders and frequencies of the resonances. Quartz is the material of choice for several reasons including its chemical stability, the low resistance it offers to wave propagation and the fact that pure quartz crystals are easily accessible and relatively cheap.

Sauerbrey quantified in 1959 the variation of the resonance frequency of quartz induced by a modification of the adsorbed mass [83] and developed equation **(1)** :

Sauerbrey's equation

$$\Delta f = -\frac{2{f_0}^2}{A\sqrt{\rho_q \mu_q}}\Delta m \qquad \textbf{(1)}$$

where f_0 is the resonant frequency, Δf is the frequency change, Δm is the mass change, A the piezoelectrically active crystal area, ρ_q is the density of quartz (ρ_q = 2.648 g/cm^3) and μ_q the shear modulus of quartz crystal.

If the surface area and the density of the adsorbed film are known, it is possible to determine, from the calculated mass of the film, its thickness. The Sauerbrev relation is valid only when the deposited film is rigid and does not damp the oscillations of the crystal. Further development of the technique by Nomura & Hattori allowed the crystal to stably oscillate in liquids [84] and, by doing so, to use QCM to investigate molecular interactions and adsorption to many different types of surfaces from solution. However, the Sauerbrey equation does not work for soft viscoelastic films often formed by proteins, lipids and other biomolecules. In such cases, a viscoelastic model is employed to interpret the data, where the viscoelastic response of the film is probed by the dissipation of acoustic energy. When an electric field is applied to the crystal with a viscoelastic adsorbed film, the oscillations of the crystal decay exponentially with a given characteristic time τ, according to equation **(2)**, as illustrated in figure 2.1.

$$A(t) = A_0 e^{\frac{-t}{\tau}} \sin(2\pi f t + \phi) \qquad \textbf{(2)}$$

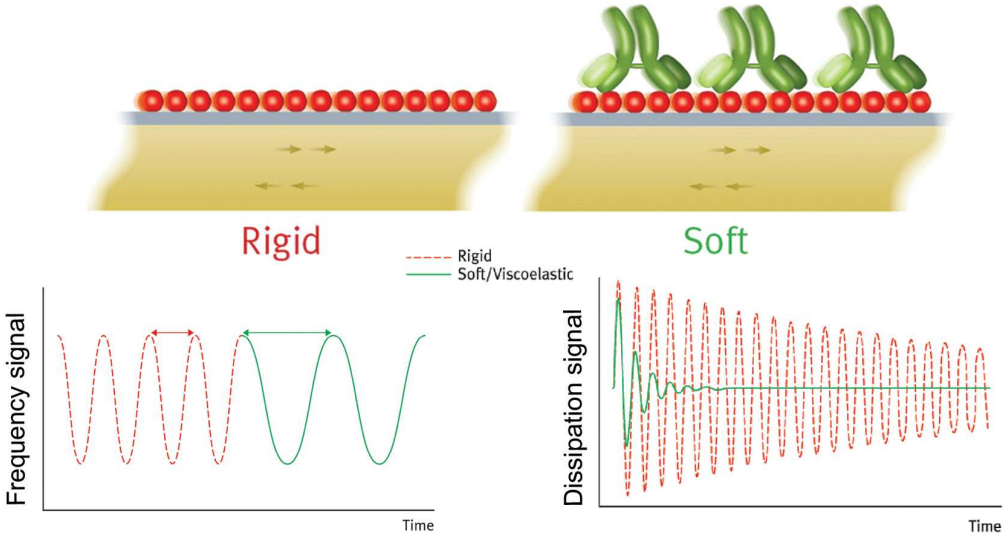

Figure 2.1: *Frequency and dissipation QCM-D signals depending on the viscoelasticity of the probed system (Image from biolinscientific.com)*

From equation **(2)**, we can obtain the resonance frequency f, and the characteristic time τ, and we can then calculate the dissipation factor D defined as in equation **(3)** :

$$D = \frac{1}{\pi f \tau} = \frac{E_{dissipated}}{2\pi E_{initial}} \qquad \textbf{(3)}$$

The initial ($E_{initial}$) and the dissipated ($E_{dissipated}$) energy taken into consideration correspond to an oscillating period [85]. Δf and ΔD can be linked to the characteristics of the adsorbed layer but modelling, based on electrical or mechanical circuits, must be performed. Two models are commonly used : the Maxwell and the Voigt models [86].

In this case, QCM-D was used as a qualitative tool to investigate the conditions of lipid deposition, and in order to avoid too many assumptions, only the resonance frequencies (Δf) and dissipation (ΔD) will be presented in the results section, chapter 4.

2.2. Neutron Reflectometry (NR)

2.2.1. Principles and contrast variation

The neutron is a sub-atomic fundamental particle discovered by James Chadwick [87] in 1932 after Rutherford predicted it in 1920. The neutron has a high penetration depth in most materials because it interacts weakly with matter and thus represents a non destructive probe. Indeed, as opposed to X-Rays interacting with electrons, neutrons interact with the nucleus of an atom via the strong nuclear force. Due to the wave-particle duality, we can associate: (i) a wavelength $\boldsymbol{\lambda}$ to each neutron by applying the de Broglie equation **(4)** :

$$\lambda = \frac{h}{m_n v} \qquad \textbf{(4)}$$

where h is Planck's constant, m_n the mass of a neutron and v the velocity; and, (ii) a related energy for each neutron with equations **(5)** :

$$E = \frac{h^2}{2m_n \lambda^2} \qquad \textbf{(5)}$$

The energy of the neutrons defines their wavelength and their applications in structural and dynamical studies of materials. We differentiate cold neutron, energies ranging typically from 10^{-5} eV to 0.025 eV, from thermal neutrons with energy around 0.025 eV and fast neutrons with energies higher than eV.

At the ILL, neutrons are produced by fission of highly enriched uranium (^{235}U) in a nuclear reactor. Cold neutrons are obtained making use of a cold source, a secondary moderator slowing down both fast neutrons coming from the core and thermal neutrons coming from the primary moderator through successive collisions of the neutrons with the atoms of the cold source. It usually consists of a small vessel, in place close to the center of the reactor, maintained at very low temperature (25K = -248°C). In consequence, the cold neutrons obtained have energies corresponding to wavelengths in the range of 2 to 40 Å suitable for investigating matter at the nanometer length scale.

Most of the work performed in order to characterize the phospholipid bilayers presented in this manuscript, involved neutron scattering techniques. The choice of such an uncommon characterization tool finds its origin in the properties of neutrons and the nature of the samples investigated.

Neutron scattering is defined by the change in direction of the neutron implying a change in the momentum transfer vector Q, a change of its energy ΔE or a change in its spin orientation. The magnetic properties of neutrons are not used in this work and therefore they are not discussed. Also, only elastic scattering events will be considered, and thus we are interested only in the change of the momentum transfer Q.

The neutron wave function is given by the Schrödinger equation :

$$H\psi = E\psi \qquad \textbf{(6)}$$

$$\left[-(\frac{\hbar^2}{2m_n})\nabla^2 + \hat{V}(r) \right]\psi(r) = E\psi \qquad \textbf{(7)}$$

Where $\psi(r)$ is the neutron wave function, E its energy and m_n its mass. $\hbar$ is Planck's constant divided by 2π and V(r) is the potential energy operator that describes the interaction of the neutron with the surrounding matter. By considering the neutron as a propagating plane wave, by convention in the z direction, V(r) can be expressed as in equation **(8)** for an assembly of nuclei situated in the xy-plane at positions r_j:

$$V(r) = \frac{h^2}{2\pi m_n}\left\langle \sum_j b_j \delta(\vec{R} - \vec{r_j}) \right\rangle \qquad \textbf{(8)}$$

where R is the neutron position. The δ function implies that V(r) is different from 0 when $R = r_j$. The thermal neutron wavelengths (~10^{-10} m) are much larger than the radii of the nuclei (~10^{-15} m), thus they are defined as point-like scatterers. Finally, the coherent neutron scattering length represented by the constant b_j, characteristic to each type of nucleus, essentially measures the strength of interaction between a given nucleus and a neutron. The Born approximation assumes that due to the weak interaction of neutrons with matter, and given the fact that we investigate thin films, the probability of two scattering events occurring for one neutron is null. We can then define ρ as the scattering length density (SLD) of a given homogeneous material with the following equation :

$$\rho = \sum_j b_j v_j \qquad \textbf{(9)}$$

where v_j is the molecular volume of the atom j. The unit obtained for SLD is $Å^{-2}$.

By looking at the coherent scattering lengths (figure 2.2) of different atoms, we can observe that neutrons are almost equally sensitive to light and heavy elements.

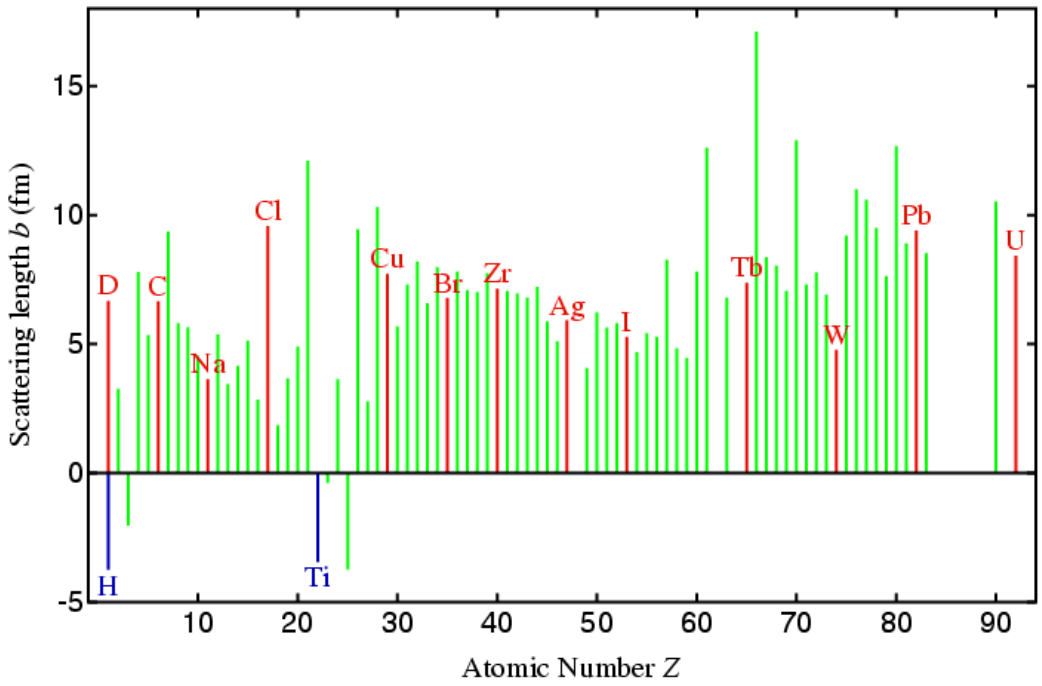

Figure 2.2 : *Scattering power of neutrons depending on elements and isotopes [88].*

The scattering force is not increasing linearly with atomic number as for X-Rays, but seems erratic while going across the periodic table. We also note that the neutron scattering length differs between isotopes of the same element. Using neutrons as a probe thus gives the ability to differentiate isotopes, which forms the foundation of the contrast variation method.

Contrast variation is a key element in the use of neutrons for soft-matter systems and mainly utilizes the difference of scattering power between the most common atom in the universe, Hydrogen ^{1}H (one proton, no neutron), and its first isotope, Deuterium (< 0,012% natural abundance on earth - one proton and one neutron) equally expressed as ^{2}H or D. Among all the isotopes, those two present a significant difference in scattering length enhanced by the negative value of hydrogen. Another important fact is the high concentration of hydrogens in ubiquitous molecules for life with water as first and major example. Indeed, by mixing light water (H_2O) and heavy water (D_2O), it is possible to access a large range of neutron SLD values which is often used to vary the contrast of aqueous samples.

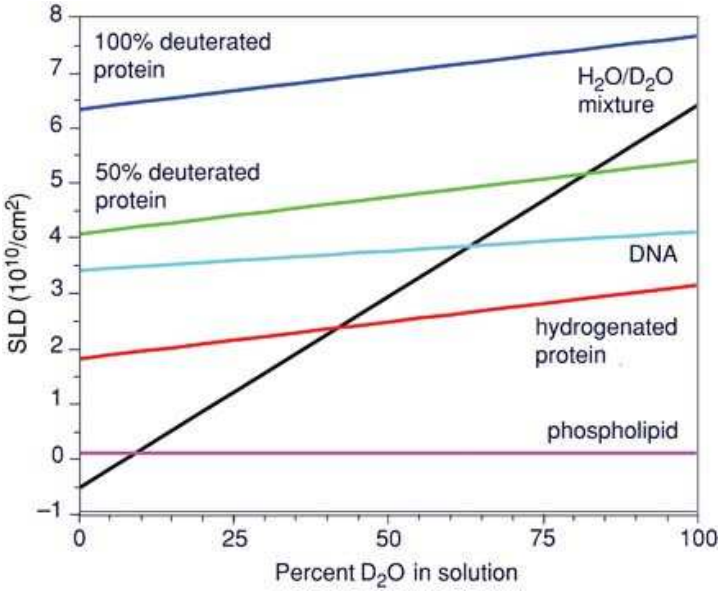

Figure 2.3 : *Generic neutron contrast match chart in aqueous conditions [89].*

Figure 2.3 displays the SLDs values of the main classes of biologically relevant molecules in the range allowed by mixtures of light and heavy water, represented by the black line, from -0.56 to 6.36 $10^{10}/cm^2$ (or 10^{-6} $Å^{-2}$). Indeed contrasts are reached by increasing (D_2O > H_2O) or decreasing (D_2O < H_2O) the amount of deuterium in the medium. Proteins and DNA are shown to have their SLDs increasing more or less as the percentage of D_2O increases. This is due to labile hydrogens that can be exchanged

with the deuterium present in the surrounding medium. This modification in composition impacts the overall scattering length density of the molecule which increases as H is exchanged with D.

We also note that a phospholipid is represented with a constant SLD, reflecting absence of labile hydrogens. This is not true for all phospholipids but is verified for phosphocholines, the synthetic phospholipid's class mostly in use in biophysical studies [11, 32, 39, 42, 44, 46-48]. Indeed, if the aliphatic chains of the phospholipids does not contain labile hydrogens, the headgroup, depending on its nature, sometimes can. It is thus important to assign a correct SLD to each phospholipid in relation to the contrast employed. Those calculations and assignments in relation to the samples investigated in this work are detailed in chapter 3.5.1.

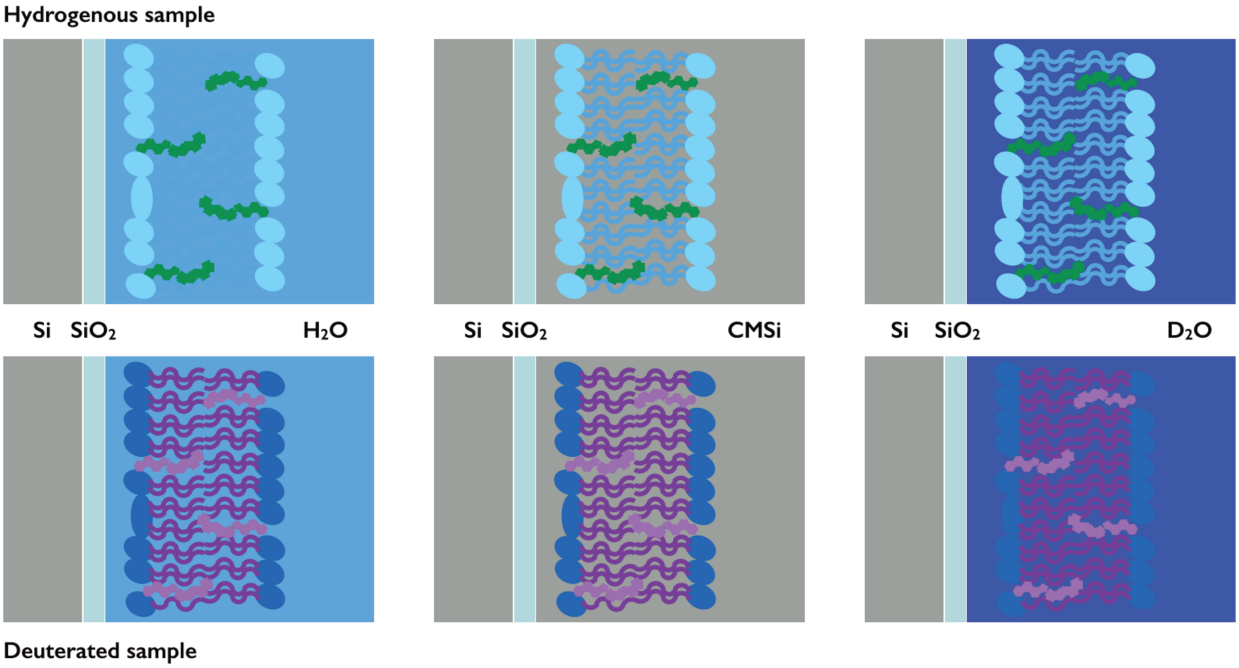

Figure 2.4 : *The principle of contrast matching of lipid bilayers in aqueous solution where the surroundings and the sample nature determine how well we 'see' it with neutrons. CMSi stands for Contrast Match Silicon. Note that the Silicon SLD (2.07 10^{-6} $Å^{-2}$) is similar to that of the hydrogenous phospholipid headgroups.*

The intersection points with the black line displayed in figure 2.3 allow to 'match out', i. e. render invisible to neutrons, a specific compound (or part of it) while using neutron as a probe in the corresponding mixture of light and heavy water. By modifying the surrounding of a sample, we modify the ability to 'see' it while illuminated with neutrons. Deuteration of components of a given sample, and not only the surrounding,

is also possible when deuterated molecules are accessible, and is extensively used for gain of contrast. These concepts are depicted in figure 2.4.

The contrast variation method is also of prime importance for solving the phase problem. As for all other scattering techniques, the phase of the neutrons, contained in the amplitude of the scattered waves, is lost during neutron scattering measurements that record only the intensity of each reflection. Contrast variation can be used to measure several sets of data from the same sample in different scattering contrasts, which allows to narrow down the number of possible solutions to the phases by simultaneous fitting of all the scattered data [90].

2.2.2. Neutron Reflection from an interface

Investigation of surfaces via neutron reflectometry allows to probe simultaneously, without damaging the samples, the thicknesses of adsorbed layers at different interfaces (solid/air, liquid/air, liquid/liquid or solid/liquid as it is the case in the present work), their roughnesses and their nuclear composition in the direction normal to the interface [37, 90].

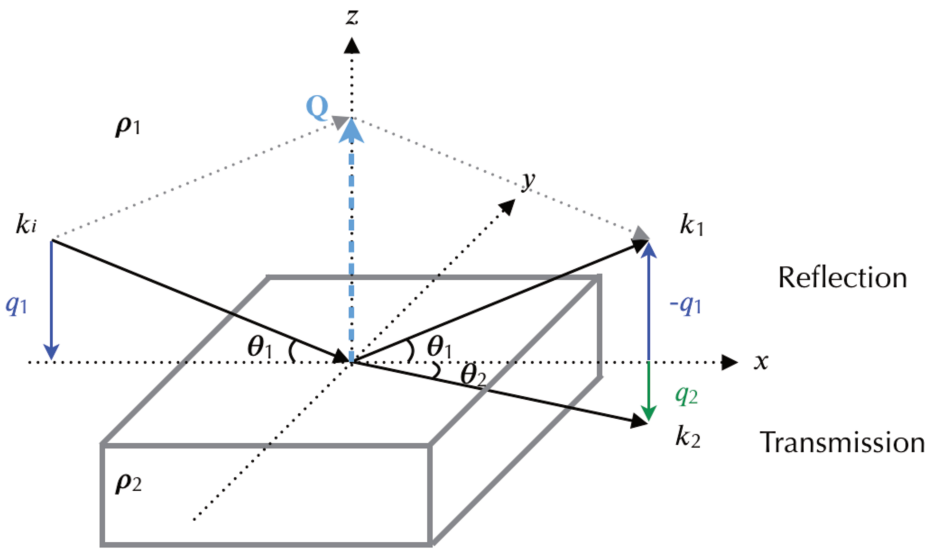

Figure 2.5 : *Illustration of neutron specular reflection and transmission on a flat interface between two media of different scattering length densities* ρ_1 *and* ρ_2*. ki is the incident wave vector,* k_1 *and* k_2 *respectively the reflected and transmitted wave vectors* ($k=2\pi/\lambda$)*;* θ_1 *is the incident and reflected angle and* θ_2 *the transmitted one. All angles are in the xz-plane.* q_1 *and* q_2 *are the scattering vectors* ($q = 2k \sin\theta$)*.*

For specular reflection, i.e. the angles of incidence and reflection are equal, the change of momentum arises from the fact that on a homogeneous surface, given equations **(8)** and (9), the Fermi pseudo-potential of the incident neutrons is :

$$V(r) = \frac{h^2 \rho}{2\pi m_n} \qquad \textbf{(10)}$$

For homogeneous media in the xy-plane the potential can only be function of z. Thus, the wave function can be averaged over y and we obtain :

$$\psi(x,z) = e^{ik_x}\psi(z) \qquad \textbf{(11)}$$

where k_x is the wave vector parallel to the interface, invariant in the case of elastic scattering events. Combining the Schrödinger equation **(7)** with **(11)** we obtain :

$$\frac{\partial^2 \psi}{\partial z^2} + q^2 \psi = 0 \qquad \textbf{(12)}$$

with q, the momentum transfer or scattering vector normal to the interface defined as :

$$q^2(z) = \frac{8\pi^2 m_n}{h^2}\Big[E - V(z)\Big] - k_x^2 \qquad \textbf{(13)}$$

When the neutron wave impinges on the surface, it will be partially reflected and partially transmitted. The probabilities of reflection and transmission are respectively expressed with r and t coefficients. Thus,

$$\psi(z) = \left\{ \begin{array}{c} e^{(iq_1 z)} + re^{(-iq_1 z)} \\ te^{(iq_2 z)} \end{array} \right\} \qquad \textbf{(14)}$$

z is positive for reflections and negative for transmissions (see figure 2.5). Also, since at the boundary condition (at z=0), $\Psi(z)$ and its derivatives are continuous, r and t must respect :

$$1 + r = t \qquad \textbf{(15)} \qquad \text{and} \qquad q_1 - q_1 r = q_2 t \quad . \qquad \textbf{(16)}$$

The scattering vector q_1 and q_2, respectively for reflection above and refraction below the interface, are depicted in figures 2.5 and 2.6.

It is hence possible to express the probability of reflection r as : $r = \frac{q_1 - q_2}{q_1 + q_2}$ **(17)**

and the probability of transmission t as : $t = \frac{2q_1}{q_1 + q_2}$. **(18)**

These two coefficients are the Fresnel reflection and transmission coefficient at a planar interface between two homogeneous media.

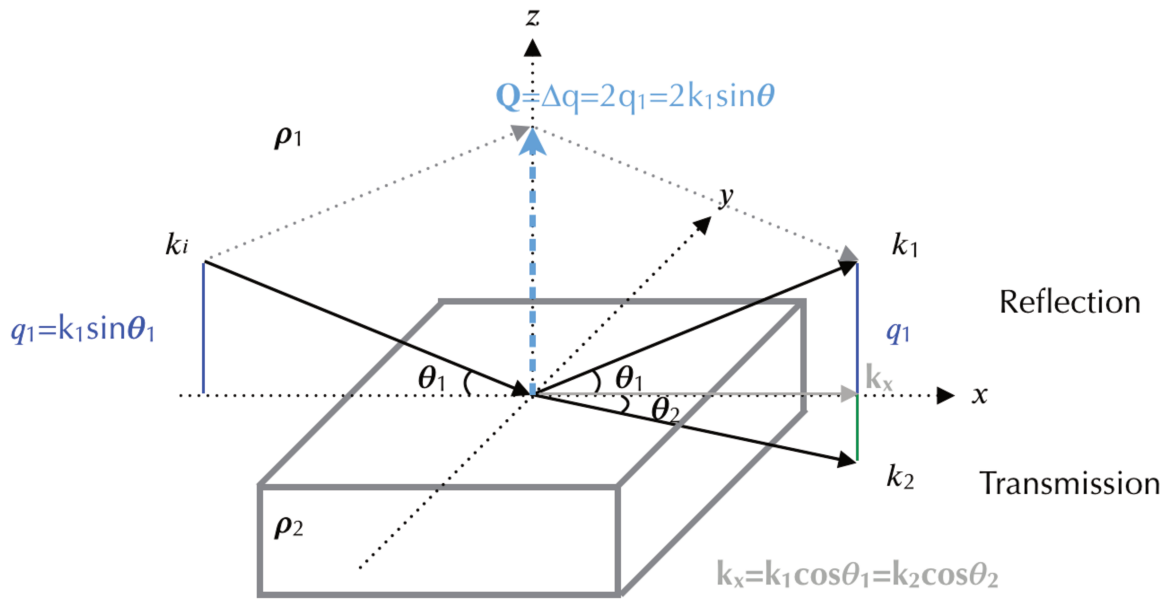

Figure 2.6 : *Illustration of neutron specular reflection and transmission on a flat interface, optical considerations. All parameters were defined in figure 2.5.*

For elastic scattering, as shown in figure 2.6, $k_1\cos\theta_1 = k_2\cos\theta_2$ **(19)**

and the momentum transfer vectors are $q_1 = k_1\sin\theta_1$ and $q_2 = k_2\sin\theta_2$ **(20)**

Also, $$k_i^2 = k_x^2 + q_i^2$$ **(21)**

So, combining **(21)** and **(13)** we obtain : $$k_i^2 = \frac{8\pi^2 m_n}{h^2}(E - V_i)$$ **(22)**

The neutron refractive index, can be defined using the convention in optics :

$$n_{12} = \frac{k_2}{k_1}$$ **(23)**

Snell's law is obtained when combining **(19)** and **(23)** : $$n_{12} = \frac{\cos\theta_1}{\cos\theta_2} \quad \textbf{(24)}$$

And combining **(23)** and **(22)** : $$n_{12} = \frac{E - V_1}{E - V_2} \quad \textbf{(25)}$$

By expressing the energy from de Broglie relation **(5)** and the potentials as in **(10)** into **(25)** we obtain a first relationship between neutron refractive index and scattering length densities :

$$n_{12} = \frac{\pi - \rho_1 \lambda^2}{\pi - \rho_2 \lambda^2} \quad \textbf{(26)}$$

Simplifying to first order as : $$n_{12} = 1 - \frac{\lambda^2}{2\pi}(\rho_2 - \rho_1) \quad \textbf{(27)}$$

If we consider that total reflection occurs when θ_2=0, we obtain through Snell's law :

$$\cos\theta_c = 1 - \frac{\lambda^2}{2\pi}(\rho_2 - \rho_1) \quad \textbf{(28)}$$

where θ_c is the angle of total reflection. It was demonstrated that the reflection occurs at the interface between two different homogeneous media, but from **(28)**, we can state that total reflection is only observed when the wave propagates from a medium with a lower scattering length density towards one with a higher scattering length density. The associated critical momentum transfer Q_c is given by :

$$Q_c = \frac{4\pi \sin\theta_c}{\lambda} \quad \textbf{(29)}$$

2.2.3. Neutron Reflection from an adsorbed layer

In soft matter experiments, it is often of interest to investigate thin films adsorbed at an interface. The presence of a film represents a further complication as two interfaces have to be considered although the Born approximation allows useful simplification.
The geometry, simplified to only one dimension since we consider only specular reflectivity in this work, is depicted in figure 2.7.

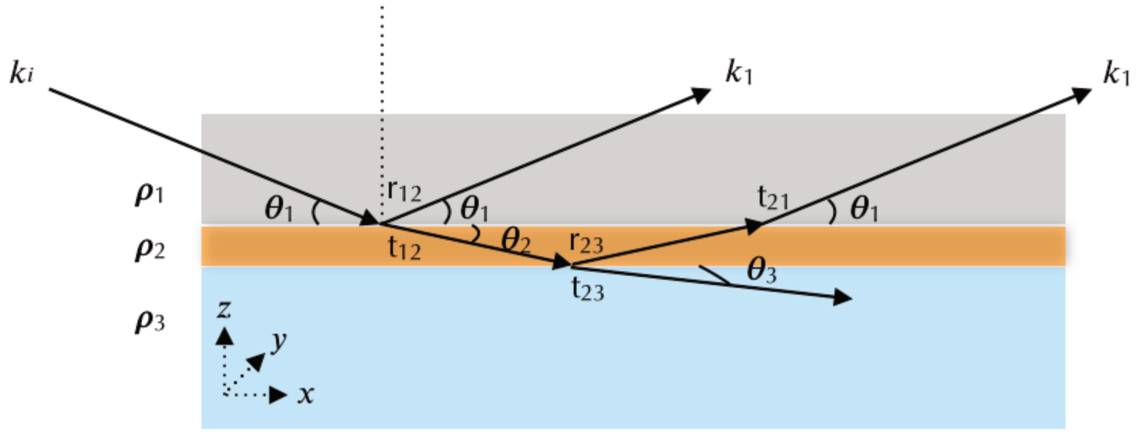

Figure 2.7 : *Representation of reflection from a thin film. With the wave vectors k_i and k_1 and angles of reflection and transmission θ_1 and θ_2 described as previously. r_{12} is the coefficient of reflection occurring at the interface between media 1 and 2 while t_{12} is the related transmission coefficient. θ_3 corresponds to the angle of refraction at the interface between media 2 and 3. ρ_1, ρ_2 and ρ_3, are the SLDs of the different media.*

By maintaining energy conservation and given the Born approximation for thin films, we can write the reflection amplitude as :

$$\underline{R} = \frac{r_{12} + r_{23}e^{2i\beta}}{1 + r_{12}r_{23}e^{2i\beta}} \qquad \textbf{(30)}$$

with β, the phase difference of a wave that has travelled through the layer once, defined as :

$$\beta_i = \frac{2\pi}{\lambda} n_i \tau_i \sin\theta_i \qquad \textbf{(31)}$$

where τ is the thickness and n_i is the neutron refractive index of a given film i.

The reflection intensity, squared modulus of the total reflection coefficient, is :

$$R = \left|\underline{R}\right|^2 = \frac{r_{12}^2 + r_{23}^2 + 2r_{12}r_{23}\cos 2\beta}{1 + (r_{12}r_{23})^2 + 2r_{12}r_{23}\cos 2\beta} \quad \textbf{(32)}$$

Note that if fringes are visible in the q-range investigated during the experiment, it is possible to estimate the thickness τ, of the layer from the positions of the reflectivity maxima and minima, as they will occur at $\cos 2\beta = \pm 1$. Thus :

$$\tau = \frac{2\pi}{\Delta Q} \quad \textbf{(33)}$$

2.2.4. Neutron Reflection from several adsorbed layers : The optical matrix method

The previous case can be more complex if we consider several layers of homogeneous, smooth materials with different SLDs. With j layers and j-1 interfaces, r and t calculations soon become tedious. A more convenient way known as the optical matrix method, developed by Abeles [91], allows expressing the reflectivity of such complex systems in a more compact manner.

A matrix describing reflection and transmission for a given layer j can be defined as :

$$\left[M_j\right] = \begin{bmatrix} \cos\beta_j & \dfrac{-i\sin\beta_j}{q_j} \\ q_j & \cos\beta_j \end{bmatrix} \quad \textbf{(34)}$$

We note also that real surfaces have a complex structure presenting shape irregularities and deviations from the perfectly flat smooth form. For silicon crystals for example, a very smooth surface is obtained by polishing, but some height irregularities are still observable, at length scales larger than the interatomic distances. This roughness appears to the incident neutrons as interdiffusion of the two materials at the interface,

and is often also evident for adsorbed layers. Roughness can be taken into consideration in the optical matrix description of the scattering process by a Gaussian smoothing function of the otherwise sharp step in the scattering length density profile. The corrected reflection coefficient r^+ can thus be expressed as :

$$r_j^+ = r_j e^{-\frac{1}{2}\kappa^2\sigma^2} \tag{35}$$

with r_j the reflection amplitude without roughness and σ the standard deviation of the gaussian equation related to the mean interfacial roughness.

We can then express **(34)** as another matrix taking into account layer thickness $\boldsymbol{\tau}$ and the neutron refractive index via $\boldsymbol{\beta}$ **(31)** as well as roughness $\boldsymbol{\sigma}$ from **(35)** :

$$\left[M_j\right] = \begin{bmatrix} e^{i\beta_{(j-1)}} & r_j^+ e^{i\beta_{(j-1)}} \\ r_j^+ e^{-i\beta_{(j-1)}} & e^{-i\beta_{(j-1)}} \end{bmatrix} \tag{36}$$

The total reflection amplitude arising from several adsorbed layers corresponds to the product of the matrices of all layers :

$$\left[M\right] = \prod_{i=1}^{n} M_i \tag{37}$$

The corresponding reflection intensity is then given by :

$$R_j = \frac{m_{12}m_{21}}{m_{11}m_{22}} = \left|r_j^+\right|^2 \tag{38}$$

2.3. Membrane Diffraction

2.3.1. General principles and theory

Diffraction occurs when a neutron interacts with a structure that is roughly of the size of the neutron wavelength. If an elastic scattering event occurs, the energy of the neutron is conserved. As before, the momentum transfer along a particular direction can thus be expressed as :

$$Q = 2k_i \sin\theta = \frac{4\pi \sin\theta}{\lambda} \qquad \textbf{(39)}$$

Moreover, the Bragg's law defines the distance d separating two atoms, or two diffraction planes leading to positive interferences of the reflected wave which leads to a diffraction pattern with distinct maxima.

$$2d \sin\theta = n\lambda \qquad \textbf{(40)}$$

Where n is the order of the Bragg reflection. n indicates that, in order to have constructive interference from individual lattice planes the optical paths must differ by an integer half-multiple (n/2) of the wavelength.

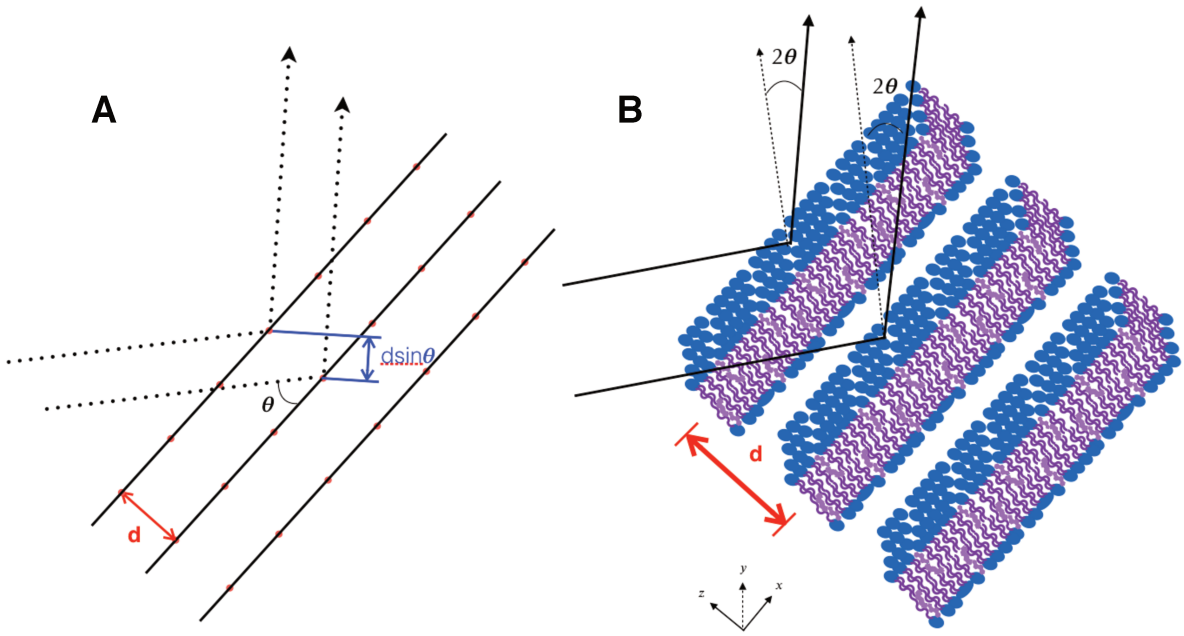

Figure 2.8 : Representation of multilayer diffraction with Bragg planes and atom positions **(A)** and corresponding stack of lipid bilayers **(B)**.

Diffraction experiments can be conducted in two ways : either by selecting a wavelength and modifying the incident angle θ by rotating the sample, or by fixing the angle while using a distribution of wavelengths in a time-of-flight experiment. Only the first case is developed in this chapter as it corresponds to the configuration employed in the experiments carried out.

The amplitude of scattering emerging from a collection of N atoms at position r_j is defined as :

$$A(Q) = \sum_{j=1}^{N} b_j \exp(iQ.r_j) \qquad \textbf{(41)}$$

where bj is the nuclear scattering length of the j^{th} atom and since the intensity I(Q) is defined by the squared modulus of the amplitudes $|A(Q)|^2$, for pairs of atoms j and k :

$$\mathrm{I}(Q) = \sum_{j,k}^{N} b_j b_k \exp\left[iQ.(r_j - r_k) \right] \qquad \textbf{(42)}$$

Neutron diffraction was historically used to locate the absolute atomic positions in a crystalline structure [92], whereas equation **(42)** uses as information a relative separation of pairs of atoms j and k. Lipid multilayers can be seen as liquid-crystalline structures and fluctuations are inherent in soft condensed matter samples. Nevertheless, a typical diffraction pattern for stack lipid multilayers gives you several types of information, including the degree of mosaicity of the sample. A very ordered sample, where the interatomic distances are constant and repeated over large distances, such as in crystals, will give very sharp and intense Bragg peaks. Mosaicity arises from misalignments of the different atom planes in different crystalline domains, and results in diffusion of the Bragg peaks. In consequence, a very ordered stack of multilayers where the symmetry is nearly perfect will diffract many intense Bragg peaks over 2θ whereas fluctuating or misaligned multilayers will not allow the observation of many Bragg peak(s). Moreover, the angular positions and intensities of 2θ of the diffraction peaks are linked to the crystal structure of the sample. Thus the peak positions and the associated real space distance(s) allow to determine the three-dimensional lipid

architecture, i.e. crystal structure of the lipid phase. Indeed, as supramolecular self assemblies, lipids can take different forms (figure 2.9).

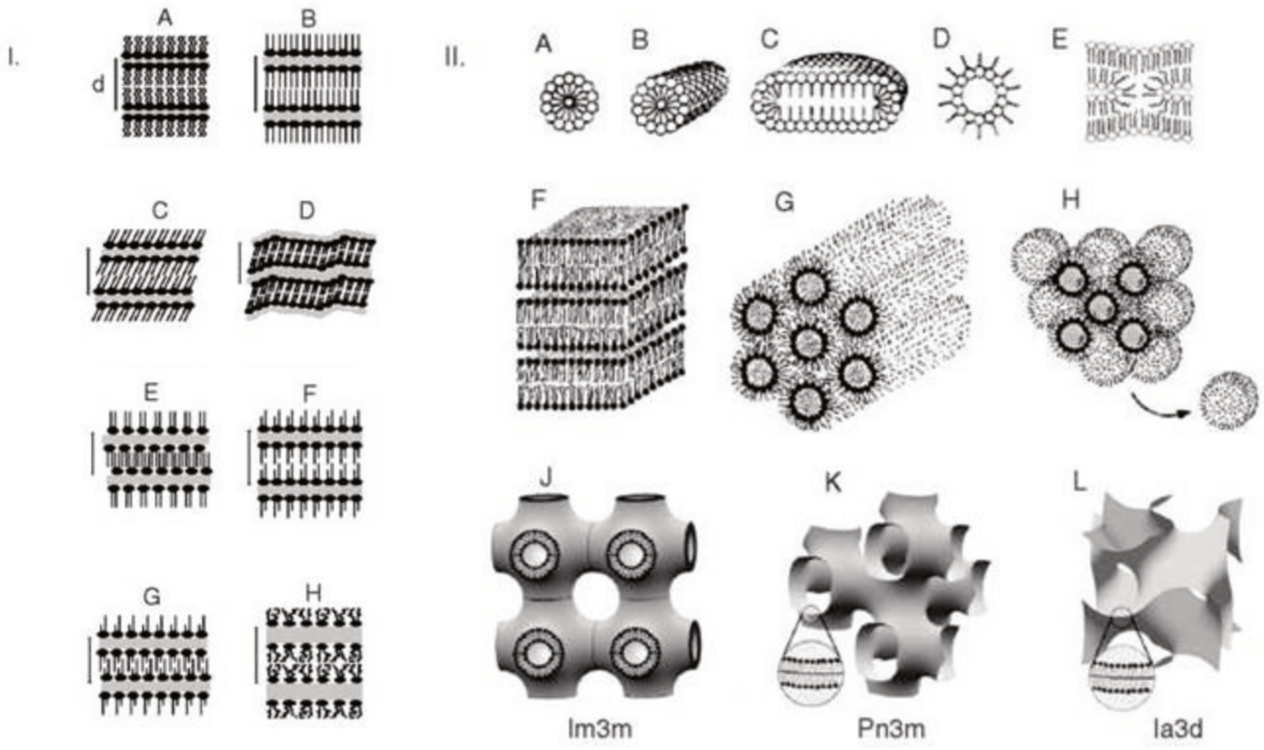

Figure 2.9 : *Lipid polymorphism* ***I.*** *Lamellar phases: (A) subgel, Lc; (B) gel, untilted chains, Lβ; (C) gel, tilted chains, Lβ′; (D) rippled gel, Pβ′; (E) fully interdigitated gel, Lβint; (F) partially interdigitated gel; (G) mixed interdigitated gel; (H) liquid crystalline, La.* ***II.*** *Mesomorphic (liquid crystalline) aggregates of various topology: (A) spherical micelles; (B) cylindrical micelles (tubules); (C) disks; (D) inverted micelles; (E) a fragment of a rhombohedral phase; (F) lamellae (G) inverted hexagonal phase; (H) inverted micellar cubic phase; (J) bilayer cubic Im3m phase; (K) bilayer cubic Pn3m phase; (L) bilayer cubic Ia3d phase. Adapted from [93].*

This polymorphism is dependent on the lipid chemical composition as well as external parameters such as temperature (thermotropic phase transitions), pressure and water content (lyotropic phase transitions) when the aggregation process is driven by the hydrophobic effect. It is thus important to take into consideration the possibility of observing other phases than the lamellar phase in diffraction experiment. The orders of reflection, the Bragg peak positions, the intensities and the diffraction patterns usually allow to determine the lipid phase without uncertainties but in the case of natural lipid the low number of diffraction order often obtained may lead to misattribution [94].

The scattering vector is inversely proportional to a real-space distance; thus, from the q-positions of the n^{th} and $n+1^{th}$ order Bragg peaks in the collected data, the characteristic lamellar d-spacing is calculated according to :

$$d = \frac{2\pi}{q_{n+1} - q_n} \quad \textbf{(43)}$$

The d-spacing includes the thickness of a lamella in the multilayer and the thickness of the water layer present between two subsequent lamellae.

2.3.2. SLD distribution

The main advantage of neutron over X-Ray diffraction is the possibility of contrast brought by deuteration. It is thus possible to determine the water and various component distributions at atomic level through thoughtful use of deuteration. Moreover, data do not need extensive model fittings as for neutron reflectometry.

Historically, membrane diffraction experiments are employed in order to reconstruct the SLD distribution within the unit cell representing the lipid bilayer by measuring a given sample in different contrasts. This is possible because the intensity of the diffraction peaks is modulated by the form factor F($\boldsymbol{\rho}$) which characterizes the neutron scattering length density distribution within the cell unit. In the case of a layered structure, the form factor is given by the Fourier transform of the SLD distribution along z, thus the intensity is :

$$\left|S(Q_z)\right|^2 \sim \left|F(\rho_{unit\,cell})\right|^2 = \int_{-d/2}^{d/2} \left|\rho_{unit\,cell}(z) e^{izQ_z} dz\right|^2 \quad \textbf{(44)}$$

In the case of a centrosymmetric system, $\boldsymbol{\rho}$(z)=$\boldsymbol{\rho}$(-z), so :

$$S(Q_z) = \int_{-d/2}^{d/2} \cos izQ_z \rho(z)\, dz \quad \textbf{(45)}$$

and has for only solutions -1 (cos(0)) and +1 (cos(180)). In order to define the phase amplitude, we fix the center of symmetry at the center of the water layer sandwiched in

between two phospholipid bilayers and vary the isotopic distribution by contrast variation of the water phase. By doing so for different isotopic mixtures, given that :

$$\rho_H(z) = \overline{\rho}_H + \frac{2}{d}\sum_n \pm\sqrt{I(n)}\cos\left(\frac{2\pi z}{d}\right) \quad \textbf{(46)}$$

it is possible to retrieve the phase information for each peak from :

$$\rho_D(z) - \rho_H(z) \quad \textbf{(47)}$$

In our case the SLD values based on lipid analysis were verified with reflectometry, however membrane diffraction can map the variations in the scattering length density distribution with a better resolution than reflectometry. But practically, a limiting factor, especially for deuterated natural lipids, is that diffraction experiment requires a large amount of sample in comparison to reflectometry. It is also worth noting that the water present in diffraction experiments is in a vapor rather than in a liquid phase. This sample restriction is necessary since the oriented stacks are not stable on a vertical geometry in liquid water.

3. MATERIALS AND METHODS

3.1. Materials

Pichia pastoris GS115A strain was obtained from Invitrogen (USA), hydrogenous glycerol $C_3H_8O_3$ (purity ≥ 99.5%) was purchased from Euromedex (France) and its deuterated version (d8, purity ≥ 98%) from Euriso-Top (France). All the salts needed for yeast growth were acquired from Sigma Aldrich (France) and used as received. Sodium chloride NaCl (≥ 99.5%), anhydrous calcium chloride $CaCl_2$ (≥ 99.0%), sulfuric acid H_2SO_4 (95 - 98%), hydrogen peroxide solution H_2O_2 (> 30%), chloroform $CHCl_3$ (≥ 99.8%), methanol CH_4O (≥ 99.8%), acetic acid glacial $C_2H_4O_2$ (≥ 99.5%), ethanol C_2H_6O (≥ 99.8%), dimethyl sulfoxide C_2H_6OS (≥ 99.9%), acetone C_3H_6O (≥ 99.8%), isopropanol C_3H_8O (≥ 99.5%), Ethyl acetate $C_4H_8O_2$ (≥ 99.5%), diethyl-ether $C_4H_{10}O$ (≥ 99.7%), n-hexane C_6H_{14} (≥ 99.0%) and heptan C_7H_{16} (≥ 99.0%) were purchased from Sigma Aldrich (France) and used without further purification. 1-palmitoyl-2-oleoyl-*sn*-glycero-3-phosphocholine (h-POPC) was purchased from Avanti Polar Lipids (USA) and the perdeuterated (d-82)POPC was synthesized chemically [49] and provided by the National Deuteration Facility (NDF, Australia). Cholesterol (h-Chol) and ergosterol (h-Erg) were obtained from Sigma Aldrich (France). Deuterated Cholesterol (d-Chol) was produced and purified by the Deuteration Laboratory team (D-Lab, ILL) [95], and deuterated ergosterol (d-Erg) was purified from deuterated yeast lipid extracts, as explained below. Amphotericin B $C_{47}H_{73}NO_{17}$ (from *Streptomyces sp.*, purity ~80%) was purchased from Sigma-Aldrich (either France or Australia) and used without further purification. H_2O was taken from a purifying system (MilliPore; resistivity >18 MΩ.cm) and D_2O (> 99%) was provided by Institut Laue-Langevin (ILL) and the Australian Nuclear Science and Technology Organization (ANSTO). The deuterated methyl pentadecanoate ($C_{15:0}$ Me) was synthesized by the STFC Deuteration Facility at the ISIS

Neutron and Muon Facility in Didcot (UK). All other phospholipid and fatty acid standards for chromatographic uses (liquid and/or gas) were purchased either from Avanti Polar Lipids (USA), Sigma Aldrich (France) or Larodan Fine Chemicals (Sweden). 80x50x15 mm^3 silicon single crystals polished on the (111) face to a typical roughness of < 3Å were purchased from Synchrotronix (France) and used for neutron reflectometry (NR) measurements whereas thin silicon wafers (40x30x0.5 mm^3) acquired from Silicon Materials (Germany) were used for neutron diffraction experiments. 80x50x15 mm^3 sapphire crystals (random orientation) were purchased from PI-KEM Limited (UK). Quartz crystal sensors QSX303 were bought from Biolin Scientific (France).

3.2. From yeasts to lipids

3.2.1. Yeast growth

3.2.1.1. *Pichia pastoris*

For the neutron reflectivity and diffraction experiments, *Pichia pastoris* (GS115A strain) was grown in the Deuteration Laboratory (D-Lab) at ILL in either hydrogenous or deuterated conditions following the same protocol as previously published [50]. Briefly : the cells were grown first at 30°C in Pichia growth medium called Buffered Glycerol-complex Medium (abbreviated as BMGY) in a shaking flask tapped with a vent cap for a couple of days. 2mL of this culture was added into 500mL of minimal medium (BSM) and grown at 30°C with permanent shaking for 2-3 days. Cells were harvested by centrifugation when the optical density at 600nm (OD_{600}) reached 20. This corresponds to the early exponential phase and allows good recovery and reproducibility in the cell phospholipid content and composition. In order to grow in perdeuterated conditions, the yeast needed to be pre-adaptated. Thus, 1mL of the hydrogenous first culture was diluted into 100 mL of perdeuterated BSM for 5 days and inoculated again few times in freshly made perdeuterated BSM medium until the growth rate improved (~3 inoculations needed). The adapted yeast was then inoculated in a 500mL deuterated batch as explained above for hydrogenous conditions.

With the aim of studying the effect of the carbon source on the yeast lipid composition, two others conditions were investigated for the growth of the Pichia pastoris (GS115A

strain) in both hydrogenous and deuterated media. In the first case, a growth with glycerol, as previously described, was followed by addition of methanol into the medium whereas in the other case, methanol was used as unique carbon source. The first condition corresponds to the protocol used for deuterated protein production [96]. Besides the changes of carbon sources, the procedure had to be adapted as such : in the first case the cells were initially grown until OD_{600}= 50 before centrifugation and resuspension into BSM to which was added 1% (in volume) of methanol per day, over 17 days. In the second conditions, inoculation at OD_{600}= 1, instead of the usual 0.1, in BSM was necessary in methanol-only conditions in order to allow cell growth at first. The amount of methanol used as carbon source was fixed at 0.5% v/v of the final volume of the medium and added everyday. Cells were harvested at OD_{600}= 30.
Perdeuterated cholesterol, purity ≥ 98%, was produced by the ILL D-Lab in Grenoble using the recombinant cholesterol producing Pichia pastoris strain CBS7435 Δhis4Δku70 Δerg5::pPpGAP-Zeocin™-[DHCR7] Δerg6::pGAP-G418[DHCR24] [97], after adaptation to growth in deuterated minimal medium. Details of the production and purification performed by the D-Lab in collaboration with the Austrian Center of Industrial Biotechnology in Gratz (Austria), will be published elsewhere [95].

3.2.1.2. *Candida glabrata*

The potential pathogenic yeast *Candida glabrata* was grown as a candidate for deuteration, lipid production and investigation of the relationship between genetic variation and virulence factors/resistance to AmB.

A *C. glabrata* gene library was created using a plasmid (P1226) by Olena Ishchuk at Lund University. The resulting gene library of plasmids, covering at least fifteen times the genome of *C. glabrata*, was used to transform the *C. glabrata* strain with a reconstituted RNA interference (RNAi) pathway. RNAi is an ancient regulatory mechanism for eukaryotic gene expression [98] that has been lost by most of the budding yeasts even though it is present in many organisms. But after *Saccharomyces castellii* was found to possess the full RNAi machinery [99], it was shown that the RNAi machinery could function in *C. glabrata* by silencing reporter genes [100]. The strain **Y1662** carrying this RNAi machinery based on the clinical BG2 isolate **Y1630**

described by Cormack & Falkow (1999) [101] and previously Fidel et al. (1996) [102] was thus created.

By introducing a plasmid carrying an antisense or a hairpin genetic element into *C. glabrata* with a reconstituted RNAi pathway, it is possible to specifically down-regulate the target gene. On the other hand, a sense fragment allows over-expression of a gene. Thus both sense and antisense DNA fragments can determine the transformant's phenotype [103] which, in this work, was focused on the antifungal drug resistance towards AmB.

The phenotype of around 2000 transformed colonies were screened by Olena Ishchuk for altered resistance/sensitivity towards a range of AmB concentrations (0.25 – 1 µg/mL) on solid media. The plasmids and the inserted sequences were isolated from 15 hits. The plasmids were then retransformed into *C. glabrata* and the phenotype (resistance/sensitivity towards AmB) verified after retransformation. Twelve were found to show the same phenotype in both rounds of screening [103]. Two of these strains were selected for firsts analytical and structural characterization experiments (Table 1).

Plasmid name / strain name	Gene info	Gene	AmB sensitive	AmB resistant	Type of plasmid
61 (Y2310)	*CSM1*	*CAGL0E00539g*		**+**	antisense
81E18 (Y2311)		*CAGL0L00157g*	**+**		antisense

Table 3.1 : *Summary of the plasmids associated to the strains that were selected for the first characterization experiments with respect to analysis of lipid contents due to their sensitivity/resistance toward AmB.*

Thus, the four *C. glabrata* strains used in this thesis are **Y1630** (clinical isolate BG2), **Y2296 (**transformed Y1662 with empty plasmid), **Y2310** (transformed Y1662 with plasmid 61 - see table 3.1) found to be more resistant in the screening against AmB than Y1630 and Y2296, and **Y2311** (transformed Y1662 with plasmid 81E18 - see table 3.1) found to be more sensitive in the screening towards AmB than Y1630 and Y2296.

For lipid production purpose, pre-culture of the four different *C. glabrata* strains listed above were prepared by direct inoculation of the cells, from stock cultures kept at

-80°C, to 3 mL of hydrogenous minimal medium SDG (2% glycerol, 1.92 g/l YNB without amino acids and $(NH_4)_2SO_4$, 5 g/L $(NH_4)_2SO_4$, H_2O, pH 6.0,) and grown at 25°C while shaking at 200 rpm. Cells were grown for up to 7 days until they reached the OD_{600} sufficient for inoculation to OD_{600} = 0.1 of 250 mL of either hydrogenous or deuterated minimal media SDG (h-glycerol and H_2O in the first case and d-glycerol and D_2O in the second case), all other constituents being unchanged, in a 1L Erlenmeyer flask kept at 25°C and shaking at 200 rpm. Cells were harvested by centrifugation after 5 days of growth (hydrogenous conditions) or 10 days (deuterated conditions).

3.2.2. Lipid extraction

The yeast cells were harvested, according to the OD_{600} values, by centrifugation quickly followed by freezing the cells in liquid nitrogen before being placed in a freeze-drier overnight. The lipids were then extracted from the dried yeast cells according to the modified Folch extraction procedure [104] as previously described by de Ghellinck et al. [50]. In brief, after grinding a pellet in a frozen mortar over dry ice, the powder was suspended in boiling ethanol for 5 minutes to prevent lipid degradation by lipase enzymes. Lipids were extracted by addition of methanol and chloroform at room temperature and the mixture was saturated with argon and stirred for at least 1 hour. After filtration through ethanol-cleaned glass wool, cell remains were rinsed with a chloroform/methanol solution 2:1 (in volume) and NaCl 1% was then added to the filtrate. After saturation with argon and phase separation, the lower phase (mainly chloroform) containing the lipid extract was recovered and dried. As the organic phase contains methanol and a small portion of water, some water-soluble molecules can be dissolved into it. In order to remove these components, a final extraction with pure chloroform was performed. The total lipid extract obtained after drying the chloroform was stored at - 20°C until further use.

3.2.3. Analysis and quantification

The lipid analysis was adapted from the method presented in de Ghellinck et al. [50]. The total lipid extract, as described earlier, was dissolved in the minimum amount of

chloroform and the equivalent of 200 µg of lipids was deposited on a 20x20 cm glass plate coated with silica (silica gel 60, Merck) using a Hamilton syringe. In order to perform a two-dimensional thin layer chromatography (2D-TLC), a first elution was performed followed by a second one after the plate has been dried under vacuum - or a stream of argon - and rotated of 90°. The solvent systems used were chloroform/ methanol/water (65:25:4, in volume) and chloroform/acetone/methanol/glacial acetic acid/water (50:20:10:10:5, in volume).

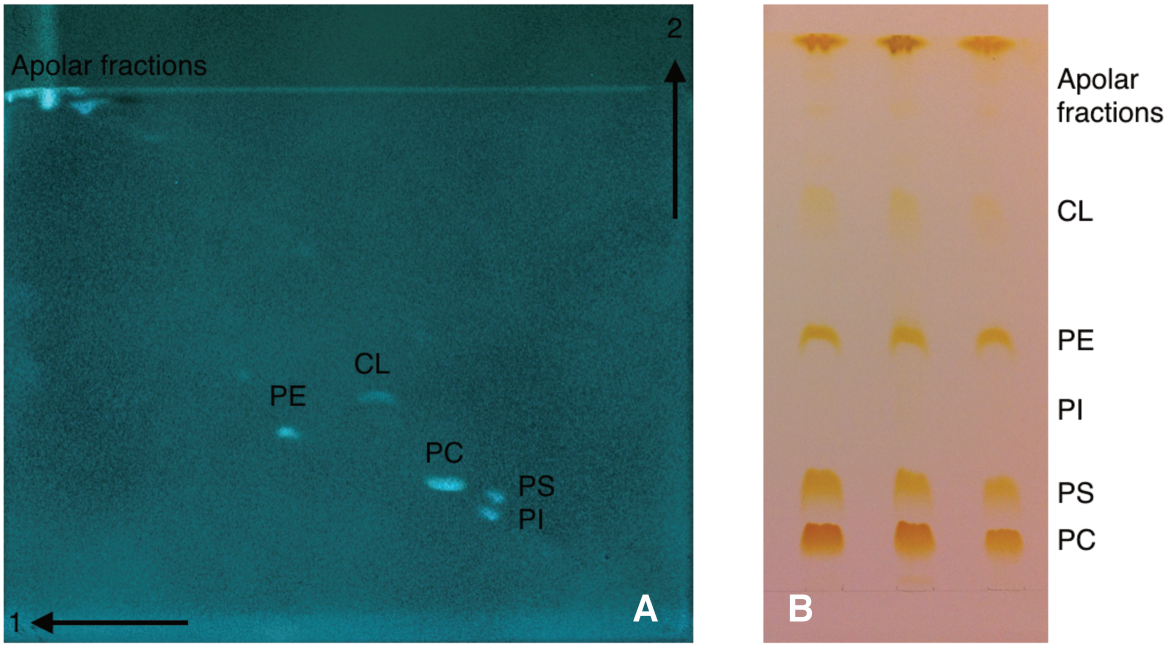

Figure 3.1 : *TLC systems and lipid attributions based on comparison with standards.* ***(A)*** *2D TLC with solvent systems chloroform/methanol/water (65:25:4, in volume) and chloroform/acetone/methanol/glacial acetic acid/water (50:20:10:10:5, in volume) used respectively for migration 1 and 2. The plate was revealed under UV light at 366 nm.* ***(B)*** *One-dimension TLC with chloroform/methanol/glacial acetic acid (65:28:8) used as solvent system. Revealing agent : I_2 vapor.*

Due to the well defined constituents of the lipid mixtures, a simplified separation [105], using a unique elution with chloroform/methanol/acetic acid (65:28:8) as solvent system was performed in order to decrease the time of analysis and thus the probability of degradation of phospholipids. Indeed, in contact with oxygen and/or light, lipids can either be oxidized or decomposed [106], modifying the composition over time and so the relevance of the mixtures.

Lipids were visualized either under ultraviolet light (UV) after the plate was stained with 8-anilino-1-naphthalenesulfonic acid (2% in volume in MeOH), or using I_2 vapor without previous staining (figure 3.1). The marked spots, assigned with respect to standards, were scraped off the TLC plates using a spatula. Each recovered silica spot, corresponding to different lipid fractions was placed in a capped tube to which 10 µL of a 0.5 µg/µL solution of hydrogenous methyl pentadecanoate was added as an internal standard for gas chromatography analysis. Hydrolysis of the phospholipids and methylation of the fatty acids were then performed by addition of 3 mL of H_2SO_4 in methanol (2.5% in volume), and the solutions heated at 100°C for one hour. The reaction was quenched by the addition of 3 mL of water and 3 mL of hexane were finally added in order to extract the fatty acid methyl esters (FAMEs) formed. The hexane extraction was repeated twice before the organic phases were combined and dried under argon. The dried FAMEs could be kept at -20°C for several months, but were usually analyzed within 24 hours.

The dried FAMEs were re-suspended in 500 µL of pure n-hexane and 5 µL was injected into a gas chromatography (Shimadzu GC 2010 Plus) coupled to a flame ionization detector (FID). The capillary column used was a BPX70 (SGE) : 70% Cyanopropyl Polysilphenylene - siloxane, with film thickness, 0.25 µm, length, 25 m and internal diameter (ID), 0.22 mm, mainly dedicated for polyunsaturated FAME analysis. The samples were injected in a split mode injector at 250°C with a split ratio of 80. The pressure and the purge were set following the SGE technical advice at respectively 120 kPa and 10 mL, the column flow being automatically adjusted. The column was firstly equilibrated for 3 minutes at 155°C and then warmed up to 180°C with a step of 2°C/min followed by an other one of 4°C/min, until 220°C was reached. This final temperature was maintained for 5 min. Helium (Purity ≥ 99.999%) was used as a carrier gas with a flow rate of 1.04 mL/min. The FID temperature was set to 260°C. FAME retention times were compared with those of hydrogenous standard FAMEs (Larodan). Deuterated FAMEs have a shorter retention time than the hydrogenous ones due to isotopic effect. The quantification of the different FAMEs was established by direct comparison to the amount of internal standard, assuming no response factors deviation between the different fatty acids, all considered as long fatty acid chains.
A first total extract FAME analysis without performing TLC was prepared and performed in order to define the microgram equivalents of fatty acids with respect to the internal

standard (methyl pentadecanoate). To do so, the peaks were assigned manually by direct comparison of retention times (figure 3.2) and the corresponding areas expressed as internal standard equivalents. The volume associated to 200 µg standard equivalents was deposited onto the TLCs. Each GC trace corresponding to each spot was analyzed as before. For each fatty acid, the quantities expressed in microgram equivalents of internal standard were calculated in nano moles with the corresponding molar mass. The molar ratio of each fatty acid corresponding to each separated classes were compared and normalized to the total amount.

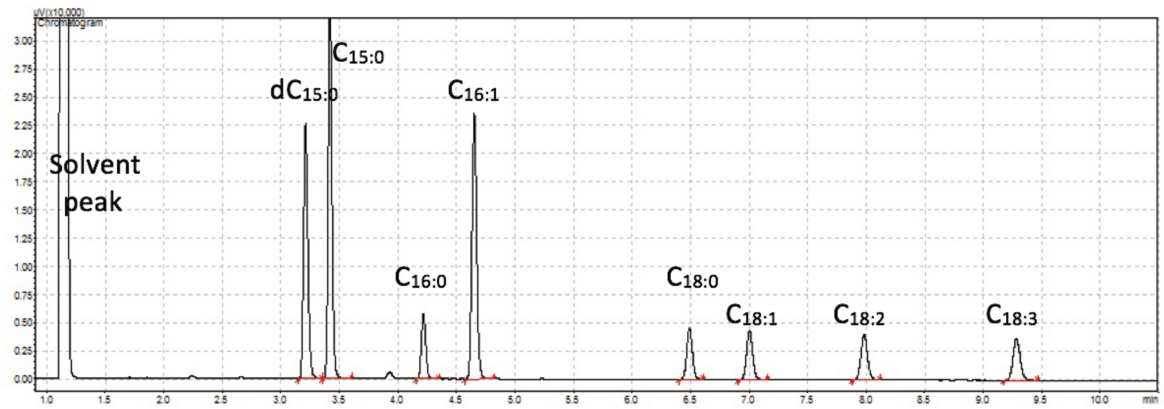

Fatty acids	*dC15:0*	*C15:0*	*C16:0*	*C16:1*	*C18:0*	*C18:1*	*C18:2*	*C18:3*
Retention time (min)	**3.21**	**3.42**	4.23	4.65	6.50	7.00	7.98	9.28

Figure 3.2 : *GC standard traces and associated retention times. We expect a ∂Rt of 0.2-0.5 min between deuterated and corresponding hydrogenous FAME.*

By using a less polar BPX5 capillary column (SGE) : Phenyl Polysilphenylene - siloxane, with film thickness 0.25 µm, length 30 m and internal diameter 0.22 mm, native sterols could also be analyzed. The program involved an injection of the samples (5 µL of a solution of 4 µg/µL of total extracts in n-hexane/EtOH 95/5 v/v) in split mode at 350°C with a split ratio 100 once the column was equilibrated at 280°C. The initial temperature was held for one minute followed with a step of 4°C/min in order to reach 350°C. The final column temperature was maintained for 5 min. The FID detector temperature was set to 360°C. The column flow of the carrier gas, Helium, was set to 1.34 mL/min. Cholesterol, lanosterol (Sigma) and ergosterol (Larodan) standards as well as the deuterated ergosterol produced and purified from *P. pastoris*, were used to define the retention times. A calibration curve with ergosterol standard was performed and

used for yeast sterol quantification. The total lipid extracts were diluted to a concentration of 100µg/µL in chloroform/methanol (2:1 in volume). 20µL were place in a GC vial and dried under argon. 500µL of a solution of hexane/ethanol (95:5 in volume) were used to solubilize the samples. 5µL were injected into the GC with the program detailed above. The corresponding quantities extracted from peak surface, calibration curve and molar masses (h and d ergosterol) were established in mol%.

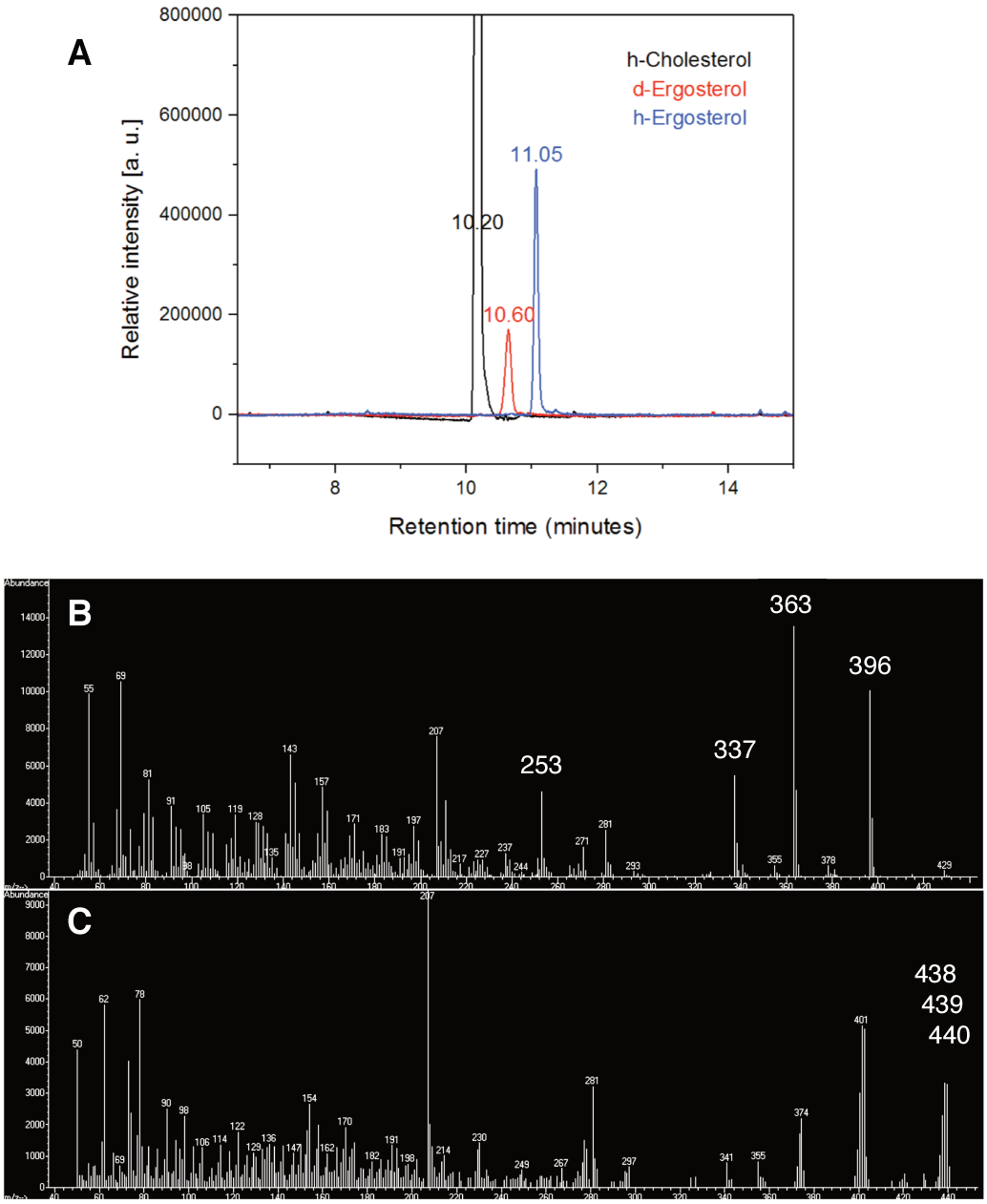

Figure 3.3 : *Separation by gas chromatography of the different sterols* ***(A)*** *and mass spectra of the hydrogenous* ***(B)*** *and the deuterated* ***(C)*** *ergosterol.*

For the apolar unknown species, mass spectrometry was performed for full determination. The measurements were performed on a GC/MS instrument, an Agilent 6890 Series GC system coupled to an Agilent 5973 Network Mass selective detector. This impact ionization detector allowed to observe the ionized molecules and fragmentations after separation on the BPX5 capillary column (SGE) described previously. The program involved is exactly the same as for sterol analysis with GC-FID. But, the instruments employed being different, the column flow of the carrier gas, Helium, was adjusted to 1.4 mL/min to maintain a constant 138kPa pressure in the system. Cholesterol standard (Sigma) was used to define its retention time. The degree of deuteration of ergosterol was defined by its mass spectra (see figure 3.3) and is consistent with perdeuteration.

3.2.4. Separation and purification

In order to obtain well defined samples, some purification and separation steps were needed. The first step was to separate the total extract into the polar phospholipids and the apolar lipids. This was carried out as described in de Ghellinck et al. [50].

Separation of the different phospholipid classes could also be performed via liquid chromatography. The different constituents of the total extract were well separated (except for PS and PI) by a single separation column using the following mobile phase on silica : $CHCl_3$/MeOH/Isopropanol/H_2O in volume ratio of 65:20:5:4. *This should be a starting point for an effective separation of lipid components from complex mixtures*. The lipid separation was performed with very good recovery ratio as less than 2% in mass were lost during the all process.

Finally, the sterol fraction, primarily containing ergosterol, was purified from the dried apolar fraction by a classical re-precipitation using the minimum amount of heptane as solvent. The apolar fractions were separated in three fractions, the pure deuterated ergosterol, a fraction of other apolar components without ergosterol and a small mixture of both components that was set apart as separation was tedious. The purity of the recovered white powders (h or d), through filtration and rinsing with a minimum of heptane, were tested on the GC and found to be of superior grade (> 95.0%) than the commercial hydrogenous ergosterol.

3.3. From lipids to samples

3.3.1. Sample preparation

All lipid fractions were stored as recommended in Christie & Han [107], i. e. dry, under argon, in a brown vial, with the cap covered with parafilm, at -20°C.

In order to prepare the samples, the different lipids or fractions were taken out of the freezer before being dissolved in a chloroform/methanol solution, 2:1 (in volume) to a given concentration. The volume of each constituent necessary for a sample was withdrawn with an Hamilton syringe (either of 10, 100 or 500µL) from these stock solutions and the constituents combined in a cleaned clear 5mL vial. Thus, the different lipids were mixed together in an organic solvent as this assures good miscibility of all the lipid species, poorly soluble in water otherwise. The solutions were dried under a stream of argon while rotating the vial horizontally. The objective was to deposit, as a uniform film as possible, the dried mixed lipids onto the glass of the vial. By doing so, the lipids were forced to be in contact with the aqueous solution successively added into the vial, and allowed quicker hydration. The specific procedures, dependent on the techniques and the lipid used, were as follows: for Quartz Crystal Microbalance with Dissipation (QCM-D) and neutron reflectometry (NR) experiments, pure water (light or heavy) was added to the dried films composed of synthetic lipids as main constituents. In the presence of a complex yeast phospholipid mixture, as deposition on the solid substrates was either partial or non existent using pure water, solutions of 100 mM NaCl and 20 mM $CaCl_2$ were used. The choice of the water was dependent on the nature of the samples, as explained for QCM-D measurement, see chapter 3.3.3. For NR, the sample geometry of the instrument also had to be taken into consideration, and this is explained in chapter 3.3.4. All solutions described above were prepared to a concentration of 0.5 mg of lipids per mL, for a total volume of 1.5 mL (QCM-D) or 3 mL (NR).

For membrane diffraction studies, the samples had to be dissolved in a mixture of chloroform and isopropanol 1:4 (v/v) at a concentration of 20 mg/ml.

The 1mM solution of AmB in D_2O-DMSO (9:1 volume ratio) was prepared from a 10 mM AmB stock solution in DMSO. Note that at least half an hour, or mild sonication, was necessary to completely dissolve the yellow powder in DMSO. If the powder was not perfectly dissolved in DMSO at the moment of the water addition, the aggregates remained even if a strong sonication was employed.

3.3.2. Surface treatments - Cleaning

The silicon and sapphire crystals (80 x 50 x 15 mm^3) used for reflectivity experiments were all prepared in the same way. After rinsing with water, they were immersed in a solution of 2% Decon Neutracon®, and sonicated for 15 min using a water sonicating bath. This allows to remove all organic material that could have been present on the crystals. After extensive rinsing with MilliQ water, the dried blocks were immersed in a mild piranha solution (H_2O, H_2SO_4 & H_2O_2 in volume proportions 5:4:1) for 30 min at 82°C. The cleaned substrates were kept in a beaker of MilliQ water until a UV/Ozone treatment (Jelight 144 AX at ANSTO or Bioforce nanosciences ProCleaner™ Plus at ILL) of 10 min was performed just before assembling and filling the reflectivity cells (see figure 3.4) with D_2O, generally the night before the beginning of the experiment.

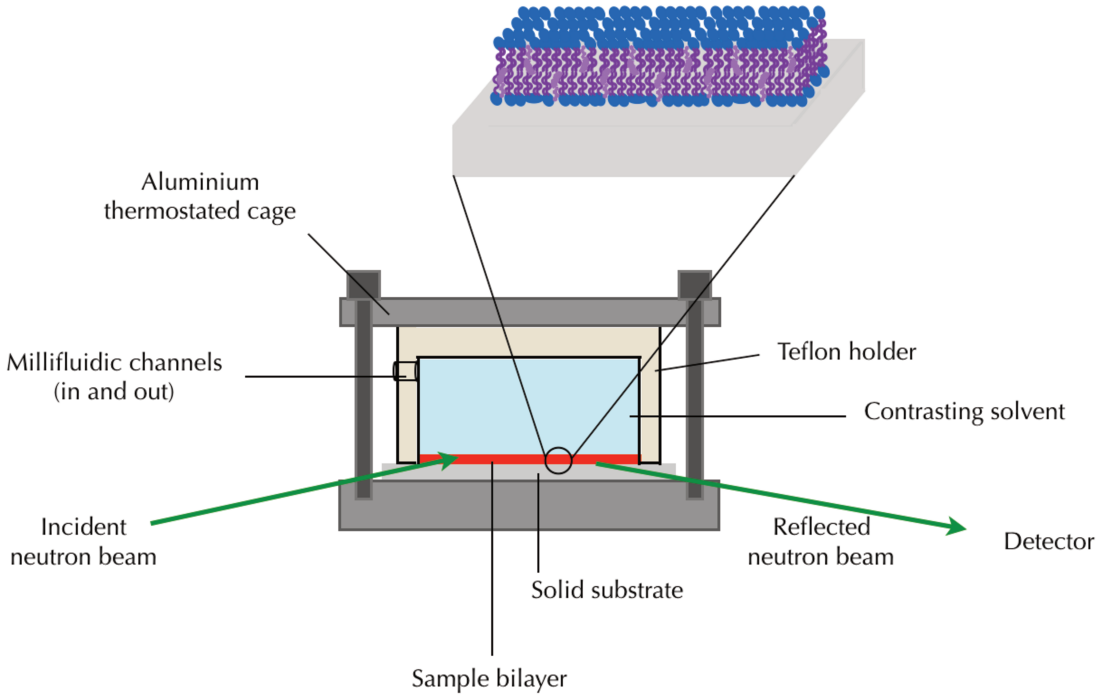

Figure 3.4 : View of a neutron solid/liquid reflectivity cell for interface study. Adapted from [108].

The PEEK cells and O-rings were sonicated in a solution of 2% Decon 90®, followed by several rinsing and sonication steps in MilliQ water. The inlet and outlet tubes were rinsed successively with Decon 90®, pure water, ethanol and MilliQ water again.

Thin silicon wafers (4 cm x 3 cm x 0.5 mm), for diffraction studies means, were cleaned by sequential sonication in chloroform, acetone, ethanol followed by Plasma or UV/Ozone Cleaner treatment (Bioforce nanosciences ProCleaner™ Plus). For the QCM-D sensors, the treatment is the same as for thin crystals, as a piranha cleaning would remove the silica and gold coatings on the quartz crystals. The other parts of the QCM-D chambers were treated as for the polyether ether ketone (PEEK) pieces.

3.3.3. Vesicle fusion - Deposition for QCM-D measurements

In QCM-D measurements, the planar supported bilayers were prepared by using the vesicle fusion method [109]. Two conditions are to be mentioned.

In the case of synthetic lipids, the samples were dispersed in pure water using a tip sonicator (Sonopuls HD 3100 - Bandelin) by repeated pulses (3'' ON, 5'' OFF) with an amplitude of 80% until the samples became clear (~5min). 900 µL of the vesicles solution were immediately injected after sonication at a flow rate of 150µL/min over 6 minutes into the QCM-D cell kept at 30°C. The flow was then stopped and the lipid suspension was incubated for 10 to 30 minutes in the cells to allow the vesicles to fuse on the crystals. Restarting the flow (150µL/min), rinsing with pure water until stable signals (Δf and ΔD) was achieved, allowed to remove the vesicles in excess and obtain a single lipid bilayer on the crystal.

In the case of samples containing extracted lipid mixtures from yeasts, they were sonicated in salt solution (100 mM NaCl and 20 mM $CaCl_2$) for at least 30 minutes. Note that with this amount of calcium, the solution remains turbid. The injection was made into the QCM-D chambers pre-heated at 52°C at a flow rate of 150µL/min over 6 minutes. After 30 minutes of incubation time, the cells were firstly rinsed with the corresponding salt solution and with pure water with a low rate of 150µL/min as long as necessary in order to obtain stable signals (Δf and ΔD). The water used in the sample preparation was chosen to match the deuteration and hence density of the sample.

Perdeuterated and mostly deuterated samples were dispersed in heavy water (or heavy water salt solution) whereas hydrogenous and mostly hydrogenous samples, in light water (or light water salts solution). Note that the QCM-D chambers were always first filled with the same solution used in the preparation of the corresponding samples and a baseline trace was obtained for the same solution density.

3.3.4. Vesicle fusion - Deposition for NR experiments

In NR experiments, the planar supported bilayers were also prepared by using the vesicle fusion method [109]. For synthetic lipids, the sonication was performed as for QCM-D and the density of the water was found to be of no significance of the deposition of deuterated or non-deuterated samples. Vesicles in solution were immediately injected after sonication into the neutron reflectivity cell. The lipid suspension was incubated for 30 minutes, typically at 30°C to mimick the yeast growth temperature, for subsequent AmB experiments. Samples were rinsed with the same water as they were prepared in.

In the case of samples containing extracted lipid mixtures from yeasts, the following procedure was adopted after two neutron experiments as the depositions of some samples were not successful. Indeed, all samples were firstly dissolved in light water while the instrument was in the 'reflection down' geometry in which the silica surface is below the solution. All hydrogenous, or mostly hydrogenous samples were deposited successfully in this geometry while all deuterated/mostly deuterated samples were displaying Bragg peaks, indicating that partial double or multiple bilayers were deposited by the deuterated vesicles sinking in the light water. The additional layers could not be removed by rinsing or osmotic shock (rinsing with pure water) and thus the interpretation of the AmB results in such circumstances is not simple. When the opposite samples displayed the same behavior in the other geometry of the instrument 'reflection up', it was understood that the deposition geometry and density of the water relative to the density of the lipids was of prime importance as in the lipid dendrimer mixtures investigated on FIGARO [110].

Thus, the samples were sonicated in a density-matched salt solution (100 mM NaCl and 20 mM $CaCl_2$) for at least 30 minutes. The injection was made into neutron cells placed

horizontally, previously filled with the corresponding salt solution, pre-heated at 52°C. After the 30 minutes of incubation time, the cells were firstly rinsed with the corresponding salt solution and with the isotopic water with the closer density towards the salt solution previously used, i.e. H_2O for H_2O salt solution and D_2O for D_2O salt solution. The temperature was then lowered to 30°C in order to mimic the conditions at which the yeasts were grown.

3.3.5. Formation of membrane stack

For diffraction studies, as deposition of multilayers is needed, the process was completely different. The method that has given more promising results was the rock'n'roll deposition [111]. 200 µl of the synthetic lipid solutions, 20 mg/ml in chloroform and isopropanol 1:4 (v/v), were spin coated (Suss MicroTec Delta 6RC) with a first step of 10 seconds at 500 rpm and a second step of 20 seconds at 3000 rpm, on the cleaned thin silicon wafers (4 cm x 3 cm x 0.5 mm). 200 µl of the natural lipid solutions (total extracts or phospholipids) were spread on the cleaned silicon wafers and let dry via evaporation in a cold room operating around 8°C. *The different deposition process is meant to leave the maximum amount of natural lipids on the surface as the diffraction pattern obtained in this case rarely gives more than two Bragg peaks. Indeed, the spin coating deposition for natural lipids either gave no or only one diffuse Bragg peak.* All the wafers, with both natural and synthetic lipids, were stored under vacuum at 50 °C for at least 6 hours before being placed on the neutron beam.

3.4. From samples to data

3.4.1. QCM-D experiments

The QCM-D device used was a model E4 purchased from QSense. The pump associated (IPC 4 Channel from Ismatec) allows a precise control of the volume and/or flow rate of the solution injected into the cell. Once the crystals were cleaned (see chapter 3.3.2) and dried, the cells were mounted, closed, filled with solution and equilibrated with both temperature and flow rate set. Note that a total volume of 300 µL was needed in order to fill entirely the cell and the associated flow paths. The experiment was initiated when the baseline, in pure water or salt solution, was stable

over the first two to three minutes, meaning the instrument was clean and equilibrated. A common 150 µL/min flow rate was used for all measurements.

After injection and deposition of the samples during which the flow was stopped for 15 to 30 minutes, the flow was restarted and the vesicles not adsorbed on the crystals were rinsed away. After stabilization of the signals, 600 µL of a solution of 1 mM of AmB were injected in the cells and left to incubate with the membrane for 30 min. A final rinsing was performed until a stable signal was reached.

In the case of complex lipid mixtures, as the membranes were deposited at 52°C, the AmB interaction characterization had to be performed in a separate measurement. Indeed, temperature has an impact on the frequencies and dissipations of the quartz crystals. It was thus necessary to lower the temperature of the cell to 30°C. Change of the rinsing solution with water was also performed, indifferently before or after change of temperature. Both temperature and water were necessary to measure a new baseline. The interaction of AmB with the lipid bilayer was then performed by injection of 900µL of a solution of 1mM of AmB at a flow rate of 150 µL/min. An incubation time of 30 min was respected and the flow rate restarted until a stable signal was obtained. Many samples and conditions, such as temperature of deposition, nature of the solution, preparation of the AmB solution have been investigated. Data were used qualitatively (direct Δf and ΔD comparisons) and the graphs were only modified for clarity using the software Q-tools.

3.4.2. NR experiments

The measurements performed on synthetic lipids were carried out on the Platypus neutron reflectometer at ANSTO (Lucas Heights, Sydney, NSW) [112] in time-of-flight mode using a neutron wavelength spectrum from 2.8 Å to 18 Å at two incident angles, 0.8° and 4° for measurement in D_2O, CMSi and H_2O and three incident angles 0.6°, 0.8° and 4° for better sensitivity towards measurements performed at contrast match 4 (CM4). This geometry allowed covering a Q-range from 0.009 to 0.25 $Å^{-1}$ in a low resolution mode ($\Delta\lambda/\lambda$ = 7%). The incident beam is guided to the sample by the control of the openings of a series of slits clearly shown on the instrument layout depicted in

figure 3.5. The choppers, needed for time-of-flight experiments, allow to segment the continuous beam and select the wavelength spectrum wanted.

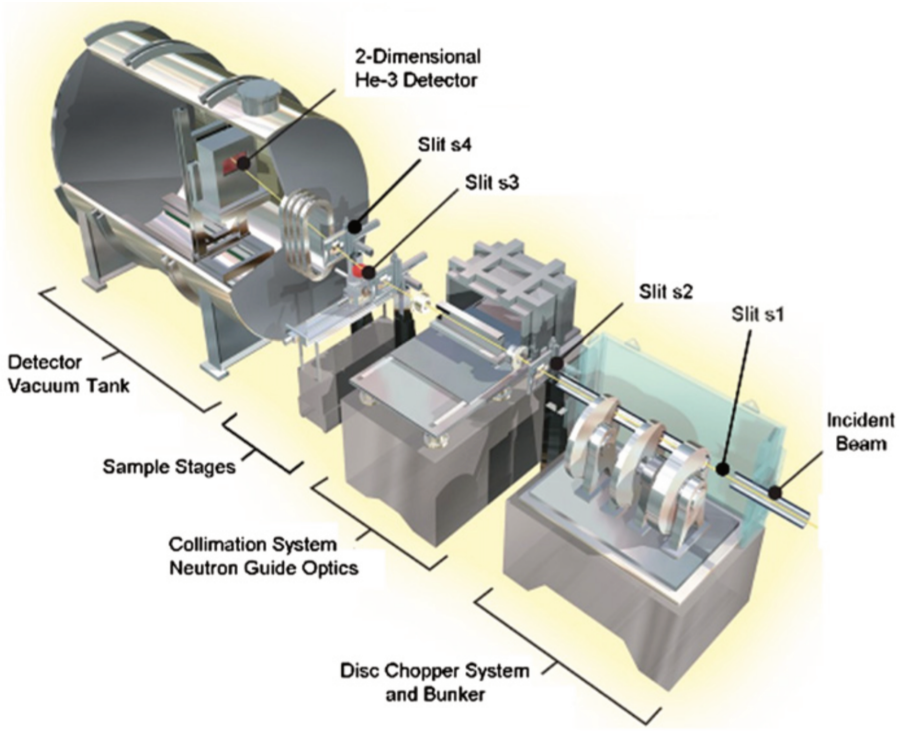

Figure 3.5 : Depiction of the Platypus time-of-flight neutron reflectometer. From [112].

The detection of the reflected neutrons was obtained thanks to a ^{3}He gas detector with a 2D area of 500 mm wide by 250 mm high and a 2 mm and a 2.5 mm vertical and horizontal resolution, respectively. The sample cell used for the measurements is a closed flow cell consisting of a 15 mm thick single crystal silicon wafer mounted onto a polyether ether ketone (PEEK) container sandwiched between aluminium holders to allow temperature control by means of water circulation (see figure 3.4). The instrument has a 'reflection up' geometry, meaning that the incoming neutron beam is slightly leaning down, penetrates the silicon block, encounters the interface(s) before being reflected up. This also means that the bilayer and the bulk solution are below the silicon block.

After careful cleaning (see 3.3.2), the cells were mounted and filled with heavy water. Each sample surface was first aligned with neutrons in order to define the position that maximizes the beam intensity at the interface. Direct neutrons beams, at different

attenuations were first measured in transmission through the silicon blocks (111) with the angle settings (slits apertures of each angle) in order to define the incoming intensity of the beam and thus to be able later to normalize the data. Direct beams were measured at 0° with the different settings inherent to each angle used during the experiment. This is done to take into account the different openings of the slits and choppers and thus possible changes in the wavelength distribution. Each 'empty' cell (i.e. bare substrate, cell filled with D_2O) was characterized with neutrons. If needed, H_2O contrast was performed to define the oxide layers of the different blocks. Then, the sample deposition was performed (see 3.3.4). After at least 30 min, the remaining vesicles were washed out with the sample solution followed by D_2O rinsing. The first contrast, D_2O, was then measured. In order to verify quickly the deposition of the different samples, by measuring at first the best contrast for a given sample, deuterated samples could have been rinsed with H_2O and measured in H_2O as first contrast. Exchange of the bulk solution, and thus of the contrast, was performed by injecting manually 15 to 20 mL of the corresponding solution through the sample cell. Once the bilayers were characterized in 3 to 4 contrasts, 3 mL of a 1 mM AmB solution (9:1 D_2O, DMSO) were injected. A period of 30 minutes of incubation was completed before rinsing with 15 to 20 mL of pure D_2O and performing the same 3 to 4 contrasts as before AmB addition. Data were fitted using the Motofit software package [113] (See 3.5.1).

The measurements of lipid mixtures from yeasts were performed on the Fluid Interfaces Grazing Angles ReflectOmeter, FIGARO at ILL (Grenoble, France) [114] or the neutron reflectometer with horizontal scattering geometry (vertical surfaces), D17 at ILL (Grenoble, France) [115]. Both instruments, depicted in figures 3.6 and 3.7 respectively, were used in time-of -flight mode, at low resolution mode $\Delta\lambda/\lambda$ = 7% for FIGARO and variable resolution, 1-10% for D17. Due to instrument differences, a neutron wavelength spectrum from 2 Å to 30 Å at two incident angles, 0.8° and 3.2° either in reflection up or reflection down geometry was used on FIGARO and a neutron wavelength spectrum from 2 Å to 27 Å at two incident angles, 0.8° and 3.0° in vertical configuration was used on D17. The covered Q-range started as low as 0.009 $Å^{-1}$ while the upper value is defined by the background of the instruments, around 0.28-0.30 $Å^{-1}$ on FIGARO and D17. The detector on FIGARO is a ^{3}He tubular aluminium monoblock gas detector with a 2D area of 500 mm wide by 250 mm high and a 2 mm and a 7 mm

vertical and horizontal resolution respectively. D17 is also equipped with a ^{3}He detector with an area of 300 mm wide by 480 mm high and corresponding resolutions of 2.2 and 4.8 mm, vertically and horizontally respectively. The reflectivity sample cell used was developed by ILL and was similar to the cell used at ANSTO. Direct beams were measured as explained before.

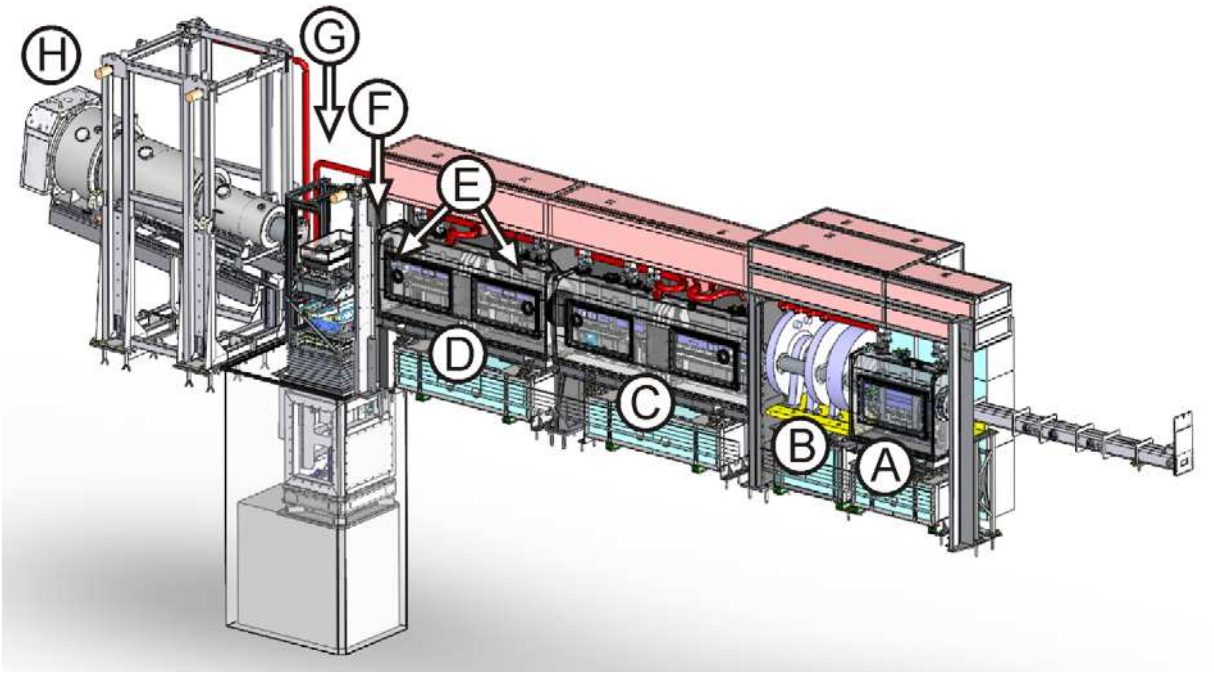

Figure 3.6 : *Side view of FIGARO and its major components: (A) frame overlap mirrors, (B) chopper assembly, (C) deflector mirrors, (D) collimation guide, (E) collimation slits, (F) beam attenuator, (G) sample position and (H) area detector. From [114].*

The natural lipid mixture deposition process is detailed in chapter 3.3.4, the volumes and concentrations involved being the same as for synthetic lipids. The contrast exchange was remotely controlled via a HPLC pump (Smartline Pump 1000) connected to a valve selector (Smartline valve drive 6) allowing both mixing of isotopically defined solutions and selection of the sample cell to flush. The flow rate was indifferently set to 1 or 2 mL/min for a total volume of 20 mL injected, assuring total isotope exchange from one contrast to an other without any perturbation of the bilayers.

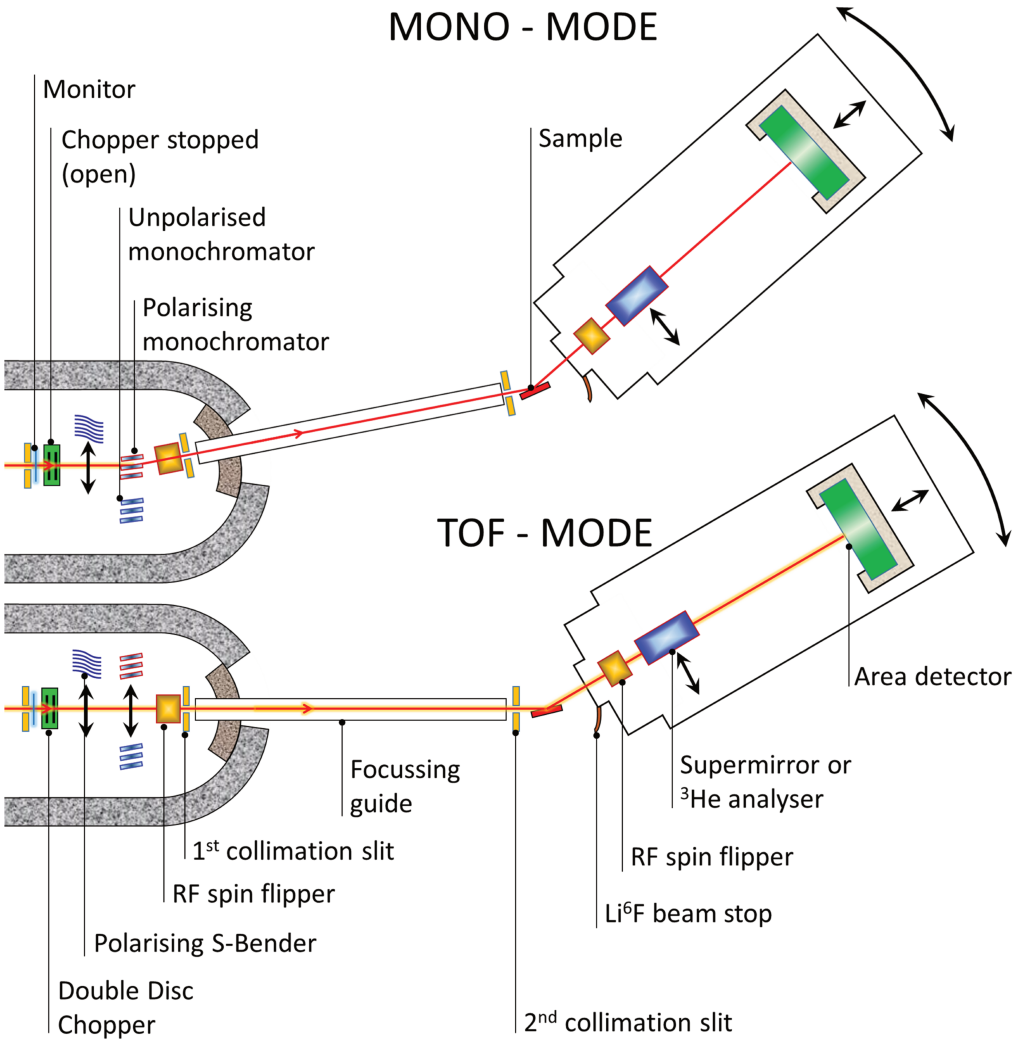

Figure 3.7 : Upper view depiction of the different configuration of D17 and its major components. From www.ill.eu.

3.4.3. Membrane diffraction experiments

Neutron diffraction experiments were performed at the cold neutron diffractometer D16 of the Institute Laue-Langevin, located in Grenoble, France [116] (see figure 3.8). Neutrons with a wavelength of 4.5 Å were selected by a highly ordered pyrolytic graphite (HOPG) monochromator. The sample to detector distance was 0.95 m and all samples were measured in reflection mode.

Figure 3.8 : *Side view of D16 with the major components highlighted. (1) Detector, (2) evacuated tubes, (3) sample position, (4) neutron guide and monochromator position, (5) water baths for temperature control.*

The coated wafers were mounted vertically on a goniometer placed in a humidity chamber (see figure 3.9) [117]. The reservoir of the humidity chamber was filled with H_2O in the case of deuterated samples and with D_2O for hydrogenous samples in order to guarantee the best contrast between the lipids and the hydration water vapor. The temperature of the sample was maintained at 30 °C throughout the measurements while the temperature of the reservoir of solvent was adjusted in order to obtain a specific relative humidity (RH) :

$$RH = \frac{\pi_{vap(T°C\_res)}}{\pi_{vap(T°C\_sample)}} \quad \textbf{(48)}$$

with $\pi_{vap(T°C\_res)}$ the vapor pressure of water at the temperature of the reservoir and $\pi_{vap(T°C\_sample)}$ the vapor pressure of water at the temperature of the sample.

Wafers were first aligned, and equilibrated at 60% RH. After the measurements in this condition, the samples were further equilibrated at 98% RH. For few samples, the same procedure was also applied at a different sample temperature.

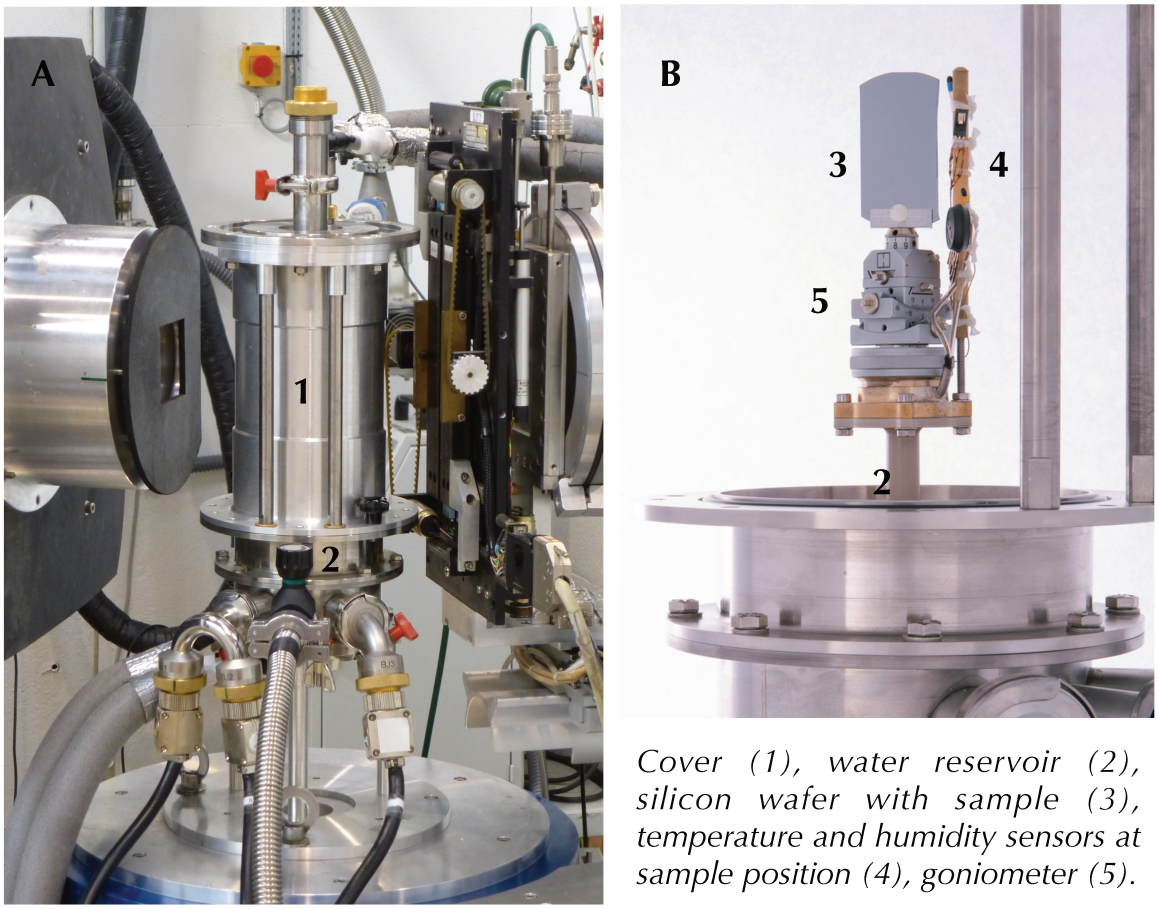

Cover (1), water reservoir (2), silicon wafer with sample (3), temperature and humidity sensors at sample position (4), goniometer (5).

Figure 3.9 : *Details of D16 humidity chambers. External view once the chamber is closed and mounted* ***(A)*** *and when the cover is removed, which reveals the aligned wafer placed on a goniometer* ***(B)****. From www.ill.eu.*

Diffraction data of total lipid extracts were collected at a detector angle (γ) of 12.5°, by scanning the sample angle (ω) in the range 0 to 6°, with a step of 0.05°. Diffraction data of natural and synthetic phospholipids were collected at a detector angle (γ) of 12°, by scanning the sample angle (ω) in the range -1 to 11°, with a step of 0.05°. In both cases, the neutron scattering intensity was recorded by a position sensitive two dimensional ^{3}He detector (320x320mm area with a spatial resolution of 1×1 mm).

3.5. Data treatment

3.5.1. NR experiments

Data collection times varied upon angles and isotopic composition of the samples and contrasts, but were in all cases adjusted to make the most of neutron beam allowance in the same time as obtaining good statistics for significant reflectivity curves (acceptable signal to noise ratio especially at high q).

After collection, raw data reduction was performed using the SLIM module of Motofit (at ANSTO) or COSMOS from the software LAMP [Large Array Manipulation Program, http:/www.ill.fr/data_treat/lamp/lamp.html] (at ILL) to subtract background and normalize data with the direct beams measurements. The combined measurements, rendered continuous by applying a scale factor taking into account the use of attenuators for the direct beam measurements, were used to normalize all data. The defined scale factor was also applied to all data measurements. Background arises principally from incoherent scattering events, relatively important in solid-liquid cells due to a large amount of liquid, as well as from the physical surrounding of the sample (solid-liquid cell materials, reflectometer components) that adds to the specular reflection on the detector. Since the background increases with q towards specular reflectivity, it is necessary to subtract it. This was achieved by determination of the number of counts centered at the specular peak on the area detector and the difference with the number of counts in the direct surrounding of the specular reflection. Thus, the number of background counts were subtracted to the counts at the specular peak. All the NR data were then analyzed through simultaneous contrast fitting using the Motofit software package [113].

Indeed, a model corresponding to a series of parallel layers of homogeneous material with a specific thickness $\boldsymbol{\tau}$, scattering length density $\boldsymbol{\rho}$ and roughness $\boldsymbol{\sigma}$ was constructed (figure 3.11 and table 3.3). The scattering length density of each layer was also pondered with a solvent interpenetration percentage ϕ. These parameters were processed by Motofit as explained in chapter 2.2 in order to calculate a reflectivity profile. This fit was compared to the experimental data and its quality determined by

the least-squares method. However, in order to obtain not only a good fit (low χ^2) but most of all a realistic model, few conditions were taken into consideration.

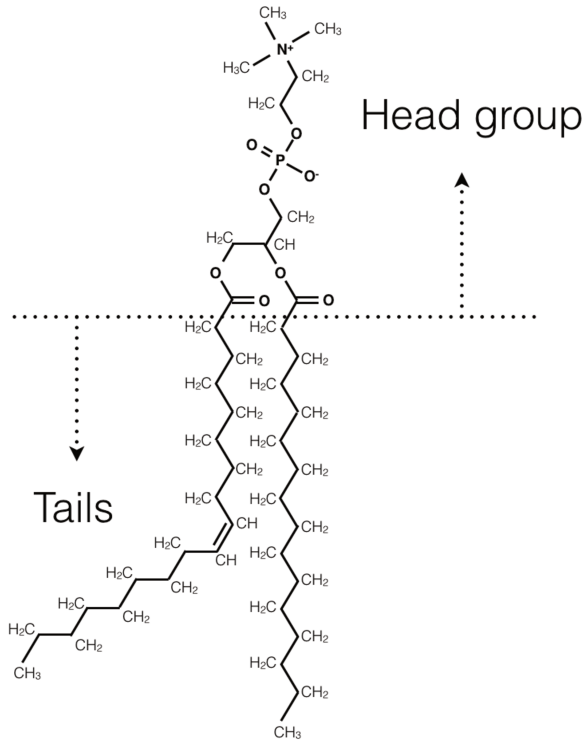

Component group	Volume (Å^3)
$C_5H_{13}N$ (choline)	120.68
PO_4 (phosphate)	52.12
C_3H_5 (Glycerol backbone)	72.48
COO (carbonyl)	38.43
C=C	42.1
CH_2	28.24
CH_3	50.41

Figure 3.10 : *Conventional separation for SLD calculations illustrated on a phosphocholine and associated components volumes [118].*

Firstly, to calculate the SLD of our mixtures, the lipids were separated in heads and tails as shown in figure 3.10. The carbonyl group, integrated to the headgroup, was by convention set as the separation limit between the two parts. The volume fractions of the different lipid constituents were obtained from literature [16, 118-122]. Thus the SLD (see equation 9 in chapter 2) was calculated for each component. Details are given in table 3.2. The exchangeable protons present in phospholipid headgroups had also to be taken into account. Indeed, in our mixtures, whereas PC does not present any labile hydrogen, the other classes (PE, PS, PI and CL) do and their composition, and thus their SLDs, varied upon the contrast used. This is also presented in table 3.2 with the chemical formula of the different headgroups in both H_2O and D_2O and the derived SLD calculations in the four contrasts used in our work. Ergosterol, cholesterol and Amphotericin B molecular volumes were obtained from literature [16, 122] and SLD calculations performed as for phospholipids. See table 3.2.

Heads		Formula H_2O	Formula D_2O	Vm (Å^3)	Relative amount	Total amount (check)	SLD D_2O	SLD 66%D_2O =CM4	SLD 38%D_2O =CmSi	SLD H_2O		AVERAGE SLD D_2O	AVERAGE SLD 66% D_2O	AVERAGE SLD 38% D_2O	AVERAGE SLD H_2O
Hydrogenated	h-PC	$C_{10}H_{18}O_8NP$	$C_{10}H_{18}O_8NP$	319	55,59		1,86	1,86	1,86	1,86		2,92	2,73	2,58	2,36
	h-PE	$C_7H_{12}O_8NP$	$C_7H_9D_3O_8NP$	233	17,27		4,03	3,57	3,19	2,68					
	h-PS	$C_8H_{11}O_{10}NP$	$C_8H_8D_3O_{10}NP$	264	7,24	100	4,39	3,99	3,65	3,20					
	h-PI	$C_{11}H_{16}O_{13}P$	$C_{11}H_{11}D_5O_{13}P$	272	11,81		5,37	4,72	4,18	3,45					
	h-CL	$C_{13}H_{16}O_{17}P_2$	$C_{13}H_{15}DO_{17}P_2$	490	8,09		2,98	2,91	2,85	2,77					
Deuterated	d-PC	$C_{10}D_{18}O_8NP$	$C_{10}D_{18}O_8NP$	319	53,03		7,35	7,35	7,35	7,35		7,73	7,52	7,34	7,11
	d-PE	$C_7H_3D_9O_8NP$	$C_7D_{12}O_8NP$	233	16,36		8,05	7,59	7,22	6,71					
	d-PS	$C_8H_3D_8O_{10}NP$	$C_8D_{11}O_{10}NP$	264	8,28	100	7,54	7,14	6,81	6,36					
	d-PI	$C_{11}H_5D_{11}O_{13}P$	$C_{11}D_{16}O_{13}P$	272	15,01		9,58	8,93	8,39	7,66					
	d-CL	$C_{13}HD_{15}O_{17}P_2$	$C_{13}D_{16}O_{17}P_2$	490	7,32		6,17	6,09	6,03	5,95					

Tails		Hydrogenous			Deuterated			Sterols						AmB
Fatty acids	Vm (Å^3)	% h-lipids	hSLD (10^{-6} A^{-2})		% d-lipids	dSLD (10^{-6} A^{-2})			Hydrogenous	Deuterated	Hydrogenous	Deuterated		Hydrogenous
14:0	394,7	0,62	-0,37		0,38	6,76			Ergosterol		Cholesterol			Amphotericin B
16:0	451,5	11,62	-0,36		8,07	6,79		Vm (Å^3)	630,3		630			983
16:1	439,7	3,74	-0,20		1,39	6,67								
16:2	427,9	1,11	-0,03		0,80	6,54		Formula	$C_{28}H_{44}O$	$C_{28}D_{44}O$	$C_{27}H_{46}O$	$C_{27}D_{46}O$	Formula D_2O	$C_{47}H_{60}D_{13}NO_{17}$
16:3	416,1	0,59	0,15		0,50	6,41							Formula H_2O	$C_{47}H_{73}NO_{17}$
18:0	508,3	10,23	-0,35		6,66	6,82		SLD (10^{-6} A^{-2})	0,44	7,70	0,21	7,81		
18:1	496,5	36,02	-0,21		60,33	6,71							SLD D_2O (10^{-6} A^{-2})	2,88
18:2	484,7	31,39	-0,06		19,26	6,60							SLD CM4 (10^{-6} A^{-2})	2,41
18:3	472,9	4,68	-0,10		2,60	6,48							SLD CmSi (10^{-6} A^{-2})	2,01
		Somme = 100			Somme = 100								SLD H_2O (10^{-6} A^{-2})	1,50
		TOTAL (h) SLD =	-0,18		TOTAL (d) SLD =	6,67								

TABLE 3.2 : *Detailed formula, molecular volumes and example of SLD calculations for P. pastoris complex lipid mixtures. Top: Headgroup, bottom left: tails, bottom center: sterols and bottom right: Amphotericin B SLD calculations.*

Headgroup and chain volumes (Vm in Å^3) were calculated from literature [16, 118-123]. The headgroup SLDs in D_2O and H_2O were calculated from their corresponding chemical formula and volumes. The headgroup SLDs in other contrasts (CM4 and CMSi) were calculated by ponderation of D_2O and H_2O SLDs. We also note here that the unique labile proton in the sterol molecules was not taken into consideration as its effect on SLD was very limited and negligible when compared to the variation of the SLD of the headgroups between different water contrasts, where the hydroxyl group was expected to take place in the bilayer.

In practice, once all the preliminary calculations were performed for all samples and contrasts, we measured and characterized the silicon oxide layer SiO_2, or the roughness of the bare substrate for sapphire, by measuring the substrate alone in different contrasts. This allowed us to fit a single layer model quite easily in the silicon case and fix the parameters for the rest of the experiment as it is an inert layer. Then, as the SLD of the different samples was calculated based on the lipid composition, it was used as starting point in the fits. The model employed to fit the lipid bilayers is composed of 3 to 4 more layers as depicted in figure 3.11. In the simplest case, the bilayer is divided in 3 layers, respectively hydrophilic inner heads, hydrophobic tails regrouping chains from both leaflets and finally the hydrophilic outer headgroup.

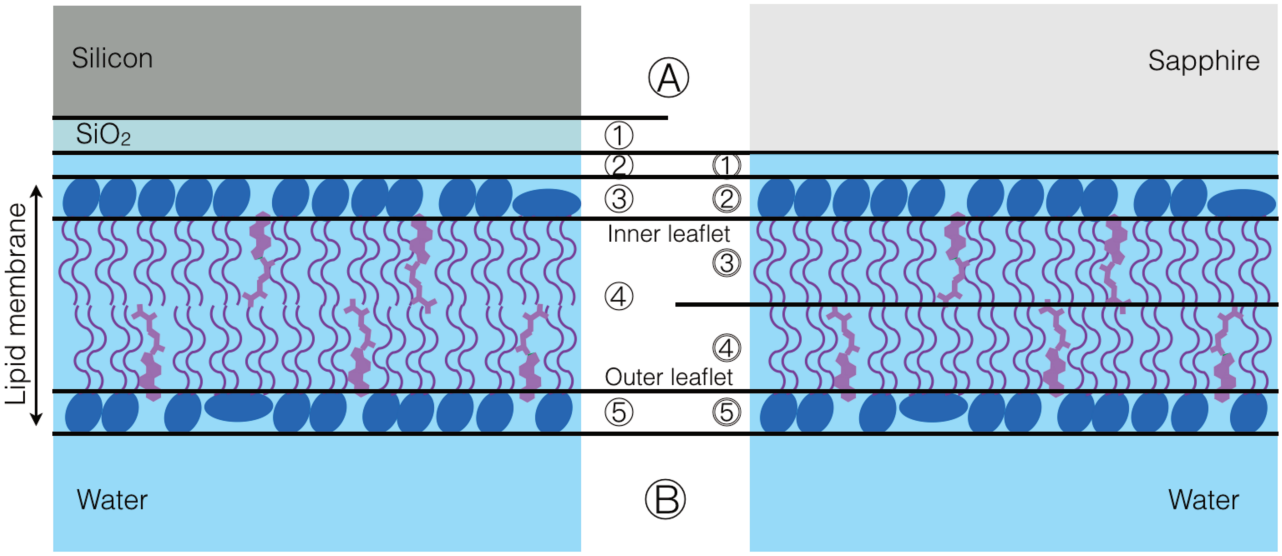

Figure 3.11 : *Representation of the division into different layers to fit the lipid bilayers.* *Ⓐ and Ⓑ were considered as layers of infinite thicknesses with a constant SLD and correspond respectively to the supporting material and the surrounding liquid. Layers were numbered from the substrate towards the liquid. ① corresponds to the silicon oxide layer, ② to an inner water layer, not always present, ③ to the inner headgroups, ④ the hydrophobic tails and ⑤ the outer headgroups. In the case of sapphire, there is no additional interface between the substrate and the sample, and thus, ① corresponds to an inner water layer, ② the inner headgroups, ③ the inner hydrophobic leaflet, ④ the outer hydrophobic leaflet and ⑤ the outer headgroups.*

In accordance with the separation of the deposited lipid membranes in different layers to model and fit the NR data, the parameters employed and associated with the best neutron reflectometry fits will be presented in the following manner :

Sample :	Sample name - χ^2 value			
Layers	τ (Å)	ρ (10^{-6} Å^{-2})	ϕ (%)	σ (Å)
Si	-	2.07	0	3 ± 1
SiO_2	9 ± 1	3.41	8 ± 4	3 ± 1
Head (in)	8 ± 2	2.9 ± 0.1	30 ± 5	3 ± 1
Chains	30 ± 1	1.2 ± 0.1	0	3 ± 2
Head (out)	8 ± 2	2.9 ± 0.1	30 ± 5	4 ± 2

Table 3.3 : Details on how the parameters of the models corresponding to the fits of the NR data will be presented in this manuscript.
τ = thickness, in Å, ρ = scattering length density of the layer, in 10^{-6} Å^{-2}, ϕ = volume fraction of water relative to the lipids, expressed in percentage (%) and σ = the roughness of the layer after each layer, given as the sigma-value of the gaussian function describing the full-width half-maximum of the interface, in Å. The thickness corresponds to the full layer thickness in absence of roughness. SLD values correspond to the part of the molecule/material excluding any solvent present and were kept constant during fitting. ϕ is also indiscriminately called hydration. Chi-squared (χ^2) is associated to the simultaneous fits in all the solvent contrasts. The errors associated with the different parameters were determined from the maximum variation acceptable to maintain a relevant fit and for a specific parameter, the value given is the value found in the most sensitive contrast associated to this parameter.

In the case of synthetic lipids and *C. glabrata* total extracts characterizations, always performed on silicon substrate, an inner water layer was not needed to obtain a good and realistic fit to the data. Also, in order to maintain symmetry, the inner and outer headgroups were set to have the same thickness and SLD while roughness and hydration were allowed to vary. The hydrophobic layer composed of both inner and outer chains was treated as one homogeneous medium. An area per molecule calculation was also performed as follows : the volume of the lipid headgroups weighted with the hydration of the headgroup layer was divided by its thickness and compared to the value of the volume of two fatty acids, weighted with hydration of the hydrophobic layer divided by the thickness (or half the thickness if the two leaflets are incorporated in one homogeneous layer). Those two area values were forced to match in the case of synthetic lipids while this parameter was not taken into account for complex mixtures. Indeed, due to large amounts of sterols and various phospholipids of very different volumes, such a value was not helpful in the search of a model. For

complex lipid bilayers, an inner water layer of few angstroms thick (non negligible) was necessary in the fits to maintain symmetry. For sapphire complex supported bilayers, after assuming symmetry with no success, asymmetry was allowed and the two hydrophobic layers were comprehended as two different entities (as represented in the right part of figure 3.11) with different thickness, SLD and roughness. The hydration of both hydrophobic layers was maintained equal.

For the fits of the bilayers after Amphotericin B incubation, the model was based on the previous corresponding bilayer characterization. The headgroups and chains thicknesses and hydration were left able to vary. The chain SLDs were no longer linked between the different contrasts and the chain SLD variation observed was used to quantify AmB insertion and sterol removal from **(49)**. Finally, if the fit needed more adaptations, an additional layer, with all the parameters left free to vary was included in the model above the bilayer. Here again, the SLDs of the layers were used to define the components with the following set of equations **(49)**.

For AmB insertion in the chain layer with sterol removal :

$$\left.\begin{aligned} SLD_{(AmB\text{-}D2O)}\,X + SLD_{(Sterol)}\,Y + SLD_{(Chains)}\,Z &= SLD_{Final\ Chain\text{-}D2O} \\ SLD_{(AmB\text{-}CM4)}\,X + SLD_{(Sterol)}\,Y + SLD_{(Chains)}\,Z &= SLD_{Final\ Chain\text{-}CM4} \\ SLD_{(AmB\text{-}H2O)}\,X + SLD_{(Sterol)}\,Y + SLD_{(Chains)}\,Z &= SLD_{Final\ Chain\text{-}H2O} \end{aligned}\right\} \text{ with } X + Y + Z = 1 \qquad \textbf{(49)}$$

Where $SLD_{(AmB\text{-}D2O)}$, $SLD_{(AmB\text{-}CM4)}$ and $SLD_{(AmB\text{-}H2O)}$ are the scattering length densities of AmB allowing for exchange for the labile hydrogens with deuterium dependent on the contrast. $SLD_{(Sterol)}$ and $SLD_{(Chains)}$ correspond to the calculated values associated with the sample composition (see table 3.2). X, Y and Z represent the volume fractions of the different components. In the case of absence of sterol, the simultaneous equations have only two variables. The errors given for the different parameters (see table 3.3) correspond to the maximum change acceptable to maintain a proper fit in the best contrast associated to the given parameter. For example, the error of the thickness of a deuterated layer was investigated with the H_2O contrast.

The propagation of theses errors for additive parameters was managed by quadrature :

$$\Delta a = \sqrt{(\Delta b)^2 + (\Delta c)^2} \qquad \textbf{(50)}$$

with Δa the final uncertainty of a given parameter (such as, for example, the total thickness of a lipid bilayer) and Δb and Δc the uncertainties associated (such as the uncertainties of the thickness of the different layers constituting the lipid bilayer).

The mean values of certain parameters, mostly concerning the lipid analysis presented in this work, but also used for the comparison of some AmB effects, were calculated and the associated uncertainty $\Delta x_{average}$ obtained form standard deviation :

$$\Delta x_{average} = \sqrt{\frac{\sum_i^N (x_i - \overline{x})^2}{N}} \quad \textbf{(51)}$$

with x_i an experimental value, $\overline{x}$ the average value of a series i with N replicates. Experimental data uncertainties Δz were calculated from :

$$\Delta z = |xy| \sqrt{\left(\frac{\Delta x}{x}\right)^2 + \left(\frac{\Delta y}{y}\right)^2} \quad \textbf{(52)}$$

with Δx and Δy the uncertainties in the measurements of the parameters x and y

3.5.2. Membrane diffraction experiments

Dealing with complex phospholipid mixtures, the ordering of a multilamellar system is relatively weak with usually 2 to 3 diffraction peaks. Thus, the information on the d-spacing was the main parameter extracted from our experiments.

The data reduction was carried out with the ILL software LAMP. The background of the data was estimated by collecting one measurement on the empty humidity chamber, then subtracted from the ones collected with the sample. The efficiency of the detector was taken into account during data treatment by loading a calibration file in LAMP. This calibration file corresponds to a measurement of H_2O scattering, which gives a good estimation of the detector efficiency. The intensity collected on the 2D detector was integrated in the ω range corresponding to the observed diffraction peaks and reduced to 1D by vertical integration in order to obtain intensity vs 2θ plots. The positions of the Bragg peaks in the plots were evaluated by fitting with a Gaussian function using the

software OriginLab. From the 2θ positions of the peaks and equation **(43)** described in chapter 2, the associated d-spacing was calculated. The peak positions and the real space distance(s) associated were used to verify the lamellar periodicity based on Bragg's law (39). Because of ratio of the reciprocal spacings of the Bragg reflections and the difference of intensity between 1st and second order, the diffraction profiles obtained were only concordant with lamellar phases, also because additional peak would have been observed with others lipid phases [124].

In one case, Bragg peaks in the parallel direction to the lamellar surface were observed. Hence the 2D detector images were integrated in the 2θ range and reduced to 1D by horizontal integration in order to obtain intensity vs ω plot, from which the in-plane correlation distance was calculated by applying equation **(43)**.

The uncertainty in the peak position of the Gaussian function was translated into uncertainty in distance via equation **(43)**.

4. LIPID PRODUCTION AND SAMPLE PRE-CHARACTERIZATION

4.1. Lipid production

4.1.1. *Candida glabrata*

The *C. glabrata* strains Y2296, Y2310 & Y2311 (see chapter 3.2) were grown in both hydrogenous and deuterated 250mL cultures at 25°C. The harvesting conditions are listed in table 4.1.

Strains	Condition	OD_{600}	Growth (days)	Lipid ratio (%)
Y2296 (vector)	Hydrogenous	4.8	5	4.2
	Deuterated	3.2	10	2.7
Y2311 (AmB sensitive)	Hydrogenous	6.8	5	4.9
	Deuterated	4.0	10	6.1
Y2310 (AmB resistant)	Hydrogenous	11.0	5	4.7
	Deuterated	4.2	10	6.0

Table 4.1 : Harvesting parameters and lipid mass ratio to the dry cell weight of different *C. glabrata* strains.

The duration of the growth was extended for the isotope-labelling conditions as the yeasts usually grow more slowly in deuterated conditions than in the corresponding hydrogenous conditions. Even though the process of adaptation to heavy water remains

unclear, the modification of growth rates in heavy water is thought to arise from the deuterium kinetic isotope effect which in general slows down all biochemical pathways [125]. However, the AmB resistant strain, Y2310, grew faster than the other strains in both conditions. Indeed, the cell density, measured as the optical density at 600nm (OD_{600}) for Y2310 was higher than for Y2296 and Y2311 after the same growth period in hydrogenous conditions. This difference was less pronounced in deuterated conditions but the fact that yeasts were all harvested in the exponential growth phase allowed direct comparison of the lipid contents in the same time it furnished the maximum amount of phospholipids [126]. The lipid ratios displayed in table 4.1 correspond to the dried lipid mass recovered after extraction divided by the yeast's freeze-dried mass before extraction. For yeasts, in normal conditions, we expected values between 2 and 7% [127].

The total fatty acids and the sterols of the different strains were quantified using GC-FID and the phospholipid class composition was reconstructed from the results using methyl pentadecanoate as an internal standard. Isotope effects can be observed by comparison of the lipid composition between the two conditions (hydrogenous and deuterated) for a same strain. In addition, by comparison of different strains in the same isotopic environment, effects of the up/down regulated genes on the lipid composition could be estimated.

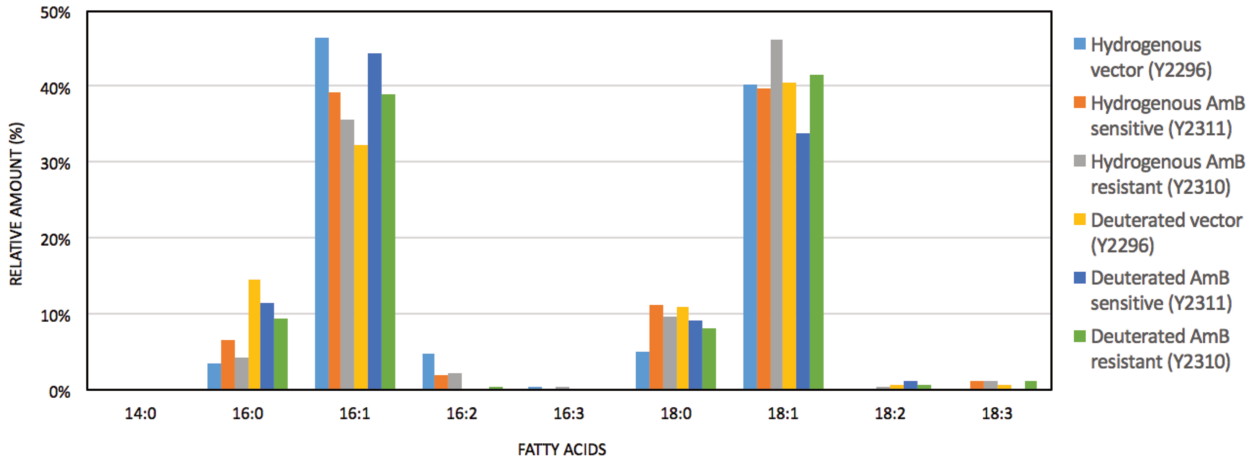

<u>Figure 4.1 :</u> Total fatty acid composition of the different *C. glabrata* strains grown. $C_{14:0}$: Myristic acid. $C_{16:0}$: Palmitic acid. $C_{16:1}$: Palmitoleic acid. $C_{16:2}$: Hexadecadienoic acid. $C_{16:3}$: Hexadecatrienoic acid. $C_{18:0}$: Stearic acid. $C_{18:1}$: Oleic acid. $C_{18:2}$: Linoleic acid. $C_{18:3}$: Linolenic acid.

As presented in figure 4.1, the selected strains all exhibited a relatively narrow fatty acid distribution with around 80% of the fatty acid chains distributed between only 2 monounsaturated species; $C_{16:1}$ and $C_{18:1}$. Very few polyunsaturated fatty acid species were found to be present and no clear trends, either related to possible isotope effects or the genetic modifications could be observed. Five to six phospholipid classes were represented in all strains and their distribution is displayed in figure 4.2. Phosphatidylcholine (PC) was the major class in hydrogenous and deuterated conditions but its proportion varied from 47 ± 4%, for h-Y2310 and d-2296, to 66 ± 4% with h-Y2296. These differences are significantly larger than the experimental variation in the measurement accuracy in the lipid composition determination (±4%). On the other hand, cardiolipin (CL) and phosphatidylinositol (PI) together with phosphatidic acid (PA) were the smallest classes present. In fact, their combined amount never exceeded the amount of the third most abundant class, either phosphatidylethanolamine (PE) or phosphatidylserine (PS). Their relative proportions in the different strains varied with PS as the second most abundant class in h-Y2296 and h-Y2310, at 25 ± 4% and 26 ± 4% respectively, whereas it was always third in abundance in deuterated conditions where the PE content remained relatively constant at around 25 ± 4%.

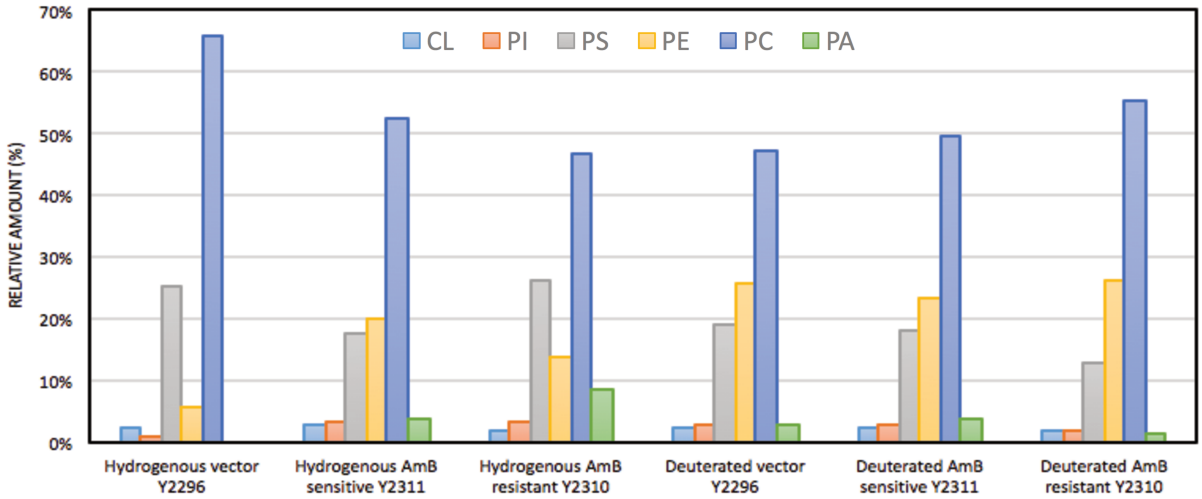

Figure 4.2 : Phospholipid composition of different *C. glabrata* strains. Cardiolipin CL (light blue), Phosphatidylinositol PI (orange), Phosphatidylserine PS (grey), Phosphatidylethanolamine PE (yellow), Phosphatidylcholine PC (dark blue), Phosphatidic acid PA (green).

Figure 4.3 shows the GC-FID traces for the sterol analysis performed on the different *C. glabrata* strains. Besides ergosterol, three other species were present. Based on column

polarity, retention times and standard GC methods [128], the molecules corresponding to the three peaks could be determined. The first peak, corresponded to the only molecule less polar than ergosterol, as its retention time was shorter (rt=8min), indicating a strongly apolar nature and was identified as squalene. Knowing the different sterol-related molecules found in yeasts [129] and the retention times corresponding to polyunsaturated sterols, lanosterol and 5,7,24(28)-Ergostatrienol were attributed to the two other peaks at hydrogenous retention times 14 and 15 min respectively. GC coupled with mass spectrometry detection was performed and allowed to confirm the attribution of squalene and lanosterol (figure 4.4). Because different response factors occur for sterols with FID, and in absence of standards for squalene, lanosterol and 5,7,24(28)-Ergostatrienol, only the ergosterol have been quantified.

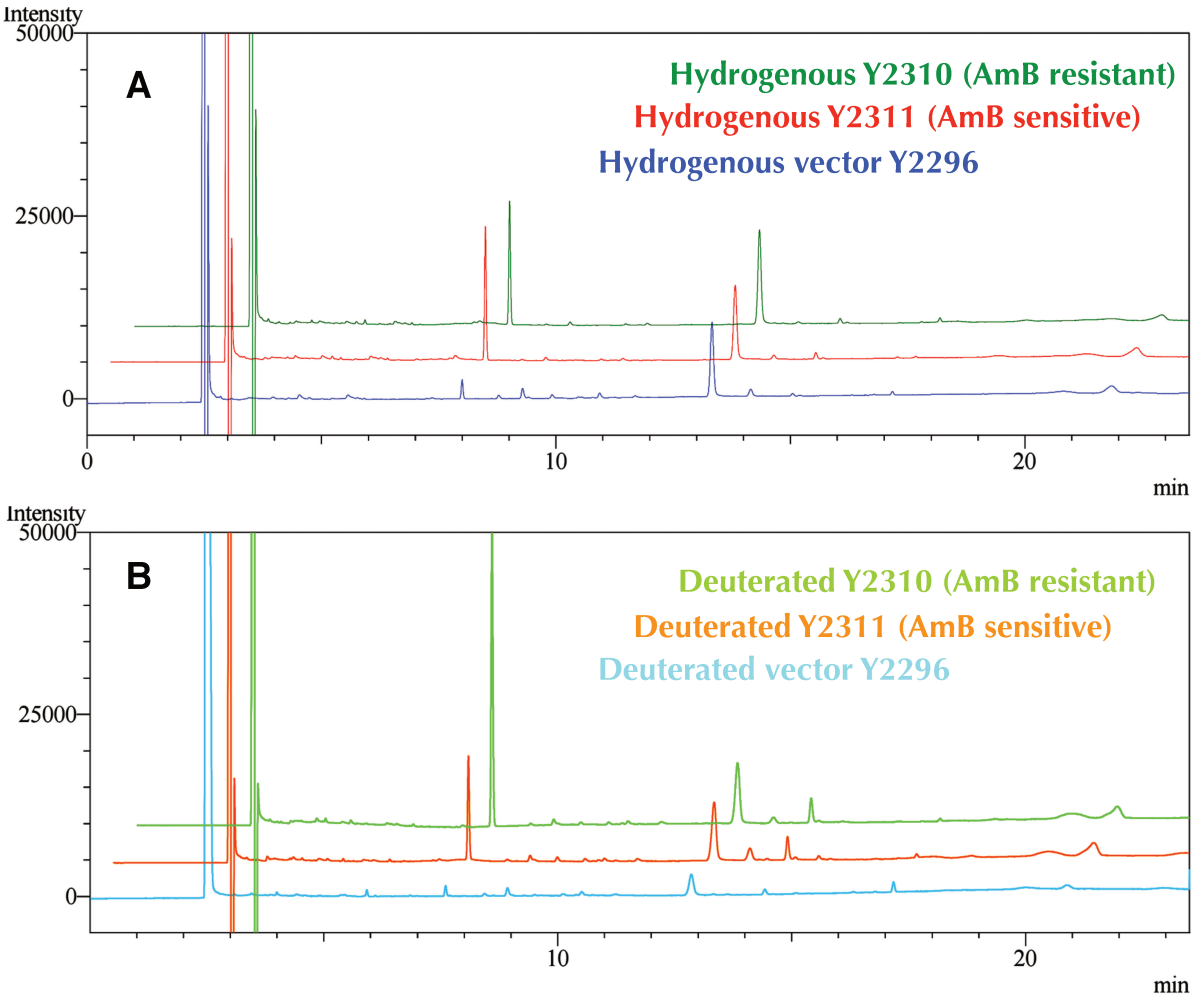

Figure 4.3 : FID traces of free protiated (A) and deuterated (B) sterols depending on strains of grown *C. glabrata*. *Y2311 and Y2310 traces are shifted respectively by +5000 and +10000 in intensity and are shifted respectively of 0.5 min and 1 min for clarity.*

In order to clarify the GC-FID data, table 4.2 shows a normalization of the different peak areas using the vector grown in hydrogenous conditions as reference. The major observation concerned squalene and 5,7,24(28)-Ergostatrienol. In comparison to the hydrogenous vector, they were over represented in all conditions but especially in deuterated conditions for Y2310, the AmB resistant strain. On the contrary, lanosterol is only significantly over expressed in deuterated conditions for Y2311, the AmB sensitive strain. In comparison to other species and to squalene especially (factor 1 to 15.5), the changes in the amount of ergosterol remained relatively limited in the different strains and conditions, (factors 0.82 to 1.1), at the exception of the hydrogenous resistant strain Y2310, with a ratio 1.37. Also, deuteration seemed to lower the ergosterol amount in the vector and resistant yeast, while it remained constant for Y2311. The ergosterol quantification is detailed in table 4.3.

Strains	Squalene : th* = 8 min & td* = 7.6 min	Ergosterol : th = 13.3 min & td = 12,8 min	Lanosterol : th = 14.1 min & td = 13.6 min	5,7,24(28)-Ergostatrienol : th = 15 min & td = 14.4 min
Hydrogenous Y2296 Vector	**1 (6982)**	**1 (51133)**	**1 (4811)**	**1 (1324)**
Hydrogenous AmB sensitive Y2311 strain	6.8	1.01	0.54	2.6
Hydrogenous AmB resistant Y2310 strain	6.2	1.37	0.26	1.9
Deuterated Y2296 Vector	1.12	0.82	0.34	4.6
Deuterated AmB sensitive Y2311 strain	5.4	1.07	2.25	9.5
Deuterated AmB resistant Y2310 strain	15.5	1.1	1.12	10.2

Table 4.2 : Ratios of the GC-FID peak areas relative to the hydrogenous vector Y2296. *th is the retention time of the hydrogenous molecule, td the retention time of the deuterated molecule. The values in parenthesis correspond to the integrated area of the peaks used as reference for each molecule.

Strains	Condition	Ergosterol (mol%)
Y2296 (vector)	Hydrogenous	13.1 ± 0.1
	Deuterated	11.0 ± 0.1
Y2311 (AmB sensitive)	Hydrogenous	13.2 ± 0.1
	Deuterated	13.2 ± 0.1
Y2310 (AmB resistant)	Hydrogenous	16.0 ± 0.1
	Deuterated	13.5 ± 0.1

Table 4.3 : Ergosterol quantification of the different *C. glabrata* samples. Error bars arise from mass and volume uncertainties during sample preparation. *NB; the mol% quantification is based on phospholipid content only.*

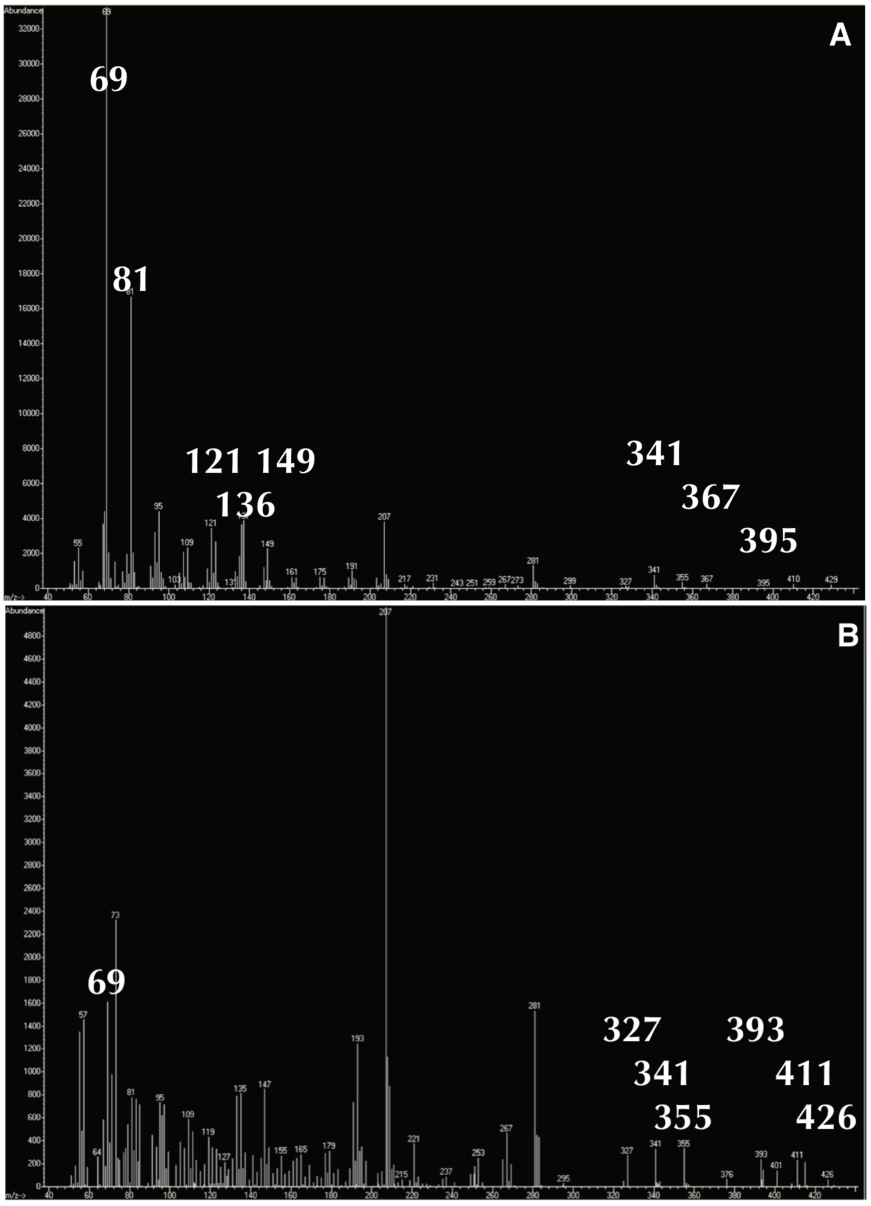

Figure 4.4 : Mass spectra of peaks at th=8 min corresponding to squalene (A) and at th= 14.1 min corresponding to lanosterol (B). m/z peaks used for the attribution are highlighted. Spectra were compared with NIST data base [130]. Peaks at m/z 57, 73, 207, 281 and 429 arise from background as bleeding of the BPX5 column [131].

4.1.2. *Pichia pastoris*

In order to explore new ways to obtain labelled phospholipids, the effect of using methanol as the carbon source on the lipid composition of *P. pastoris* was investigated. This was driven by two factors, the high cost of d_8-glycerol and the interest to investigate if the 'waste' biomass from the commonly used protein production protocols, making use of methanol as carbon source to trigger protein overexpression, could be utilized as a source of lipids.

Carbon source regime	Condition	OD_{600}	Lipid ratio (%)
Glycerol only	Hydrogenous	32.0	5.0
	Deuterated	49.0	6.9
Glycerol & Methanol	Hydrogenous	32.0	3.0
	Deuterated	49.8	3.1
Methanol only	Hydrogenous	34.0	3.0
	Deuterated	31.0	5.3

Table 4.4 : Harvesting parameters and lipid mass ratio of *P. pastoris* depending on carbon source regime.

The batches performed by Valérie Laux at the deuteration laboratory of ILL on *P. pastoris* grown with different carbon sources were analyzed concomitantly. The fatty acid distribution of *P. pastoris*, as seen in figure 4.5, included nine different species. C_{18} fatty acids were the largest group represented, with oleic acid ($C_{18:1}$) being the most abundant fatty acid in all six growth conditions even if its proportions varied significantly (from 36 ± 1% to 66 ± 4%). Only the batch grown with hydrogenous glycerol as the sole carbon source gave rise to a better balance between $C_{18:1}$ and $C_{18:2}$ at 36 ± 1% and 31 ± 1% respectively.

The observed effect of the presence of methanol in the growth media was an increase of the relative amount of $C_{18:1}$ with increasing methanol concentration. Indeed, $C_{18:1}$ amount increased in hydrogenous conditions from 36 ± 1% when no methanol was added, to 49 ± 2% when a mixture of glycerol and methanol was used and further to 57 ± 4% when only methanol was employed as the carbon source. This effect was also

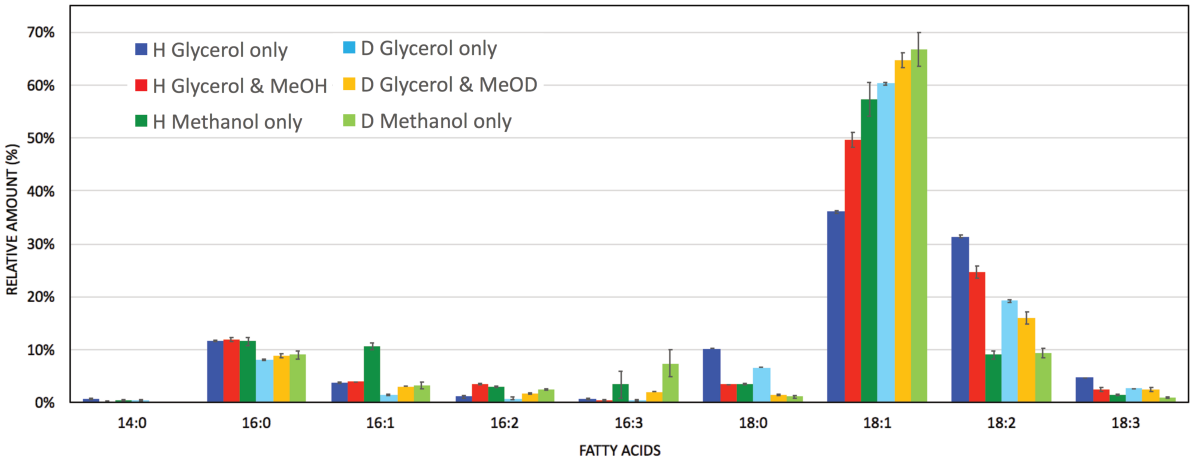

Figure 4.5 : Total fatty acid composition of *P. pastoris* grown with different carbon sources. $C_{14:0}$: Myristic acid. $C_{16:0}$: Palmitic acid. $C_{16:1}$: Palmitoleic acid. $C_{16:2}$: Hexadecadienoic acid. $C_{16:3}$: Hexadecatrienoic acid. $C_{18:0}$: Stearic acid. $C_{18:1}$: Oleic acid. $C_{18:2}$: Linoleic acid. $C_{18:3}$: Linolenic acid. *Errors bars represent standard deviation of the mean values obtained over 3 different analysis.*

observable in deuterated conditions, with an increasing amount of oleic acid, 60 ± 1%, 64 ± 2% and 67 ± 3% respectively. At the same time, methanol decreased the relative amounts of the C_{18} polyunsaturated fatty acids. Linoleic acid ($C_{18:2}$) was strongly reduced, from 31 ± 1% with h-glycerol to 25 ± 2% and 9 ± 1% with h-glycerol/ methanol and h-methanol only respectively. The same trend was observed in deuterated conditions. Finally, methanol increased the proportion of unsaturated C_{16} lipids in both hydrogenous and deuterated conditions while palmitic acid ($C_{16:0}$) was only altered by deuteration with 12 ± 1% in hydrogenous conditions and 9 ± 1% in deuterated ones.

The isotope effects from growth in D_2O on the proportions of oleic acid and C_{18} fatty acids in general were similar to the effect caused by methanol. Indeed, the use of deuterium increased the production of $C_{18:1}$ from 36 ± 1% to 60 ± 1% when the yeast were fed with d_8-glycerol only. $C_{16:3}$ was the only other fatty acid whose production seemed to be enhanced by deuteration, but to a much lower extent. All other fatty acids, the saturated $C_{16:0}$ and $C_{18:0}$, monounsaturated $C_{16:1}$ and the polyunsaturated C_{18} fatty acid proportions were reduced by deuteration.

Methanol is used in the expression of deuterated proteins [96] in *P. pastoris* and the remaining cell paste is usually not conserved for other purposes. But since both methanol and the isotope effects seemed additive and accentuated the $C_{18:1}$

predominance over other species, especially the long chain polyunsaturated fatty acids, methanol could be a good deuterated carbon source for boosting the production of perdeuterated oleic acid in *P. pastoris*, but is less suitable for the production of deuterated polyunsaturated lipids.

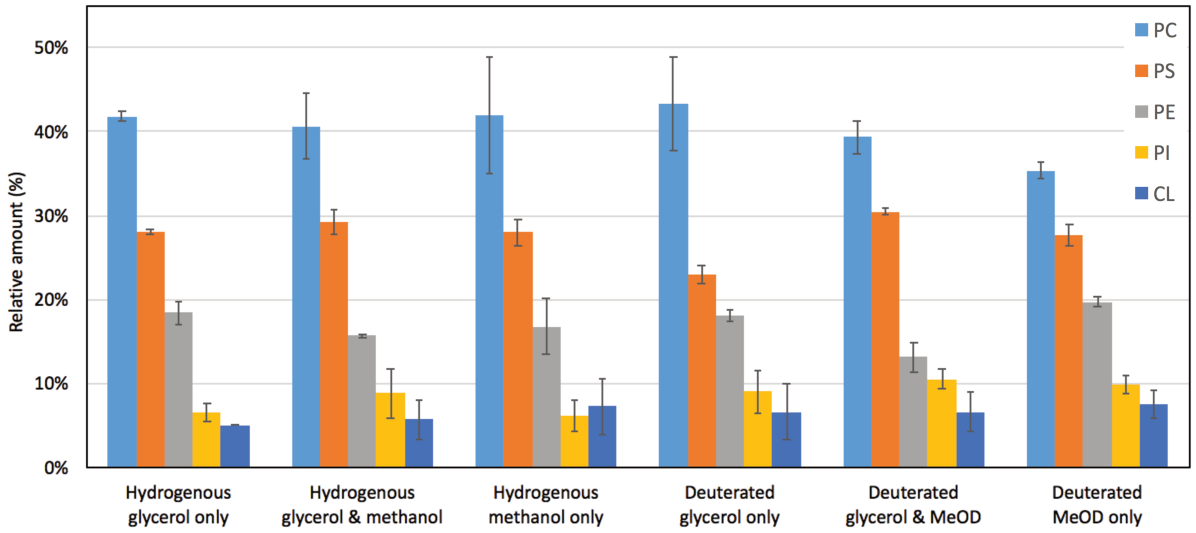

Figure 4.6 : Phospholipid composition of different *P. pastoris* strains in function of carbon source feeding. Phosphatidylcholine PC (light blue), Phosphatidylserine PS (orange), Phosphatidylethanolamine PE (grey), Phosphatidylinositol PI (yellow), Cardiolipin CL (dark blue). *Errors bars represent standard deviation of the mean values obtained over 3 different analysis*

Concerning the phospholipid classes in *P. pastoris* shown in Figure 4.6, the effect of the carbon source was limited. PC was predominant in all conditions and within the standard deviation of the analysis results, unless when deuterated methanol was employed. The amount of PC decreased to 35 ± 2% against the average value of 42 ± 6% found in the other conditions. PS was the second major class in all cases and varies from 23 ± 2% to 30 ± 1%. PE was the third class in abundance followed by PI and CL. In most cases it was difficult to confirm which one of the two smallest classes was more abundant. But when h-glycerol, d_8-glycerol/d_4-methanol and d_4-methanol were employed, PI was more abundant than CL.

Figure 4.7 displays the GC-FID traces of the whole apolar fractions of the *P. pastoris* lipids after growth in different conditions. The first observation is that in the deuterated conditions, the amount of ergosterol was lowered. Ergosterol quantification was performed as detailed in chapter 3.2.3 and values obtained from a calibration curve are

detailed in table 4.5. Methanol may also have had an impact on the sterol composition as we see two new peaks appearing in hydrogenous conditions at 19.5 and 21 min respectively. These peaks were not observed in the cells grown in deuterated conditions. They could correspond to di- and triglycerides because of their higher retention times and broad distribution due to different fatty acids. In deuterated conditions and in the presence of methanol, a large number of peaks with very low intensities were observed as well as a small peak very close to ergosterol. These peaks were not assigned as the sterol content in *P. pastoris* was dominated by ergosterol, but their appearance in the deuterated cells is nevertheless interesting as it could in the long run be used to understand the effect of deuterium on the biosynthesis pathway of ergosterol.

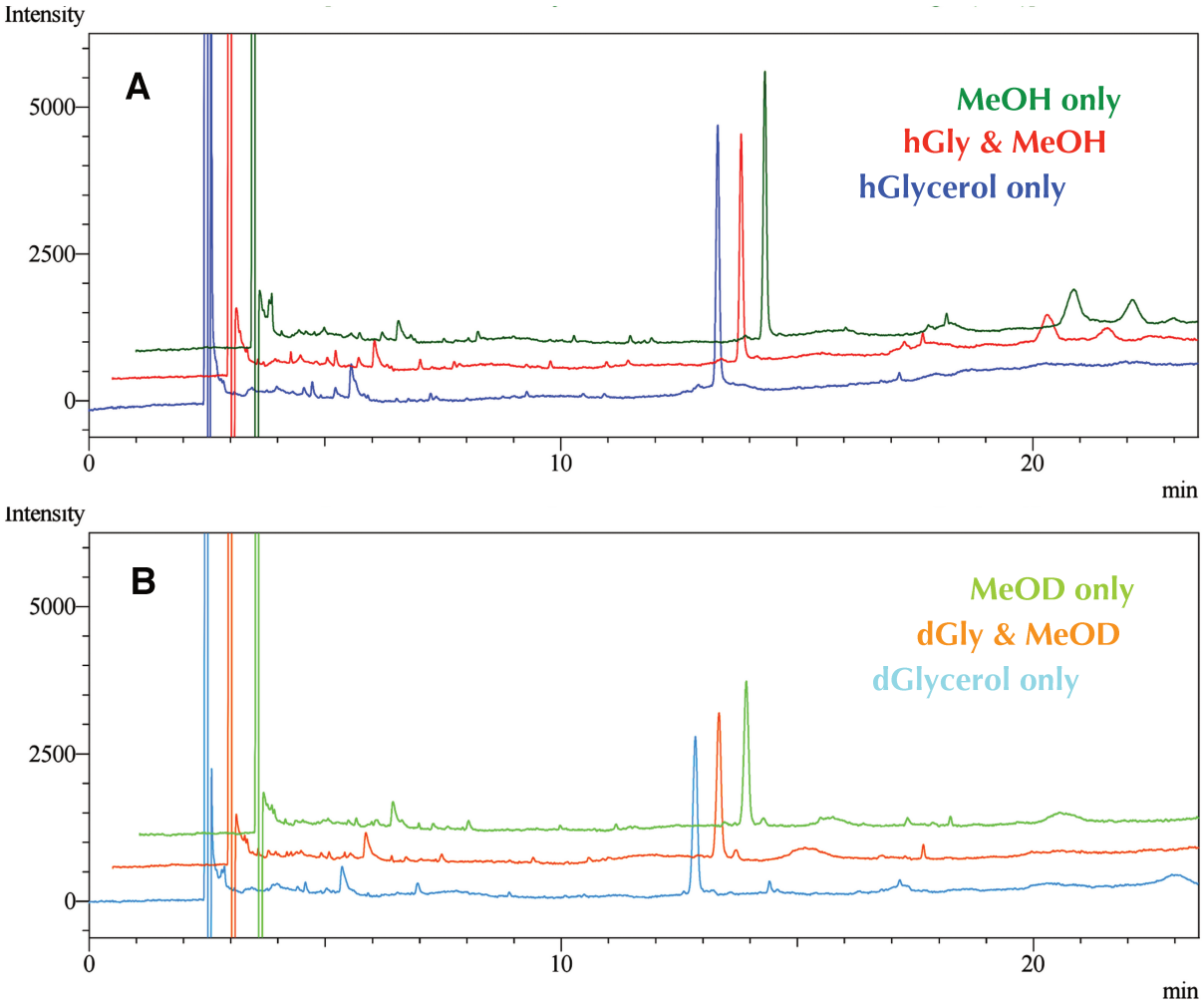

Figure 4.7 : GC-FID traces of free protiated (A) and deuterated (B) sterols depending on carbon source feeding of *P. pastoris*. *Glycerol/methanol and methanol traces are shifted respectively by +5000 and +10000 in intensity and are shifted respectively of 0.5 min and 1 min for clarity.*

Carbon source regime	Condition	Ergosterol (mol%)
Glycerol only	Hydrogenous	12.9 ± 0.1
	Deuterated	10.8 ± 0.1
Glycerol & methanol	Hydrogenous	11.3 ± 0.1
	Deuterated	10.1 ± 0.1
Methanol only	Hydrogenous	13.3 ± 0.1
	Deuterated	10.1 ± 0.1

Table 4.5 : Ergosterol quantification of *P. pastoris* samples grown with different carbon sources. Error bars arise from mass and volume uncertainties in the sample preparation process.

4.1.3. Discussion

It was observed, depending on the microorganism and the growth conditions employed, that the lipid composition, i.e. the proportion of classes, the amount and variety of sterol-like molecules and, most of all, the fatty acid composition, could be impacted by deuteration.

Although the lipid composition of a yeast is dependent on the strain, on the growth conditions and even if the amount of polyunsaturated phospholipids is higher in *P. pastoris* than in the well known budding yeast *S. cerevisiae*, the mechanisms defining the phospholipid metabolism are similar in most yeasts [132]. Complex reactions, via regulation of gene expression and post translational modifications, in response to multiple factors, stimuli and diverse elements found in the cytosol, are involved to allow the formation of the various phospholipids. A detailed review for such questions is recommended here [133]. The main aspect in relation to the present work concerns the homeostasis and production of the different fatty acids found in the phospholipids. Very briefly, the saturated fatty acids are first synthesized from carboxylation of acetyl-CoA in malonyl-CoA through the ATP-dependent reaction catalyzed by acetyl-CoA carboxylase. The product of this reaction is the two-carbon building block of the cyclic reactions catalyzed by fatty acid synthase and elongases [134]. Double bonds are introduced afterwards to the elongated fatty acids by the oxygen-dependent enzymes

known as fatty acid desaturases, in a process that is initiated by removal of hydrogens from two methylene groups, in a two step mechanism [135].

Since the deuteration of *P. pastoris* was associated with drastic changes in the unsaturation profile of the C_{18}-long acyl chains, the following desaturases found in fungal systems are of interest to this work. They correspond to the integral membrane Δ9 desaturase responsible of the conversion of stearic acid ($C_{18:0}$) to oleic acid ($C_{18:1}$), the Δ12 desaturase responsible for conversion of oleic acid to linoleic acid ($C_{18:2}$) and the Δ15 fatty acid desaturase responsible for conversion of linoleic acid to α-linolenic acid ($C_{18:3}$) [136, 137].

Concerning *P. pastoris* grown with glycerol as sole carbon source, the effects ascribed to the deuteration on the fatty acid composition (see figure 4.5), with increase of $C_{18:1}$ fatty acid upon deuteration, agreed perfectly with the initial work of Alexis de Ghellinck [50]. The accepted theory was based on the kinetic isotope effect of deuterium which due to a higher energy associated to a carbon-deuterium (C-D) over a carbon-protium (C-H) bond [138] would decrease the activity of the desaturases. Indeed, when deuterium is positioned on the first carbon, the carbon closer to the carboxylic group of the fatty acid, involved in this two step desaturation mechanism, the reaction rate decreases by a factor seven [139]. The activity of the enzymes would thus be lowered in perdeuterated conditions, and the need of several desaturation reactions impacted by the deuterium kinetic isotope effect could explain the decrease of amount of $C_{18:2}$ and $C_{18:3}$ leading to over-representation of the $C_{18:1}$ acyl chain, substrate, under normal circumstances, of the desaturases in charge of the production of the polyunsaturated species.

Interestingly, the use of different carbon sources presented in this work have shown a similar deuteration effect on the fatty acid composition of *P. pastoris* arising from the use and the amount of methanol found in the growth culture media. Use of methanol by the methylotrophic *P. pastoris* is known to involve a completely new carbon source integration pathway, via formation and incorporation of formaldehyde [140] but a modification of the phospholipid metabolism associated with this new pathway was, to our knowledge, never described. The results obtained clearly show that the more methanol was used in the growth media, the more $C_{18:1}$ fatty acid was found prevalent

over the other species. This effect also seemed additive to the kinetic isotope effect previously described in deuterated conditions. It has been shown that different alcohols, other than methanol, may have an impact on the cell growth and the lipid composition of different organisms, notably *S. cerevisiae* [141] supposedly to maintain the important physical parameter for the survival of the cells that represents the membrane fluidity. But such investigations were never informed concerning *P. pastoris*. Moreover, lipid analysis performed on peroxisome of an other *P. pastoris* strain (X33) grown with different carbon sources, including methanol, did not exhibit changes in the unsaturation profile of the acyl chains [142] and besides the large changes observed in the metabolism of the yeast during methanol-induced protein production [143] nothing seems to directly relate the methanol uptake to a decrease in the polyunsaturations of the phospholipid acyl chains.

Since the only hypothesis that methanol would provoke denaturation of proteins leading to the changes observed in acyl chain composition is more than unlikely, and given the strong resemblances between deuterium and methanol effects, the possibility that deuterium and methanol have a correlated effect through a similar mechanism is to be questioned. Indeed, one can think of the modifications of the fatty acids as a response of the microorganism to control the membrane fluidity, often simplistically summarized by the ratio of saturated and unsaturated lipids [141]. Indeed, the membrane fluidity is a complex parameter influenced by biophysical and biochemical factors such as temperature, pH, lipid composition, unsaturations and sterol content, among others, essential for the survival and the proper functioning of cells. Nonetheless, membrane fluidity was shown to be greatly impacted by the chain length and the degree of unsaturations of the phospholipid acyl chains [144]. Longer acyl chains, and lesser unsaturations are related to a decrease in fluidity while shorter acyl chains and more (poly)unsaturations involve a greater membrane fluidity. Thus, the phospholipid membranes from *P. pastoris* grown in presence of methanol, where $C_{18:1}$ increased at the expense of the polyunsaturated $C_{18:2}$ and $C_{18:3}$ acyl chains are less fluid than the membranes obtained from *P. pastoris* grown with glycerol only. Deuteration is also known to impact physically the lipids, mostly by changing the chain melting temperatures corresponding to the phase transition of the phospholipid from gel to liquid-crystalline phase. Indeed, deuterated phospholipids present a shift of their phase transition temperatures, of about -4°C in comparison to the hydrogenous molecules

[55]. Thus, one can think that for a given growth temperature, the yeast need lesser 'fluid' lipids, such as the polyunsaturated phospholipids, in deuterated rather than in hydrogenous conditions. This in order to maintain a similar membrane fluidity since the deuterated lipids found in gel phase are already less ordered than the equivalent hydrogenous molecules. Also, it was shown that by lowering the growth temperature the proportions of the polyunsaturated lipids increased [50]. This can be linked to the necessity of an increased fluidity of the membrane, needed at lower growth temperature. However, it is difficult to make assumptions on the overall fluidity of a membrane only based on its fatty acid composition. Phospholipid headgroups, and the amount and nature of sterols, as it will be discussed later, also affect the overall fluidity of a membrane. It would thus be interesting to probe experimentally and compare the fluidity of the different membranes either by comparison of the lateral motions of the molecule with fluorescence recovery after photobleaching [145], or the rotational correlation time of spin probes via electron spin resonance [146] or measurements of the compressional modulus on Langmuir monolayers [147]. But, even if the question of a general stress response mechanism in yeasts, necessary for the cell to adapt to external conditions, with permanent adjustments of the membrane fluidity, especially via modulation of the unsaturation profile of the phospholipid chains, has been intensively studied [148-150], its complexity and the determination of the impacted cellular mechanisms involve the use of protocols and techniques out of the domain of expertise of this thesis. The demonstration and understanding of a possible link between methanol and deuterium use and a mechanism of modulation of the phospholipid acyl chains composition and the sterol contents is possible but still hypothetical. Anyway, the understanding of these different behaviors and the effect of the growth parameters surely would be of interest towards the aim of the controlled production of deuterated lipids from yeast biomass.

The phospholipid class composition of *P. pastoris* (see figure 4.6) was not found as previously demonstrated for a growth with glycerol [50], the main difference concerning the inversion of the proportions of PE and PS. Practically the analytical method was adjusted as detailed in the materials and methods chapter, and the clear attribution of the different species on TLC, PS and PE being clearly separated, as well as the fact that replicates were performed and were consistent one to another, do not

allow to explain the changes observed. Mass spectrometry should be performed to verify the attribution of PS and PE in both analytical method.

Finally, the outcomes of the preliminary work performed to link a selected phenotype such as the sensitivity to AmB, with a possible change in lipid composition of *C. glabrata* was difficult to determine as no clear trends were observed between the fatty acids or the classes compositions. Replicates should be performed in order to be able to make clearer observations (see figures 4.1 and 4.2). Nevertheless, interesting effects were observed in the composition of the apolar fractions as variations, depending on the phenotype and deuteration were observed between the different strains (see figure and table 4.3). The sterol synthesis steps in *C. glabrata* from squalene to lanosterol and ergosterol as well as the numerous genes and enzymes involved are well described [151]. The main observation is the larger amount of ergosterol produced by the resistant strain Y2310 together with lower proportions of intermediates than in the AmB-sensitive strain which could reveal a more efficient ergosterol production in the AmB-resistant *C. glabrata* than in the AmB-sensitive strain. This observation was opposite in deuterated conditions where the intermediates, especially squalene, were more represented in the AmB-resistant than in the AmB-sensitive *C. glabrata*. But the ratio of ergosterol to intermediates found in the hydrogenous AmB-resistant strain was slightly higher than the one in hydrogenous AmB-sensitive, which is in contradiction to the conclusions of many studies found in literature stipulating that microorganisms with lower amounts of ergosterol and larger proportions of sterol intermediates are associated to greater AmB-resistance [151-152]. But in the present work, unlike in the other studies, the sterol intermediates differences in hydrogenous conditions were subtle and the higher ergosterol content seems to be related to higher resistance towards AmB.

After deuteration, the differences in sterol composition observed in hydrogenous conditions were modified with an almost equivalent amount of ergosterol in the two strains, but much larger proportions of intermediates were found in the resistant strain, principally due to squalene and to a lower extent to the 5,7,24(28)-Ergostatrienol whereas lanosterol was found more concentrated in the AmB sensitive strain by a factor two compared to the AmB-resistant strain. Even if quantification needs to be performed for each intermediate, it is difficult to justify the changes in the sterol metabolism only by the kinetic isotope effect of deuterium. In fact, a modulation seems to happen

induced by deuteration, but it is different depending on the strains. Thus, as for the fatty acid composition in *P. pastoris*, biomolecular investigations of the sterol biosynthesis in deuterated conditions of *C. glabrata* would be of interest to understand the implications and the parameters involved in order to be able to tune the lipid production of deuterated sterol-like molecules.

Even though the reasons behind the changes observed in the lipid composition are not fully elucidated, this work defined some strains and parameters to access a large variety of perdeuterated lipid molecules.

4.2. Pre-characterization and sample preparation

In the paragraphs below, the pre-characterization by QCM-D of the deposition of synthetic and natural bilayers was investigated before and after AmB interaction.

4.2.1. Conditions and formation of supported bilayers with QCM-D

Before neutron reflection experiments, it was important to study the deposition of the lipid systems employed. This is routinely performed using QCM-D, which allows the process of vesicle fusion to be followed and the quality of the bilayers to be estimated. The variation of frequencies is related to the amount of lipids deposited on the surface of the QCM-D sensor and the variation of energy dissipation, to the viscoelasticity of the deposited layer (see chapter 2.1 and [43]).

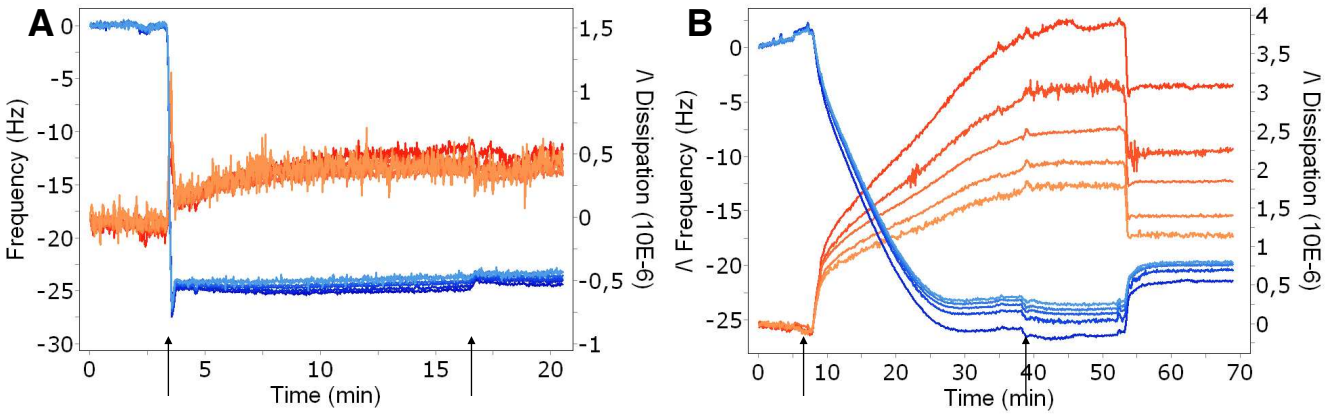

Figure 4.8 : QCM-D traces of a hydrogenous POPC bilayer deposition at 30°C in H_2O (**A**) and of the hydrogenous mixture of phospholipids extracted from *P. pastoris* at 52°C in salt solution of 100mM NaCl and 20mM $CaCl_2$ (**B**). Blue tones represents the changes of frequencies and the red tones, the changes of dissipation. Arrows : injection and rinsing.

Figure 4.8 (panel A) shows that the deposition of the bilayer of POPC was nearly instantaneous as the vesicles fused just after coming into contact with the surface. This was represented by the small troughs in the frequencies and peaks in dissipation at t=3.5 min, before the signal stabilized. Generally, the lower the frequencies, the higher is the mass deposited on the QCM-D sensor. And the higher the dissipation is, the more viscoelastic is the deposited film. So the troughs in frequencies indicate a rapid decrease of mass when at the same time the peak in dissipation shows that the film on the sensor surface became less viscoelastic. This is typical of adsorbed vesicle disruption and bilayer formation. Moreover, if all the frequency overtones superimpose, and the dissipation values stay low, it implies a compact lipid bilayer that does not exhibit a viscoelastic response characteristic of a thick highly hydrated layer. Once the flow of solvent was restarted to remove the excess of vesicle solution, at t=16.5 min, the Δf value (-25Hz) was almost constant with all overtones superimposed. The dissipation followed the same behavior as it increased to nearly $1x10^{-6}$ when the vesicles were inserted to fall back and stabilize around $0.5x10^{-6}$. In conclusion, the deposition was fast, performed at 30°C and in pure water with the characteristics values expected from such systems as seen in literature. Indeed, values around -25Hz in Δf are typical of homogeneous and continuous deposited lipid bilayers while small but non-zero ΔD values correspond to thin lipid bilayers in close interaction with the crystal surface with few or no adsorbed vesicles attached [43].

On the contrary, the deposition of the phospholipid mixture extracted from *P. pastoris* was performed at 52°C, using a salt solution composed of 100mM NaCl and 20mM of $CaCl_2$. This was previously found necessary in order to succeed with vesicle fusion of yeast lipids [16, 82]. The high temperature was necessary to assure fluidity and mixing of all lipids and the salts were necessary to allow bilayer deposition (See Figure 4.9). Panel B of figure 4.8 shows that deposition of the complex mixture is nevertheless much more slow than the deposition of POPC. The Δf decreased slowly, even after the flow of the vesicle solution was stopped, and stabilized around -25Hz. At the same time, the dissipation increased until it stabilized between 2 and $4x10^{-6}$ when the rinsing was restarted after 30 minutes of deposition, at t=39 min. After nearly 15 minutes of rinsing, a drop in dissipation and a slight increase in frequencies was observed. It corresponded to the removal of the remaining vesicles interacting with either the support surface or the supported lipid bilayer.

The deposition of the complex yeast phospholipid mixture was thus very different from synthetic lipids. The variety of the different phospholipids, with different headgroup, negatively charged (PS/PA and PG) or positively charged (PE), have an effect on the electrostatic interaction of vesicles with the surface as seen independently or in mixtures of two to three different lipids [153]. Thus the overall interaction behavior of a complex mixture of different phospholipid classes is the sum of the attractive and repulsive contributions of the different lipid constituents. This is also where the salt concentration, and thus the ionic strength of the solution, helps to counterbalance the charge of the vesicles and allows attractive interaction with the surface leading to vesicle disruption. Practically, not only the presence of two different salts impact the ionic strength of the solution but depending on their valence degree, monovalent for sodium and divalent for calcium, they can allow direct interaction between lipids and the surface [43]. Moreover, calcium at a concentration of 20mM rendered the samples turbid, meaning that the dimensions of the vesicles were big enough to diffract light, which also explains why the vesicle deposition was slow because of the higher stability of larger vesicles [61, 154]. Aggregates could even be seen after manual agitation or a few minutes resting after sonication (see Picture 4.1).

Figure 4.9 : Representative sample after sonication showing the turbidity of all the *P. pastoris* lipid-containing samples prepared with high calcium presence (100mM NaCl and 20mM $CaCl_2$). The same samples prepared in 100mM NaCl only or no salt at all (plain water) were perfectly clear after sonication.

The importance of calcium in the deposition process was then studied for both hydrogenous and deuterated *P. pastoris* phospholipid mixtures and representative results obtained with the perdeuterated sample are presented in Figure 4.9.

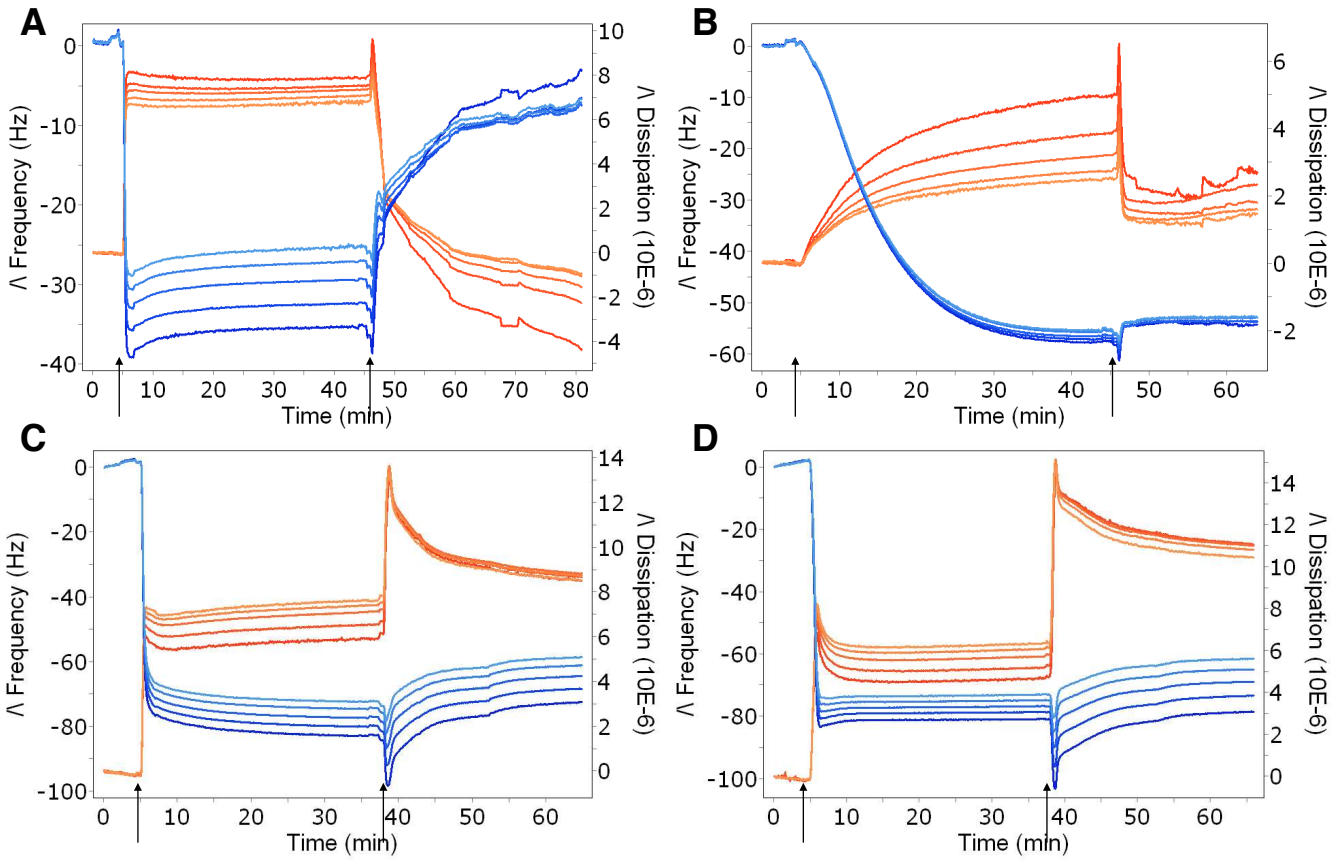

Figure 4.10 : QCM-D traces of the bilayer's deposition of the deuterated mixture of phospholipids extracted from *P. pastoris* at 52°C in salt solutions; 100mM NaCl (**A**), 100mM NaCl and 5mM $CaCl_2$ (**B**), 100mM NaCl and 10mM $CaCl_2$ (**C**) and 100mM NaCl and 20mM $CaCl_2$ (**D**). Blue tones represents the changes of frequencies and the red tones, the changes of dissipation. Arrows correspond to lipid injection and rinsing.

Panels C and D in figure 4.10 depict very similar deposition processes of the deuterated yeast phospholipids when 5 and 10mM of $CaCl_2$ were present in solution. The deposition was quick, similar to that in figure 4.8 for POPC. The main difference to POPC, besides the fact that the frequencies did not superimpose, concerned the large values reached both for Δf and ΔD when the signal stabilized. Before rinsing, Δf in both cases was between -80 and -70Hz while ΔD stabilized around 6 and 7×10^{-6}. After rinsing, even if Δf was diminished, ΔD rose to even higher values, 8.5 and 11×10^{-6} for C and D respectively, which did not correspond to a single supported lipid bilayer. Panels A and B, on the contrary, displayed very different behavior. When no calcium was added, the vesicles interacted with the surface as shown by both the frequency and dissipation changes, but were rinsed away when the flow was restarted as Δf and ΔD returned back to zero, even before rinsing with plain water.

Only the solution containing 20mM $CaCl_2$ (panel B) allowed the clear observation of vesicle fusion, with a drop of dissipation from 2.5-5 to 1.5-2.5x10^{-6} and stable frequencies after t=47 min.

From the experiments performed on QCM-D it was learned that the deposition of the complex lipid mixtures is relatively slow. It was thus important to allow at least 30 minutes for it during neutron experiments. Besides this factor, the high temperature facilitates the deposition and the presence of calcium in relatively large quantities in the solution (20mM) was necessary for successful vesicle interaction and fusion to a bilayer when rinsing.

4.2.2. Monitoring the effect of AmB on SLB with QCM-D

To characterize the interaction of Amphotericin B with lipid bilayers, bilayer deposition was followed by AmB injection, diluted in a solution 9:1 of water and DMSO. The bilayer deposition, visible during the first 15 min in figure 4.11 was performed correctly as we observed Δf = -24 Hz and ΔD values smaller than 1x10^{-6}. Addition of AmB, followed at t= 15 min (panel A) and t= 25 min (panel B) and the flow was stopped after 1 min. The large signal changes during the equilibration are due to the change in the solvent viscosity due to the presence of DMSO. The flow was restarted after stabilization of frequency and dissipation values or after 30 minutes maximum. The Δf and ΔD measured before and after AmB addition defines its effect on bilayers. It was observed in the case of pure POPC membrane that the AmB interacts quickly with the bilayer but once rinsed away, the changes were minimal; Δf= -4Hz and ΔD= +2x10^{-6}.
In the case of the ergosterol-containing POPC membrane, the AmB interaction equilibrated over a longer period of time, to reach lower values of Δf and higher values of ΔD than for pure POPC membrane. After rinsing, changes were more substantial with Δf= -30Hz and ΔD= +11x10^{-6}. In both cases, much more than in the POPC-ergosterol sample, material was added to the bilayer leading to a more viscoelastic membrane. These observations of a higher effect of AmB in ergosterol membranes are consistent with literature [68-70] and the high dissipation with ergosterol suggest that a highly hydrated layer similar to the sponge layer observed by Anderson et al. [5] is present.

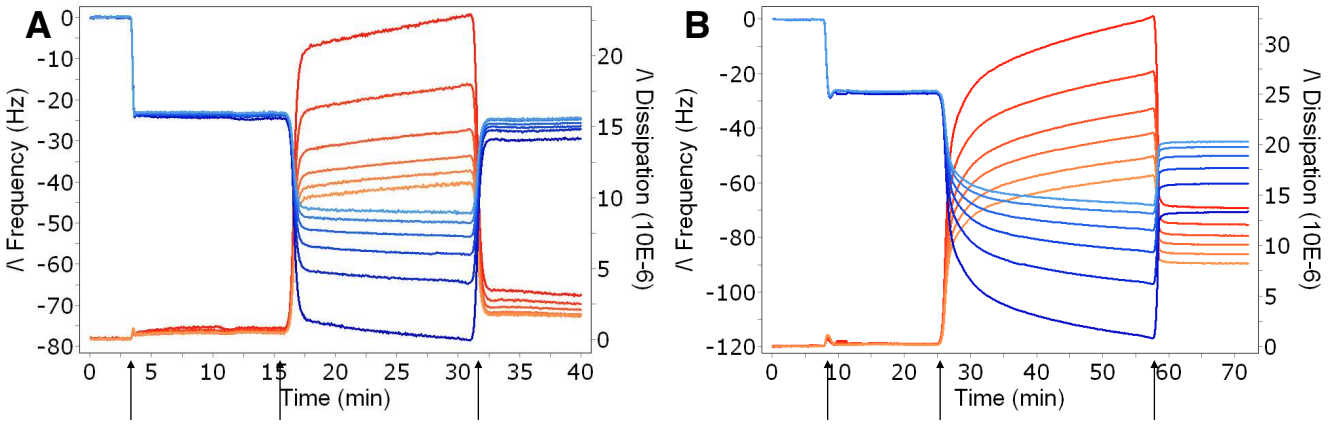

Figure 4.11 : QCM-D traces of POPC bilayer deposition followed by AmB action (1mM) at 30°C in H_2O (**A**) and of a mixture of POPC-Ergosterol (30mol%) bilayer followed by AmB action (1mM) at 30°C in H_2O (**B**). Blue tones represents the changes of frequencies and the red tones, the changes of dissipation. Arrows point out the lipid vesicles injection, the AmB addition and the rinsing, in this order over time.

The same experiment was performed with three other samples; the hydrogenous phospholipid mixture extracted from *P. pastoris*, as well as the phospholipid fraction containing either cholesterol or ergosterol and results are presented in figure 4.12.

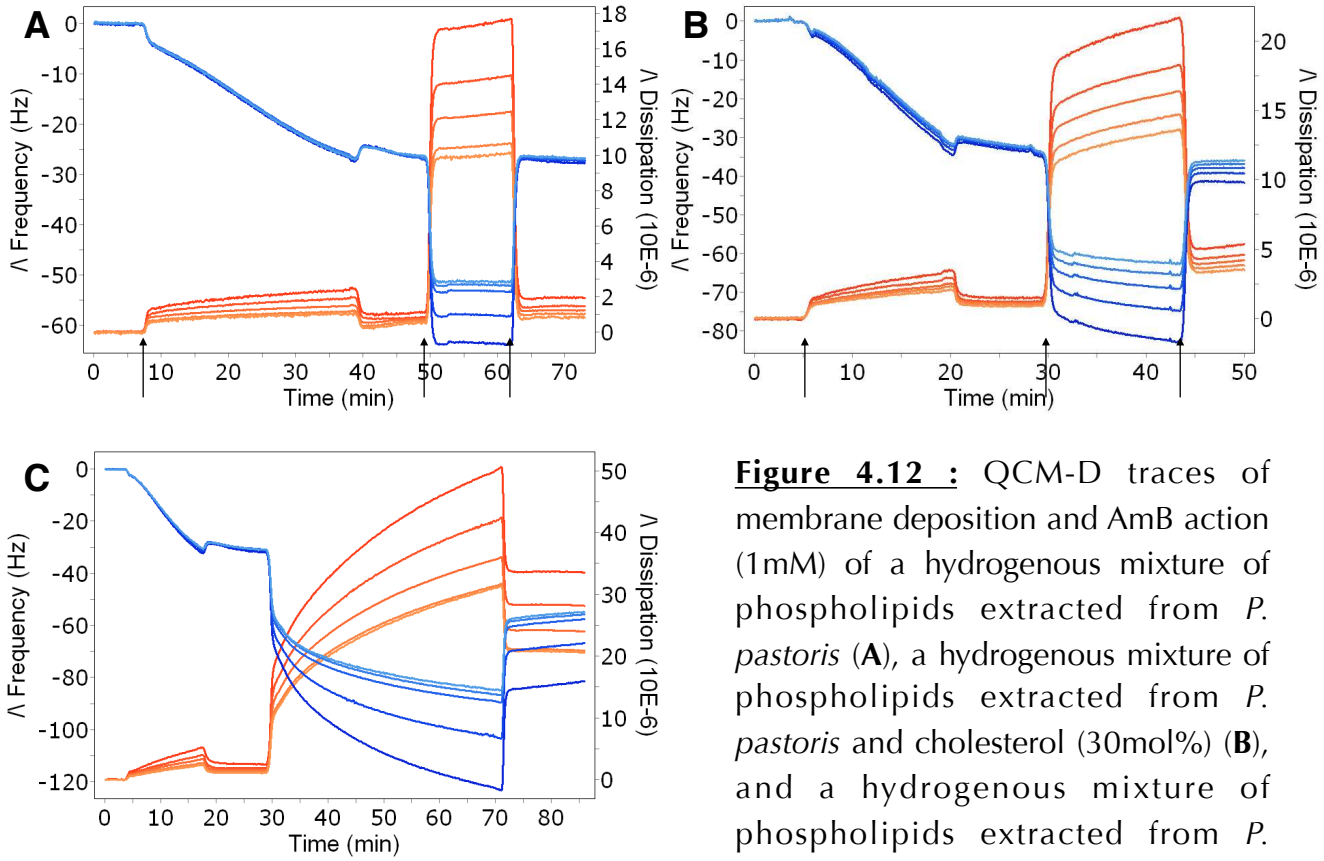

Figure 4.12 : QCM-D traces of membrane deposition and AmB action (1mM) of a hydrogenous mixture of phospholipids extracted from *P. pastoris* (**A**), a hydrogenous mixture of phospholipids extracted from *P. pastoris* and cholesterol (30mol%) (**B**), and a hydrogenous mixture of phospholipids extracted from *P. pastoris* and ergosterol (30mol%) (**C**) at 30°C in a salt solution of 100mM NaCl and 20mM $CaCl_2$. Blue tones represents the changes of frequencies and the red tones, the changes of dissipation. Arrows point out the lipid vesicles injection, the AmB addition and the rinsing, in this order over time.

The deposition was performed at 30°C, the temperature employed for the growth of *P. pastoris*, and it was controlled by starting to rinse when Δf reached -25Hz and AmB was added after 10 min rinsing. The incubation of AmB was stopped after stabilization of frequency and dissipation values or after 30 minutes maximum by restarting the flow. As for POPC in contact with AmB, the *P. pastoris* yeast phospholipid bilayer shown in figure 4.12 Panel A, presented a quick equilibration with nearly no changes of Δf and ΔD whereas the ergosterol containing bilayer (Panel C) had a long smooth equilibration and differences after rinsing were significant; Δf = -35Hz and ΔD = $+24x10^{-6}$. The cholesterol containing membrane presented an intermediate behavior with small changes before and after AmB incubation; Δf = -10Hz and ΔD = $+3.5x10^{-6}$.

These measurements gave insight into the importance of lipid composition in Amphotericin B action since the ΔD changes were completely different depending on sterol content but also on phospholipid composition. Not only were the effects more limited in POPC than in the yeasts phospholipid bilayers but the variations during the AmB interaction with the membrane were also of different intensities. These outcomes needed further investigations by neutron reflection to determine their structural origin.

4.3. Effect of gravity and sample density on the formation of lipid bilayers in neutron reflectometry cells.

Lipid bilayer formation monitored with QCM-D measurements is a good way to reproduce the deposition performed during neutron experiments. However, some important additional parameters were observed during reflectometry experiments.

The relationship between the geometry of deposition that is, whether the solution was above or below the silicon substrate, and the sample density, both in terms of isotopic labelling of the lipids and of the surrounding solution, gave rise to very different bilayer deposition results. Figure 4.13, panels A and C, show the reflectivity curves and scattering length density profiles for a hPolar dErg (30mol%) deposited in D_2O and H_2O with the solution in both cases below the substrate. The observations made with these samples are applicable to all samples containing the hydrogenous phospholipids

extracted from *P. pastoris*. The importance of matching the isotopic composition of the lipids to the solution in terms of their physical density can immediately be observed. The hPolar dErg bilayer deposited in D_2O in this geometry shows a Bragg peak at Q= 0.12 $Å^{-1}$, indicating multilayer deposition. Such multilayer samples could not be used for reflectometry studies of the AmB action as it would be difficult to interpret the mechanism of interaction. On the other hand, when the same sample was deposited in H_2O, this gave good results as seen in the fitted scattering length density profile which corresponds to a high-quality single bilayer (see panel C and table 4.6).

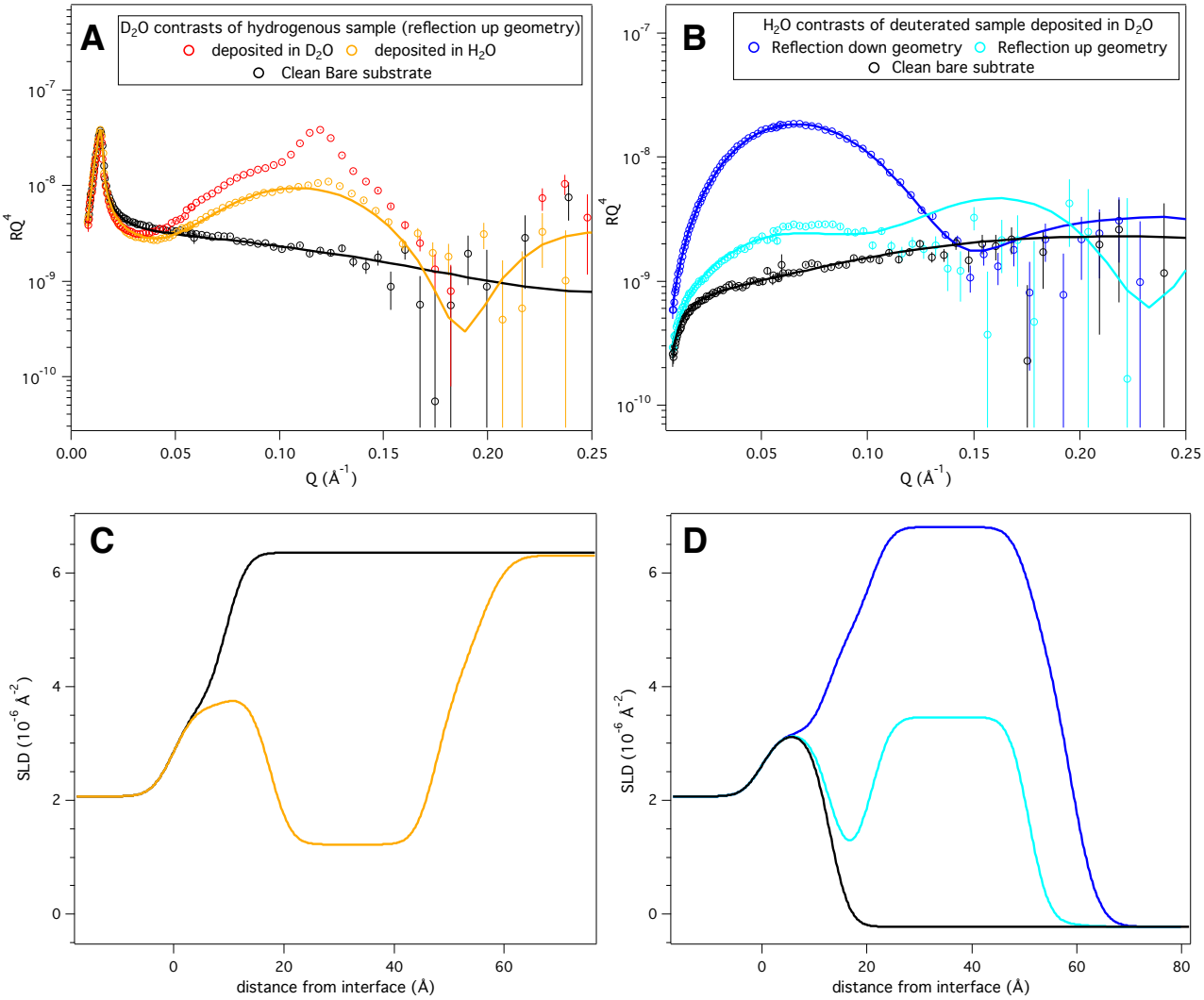

Figure 4.13 : Bilayers reflectivity data and fits of hPolar dErg (30mol%) when the deposition was performed either in H_2O (yellow) or D_2O (red) **(A)** and corresponding SLD profiles **(C)** and bilayers reflectivity data and fits of dPolar dErg (30 mol%) in D_2O when the deposition was performed either in reflection up (light blue) or reflection down (dark blue) **(B)** and corresponding SLDs **(D)**.

Samples	Fit panel C				Fit panel D			
Layers	τ (Å)	ρ (10^{-6} Å^{-2})	ϕ (%)	σ (Å)	τ (Å)	ρ (10^{-6} Å^{-2})	ϕ (%)	σ (Å)
Si	-	2.07	0	3 ± 1	-	2.07	0	3 ± 1
SiO_2	9 ± 1	3.41	8 ± 4	3 ± 1	13 ± 1	3.41	7 ± 5	3 ± 1
Head (in)	8 ± 2	2.9 ± 0.1	30 ± 5	3 ± 1	8 ± 2	7.1 ± 1	30 ± 8 85 ± 5	3 ± 1
Chains	30 ± 1	1.2 ± 0.1	0	3 ± 2	30 ± 2	6.8 ± 0.2	0 48 ± 4	3 ± 2
Head (out)	8 ± 2	2.9 ± 0.1	30 ± 5	4 ± 2	8 ± 2	7.1 ± 1	30 ± 9 90 ± 6	4 ± 2

Table 4.6 : Fitted parameters for hPolar dErg (30mol%) bilayer deposited in refection up in H_2O (panel C) and for dPolar dErg (30mol%) bilayer depending on the geometry of deposition, reflection down/reflection up (panel D).
As described in chapter 3, τ = thickness, in Å, ρ = scattering length density of the layer, in 10^{-6} Å^{-2}, ϕ = volume fraction of water relative to the lipids, expressed in percentage (%) and σ = the roughness of the layer after each layer, given as the sigma-value of the gaussian function describing the full-width half-maximum of the interface, in Å. The thickness corresponds to the full layer thickness in absence of roughness. SLD values correspond to the part of the molecule/material excluding any solvent present and were kept constant during fitting. ϕ is also indiscriminately called hydration. Chi-squared (χ^2) is associated to the simultaneous fits in all the solvent contrasts. The errors associated with the different parameters were determined from the maximum variation acceptable to maintain a relevant fit and for a specific parameter, the value given is the value found in the most sensitive contrast associated to this parameter.

Furthermore, the same effects were observed in the opposite isotopic contrast for all the samples containing the deuterated phospholipids extracted from *P. pastoris* when the geometry of deposition was reversed, i.e. reflection down, where the solution is above the substrate (not shown). The geometry aspect of the deposition on the yeast phospholipid mixtures was thus further investigated and results are shown in panel B and D of figure 4.13. The dPolar dErg sample in H_2O, was deposited either in reflection down or reflection up geometry. Good deposition was observed in the reflection down geometry whereas only 50% deposition was observed in the reflection up geometry, when the solution was below the substrate.

Gravity and its effect on the lipid vesicles in solution was interpreted to be the origin of the observed effects. Indeed, when taking into account the density of the lipids and that

of the solution, the quality of deposition was correlated to the geometry employed. On one hand, hydrogenous lipids tend to float in D_2O which explains the multilayer deposition observed in reflection up (figure 4.13 panel A) whereas the same vesicles were more homogeneously distributed in H_2O as it has a similar density to the lipids. On the other hand, deuterated lipids tend to sink in D_2O which explains the bilayer deposition observed in reflection down geometry while low deposition in reflection up geometry was observed (figure 4.13 panel B). It is worth noting that the deuterated lipids in H_2O showed multilayer deposition in reflection down geometry and no deposition in reflection up, demonstrating the importance of matching the composition of the samples and the solution. Thus, geometry of deposition and density matching of the samples were additional parameters taken into account in the subsequent experiments in order to obtain satisfactory single lipid bilayers of the yeast lipid mixtures. The fact that such effects were not observed in the deposition process for the samples prepared with POPC as the main lipid will be discussed in the next chapter.

Within the pre-characterization of the samples, the major outcome and practical issue concerned the gravity effect observed during the deposition process. And besides differences in the lipid compositions of the different samples tested, the isotopic labelling of the sample seemed to be the main parameter affecting the deposition success.

Formation of supported lipid bilayers via vesicle fusion is a quick and efficient technique widely used with a large variety of conditions (temperature, salt concentration, lipid vesicle concentration, flow rates) to be monitored in order to achieve a proper deposition [61, 153-154]. These parameters allowing to control the deposition process were largely studied but need to be adapted to the samples and surfaces employed. We confirmed the importance of the presence of the bivalent calcium ion and the need of appropriated treatment and activation of the substrate surfaces.

The real novelty concerned the gravity effect observed, affecting dramatically the deposition process to the point of either impeaching the deposition of a single bilayer or leading to partial but very stable multilayers. Such structures being problematic for the neutron reflectometry studies and determination of the membrane structures, a solution

needed to be brought in order to obtain the deposition of a uniform single bilayer for all the needed samples. The presence of calcium, necessary for vesicle disruption, caused great levels of turbidity of the sonicated samples which is correlated to large-sized vesicles, as they have sufficient radius to diffract light [155]. Bigger objects being more influenced by gravity than smaller ones, such effect was not observed in previous studies involving deposition of supported bilayers via vesicle fusion, where turbidity was not reported [61, 153-154]. Thus, depending on the isotopic contrast of the components of the sample, there was probably a concentration gradient of these large vesicles dispersed in the water solution which resulted in depletion near an upper surface but also enrichment near a lower surface in the case of deuterated lipids in H_2O salt solution, or the other way around for hydrogenous lipids in D_2O salt solution, facilitating or not the interaction between the lipids and the substrate depending on the employed geometry.

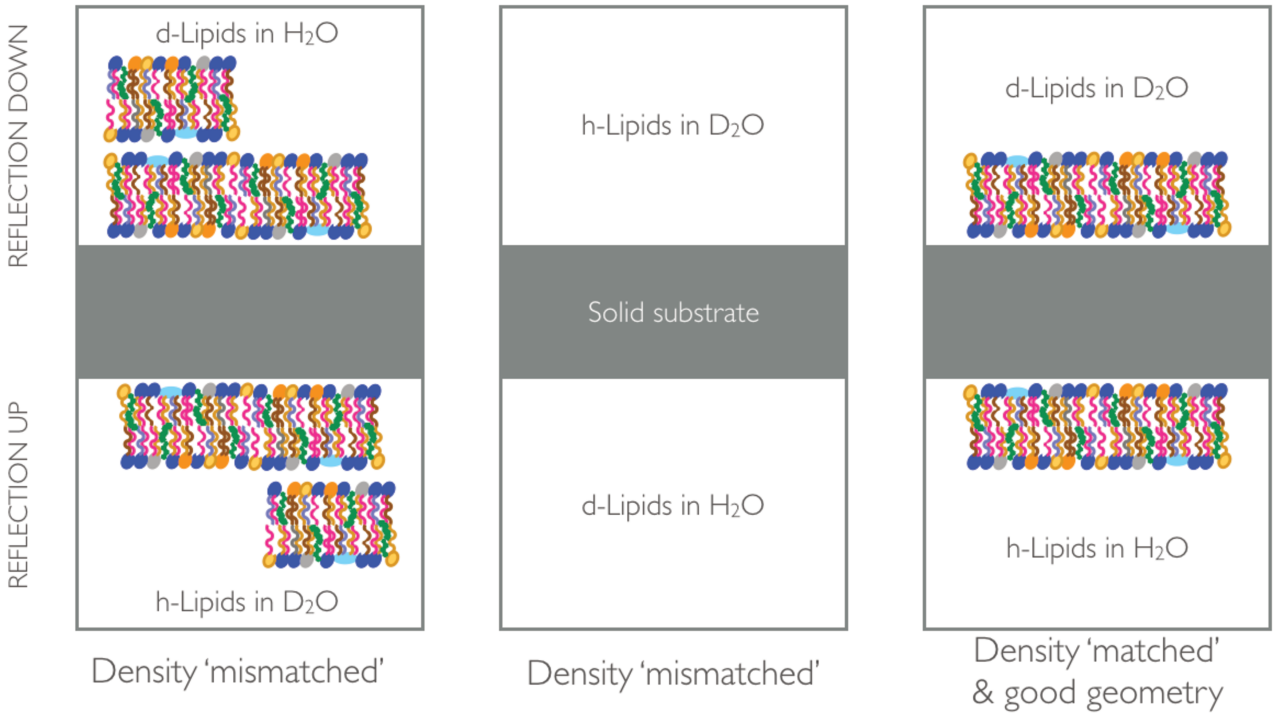

Figure 4.14 : Schematization of the gravity effect. It represents the relation between the geometry of deposition and the isotopic labelling of the samples (lipids and solution) together with its implication for lipid bilayer deposition.

Similar gradients were found on different systems by R. Campbell e al., who first investigated these effects for hexagonal phase aggregates present in an oppositely charged synthetic polyelectrolyte/surfactant mixture [156] and later focused on to

lamellar phase aggregates present in a dendrimer/phospholipid vesicle mixture [110]. In the former case, the rate of particle interactions with a solid interface was studied in relation to the isotopic contrast of the aggregates and bulk solution. In the latter case, it was shown that particle attachment to a solid interface occurred preferentially only when oriented above the solution. Note that these findings could only be possible by using FIGARO which allows both reflection up and reflection down configurations [114].

The empirical observations made for a unique bilayer deposition of the yeast-extracted phospholipids are depicted in figure 4.14. Optimal conditions involved to match the isotopic labelling of the lipids with the surrounding water, placing the substrate below when the deposition concerned deuterated samples and the substrate above in the case of hydrogenous sample deposition.

5. CHARACTERIZATION BY NEUTRON REFLECTOMETRY

With the aim to develop and demonstrate the necessity of new model membranes of higher relevance towards physiological systems, the action of Amphotericin B was compared on lipid bilayers of increasing complexity. The following chapter describes first the structural characterization of the bilayers by neutron reflectometry, followed by the effect of AmB on the structures. The results from a single synthetic lipid (POPC) and binary mixtures of POPC and a sterol (ergosterol or cholesterol) are compared to the samples composed of phospholipid mixtures extracted from *P. pastoris*. The effect of changing the substrate surface from silicon to sapphire on the deposition and structure of *P. pastoris* membranes was also investigated. Finally, the results obtained with bilayers composed of the total lipid extracts from the pathogenic yeasts *C. glabrata* are described. After demonstration of the ability to deposit single bilayers of yeast lipid mixtures, the purpose of neutron reflectometry experiments was to determine if differences could be observed in their structural organization or their response to the fungicidal drug AmB based on their chemical composition or biological origin.

5.1. Synthetic lipid (POPC) - Bilayer structural characterization

With access to the synthesized perdeuterated d_{82}POPC [49], the samples listed in table 5.1 were investigated via neutron reflectometry.

Samples	Contrasts measured before AmB interaction	Contrasts measured after AmB interaction
hPOPC	D_2O, CM4 and H_2O	D_2O, CM4 and H_2O
d_{82}POPC	D_2O, CM4 and H_2O	D_2O, CM4 and H_2O
hPOPC hErg (15 mol%)	D_2O, CM4 and H_2O	D_2O, CM4 and H_2O
hPOPC dErg (15 mol%)	D_2O, CM4 and H_2O	D_2O, CM4 and H_2O
d_{82}POPC hErg (15 mol%)	D_2O, CM4 and H_2O	D_2O, CM4 and H_2O
hPOPC hChol (15 mol%)	D_2O, CM4, CMSi and H_2O	D_2O, CM4, CMSi and H_2O
hPOPC dChol (12 mol%)	D_2O, CM4, CMSi and H_2O	D_2O
d_{82}POPC hChol (15 mol%)	D_2O, CM4, CMSi and H_2O	D_2O, CM4, CMSi and H_2O
d_{82}POPC dChol (15 mol%)	D_2O, CM4, CMSi and H_2O	D_2O and CM4

Table 5.1 : List of the samples and the contrasts measured on Platypus at ANSTO.

5.1.1. Monomolecular system : hPOPC and d_{82}POPC

hPOPC and d_{82}POPC bilayers were compared in order to elucidate any structural differences induced by deuteration. Figure 5.1 shows the reflectivity curves and scattering length density profiles corresponding to the best fits to the data for POPC and d_{82}POPC bilayers in three different water contrasts (D_2O, CM4 and H_2O). Table 5.2 displays the parameters associated with the fits presented in figure 5.1. The quality of the fits that used the SLDs calculated as described in the Material and Methods section, was determined by the χ^2 of the simultaneous fits of the different contrasts with values of 8.4 and 5.2 for POPC and d_{82}POPC bilayers respectively.

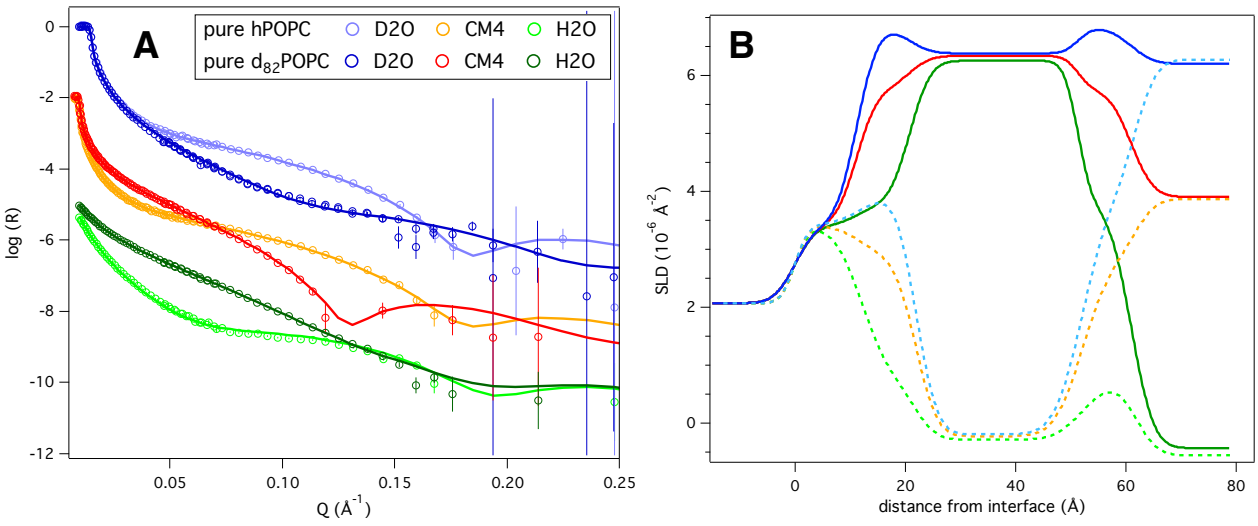

Figure 5.1 : Bilayers reflectivity data and fits **(A)** and corresponding SLD profiles **(B)** of hPOPC (light colors) and d_{82}POPC (dark colors).

Samples	hPOPC bilayer			χ^2 = 5.8	d_{82} POPC bilayer			χ^2 = 4.8
Layers	τ (Å)	ρ (10^{-6} Å^{-2})	ϕ (%)	σ (Å)	τ (Å)	ρ (10^{-6} Å^{-2})	ϕ (%)	σ (Å)
Si	-	2.07	0	3 ± 2	-	2.07	0	3 ± 2
SiO_2	11 ± 1	3.41	2 ± 2	3 ± 2	12 ± 2	3.41	4 ± 4	4 ± 2
Head (in)	10 ± 2	1.86 ± 0.1	46 ± 6	4 ± 2	10 ± 1	7.35 ± 0.2	48 ± 4	4 ± 2
Chains	30 ± 2	-0.29 ± 0.05	1 ± 1	3 ± 2	31 ± 1	6.39 ± 0.05	1 ± 1	3 ± 2
Head (out)	10 ± 2	1.86 ± 0.1	46 ± 6	4 ± 2	10 ± 1	7.35 ± 0.2	48 ± 4	4 ± 2

Table 5.2 : Fitted parameters of the hydrogenous and perdeuterated POPC supported bilayers. Parameters were defined in chapter 3 and in table 4.6.

It was observed that besides the small differences of the silicon oxide layers, both samples were well deposited and could be fitted with the same structural model (see table 5.2). The quality of the bilayers was assessed by the water content found in the hydrophobic chains. Indeed, the small variation of the SLD of the lipid chain region in the different water contrasts, in both samples, was due the presence of a small amount of solvent (<2%) in the chain region. This solvent is related to the discontinuity of the bilayer over the surface illuminated with neutrons and increases with a low surface coverage, as more holes filled with water are present between membranes patches. Thus it directly correlates to the quality of the deposition, with a good quality needed for both the structural characterization and a relevant interpretation of the AmB mechanism. The fits were constrained with the requirement that the lipid chains and headgroups (including or not the associated water molecules) occupy the same area per molecule which could be calculated from the estimated molecular volumes of the different lipid parts and the layer thicknesses obtained from the fit. The best fit to the data using this constraint resulted in a dry area per molecule of 62 ± 4 Å^2. This value is well correlated to 64.3 Å^2, found in literature [157]. The errors in the area per molecule were propagated from the uncertainties in thicknesses and hydration of the chain region displayed in table 5.2.

5.1.2. Bimolecular system : POPC and ergosterol

Bilayers of deuterated and non-deuterated POPC with ergosterol were investigated to observe the effect of the fungal sterol on the membrane structures and to mimic the

sterol content of fungal membranes for the investigation of the AmB mechanism. Indeed, samples containing 15mol% of ergosterol were chosen as it represents a content often found in yeasts [158] and close to the amounts we obtained in *P. pastoris*.

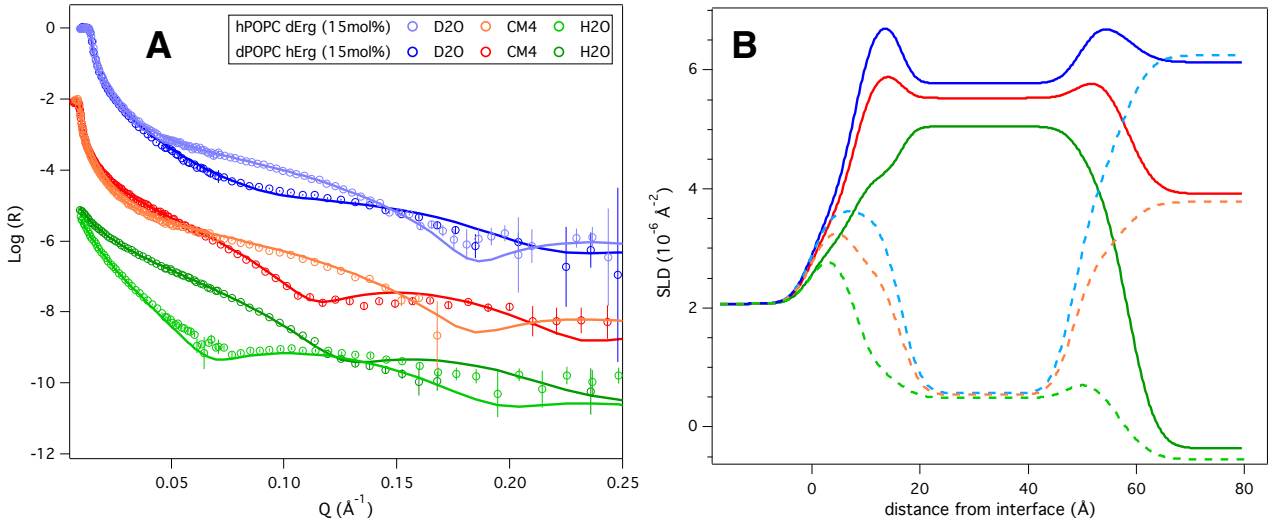

Figure 5.2 : Bilayers reflectivity data and fits **(A)** and corresponding SLD profiles **(B)** of mixtures of hPOPC with 15mol% deuterated ergosterol (light colors) and d_{82}POPC with 15mol% hydrogenous ergosterol (dark colors).

Samples	**hPOPC dErg (15 mol%) bilayer χ^2 = 9.3**				**d_{82} POPC hErg (15mol%) bilayer χ^2 = 8.8**			
Layers	τ (Å)	ρ (10^{-6} Å^{-2})	ϕ (%)	σ (Å)	τ (Å)	ρ (10^{-6} Å^{-2})	ϕ (%)	σ (Å)
Si	-	2.07	0	3 ± 1	-	2.07	0	3 ± 1
SiO_2	8 ± 0.6	3.41	10 ± 4	3 ± 2	8 ± 0.6	3.41	10 ± 4	3 ± 2
Head (in)	8 ± 2	1.86 ± 0.1	38 ± 6	3 ± 2	9 ± 2	7.35 ± 0.2	39 ± 6	3 ± 2
Chains	32 ± 2	0.51*±0.07	2 ± 2	3 ± 2	32 ± 2	5.73**±0.01	11± 3	3 ± 2
Head (out)	8 ± 2	1.86 ± 0.1	38 ± 6	4 ± 2	9 ± 2	7.35 ± 0.2	39 ± 6	4 ± 2

Table 5.3 : Fitted parameters of the bilayers composed of hPOPC and 15 mol% deuterated ergosterol and d_{82}POPC with 15 mol% hydrogenous ergosterol. Parameters were defined in chapter 3 and in table 4.6. *Corresponds to the SLD calculated from the nominal composition of 15mol% of d-ergosterol and 85mol% POPC. **Corresponds to the SLD calculated from the nominal composition of 15mol% of h-ergosterol and 85mol% d_{82}POPC

Figure 5.2 shows the reflectivity curves and scattering length density profiles corresponding to the best fits to the data for hPOPC dErg (15 ± 2mol%) and d_{82}POPC hErg (15 ± 1mol%) bilayers in three different water contrasts (D_2O, CM4 and H_2O). The

chain SLD used for the best fits shown here corresponded to the calculated values and thus confirmed the 15mol% ergosterol (11% v/v) content. The compositional uncertainty was assessed from the uncertainty of the SLD of the chain region, as neutron are very sensitive to it and because we observed that the deposition process led in most cases to variations higher than the expected experimental uncertainty in the preparation of the sample (of ± 2mol%). Depending on the sample composition and the contrast, the uncertainties in the SLD of the chain region varies. The values given correspond to the values obtained in the most sensitive contrast in each case (e.g. in H_2O for d_{82} POPC hErg).

The quality of the fits determined by the χ^2 of the simultaneous fits of the different contrasts is given in table 5.3. In this case, the data for the two samples could also be fitted with the same symmetrical structural model even if the deuterated bilayer had a somewhat lower surface coverage (89 ± 3%) as represented by the water presence in the chains and chain SLD changes between the solvent contrasts. The data for the fully hydrogenous sample (hPOPC hErg, 15 ± 8 mol%) (Chain SLD = -0.21 ± 0.04 10^{-6} $Å^{-2}$) could be fitted with the same model as that presented in table 5.3 for hPOPC dErg. The higher compositional uncertainty arises from poor contrast between the phospholipid and the ergosterol, when they are both hydrogenous.

The chain region of the three ergosterol-containing POPC bilayers were found to have the same thickness of 32 ± 2Å. Although the fits suggest some thickening with respect to the sterol-free POPC chain layers (30 ± 2Å and 31 ± 1Å for hPOPC and d_{82}POPC respectively), the changes observed +2 ± 3Å between hPOPC and hPOPC dErg or hPOPC hErg, and +1 ± 2Å between d_{82}POPC and d_{82}POPC hErg) were lower than the uncertainties associated to the thickness of the chain layer. The headgroup layers, with hydrations of 38 ± 6% for both hPOPC hErg and hPOPC dErg bilayers and 39 ± 6% for the d_{82}POPC hErg sample also seemed less hydrated than in the sterol-free membranes (46 ± 6% and 48 ± 4% for hPOPC and d_{82} POPC respectively). But the diminution of hydration between the hPOPC bilayers was not significant (-8 ± 8%) due to larger uncertainties than for the d_{82}POPC bilayers, with -9 ± 7% hydration associated to ergosterol presence. Similar structural changes were already observed with neutron reflection in monolayer systems of POPC and ergosterol [48]. A strong increase of the thickness (4 ± 1Å) of the chain region of POPC monolayers, due to addition of 30 mol%

ergosterol, and a reduction in the hydration of the headgroup of 10 ± 3%, were observed in the monolayer data. In the present case, it was considered that the ergosterol is oriented normal to the bilayer plane with the hydroxyl group located at the junction of the chain and head layers (as defined in Material and Methods) because of the SLD homogeneity found in the chain region. Indeed, a possible asymmetry in the SLD of the two distinct chain leaflets was investigated but did not lead to better models than the symmetrical ones presented here. The position of the sterol in the bilayer, parallel to the phospholipids, is supported by molecular dynamics simulation studies [159] which show that the ergosterol ring has a tilt angle with respect to the bilayer normal distributed between 0 and 45°, and an average value of 25.2° at 11mol% in DMPC. Experimental diffraction data also support this localization with the total length of the sterol molecule found normal to the bilayer [47]. The lipid ordering of ergosterol in both chain and headgroups have been probed with NMR, FTIR or fluorescence spectroscopy, among other techniques, and its condensing effect could explain the reduction of the headgroup hydration [160]. Indeed, calculating the areas per molecule, without taking into account the water content present in chains, the sterol increased the lateral packing of the lipids to give a dry area per molecule of 57 ± 4 $Å^2$ for POPC-Ergosterol (15mol%) membranes. This is in good agreement with previously published data on the condensing effect of ergosterol in POPC bilayers [161].

5.1.3. Bimolecular system : POPC and cholesterol

Bilayers of deuterated and non-deuterated POPC with 15 mol% cholesterol were investigated to mimic mammalian membranes for the investigation of the AmB toxicity mechanism and to compare its effect on the structure of POPC with or without ergosterol. Indeed, due to the small molecular volume difference between ergosterol and cholesterol, the 15mol% sterol samples were considered equivalent.

The data for the four cholesterol-containing samples shown in figure 5.3 could all fitted to a similar model (see table 5.4) apart from differences in the substrate surface structure. The only exceptions concerned the lower surface coverage obtained for the samples containing deuterated POPC with 7 ± 2% v/v of water found in the hydrophobic chains in both cases. The four solvent contrasts measured for each sample allowed a good refinement of the model with χ^2 of 7.2, 6.3, 7.0 and 3.0 respectively for

hPOPC hChol (15 ± 7 mol%), d_{82}POPC dChol (15 ± 7 mol%), d_{82}POPC hChol (15 ± 3 mol%) and hPOPC dChol (12 ± 2 mol%). For the hPOPC dChol sample, the SLD of the hydrophobic chain layer was found to be lower than calculated from the nominal composition of 89% v/v POPC and 11% v/v cholesterol. Indeed, since no satisfactory fit could be found with the expected value of 0.57 10^{-6} $Å^{-2}$, the parameter was fitted to be 0.31 ± 0.06 x 10^{-6} $Å^{-2}$. This corresponds to 8.6 ± 1.6% v/v d-cholesterol, equivalent to 12 ± 2mol%. By taking into account the uncertainty, the final value is relatively close to the 15mol% expected from the nominal composition which explains that no other major differences in the model could be seen. Since the SLD of the other samples corresponded to their nominal composition, it is most likely that the error do not come from the preparation of the lipid stock solutions, but probably come from experimental biased in the volume taken from the d-cholesterol stock solution (2µL less than needed). Another observation evident from the data is that the dry area per molecule calculated was lower with cholesterol than with ergosterol. The value calculated from the fits of the three 15mol% cholesterol-containing samples of 55 ± 3$Å^2$ correlates very well with the values described for POPC monolayers comprise between 53 and 58$Å^2$ for 10 and 20 mol% cholesterol respectively [162].

All four cholesterol-containing POPC bilayers were found to have very similar chain region thicknesses with 33 ± 1Å and 32 ± 2Å for hPOPC hChol and hPOPC dChol samples and 33 ± 2Å for both d_{82}POPC cholesterol-containing bilayers. Although the fits suggest some thickening with respect to the sterol-free POPC chain layers (30 ± 2Å and 31 ± 1Å for hPOPC and d_{82} POPC respectively), the change observed was of the same order of magnitude or higher than the uncertainties associated to the thickness of the chain layer with +2 ± 2Å or +2 ± 3Å, unless for hPOPC hChol and hPOPC with a thickening of +3 ± 2Å. The hydration of the headgroups were nearly unchanged in comparison to the membranes constituted only by POPC molecules. The increase of the roughnesses between the outer headgroups and the bulk solution observed in the three 15mol% cholesterol-containing samples, in comparison to the membranes with or without ergosterol, could be explained by roughness of the chain-head interface of the phospholipids with cholesterol, as previously suggested by X-Ray reflectivity measurements on DPPC sterol-containing monolayers [163]. Note that the cholesterol is also considered to be oriented normal to the bilayer plane with the hydroxyl group at the junction of the chain and head layers, because it was not possible to model any

SLD inhomogeneities in the chain region in the fits. As for ergosterol, this orientation is also supported by molecular dynamics simulation which investigate to tilt of the cholesterol in DPPC in function of the sterol concentration. The tilt of cholesterol, with respect to the bilayer normal thus evolves from 20 ± 3° at low concentrations to 11 ± 1° [164]. Experimentally, previous measurements using neutron diffraction, has shown that cholesterol is nearly fully extended in POPC bilayer normal [47].

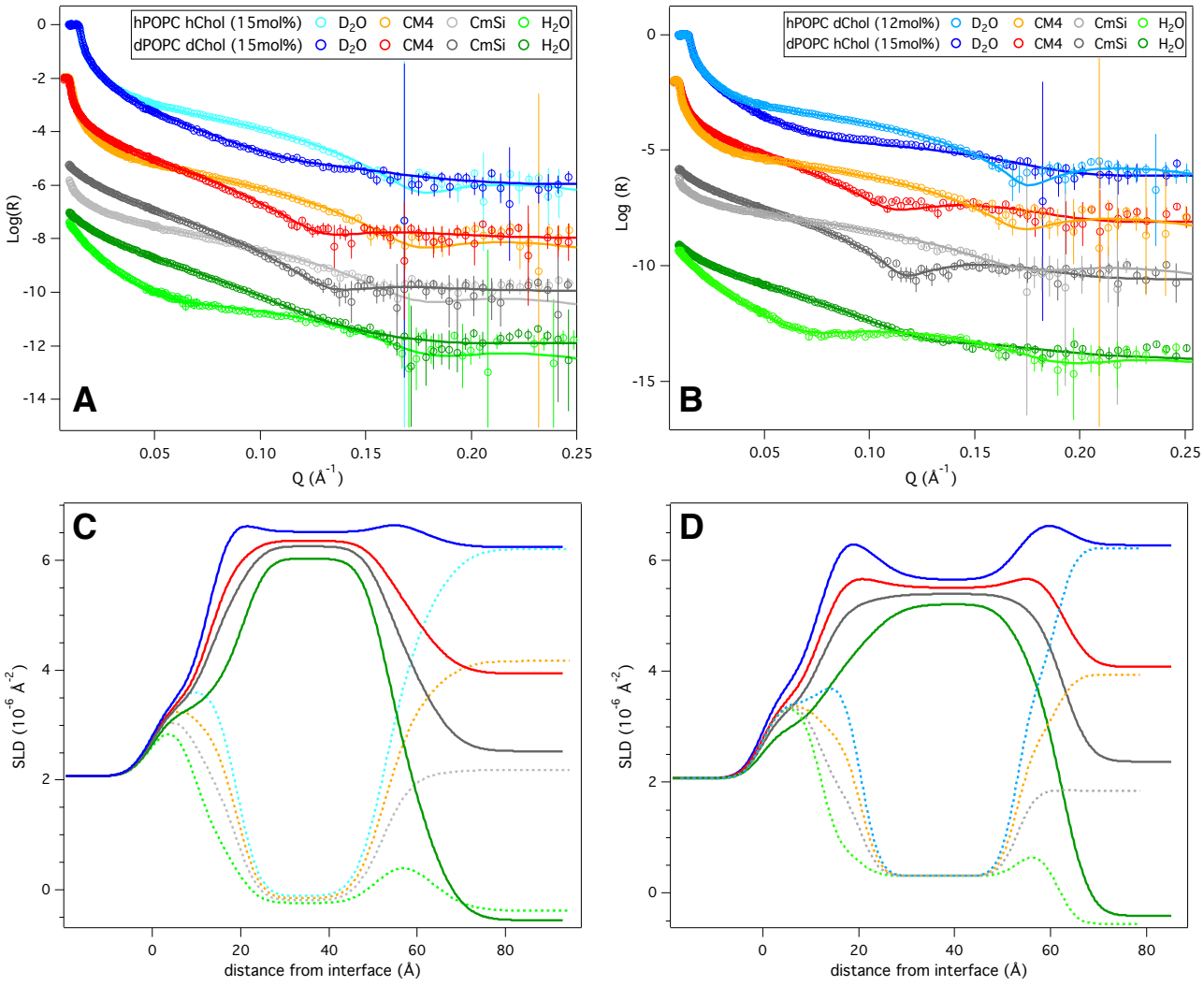

Figure 5.3 : Bilayers reflectivity data and fits of mixtures of hPOPC with 15mol% hydrogenous Cholesterol (light colors) and d_{82}POPC with 15mol% deuterated cholesterol (dark colors) **(A)** and corresponding SLD profiles **(C)** and bilayers reflectivity data and fits of mixtures of hPOPC with 12mol% deuterated ergosterol (light colors) and d_{82}POPC with 15mol% hydrogenous ergosterol (dark colors) **(B)** and corresponding SLD profiles **(D)**. All samples were measured in 4 contrasts (D_2O, CM4, CMSi and H_2O)

Samples	hPOPC hChol (15 mol%) bilayer χ^2 = 7.2				hPOPC dChol (12mol%) bilayer χ^2 = 3.0			
Layers	τ (Å)	ρ (10^{-6} Å^{-2})	ϕ (%)	σ (Å)	τ (Å)	ρ (10^{-6} Å^{-2})	ϕ (%)	σ (Å)
Si	-	2.07	0	4 ± 1	-	2.07	0	3 ± 2
SiO_2	10 ± 2	3.41	6 ± 4	4 ± 1	12 ± 2	3.41	1 ± 1	3 ± 2
Head (in)	9 ± 2	1.86 ± 0.1	42 ± 6	4 ± 2	8 ± 2	1.86 ± 0.3	46 ± 8	3 ± 2
Chains	33 ± 1	-0.23*±0.03	1 ± 1	5 ± 1	32 ± 2	0.31**±0.06	1 ± 1	3 ± 2
Head (out)	9 ± 2	1.86 ± 0.1	42 ± 6	7 ± 2	8 ± 2	1.86 ± 0.3	46 ± 8	3 ± 2
Samples	**d_{82}POPC dChol (15 mol%) bilayer χ^2=7.0**				**d_{82} POPC hChol (15mol%) bilayer χ^2=7.0**			
Layers	τ (Å)	ρ (10^{-6} Å^{-2})	ϕ (%)	σ (Å)	τ (Å)	ρ (10^{-6} Å^{-2})	ϕ (%)	σ (Å)
Si	-	2.07	0	3 ± 2	-	2.07	0	3 ± 1
SiO_2	13 ± 2	3.41	4 ± 4	4 ± 1	11 ± 2	3.41	11 ± 6	3 ± 1
Head (in)	8 ± 1	7.35 ± 0.2	45 ± 5	4 ± 2	9 ± 1	7.35 ± 0.2	44 ± 5	4 ± 1
Chains	33 ± 2	6.54*±0.07	7 ± 1	4 ± 2	33 ± 2	5.62*±0.05	7 ± 2	4 ± 2
Head (out)	8 ± 1	7.35 ± 0.2	45 ± 5	7 ± 2	9 ± 1	7.35 ± 0.2	44 ± 5	5 ± 2

Table 5.4 : Fitted parameters of the different bilayers composed of POPC and cholesterol. Parameters were defined in chapter 3 and in table 4.6. *Corresponds to 15mol% of h-cholesterol **Corresponds to 12mol% of d-cholesterol.

5.2. Synthetic Lipids - AmB effect

Once the bilayers structures were measured in 3 to 4 solvent contrasts, 3mL of a 1mM solution of AmB in D_2O/DMSO (9:1 v/v) was injected into the neutron reflectivity cell and incubated at 30°C for 30 minutes (see Materials and Methods). After rinsing with plain D_2O to remove the DMSO, the bilayers structures were measured again. The changes in reflectivity curves before and after AmB addition are presented below, in figures 5.4 to 5.8 with the parameters detailed in tables 5.5 to 5.9.

5.2.1. Monomolecular system : hPOPC and d_{82}POPC

Figure 5.4 shows the data before and after AmB addition for hPOPC and d_{82}POPC in 3 water contrasts (D_2O, CM4 and H_2O). The parameters corresponding to the fits after AmB addition are given in table 5.5.

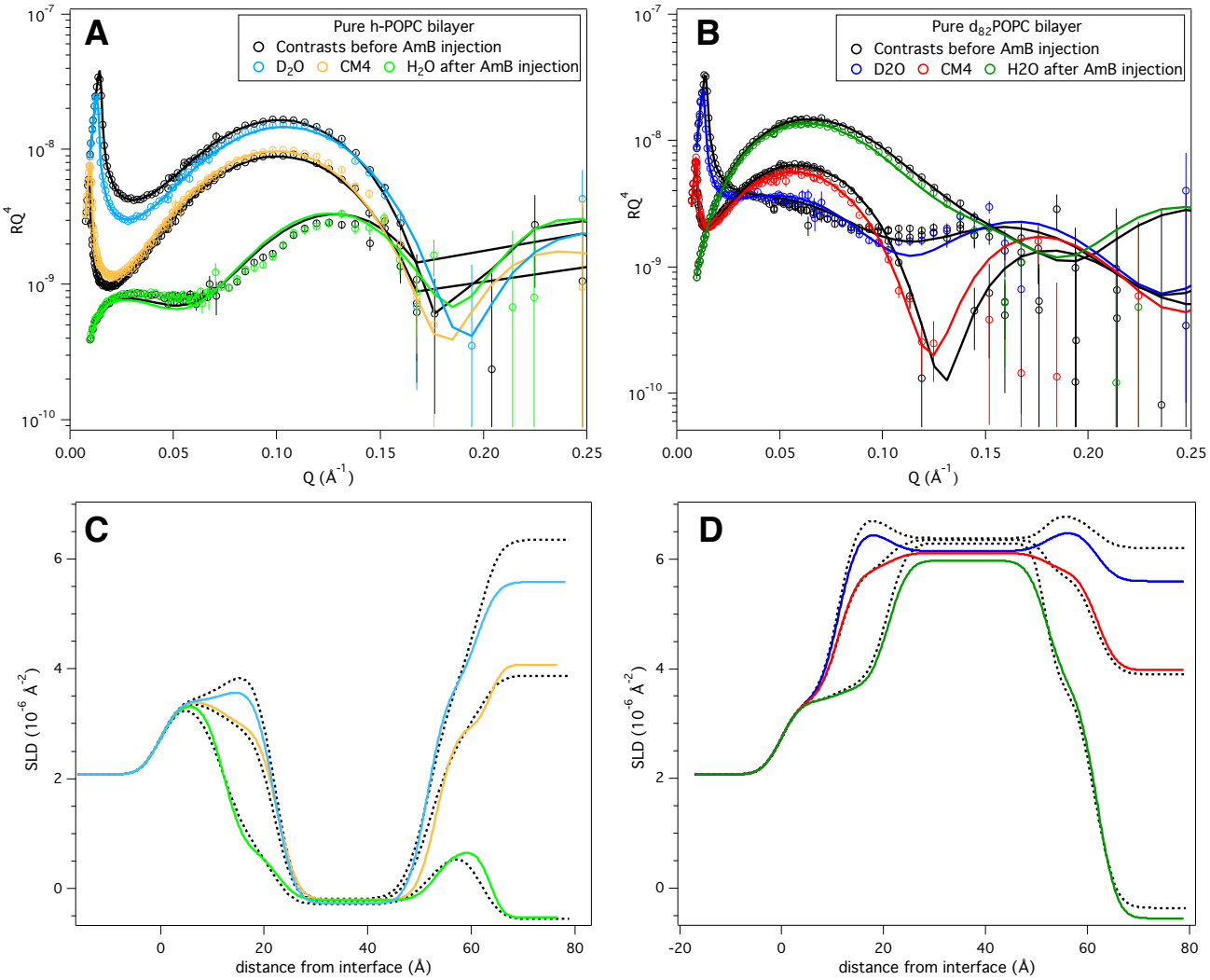

Figure 5.4 : Bilayers reflectivity data and fits of hPOPC before (black) and after AmB addition (light colors) **(A)** and corresponding SLD profiles **(C)**, and bilayers reflectivity data and fits of d_{82}POPC before (black) and after AmB addition (dark colors) **(B)** and corresponding SLD profiles **(D)**.

Samples	**hPOPC bilayer after AmB addition χ^2 = 7.4**				**d_{82}POPC bilayer after AmB addition χ^2 = 4.9**			
Layers	τ (Å)	ρ (10^{-6} Å^{-2})	ϕ (%)	σ (Å)	τ (Å)	ρ (10^{-6} Å^{-2})	ϕ (%)	σ (Å)
Si	-	2.07	0	3 ± 2	-	2.07	0	3 ± 2
SiO_2	11 ± 1	3.41	2 ± 2	3 ± 2	12 ± 2	3.41	4 ± 4	3 ± 2
Head (in)	10 ± 2	1.86 ± 0.1	51 ± 5	3 ± 2	10 ± 1	7.35 ± 0.2	46 ± 4	3 ± 2
Chains	31 ± 2	-0.17±0.06*	1 ± 1	3 ± 2	31 ± 1	6.16±0.08**	2 ± 2	3 ± 2
Head (out)	10 ± 2	1.86 ± 0.1	51 ± 5	3 ± 2	10 ± 1	7.35 ± 0.2	46 ± 4	3 ± 2

Table 5.5 : Fitted parameters of POPC and d_{82}POPC bilayers after AmB addition. Parameters were defined in chapter 3 and in table 4.6. *in D_2O, -0.18 ± 0.06 x 10^{-6} Å^{-2} in CM4 and -0.21 ± 0.07 x 10^{-6} Å^{-2} in H_2O. **in D_2O, 6.15 ± 0.07 x 10^{-6} Å^{-2} in CM4 and 6.09 ± 0.04 x 10^{-6} Å^{-2} in H_2O.

At first view, the changes induces by AmB in the pure POPC bilayers seemed limited with the exception of the D_2O contrast, where a change of critical angle occurred due to the presence of 10% v/v DMSO in the AmB-D_2O solution. This lowers the scattering length density of the solution to 5.67 10^{-6} $Å^{-2}$, which has the effect of lowering the critical Q-value to 13.4 10^{-3} $Å^{-1}$. By using this value for the solvent SLD, the data could be fitted. This was only observed in these first two samples measured, after which all subsequent samples were rinsed with D_2O to remove the DMSO before the neutron measurements.

The major change that could be observed as a consequence of the AmB addition was the modification of the SLD of the chain layer. Indeed, in order to fit the data properly after AmB addition, it was assumed that the AmB molecules could insert into the chains and influence the SLD upon contrasts. This was allowed as the models and SLD variations were not only explained with solvent penetration into the chains. The SLDs of the chain layer were thus approached separately in each contrast, i.e. that the SLD of the chain layer could vary independently between contrasts. This derives from the fact that AmB presents 13 labile protons, so its SLD varies significantly from 1.50 10^{-6} $Å^{-2}$ in H_2O to 2.88 10^{-6} $Å^{-2}$ in D_2O (see table 3.2). In consequence, with insertion of AmB, the SLD of the chains should increase from H_2O to D_2O contrasts, and the differences in SLD allows to relate to the proportions of AmB found in the chain layer, among the other components (see equation **49**). Also, AmB insertion implies that the SLD of hydrogenous chains will increase while the SLD of deuterated chains will decrease.

For d_{82}POPC bilayer, the SLD of the chain layer decreased after AmB addition from 6.39 ± 0.05 10^{-6} $Å^{-2}$ to 6.09 ± 0.04 10^{-6} $Å^{-2}$ in the most sensitive contrast, H_2O. This corresponds to 6 ± 1% v/v of AmB insertion into the chain layer. For hPOPC the contrast of the lipid chains to AmB molecules is poorer than in the perdeuterated membrane, but small changes in SLD could still be observed with and increase from -0.29 ± 0.05 10^{-6} $Å^{-2}$ before to -0.17 ± 0.06 10^{-6} $Å^{-2}$ in D_2O after AmB addition, corresponding to 4 ± 2% v/v of AmB insertion. While high hydration changes (+ 28 ± 3% v/v) were previously observed in pure POPC monolayers after AmB addition [48], in which AmB was interpreted to insert into the monolayers, in both cases here, the headgroup hydration of the bilayers did not vary significantly once taken into consideration the uncertainties. Due to the relative low amount of AmB inserted, the

area per molecule for the lipids did not change significantly from those in pure lipid bilayers. Neither roughness nor thickness effects due to AmB insertion could be observed because of uncertainties of the same order of magnitude as the changes. Finally, no significant water insertion could be observed in either cases, that could have indicated pore formation [74-75].

5.2.2. Bimolecular system : POPC and Ergosterol

Figures 5.5 and 5.6 show data recorded before and after AmB addition for hPOPC dErg (15 ± 2mol%), d_{82}POPC hErg (15 ± 1mol%) and hPOPC hErg (15 ± 8mol%) samples in 3 contrasts (D_2O, CM4 and H_2O). The corresponding tables 5.6 and 5.7 detail the parameters associated with the fits.

These contrasts were measured in order to detect the possible mechanisms of AmB in sterol-containing membranes, which include pore formation [74-75] and sterol extraction [5]. Each contrast is sensitive to a different part of the system depending on the sample. D_2O contrast is by definition sensitive to hydrogenous molecules, and will allow to observe the overall bilayer structure for hPOPC hErg as well as the phospholipids and the AmB in hPOPC dErg and finally the ergosterol and the AmB in d_{82}POPC hErg. CM4 is interesting to focus on AmB molecules, especially in d_{82}POPC hErg or to a lower extent in hPOPC dErg where the SLD changes in the chain region before and after AmB addition are highlighted. H_2O is particularly interesting to follow the deuterated ergosterol and the overall structure of membranes composed of d_{82}POPC.

In presence of 15mol% ergosterol, the effect of AmB on the bilayers was more pronounced than for POPC alone. Each of the three samples measured gave different insights into the mechanism because of the different contrast sensitivity. AmB action in hPOPC dErg caused small but complex changes in the lipid chain SLD, which were dependent on the solvent contrast. The values corresponding to the best simultaneous fit to all contrast implied the removal of more than half of the ergosterol originally present in the membrane (6 ± 1% v/v removed and 5 ± 1% v/v remaining) at the same time as AmB inserted up to 4 ± 3% v/v, similar to what was observed in the pure hPOPC system. At first, the fits suggested that the volume of ergosterol removed

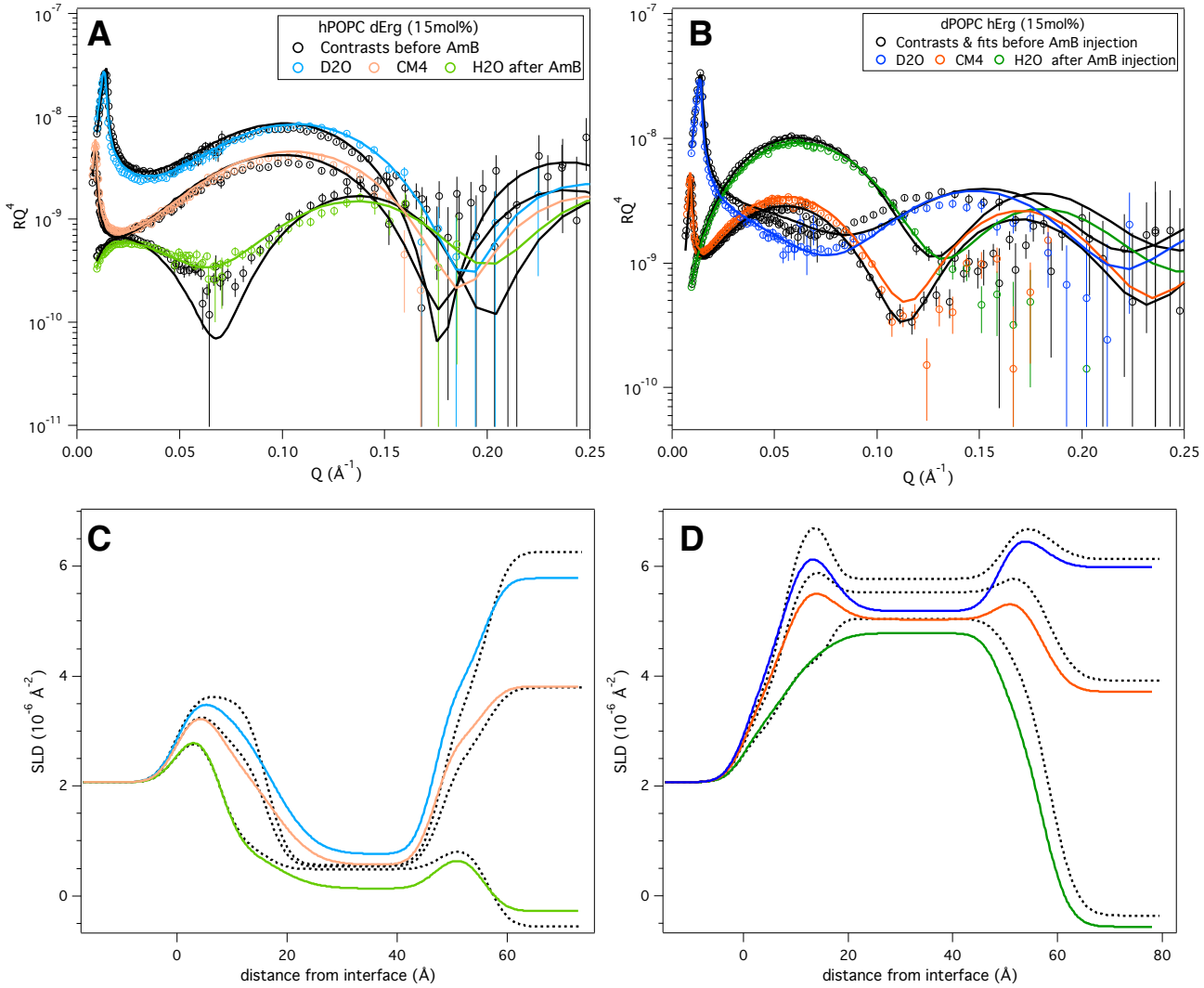

Figure 5.5 : Reflectivity data and fits of hPOPC dErg bilayer before (black) and after AmB addition (light colors) **(A)** and corresponding SLD profiles **(C)**, and reflectivity data and fits of d_{82}POPC hErg bilayer before (black) and after AmB addition (dark colors) **(B)** and corresponding SLD profiles **(D)**.

Samples	**hPOPC dErg (15mol%) bilayer after AmB addition χ^2 = 7.3**				**d_{82}POPC hErg (15mol%) bilayer after AmB addition χ^2 = 9.7**			
Layers	τ (Å)	ρ (10^{-6} Å^{-2})	ϕ (%)	σ (Å)	τ (Å)	ρ (10^{-6} Å^{-2})	ϕ (%)	σ (Å)
Si	-	2.07	0	3 ± 1	-	2.07	0	3 ± 1
SiO_2	8 ± 0.6	3.41	10 ± 4	3 ± 2	8 ± 0.6	3.41	10 ± 4	4 ± 2
Head (in)	9 ± 1	1.86 ± 0.1	46 ± 6	6 ± 2	8 ± 1	7.35 ± 0.2	38 ± 6	4 ± 2
Chains	30 ± 1	0.23 ± 0.09*	10 ± 2	5 ± 2	33 ± 1	5.17±0.09**	2 ± 1	4 ± 2
Head (out)	9 ± 1	1.86 ± 0.1	50 ± 9	5 ± 2	8 ± 1	7.35 ± 0.2	49 ± 9	4 ± 2

Table 5.6 : Fitted parameters of ergosterol-containing POPC bilayers after AmB addition. Parameters were defined in chapter 3 and in table 4.6. *in D_2O, 0.22 ± 0.08 10^{-6} Å^{-2} in CM4 and 0.18 ± 0.06 10^{-6} Å^{-2} in H_2O. **in D_2O, 5.07 ± 0.05 10^{-6} Å^{-2} in CM4 and 4.92 ± 0.05 10^{-6} Å^{-2} in H_2O.

corresponded to the volume of AmB molecules inserted, but the uncertainties do not allow to conclude as such. Also, water insertion in the hydrophobic region (+8 ± 3% v/v) was detected and implied that the volume of ergosterol removed was filled with the volume of both water and AmB content.

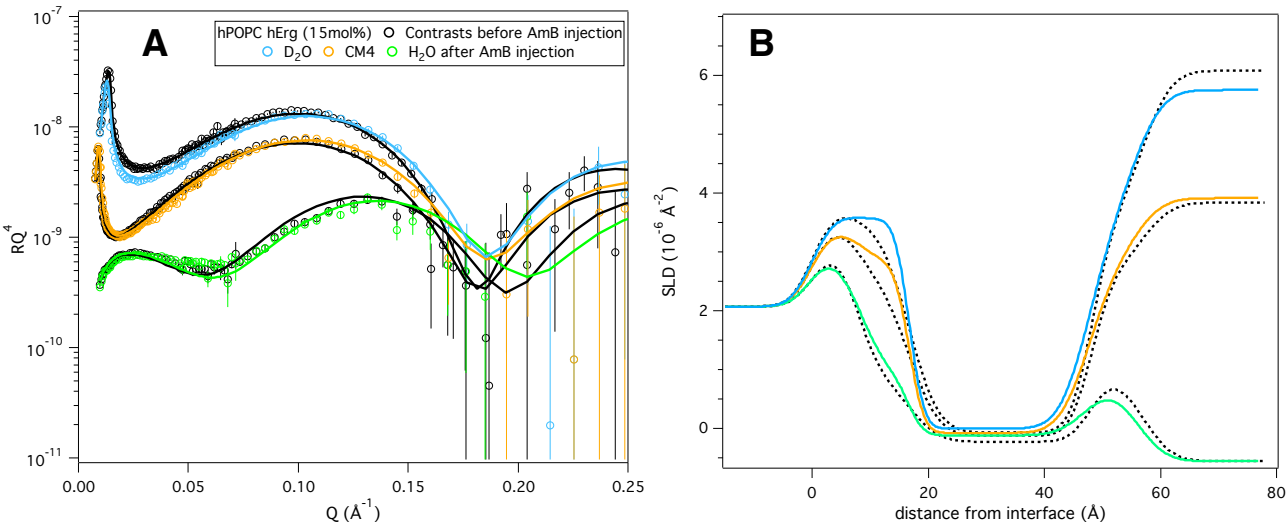

Figure 5.6 : Reflectivity data and fits of hPOPC hErg (15mol%) bilayer before (black) and after AmB addition (light colors) **(A)** and corresponding SLD profiles **(B)**.

Samples	**hPOPC hErg (15mol%) bilayer before AmB addition χ^2 = 4.6**				**hPOPC hErg (15mol%) bilayer after AmB addition χ^2 = 4.8**			
Layers	τ (Å)	ρ (10^{-6} Å^{-2})	ϕ (%)	σ (Å)	τ (Å)	ρ (10^{-6} Å^{-2})	ϕ (%)	σ (Å)
Si	-	2.07	0	3 ± 1	-	2.07	0	3 ± 1
SiO_2	8 ± 0.6	3.41	10 ± 4	3 ± 2	8 ± 0.6	3.41	10 ± 4	4 ± 2
Head (in)	9 ± 2	1.86 ± 0.1	38 ± 6	4 ± 2	10 ± 2	1.86 ± 0.2	36 ± 5	4 ± 2
Chains	30 ± 2	-0.21*±0.04	1 ± 1	3 ± 2	29 ± 2	-0.14±0.1**	1 ± 1	4 ± 2
Head (out)	9 ± 2	1.86 ± 0.1	38 ± 6	4 ± 2	10 ± 2	1.86 ± 0.2	53 ± 9	4 ± 2

Table 5.7 : Fitted parameters of hPOPC hErg (15 mol%) bilayer before and after AmB addition. Parameters were defined in chapter 3 and in table 4.6. *Corresponds to the SLD calculated from the nominal composition of 15mol% of ergosterol and 85mol% POPC.**in D_2O, -0.16 ± 0.15 x 10^{-6} Å^{-2} in CM4 and -0.2 ± 0.3 x 10^{-6} Å^{-2} in H_2O.

In the opposite contrast, in d_{82}POPC hErg membrane (figure 5.5 and table 5.6), the fits indicated that AmB was present in the lipid chains at 21 ± 7% v/v while the ergosterol removed was difficult to quantify due to a large uncertainty with 5 ± 4% v/v out of the

11 ± 1% v/v initially present. Such large SLD changes and AmB insertion could be related to the low initial surface coverage of the bilayer as the drug could have filled the existing defects (89 ± 3% v/v and 98 ± 1% v/v before and after AmB addition). Indeed, using the constraint that in the absence of AmB the chain SLD should remain constant between the water contrasts, or that it should increase from H_2O to D_2O contrasts in presence of AmB, the only possibility to fit the changes involved by AmB was this large AmB insertion together with a diminution of the hydration of the chain layer. In hPOPC hErg (figure 5.6 and table 5.7), the AmB effect was intermediate. Indeed, nearly half of the ergosterol was removed (5 ± 4% v/v out of the 11 ± 8% v/v in total) and AmB inserted up to 4 ± 4% while no water insertion could be observed .

The action of AmB, from 50% to complete ergosterol removal, was evident in all samples as well as AmB insertion in the chain region, normal to the bilayer plane, especially in hPOPC dErg and d_{82}POPC hErg. The proportion of AmB insertion was dependent on the surface coverage and the water insertion, linked to the pore formation model, was only observed in hPOPC dErg. hPOPC hErg is the least sensitive contrast to AmB insertion and the relatively low surface coverage of d_{82}POPC hErg rendered the AmB investigation difficult. The results are thus in part consistent with the pore formation model and with ergosterol extraction as a plausible mechanism of AmB in this case. However, the AmB sponge-extracting mechanism is not consistent with our results, as no upper layer of AmB was observed in contact with any of the POPC or POPC-ergosterol bilayers.

5.2.3. Bimolecular system : POPC and Cholesterol

Cholesterol-containing samples were investigated to mimic mammal cell membranes and determine the mechanism that could explain the toxic side effect of AmB. It has been shown before that AmB is more selective towards ergosterol over cholesterol explaining the specificity towards fungal cells [165]. Nevertheless, the weaker interaction with cholesterol is thought to be one of the origins of toxicity in mammalian cells. The bilayers containing hydrogenous cholesterol, hPOPC hChol (15 ± 7 mol%) and d_{82}POPC hChol (15 ± 3 mol%) are described in figure 5.7 and table 5.8, and were measured in 4 contrasts before and after AmB (D_2O, CM4, CMSi and H_2O).

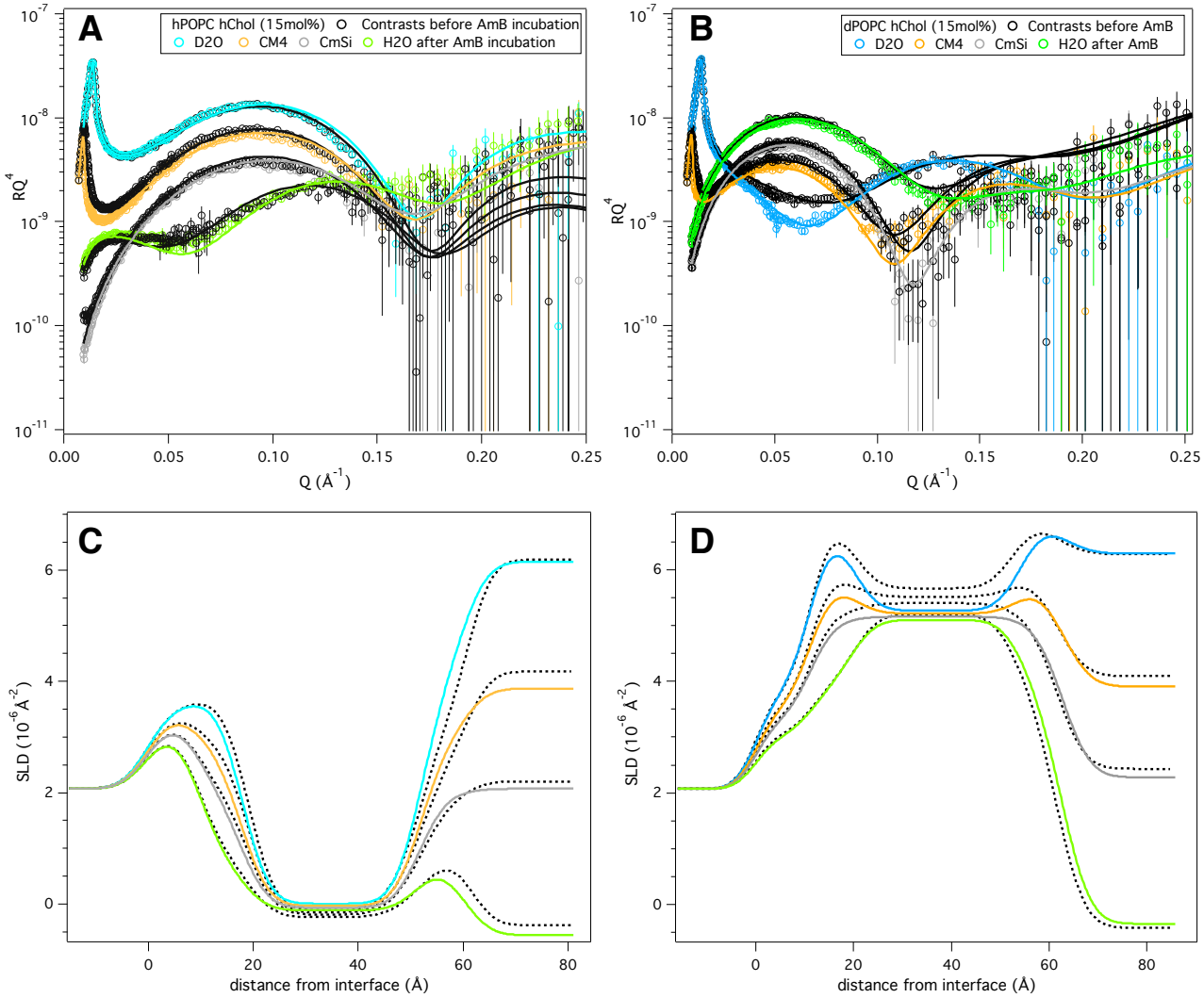

Figure 5.7 : Reflectivity data and fits of hPOPC hChol (15 mol%) bilayer before (black) and after AmB addition (light colors) **(A)** and corresponding SLD profiles **(C)**, and reflectivity data and fits of d_{82}POPC hChol (15mol%) bilayer before (black) and after AmB addition (dark colors) **(B)** and corresponding SLD profiles **(D)**.

Samples	**hPOPC hChol (15mol%) bilayer after AmB addition χ^2 = 3.4**				**d_{82}POPC hChol (15 mol%) bilayer after AmB addition χ^2 = 3.2**			
Layers	τ (Å)	ρ (10^{-6} Å^{-2})	ϕ (%)	σ (Å)	τ (Å)	ρ (10^{-6} Å^{-2})	ϕ (%)	σ (Å)
Si	-	2.07	0	4 ± 1	-	2.07	0	3 ± 1
SiO_2	10 ± 2	3.41	6 ± 4	4 ± 1	11 ± 2	3.41	11 ± 6	4 ± 2
Head (in)	8 ± 2	1.86 ± 0.1	32 ± 11	4 ± 2	9 ± 1	7.35 ± 0.2	42 ± 5	4 ± 2
Chains	34 ± 1	0.01±0.09*	1 ± 1	4 ± 2	34 ± 2	5.3±0.2**	1 ± 1	4 ± 2
Head (out)	8 ± 2	1.86 ± 0.1	50 ± 12	4 ± 2	9 ± 1	7.35 ± 0.2	45 ± 6	5 ± 2

Table 5.8 : Fitted parameters of hPOPC hChol (15 mol%) and d_{82}POPC hChol (15 mol %) bilayers after AmB addition. Parameters were defined in chapter 3 and in table 4.6. *in D_2O, -0.03 ± 0.1 x 10^{-6} Å^{-2} in CM4, -0.06 ± 0.05 x 10^{-6} Å^{-2} in CMSi and -0.11 ± 0.9 x 10^{-6} Å^{-2} in H_2O. **in D_2O, 5.22 ± 0.05 x 10^{-6} Å^{-2} in CM4, 5.16 ± 0.06 x 10^{-6} Å^{-2} in CMSi and 5.10 ± 0.08 x 10^{-6} Å^{-2} in H_2O.

The samples containing perdeuterated cholesterol, were fully characterized before AmB addition, but in 2 contrasts (D2O and CM4 for d82POPC hChol (15 ± 7 mol%)) and 1 contrast (D2O for hPOPC dChol (12 ± 2 mol%)) after AmB addition due to problems with the neutron beam at ANSTO during our last experiment. Nevertheless, the results shown in figure 5.8 and table 5.9 complement the data obtained using non-deuterated cholesterol and provide good additional insight into the mechanism of AmB in cholesterol-containing membranes.

The hPOPC hChol lipid bilayer was nearly unchanged by AmB addition and the major observation was that a change in the chain SLD, albeit small, which indicated that only a very small amount of cholesterol, if any, was removed (less than 2% v/v) while AmB insertion was observed (8 ± 7% v/v). It should be noted that the relatively high uncertainty arises from this sample having less contrast to probe AmB insertion. However, the same behavior was also found in the deuterated sample; d_{82}POPC hChol in which little or no cholesterol was removed (less than 2% v/v) and 12 ± 4% v/v of Amphotericin B was inserted in the bilayer. The bilayer composed of hPOPC dChol (12 ± 2mol%) could also be fitted with little or no cholesterol removal (less than 2% v/v) but smaller AmB insertion 6 ± 2% v/v. In this case the absence of additional contrasts for this sample however means that the fitting results may not be unique. In the fully perdeuterated sample d_{82}POPC dChol, which has the highest contrast to AmB, the SLD changes in the hydrophobic region indicated nearly no cholesterol removal (less than 2% v/v) but large AmB insertion (22 ± 2% v/v). Here again, only two contrasts were used to fit the data, but the relatively large changes observed and the sensitivity to AmB insertion of such contrasts support the idea of a large AmB insertion. An important insertion correlated with a reduction of the water content found in the chain of 5 ± 2% and 6 ±2 % v/v for d_{82}POPC dChol, and d_{82}POPC hChol, respectively.

Thus, considering the sensitivity of the different contrasts to both AmB and cholesterol, these results are consistent with each other and with the notion that if AmB extracts cholesterol, it does so to a much smaller degree than it extracts ergosterol. At the concentration employed (1mM), AmB is mostly in an aggregated form, mentioned to be at the origin of AmB toxic side effect, by extraction of cholesterol [166], which is very limited in POPC bilayers presented the present work. Instead, AmB inserts into the cholesterol-containing bilayer to the same or higher degree than for ergosterol-

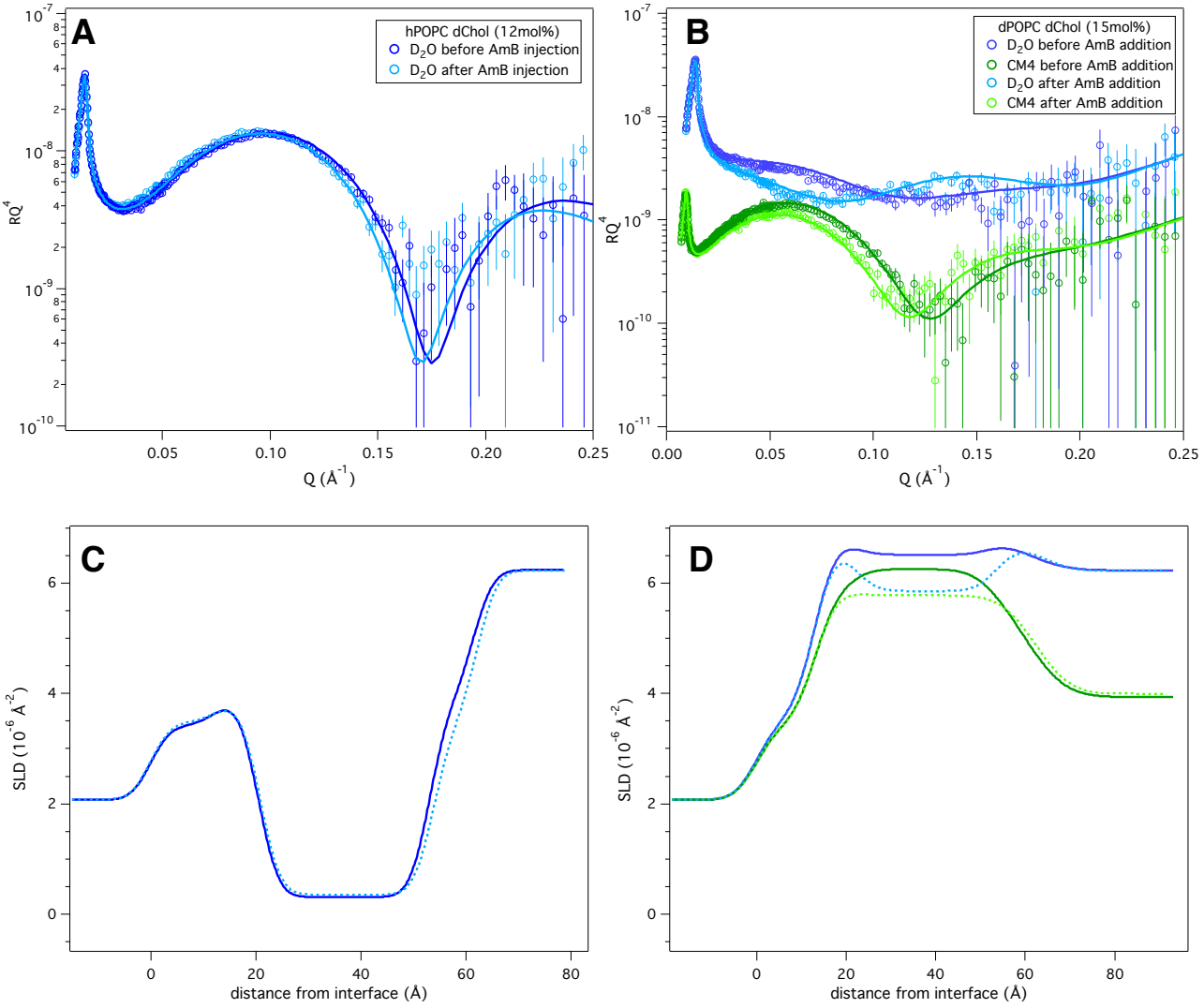

Figure 5.8 : Reflectivity data and fits of hPOPC dChol (12 mol%) bilayer before (dark colors) and after AmB addition (light colors) **(A)** and corresponding SLD profiles **(C)**, and reflectivity data and fits of d_{82}POPC dChol (15mol%) bilayer before (dark colors) and after AmB addition (light colors) **(B)** and corresponding SLD profiles **(D)**. *An offset of -1x10^{-8} was apply in Y direction at CM4 contrasts for clarity.

Samples	**hPOPC dChol (12mol%) bilayer after AmB addition χ^2 = 4.4**				**d_{82}POPC dChol (15mol%) bilayer after AmB addition χ^2 = 4.0**			
Layers	τ (Å)	ρ (10^{-6} Å^{-2})	ϕ (%)	σ (Å)	τ (Å)	ρ (10^{-6} Å^{-2})	ϕ (%)	σ (Å)
Si	-	2.07	0	3 ± 2	-	2.07	0	4 ± 2
SiO_2	12 ± 2	3.41	1 ± 1	3 ± 2	13 ± 2	3.41	4 ± 4	4 ± 2
Head (in)	9 ± 2	1.86 ± 0.1	44 ± 7	3 ± 2	8 ± 2	7.35 ± 0.2	44 ± 15	4 ± 2
Chains	33 ± 2	0.35 ± 0.06*	1 ± 1	3 ± 2	33 ± 2	5.87±0.04**	2 ± 2	4 ± 2
Head (out)	9 ± 2	1.86 ± 0.1	38 ± 6	3 ± 2	8 ± 2	7.35 ± 0.2	47 ± 17	6 ± 2

Table 5.9 : Fitted parameters of hPOPC dChol (12 mol%) and d_{82}POPC dChol (15 mol %) bilayers after AmB addition. Parameters were defined in chapter 3 and in table 4.6. *in D_2O. **in D_2O and 5.77 ± 0.05 10^{-6} in CM4.

containing bilayers. As AmB is known to be more selective towards ergosterol than cholesterol in different lipid environments [70-74], the differences in the proportions of extraction seems directly related to this enhanced affinity. However, the extraction of the ergosterol observed in this work does not seem to be related to a sponge extraction model as the data are well fitted without the presence of an AmB upper layer [5]. Also, it could not be observed any significant water insertion ascribed to AmB action in these four cholesterol-containing samples, that could have indicated a pore formation mechanism.

5.3. Natural phospholipids (*P. pastoris*) Bilayer structural characterization

Previous neutron reflectivity studies of *P. pastoris* phospholipid bilayers focused on the total lipid extracts with and without their ergosterol content [16]. Because of the low contrast in the hydrogenous synthetic bilayers composed of 15mol% sterols with respect to AmB, it was decided to investigate samples with 30mol% sterol to observe the AmB effects on the sterol more clearly. In fact, 30mol% is also consistent with the sterol ranges found in different fungal and mammal systems [167-168].

The following samples were investigated and prepared with a nominal composition of 30mol%. The molar ratio of sterol given in the table 5.10 correspond to the value calculated from the SLD value fitted. Differences will be discussed later. hPolar refers to the hydrogenous phospholipids while dPolar refers to the deuterated phospholipids extracted from *P. pastoris*.

Samples	Contrasts measured before AmB interaction	Contrasts measured after AmB interaction
hPolar hErg (30 ± mol%)	D_2O, CM4, CMSi and H_2O	D_2O, CM4 and H_2O
dPolar dErg (30 ± mol%)	D_2O, CM4, CMSi and H_2O	D_2O, CMSi and H_2O
hPolar dErg (39 ± mol%)	D_2O, CM4, CMSi and H_2O	D_2O, CM4, CMSi and H_2O
dPolar hErg (15 ± mol%)	D_2O, CM4, CMSi and H_2O	D_2O, CM4, CMSi and H_2O
hPolar hChol (30 ± mol%)	D_2O, CM4 and H_2O	D_2O, CM4 and H_2O
dPolar dChol (30 ± mol%)	D_2O, CM4, CMSi and H_2O	D_2O, CMSi and H_2O
hPolar dChol (30 ± mol%)	D_2O, CM4 and H_2O	D_2O, CM4 and H_2O
dPolar hChol (40 ± mol%)	D_2O, CM4, CMSi and H_2O	D_2O, CM4, CMSi and H_2O

Table 5.10 : List of the samples and the contrasts measured on FIGARO and D17 at ILL.

Regarding the model employed to fit the data from the lipid bilayers composed of the phospholipid mixtures extracted from yeasts, an inner water layer of few Ångströms (1.5 to 3 Å) was needed in all cases. This thin layer situated between the silicon oxide layer and the inner headgroup layer constituted the first difference with respect to the mono or bimolecular POPC systems seen previously. The diversity of phospholipids in the yeast samples and the repulsion between the negatively charged silica surface and the charged lipid, as well as the roughness of the yeast lipid bilayers are possible reasons for the presence of this water layer between the substrate and the bilayer. In fact, water layers (3 ± 1Å thick) were also observed in NR studies of supported lipid bilayers mixtures of 9:1 DMPC:DPPS on silicon substrate and more recently for soybean phospholipid mixtures (containing equal proportions of PC, PE and PI) [169-170]. Otherwise, the data could be fitted using the SLDs for headgroups and hydrophobic chains calculated from lipid analysis (see table 3.2) with the exception of the partially deuterated samples in which the sterol and the phospholipids were isotopically different. Indeed, for these samples, the SLDs of the headgroups were found to be influenced by the presence of the sterol, which was interpreted to arise from the roughness of the chain-head interfaces. The bilayer structures remained relatively symmetrical even if the two headgroup leaflets were considered as two distinct entities, with the hydration and thickness allowed to vary independently as opposed to what was done for POPC-based membranes. This was performed to allow a possible asymmetry that could arise from segregation of the different molecules. Also, the area per molecule calculations were not done for these complex lipid bilayers since a significant uncertainty would arise from the large number of components and high sterol content (30mol%). Finally, the outer headgroups were in most cases more hydrated than the inner headgroups. This was probably due to the presence of the water layer in which part of the inner headgroups hydration was hidden as the boundary between the two layers is often difficult to define and influenced by the substrate [171].

5.3.1. Ergosterol-containing *P. pastoris* phospholipid membranes

Figure 5.9 shows the reflectivity curves and scattering length density profiles corresponding to the best fits to the data for hPolar hErg and dPolar dErg (30 ± 5 and 30 ± 3mol% respectively) bilayers in four different water contrasts (D_2O, CM4, CMSi and H_2O).

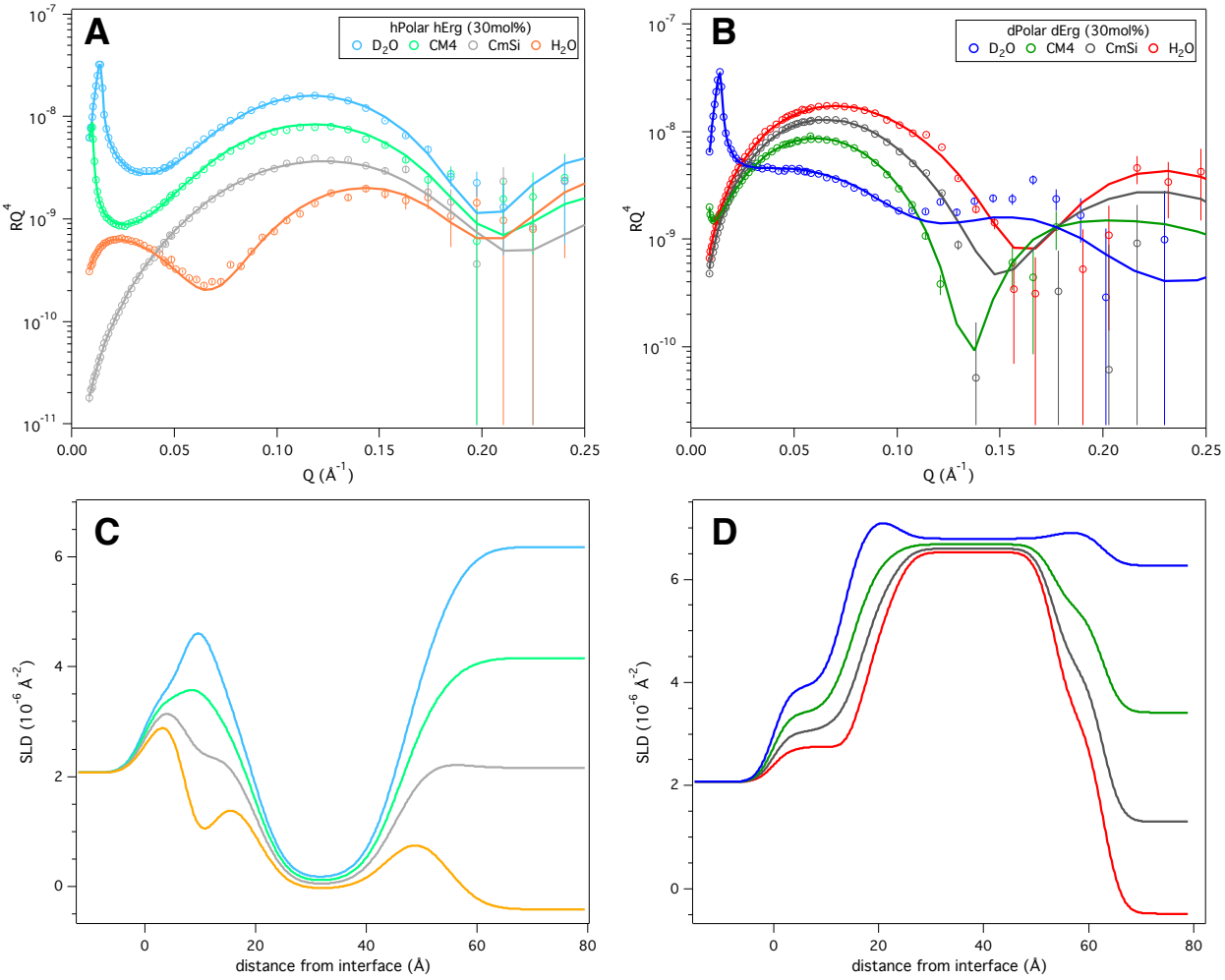

Figure 5.9 : Reflectivity data and fits of hydrogenous *P. pastoris* phospholipids and hydrogenous ergosterol (30mol%) lipid bilayer **(A)** and corresponding SLD profiles **(C)**, and reflectivity data and fits of deuterated *P. pastoris* phospholipids and deuterated ergosterol (30mol%) lipid bilayer **(B)** and corresponding SLD profiles **(D)**.

Samples	**hPolar hErg (30 mol%) bilayer χ^2 = 7.5**				**dPolar dErg (30 mol%) bilayer χ^2 = 12.5**			
Layers	τ (Å)	ρ (10^{-6} Å^{-2})	ϕ (%)	σ (Å)	τ (Å)	ρ (10^{-6} Å^{-2})	ϕ (%)	σ (Å)
Si	-	2.07	0	3 ± 2	-	2.07	0	2 ± 1
SiO_2	8 ± 1	3.41	10 ± 4	2 ± 1	13 ± 1	3.41	18 ± 3	3 ± 1
Water	3 ± 1	Solvent	100	4 ± 2	2 ± 0.8	Solvent	100	4 ± 2
Head (in)	9 ± 2	2.9# ± 0.1	25 ± 5	4 ± 1	8 ± 2	7.9# ± 0.2	27 ± 3	3 ± 2
Chains	26 ± 2	-0.03*±0.03	3 ± 2	5 ± 2	30 ± 1	6.81* ± 0.03	4 ± 3	3 ± 2
Head (out)	8 ± 2	2.9# ± 0.1	28 ± 8	5 ± 2	9 ± 2	7.9# ± 0.2	51 ± 11	3 ± 2

Table 5.11 : Fitted parameters of hPol hErg and dPol dErg bilayers. #The headgroups SLD varied depending on contrasts and composition; see table 3.2. Parameters were defined in chapter 3 and in table 4.6. *Corresponds to the SLD calculated from the nominal composition of 30mol% of ergosterol and 70mol% Polar fractions.

The headgroups SLD values used for hPolar hErg were 2.9 10^{-6} $Å^{-2}$, 2.7 10^{-6} $Å^{-2}$, 2.6 10^{-6} $Å^{-2}$ and 2.4 10^{-6} $Å^{-2}$ and 7.9 10^{-6} $Å^{-2}$, 7.7 10^{-6} $Å^{-2}$, 7.6 10^{-6} $Å^{-2}$ and 7.3 10^{-6} $Å^{-2}$ for dPolar dErg in D_2O, CM4, CMSi and H_2O respectively. These values correspond to the values calculated from the compositional analysis and are presented in the table 3.2 in the Material and Methods chapter. The different values in different solvent contrasts are related to the labile protons of some of the headgroups which means that the SLD changes depending on the solvent deuteration level. These values allowed satisfactory models to be fitted to all the data. The table 5.11 gives details of the parameters corresponding to the fits presented in figure 5.9. The main difference between the phospholipid samples with added ergosterol (hPolar hErg and dPolar dErg), was the smaller thickness (by 4 ± 2Å) of the hydrophobic layer of the hydrogenous sample, which, as also previously published by de Ghellinck et al. [16] is related to the acyl chain composition, containing more polyunsaturated species compared to the deuterated samples which has predominantly $C_{18:1}$ acyl chains. Besides this, the models were structurally very similar and a good surface coverage was obtained in both cases (97 ± 2% and 96 ± 3% for hPolar hErg and dPolar dErg bilayers respectively).

The hPolar dErg (39 ± 2mol%) and dPolar hErg (15 ± 2mol%) samples showed large variations from the expected SLD chain values (30mol% sterol), but nevertheless brought further observations due to the enhanced contrast between the phospholipids and the sterol. Figure 5.10 shows the reflectivity curves and scattering length density profiles corresponding to the best fits to the data for these two samples measured in four different water contrasts (D_2O, CM4, CMSi and H_2O). The table 5.12 details the parameters corresponding to the fits.

The SLD values of the chains used in the fit were different from the nominal values in both cases. In comparison to the sole POPC-based sample that was not reaching the nominal composition - hPOPC dChol (12mol%) -, here the differences between the expected and the measured compositions are very important. It is most likely that the sterol is inhomogeneously distributed in the vesicles leading to such deviations. Similar effects with vesicle fusion deposition of various phospholipid mixtures probed with NR are described in literature [172]. At the same time, the SLD of the headgroup was different from the expected value for the lipids.

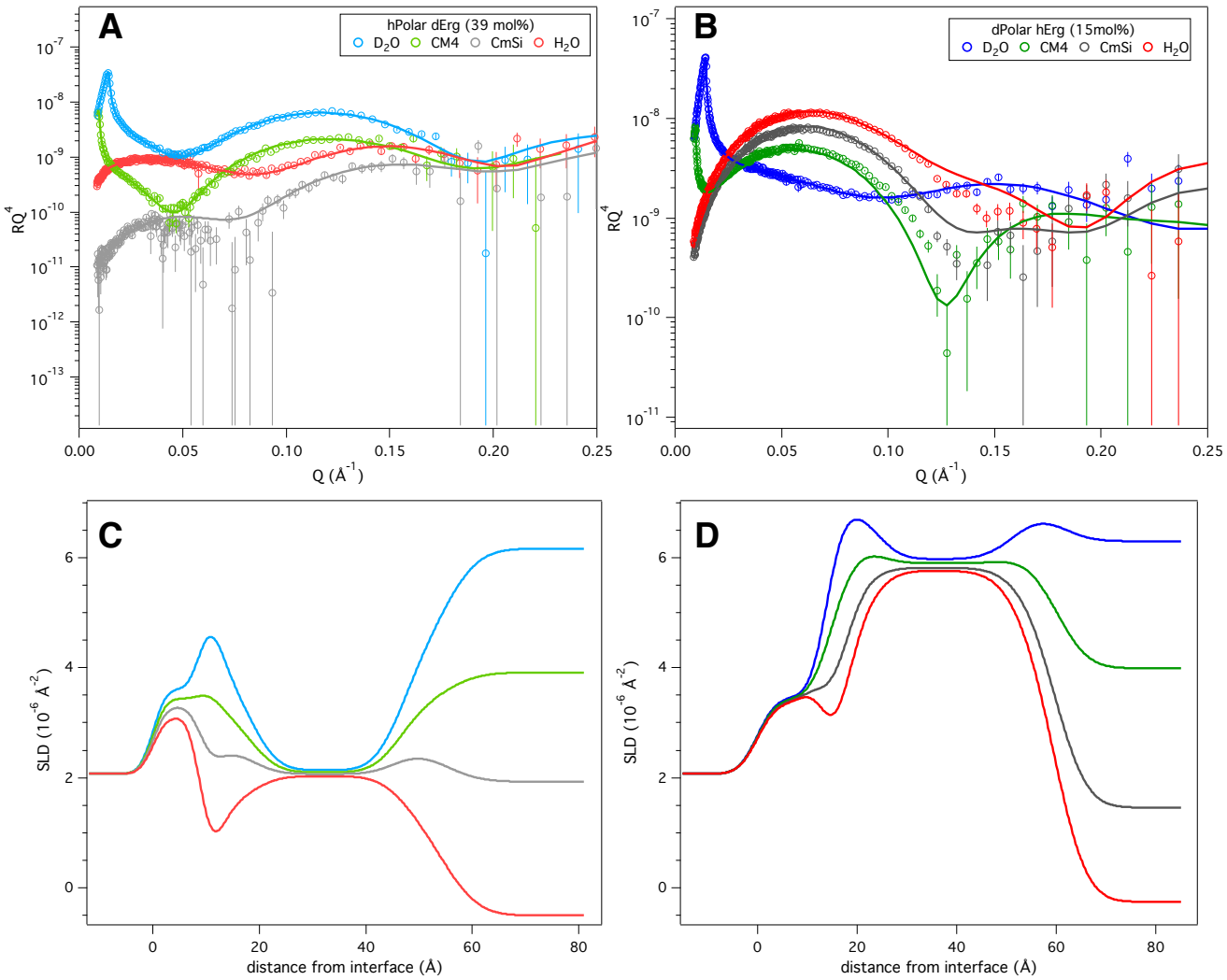

Figure 5.10 : Reflectivity data and fits of hydrogenous *P. pastoris* phospholipids and deuterated ergosterol (30mol%) lipid bilayer **(A)** and corresponding SLD profiles **(C)**, and reflectivity data and fits of deuterated *P. pastoris* phospholipids and hydrogenous ergosterol (30mol%) lipid bilayer **(B)** and corresponding SLD profiles **(D)**.

Samples	**hPolar dErg (39 mol%) bilayer χ^2 = 2.6**				**dPolar hErg (15 mol%) bilayer χ^2 = 6.3**			
Layers	τ (Å)	ρ (10^{-6} Å^{-2})	ϕ (%)	σ (Å)	τ (Å)	ρ (10^{-6} Å^{-2})	ϕ (%)	σ (Å)
Si	-	2.07	0	2 ± 1	-	2.07	0	3 ± 1
SiO_2	9 ± 2	3.41	8 ± 7	2 ± 1	14 ± 2	3.41	2 ± 2	2 ± 1
Water	2 ± 0.5	Solvent	100	3 ± 2	2 ± 0.5	Solvent	100	4 ± 2
Head (in)	8 ± 2	3.2# ± 0.2	25 ± 8	4 ± 2	8 ± 2	7.3# ± 0.3	25 ± 4	4 ± 2
Chains	28 ± 2	2.07* ± 0.07	2 ± 2	4 ± 2	29 ± 2	5.97**±0.06	4 ± 2	5 ± 3
Head (out)	8 ± 2	3.2# ± 0.2	24 ± 11	5 ± 2	8 ± 2	7.3# ± 0.3	37 ± 8	5 ± 3

Table 5.12 : Fitted parameters of hPol dErg and dPol hErg bilayers. #The headgroups SLD varied differently than calculated. The values employed are reported in the text below. Parameters were defined in chapter 3 and in table 4.6. *Corresponds to 39mol% of d-ergosterol and 61mol% Polar fraction. **Corresponds to 15mol% of ergosterol and 85mol% dPolar fraction.

In the case of hPolar dErg the headgroup values used in the fits were slightly different than the combination of all hydrogenous headgroups with 3.2 10^{-6} Å^{-2}, 3.0 10^{-6} Å^{-2}, 2.7 10^{-6} Å^{-2} and 2.1 10^{-6} Å^{-2}, for D_2O, CM4, CMSi and H_2O respectively. For dPolar hErg, the headgroup values that fitted to the data were lower than calculated from the deuterated headgroup composition with 7.3 10^{-6} Å^{-2}, 7.0 10^{-6} Å^{-2}, 6.7 10^{-6} Å^{-2} and 6.6 10^{-6} Å^{-2}, in D_2O, CM4, CMSi and H_2O respectively. These differences between the SLD observed in the headgroups of the partially deuterated samples show that there is some ergosterol in the headgroup regions as well as the chains, as values for the headgroups were higher than expected when deuterated ergosterol was involved and lower with hydrogenous ergosterol. The fact that this effect was not observed in any of the partially deuterated POPC-sterol samples suggests that it is related to the large number of different lipid components present in the yeast samples, which means that it may be difficult to assign a clear location for the chain-headgroup interface. In previously published work performed on total yeast lipid extracts, the fits also had a high roughness at the chain-headgroup interfaces and could be related to the same effect [16]. Due to the low contrast between the lipids and sterols, these differences were not seen in the first two samples that were either fully deuterated or non-deuterated. It is worth noting that this presence of ergosterol in the headgroup was symmetrical and the same values could be used in both inner and outer leaflets.

Otherwise, the models used to fit the data of the ergosterol-containing lipid bilayers were similar structurally even if the fraction of ergosterol varied between samples. The difference in the thickness of the hydrophobic layer observed between hPolar hErg and dPolar dErg membranes was not observed for the two complementary samples probably due to the significantly higher sterol content in the hPolar dErg bilayer (39 ± 2mol%) than in dPolar hErg bilayer (15 ± 2mol%), which could have compensated for the difference in lipid polyunsaturation.

5.3.2. Cholesterol-containing *P. pastoris* phospholipids membranes

For the same reasons evoked for POPC-cholesterol bilayers, yeast phospholipid membranes containing 30mol% cholesterol were investigated. The advantages are that this amount is more representative of the fraction of cholesterol found in mammalian cells (30-50mol%), while the yeast lipid composition is also more representative of the

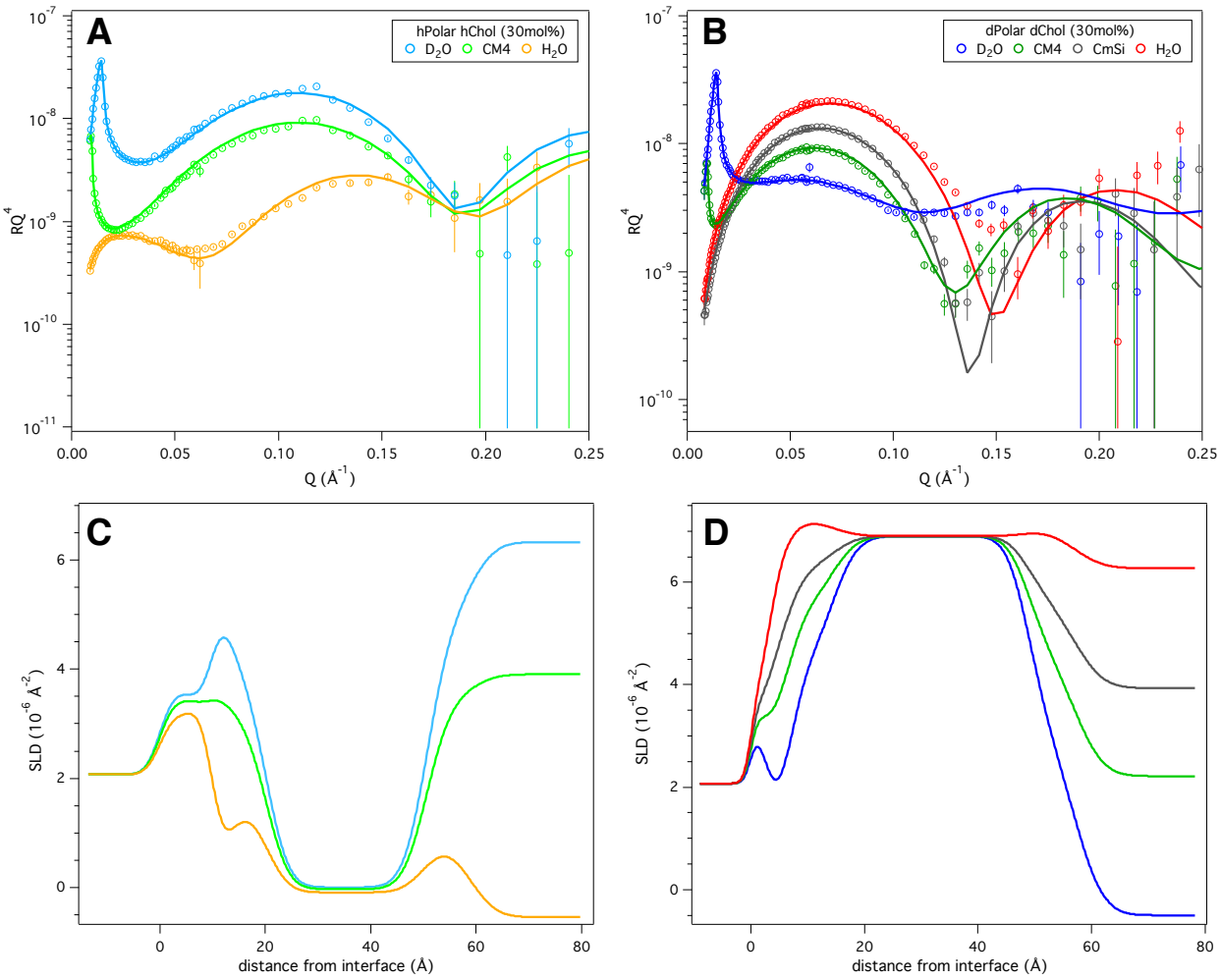

Figure 5.11 : Reflectivity data and fits of hydrogenous *P. pastoris* phospholipids and hydrogenous cholesterol (30mol%) lipid bilayer **(A)** and corresponding SLD profiles **(C)**, and reflectivity data and fits of deuterated *P. pastoris* phospholipids and deuterated cholesterol (30mol%) lipid bilayer **(B)** and corresponding SLD profiles **(D)**.

Samples	**hPolar hChol (30 mol%) bilayer χ^2 = 18.1**				**dPolar dChol (30 mol%) bilayer χ^2 = 18.3**			
Layers	τ (Å)	ρ (10^{-6} Å^{-2})	ϕ (%)	σ (Å)	τ (Å)	ρ (10^{-6} Å^{-2})	ϕ (%)	σ (Å)
Si	-	2.07	0	2 ± 1	-	2.07	0	1 ± 0.5
SiO_2	10 ± 1	3.41	6 ± 3	2 ± 1	2 ± 1	3.41	5 ± 5	2 ± 1
Water	2 ± 0.5	Solvent	100	3 ± 2	2 ± 0.5	Solvent	100	2 ± 1
Head (in)	9 ± 2	2.9# ± 0.1	38 ± 5	3 ± 2	9 ± 2	7.9# ± 0.2	38 ± 6	3 ± 1
Chains	30 ± 2	-0.086*±0.04	1 ± 1	4 ± 2	34 ± 1	6.90* ± 0.03	1 ± 1	3 ± 2
Head (out)	8 ± 2	2.9# ± 0.1	48 ± 9	4 ± 2	8 ± 2	7.9# ± 0.2	46 ± 6	4 ± 2

Table 5.13 : Fitted parameters of hPol hErg and dPol dErg bilayers. #The headgroups SLD varied depending on contrasts and composition; see table 3.2. Parameters were defined in chapter 3 and in table 4.6. *Corresponds to 30mol% cholesterol and 70mol% Polar lipids.

lipids found in mammalian cell membranes than POPC [168]. Figure 5.11 shows the reflectivity curves and scattering length density profiles corresponding to the best fits to the data for hPolar hChol and dPolar dChol bilayers (30 ± 10 and 30 ± 8mol% respectively) in four different water contrasts (D_2O, CM4, CMSi and H_2O) and the parameters of the fits are found in table 5.13.

Note that for all the cholesterol-containing bilayers, a 2 ± 0.5Å inner water layer, independently of the silicon oxide layer characteristics, was also needed to fit the data. The calculated sample SLD values were used and allowed satisfactory fits to be obtained for the fully hydrogenous (hPolar hChol) and fully deuterated (dPolar dChol) samples. Again, the hydrophobic layer of the deuterated sample was thicker (34 ± 1Å) than in the hydrogenous bilayer (30 ± 2Å), giving the same difference of 4 ± 2Å also found between the ergosterol-containing hydrogenous and deuterated phospholipid extracts from yeasts, due to the polyunsaturation differences observed in the acyl chain composition. Also, at the same concentration, the cholesterol bilayers are thicker by 4 ± 3Å and 4 ± 1Å for the hydrogenous and the deuterated membranes respectively. This demonstrates a larger condensing effect of cholesterol compared to ergosterol in complex lipid mixtures, already suspected with the POPC bilayers of the present work and recently demonstrated with X-Ray lamellar diffraction of POPC sterol-containing bilayers [173]. The larger uncertainties in the hydration and thickness did not allow conclusions to be drawn with certainty for a similar effect in the headgroups. Besides this observation, both models could be considered structurally equivalent.

The partially deuterated samples were less trivial to fit as the chains and headgroup SLD value differed from the calculations. Figure 5.12 and table 5.14 shows the reflectivity curves, scattering length density profiles and the parameters of the best fits for hPolar dChol (30 ± 2mol%) and dPolar hChol (40 ± 2mol%). Headgroup SLD values of 7.1 10^{-6} $Å^{-2}$, 6.6 10^{-6} $Å^{-2}$, 6.5 10^{-6} $Å^{-2}$ and 6.4 10^{-6} $Å^{-2}$, for D_2O, CM4, CMSi and H_2O were used for the dPolar hChol membrane. The high cholesterol content in dPolar hChol (40 ± 2mol%) bilayer was also found to be present in the headgroup layers, linked to the difficulty to define an exact location for the chain/headgroup interface with the lipid mixtures extracted from *P. pastoris*.

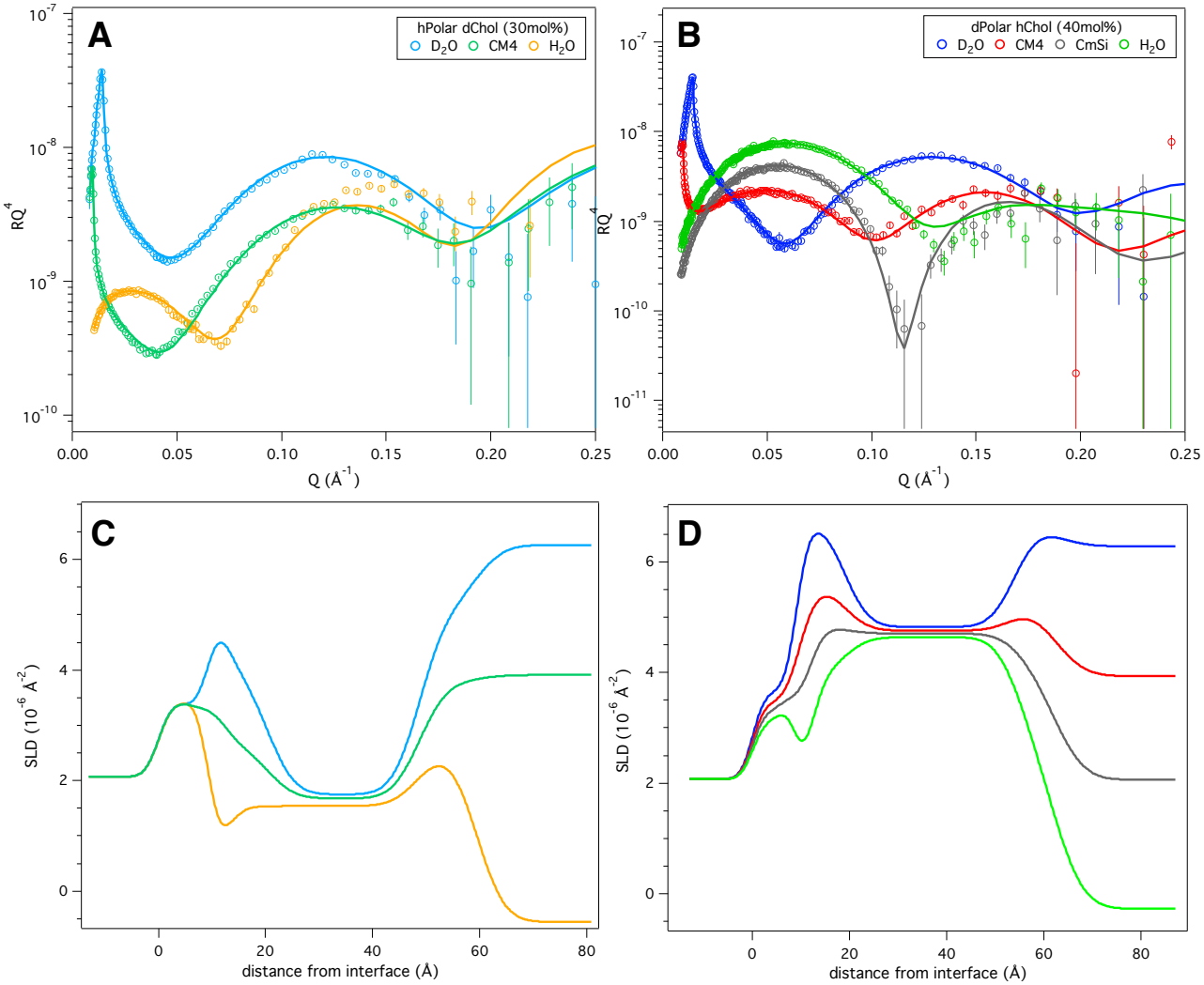

Figure 5.12 : Reflectivity data and fits of hydrogenous *P. pastoris* phospholipids and deuterated cholesterol (30mol%) lipid bilayer **(A)** and corresponding SLD profiles **(C)**, and reflectivity data and fits of deuterated *P. pastoris* phospholipids and hydrogenous cholesterol (40mol%) lipid bilayer **(B)** and corresponding SLD profiles **(D)**.

Samples	**hPolar dChol (30 mol%) bilayer χ^2 = 5.7**				**dPolar hChol (40 mol%) bilayer χ^2 = 2.2**			
Layers	τ (Å)	ρ (10^{-6} Å^{-2})	ϕ (%)	σ (Å)	τ (Å)	ρ (10^{-6} Å^{-2})	ϕ (%)	σ (Å)
Si	-	2.07	0	2 ± 2	-	2.07	0	2 ± 1
SiO_2	7 ± 2	3.41	1 ± 1	2 ± 1	9 ± 2	3.41	8 ± 7	2 ± 1
Water	1.5 ±0.5	Solvent	100	3 ± 2	2 ± 0.5	Solvent	100	3 ± 2
Head (in)	9 ± 2	3.1# ± 0.4	26 ± 6	4 ± 2	9 ± 2	7.1# ± 0.3	37 ± 6	4 ± 2
Chains	28 ± 2	1.64±0.05 *	3 ± 2	4 ± 2	35 ± 2	4.78±0.05**	3 ± 3	4 ± 2
Head (out)	11 ± 3	4.7# ± 0.9	31 ± 9	4 ± 2	8 ± 2	7.1# ± 0.3	49 ± 11	5 ± 2

Table 5.14 : Fitted parameters of hPol hChol and dPol dChol bilayers. #The headgroups SLD varied depending on contrasts differently than calculated before (see table 3.2). The values employed are reported in the text above. *Corresponds to 30 ± 2mol% **Corresponds to 40 ± 2mol%. Parameters were defined in chapter 3.

The hPolar dChol bilayer was unique as the only way to satisfactorily fit the data, especially the H_2O contrast, was an asymmetry in the headgroup SLD values. 3.1 ± 0.4 10^{-6} $Å^{-2}$, 2.4 ± 0.4 10^{-6} $Å^{-2}$ and 2.0 ± 0.6 10^{-6} $Å^{-2}$, in D_2O, CM4 and H_2O were fitted for the inner headgroup layer of the hPolar dChol bilayer whereas higher SLD values were obtained for the outer headgroup layer with 4.7 ± 0.9 10^{-6} $Å^{-2}$, 4.3 ± 0.8 10^{-6} $Å^{-2}$ and 3.9 ± 0.5 10^{-6} $Å^{-2}$, in D_2O, CM4 and H_2O respectively. An asymmetry of sterol distribution in the chain layers in agreement with the higher cholesterol content found in the outer headgroup leaflet, i.e. with more cholesterol on the outer leaflet, could not be achieved. The features found in the D_2O contrast at Q (0.12-0.15 $Å^{-1}$) together with the impossibility to fully fit the H_2O contrast with a high reflection at high Q and the asymmetry only found in the headgroup layers are additional reasons to prepared and measure again this sample for further investigations.

5.4. Natural phospholipids (*P. pastoris*) - Amphotericin B effect

The changes in the *P. pastoris* samples before and after AmB addition are presented below, in figures 5.13 to 5.16 and tables 5.15 to 5.18. The phospholipid composition of the mixtures extracted from yeast allows to model either fungal membranes (with ergosterol) or mammalian membranes (with cholesterol), which constitute a valuable system to understand the differences between the therapeutic and the toxic side effects of AmB.

5.4.1. Ergosterol-containing *P. pastoris* phospholipids membranes

By looking into details, the reflectivity curves and the fits of the hPolar hErg and dPolar dErg samples after AmB addition, presented in figure 5.13 and table 5.15, many aspects were changed after the incubation with AmB. The hydrogenous ergosterol-containing hPolar hErg membrane reacted strongly, as additional minima could be seen in all the reflectivity curves after the incubation with AmB. This was contrasted with the perdeuterated sample dPolar dErg, where the main observation concerned the D_2O contrast after AmB addition where two minima could be observed, implying that a hydrogenous layer was formed on top of the lipid membrane. From the changes in the SLD of the chains it was observed that, in both cases, 7 ± 3% v/v of ergosterol remained in the bilayer out of the 22 ± 4% v/v initially present. AmB also inserted into both membranes to 8 ± 2% v/v. The removal of two-thirds of the ergosterol content of the bilayers induced important structural changes as seen by the shrinking of the hydrophobic layer, especially evident for the perdeuterated membrane, from 30 ± 1Å to 23 ± 2Å. This observation is in contradiction with previous work where the polyunsaturation of total lipid extracts bilayers was related to larger thinning of the membranes induced by AmB as well as larger insertion of AmB [16]. The apolar lipid fractions present in the total extracts and not included in this work could thus play an important role in the susceptibility towards AmB.

The presence of an approximately 30Å thick layer of AmB on the top of the lipid membranes, called 'AmB upper layer' as composed mainly of AmB molecules, was similar to the recently postulated AmB sponge layer responsible for extracting ergosterol [5]. Such a thick layer could not be seen for any of the monomolecular or bimolecular

systems involving POPC. The phospholipid content thus seems to be important in the AmB upper layer formation or stabilization, most likely due to the different headgroup classes present or less likely due to the diversity of the acyl chains. Even if the thickness of the AmB layer was relatively similar in the two samples, its composition and hydration was very different. hPolar hErg presented a relatively concentrated AmB layer with 50 ± 5% hydration and a volume ratio 1:1 of AmB and ergosterol, whereas in dPolar dErg it was very hydrated 94 ± 3% with a volume ratio between drug and sterol of 4:1.

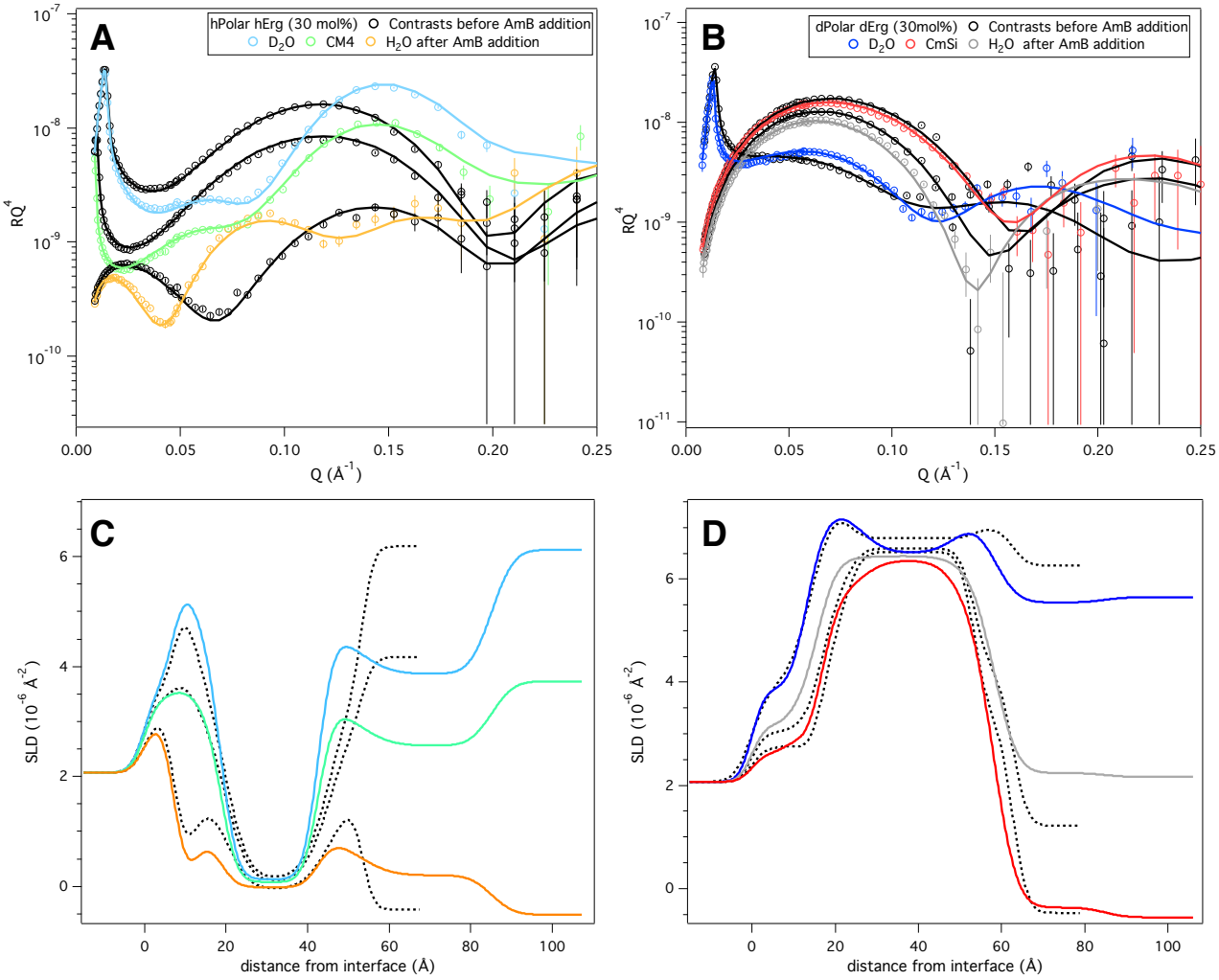

Figure 5.13 : Reflectivity data and fits of hPolar hErg (30 mol%) bilayer before (black) and after AmB addition (light colors) **(A)** and corresponding SLD profiles **(C)**, and reflectivity data and fits of dPolar dErg (30 mol%) bilayer before (black) and after AmB addition (dark colors) **(B)** and corresponding SLD profiles **(D)**.

Samples	hPolar hErg (30 mol%) bilayer after AmB χ^2 = 9.2				dPolar dErg (30 mol%) bilayer after AmB χ^2 = 27.2			
Layers	τ (Å)	ρ (10^{-6} Å^{-2})	ϕ (%)	σ (Å)	τ (Å)	ρ (10^{-6} Å^{-2})	ϕ (%)	σ (Å)
Si	-	2.07	0	3 ± 2	-	2.07	0	2 ± 1
SiO_2	8 ± 1	3.41	10 ± 4	2 ± 1	13 ± 1	3.41	18 ± 3	3 ± 1
Water	3.5 ± 1	Solvent	100	3 ± 1	2 ± 0.8	Solvent	100	4 ± 1
Head (in)	8 ± 2	2.9# ± 0.1	49 ± 9	3 ± 2	11 ± 2	7.9# ± 0.2	24 ± 8	4 ± 1
Chains	24 ± 2	0.1* ± 0.1	1 ± 1	3 ± 2	23 ± 2	6.52**±0.05	3 ± 3	5 ± 2
Head (out)	10 ± 2	2.9# ± 0.1	54 ± 7	5 ± 2	8 ± 2	7.9# ± 0.2	24 ± 9	5 ± 2
AmB layer	32 ± 1	1.6§ ± 0.2	50 ± 5	6 ± 2	27 ± 6	3.85§§ ±0.35	94 ± 3	5 ± 2

Table 5.15 : Fitted parameters of hPolar hErg (30 mol%) and dPolar dErg (30 mol%) bilayers after AmB addition. Parameters were defined in chapter 3 and in table 4.6. #The headgroups SLD varied depending on contrasts and composition; see table 3.2. *in D_2O, 0.06 ± 0.14 10^{-6} Å^{-2} in CM4 and -0.01 ± 0.22 10^{-6} Å^{-2} in H_2O. §in D_2O, 1.4 ± 0.3 10^{-6} Å^{-2} in CM4, and 0.9 ± 0.3 10^{-6} Å^{-2} in H_2O. **in D_2O, 6.50 ± 0.04 10^{-6} Å^{-2} in CMSi and 6.44 ± 0.04 10^{-6} Å^{-2} in H_2O. §§in D_2O, 3.50 ± 0.25 10^{-6} Å^{-2} in CMSi and 2.80 ± 0.42 10^{-6} Å^{-2} in H_2O.

The partially deuterated samples (hPolar dErg and dPolar hErg) confirmed the presence of the upper AmB layer. The reflectivity curves and scattering length density profiles corresponding to the best fits to these bilayers after AmB addition in three different water contrasts (D_2O, CM4, CMSi and H_2O) are shown in figure 5.14 and table 5.16. In both cases, an AmB upper layer was observed with similar hydration and composition, corresponding to a volume ratio of 4:1 Amphotericin B to ergosterol. The deuterated-ergosterol containing membrane hPolar dErg showed 6 ± 4% v/v AmB insertion and only 3 ± 2% v/v ergosterol removal in this concentrated sample initially containing 29 ± 2% v/v or ergosterol. The SLD value of the headgroup stayed higher than suggested by the calculation of phospholipid mixture without sterol, as it was before interaction with AmB, supporting the idea that the sterol was not largely removed in this case. On the contrary, the effects of AmB on the dPolar hErg (15mol%) bilayers were similar to what was observed with hPolar hErg and dPolar dErg, with a significant amount of ergosterol extracted (8 ± 2%v/v out of the 10 ± 2% v/v in chains) and insertion of AmB up to 11 ± 5% v/v. In this case, the SLD of the headgroup was also found to increase back to the values of a dPolar bilayer, supporting the idea that the ergosterol was initially partly mixed in the headgroup layer as its removal by AmB was associated with an increase in

the SLD of the headgroup (7.6, 7.4, 7.2 and 7.0 10^{-6} Å^{-2} in D_2O, CM4, CMSi and H_2O respectively).

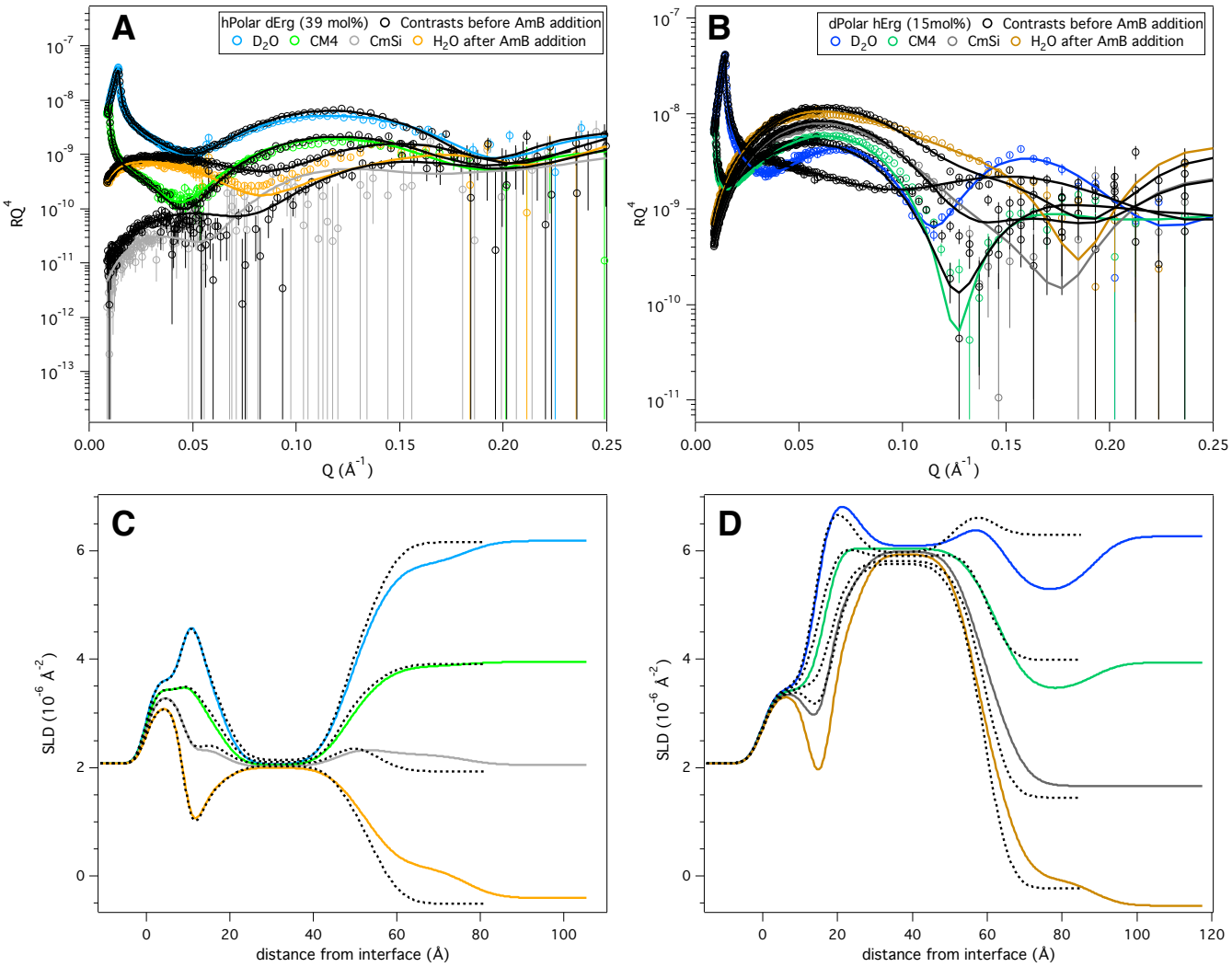

Figure 5.14 : Reflectivity data and fits of hPolar dErg (39 mol%) bilayer before (black) and after AmB addition (light colors) **(A)** and corresponding SLD profiles **(C)**, and reflectivity data and fits of dPolar hErg (30 mol%) bilayer before (black) and after AmB addition (dark colors) **(B)** and corresponding SLD profiles **(D)**.

Thus, AmB inserts into all bilayers and removes ergosterol, as seen previously with synthetic lipid membranes, but it also forms an additional layer above the lipid membrane, particularly evident in the reflectivity curves of the hydrogenous ergosterol-containing samples. It is also worth noting that no significant water insertion was found in the yeast lipid bilayers after interaction with AmB. Indeed, it usually lowered the water content, if present at first.

Samples	hPolar dErg (39 mol%) bilayer after AmB χ^2 = 2.9				dPolar hErg (15 mol%) bilayer after AmB χ^2 = 7.3			
Layers	τ (Å)	ρ (10^{-6} Å^{-2})	ϕ (%)	σ (Å)	τ (Å)	ρ (10^{-6} Å^{-2})	ϕ (%)	σ (Å)
Si	-	2.07	0	2 ± 1	-	2.07	0	3 ± 1
SiO_2	9 ± 2	3.41	8 ± 7	2 ± 1	14 ± 2	3.41	2 ± 2	2 ± 1
Water	2 ± 0.5	Solvent	100	3 ± 2	3 ± 1	Solvent	100	3 ± 1
Head (in)	7 ± 2	3.2# ± 0.2	32 ± 9	4 ± 2	8 ± 2	7.6# ± 0.3	43 ± 5	3 ± 2
Chains	29 ± 2	2.06* ± 0.09	2 ± 2	5 ± 2	29 ± 2	6.09**±0.13	2 ± 2	4 ± 2
Head (out)	7 ± 2	3.2# ± 0.2	28 ± 12	6 ± 2	9 ± 2	7.6# ± 0.3	56 ± 9	5 ± 2
AmB layer	24 ± 2	3.8§± 0.9	82 ± 9	6 ± 3	25 ± 3	2.4§§±0.6	73 ± 4	6 ± 3

Table 5.16 : Fitted parameters of hPolar dErg (39 mol%) and dPolar hErg (15 mol%) bilayers after AmB addition. Parameters were defined in chapter 3 and in table 4.6. #The headgroups SLD varied as detailed in the text below. *in D_2O, 2.04 ± 0.11 10^{-6} Å^{-2} in CM4, 2.02 ± 0.17 10^{-6} Å^{-2} in CMSi and 1.99 ± 0.19 10^{-6} Å^{-2} in H_2O. §in D_2O, 3.5 ± 0.9 10^{-6} Å^{-2} in CM4, 3.1 ± 1.2 10^{-6} Å^{-2} in CMSi and 2.7 ± 2 10^{-6} Å^{-2} in H_2O. **in D_2O, 6.04 ± 0.10 10^{-6} Å^{-2} in CM4, 5.99 ± 0.14 10^{-6} Å^{-2} in CMSi and 5.94 ± 0.14 10^{-6} Å^{-2} in H_2O. §§in D_2O, 2.0 ± 0.5 10^{-6} Å^{-2} in CM4, 1.7 ± 0.4 10^{-6} Å^{-2} in CMSi and 1.3 ± 0.4 10^{-6} Å^{-2} in H_2O.

5.4.2. Cholesterol-containing *P. pastoris* phospholipids membranes

Figure 5.15 shows the reflectivity curves and scattering length density profiles corresponding to the best fits to the data for hPolar hChol (30 ± 10mol%) in three different water contrasts (D_2O, CM4 and H_2O) and dPolar dChol bilayers (30 ± 8mol% respectively) in three different water contrasts (D_2O, CMSi and H_2O) after the addition of AmB. The parameters of the fits presented in figure 5.15 are found in table 5.17.

The main observation of AmB in the hPolar hChol bilayer was insertion of water (10 ± 5% v/v) in the lipid chain region. AmB inserted in the hydrophobic chain layer to 8 ± 4% v/v and removal of cholesterol was very limited with less than 2 ± 2% v/v cholesterol removed. Besides water insertion, no major changes in the structure of the bilayer itself were observed but a relatively thick AmB upper layer (38 ± 6Å), very hydrated, up to 94% v/v, mainly composed of AmB (less than 1% v/v of cholesterol) could be used to fit the data. The existence of the AmB upper layer, with such high hydration could be questioned but its inclusion in the model structure improved the

quality of the fits by a $\Delta\chi^2 \geq 5$. Also, the presence of water in the hydrophobic chain induced by AmB supports the idea of a pore formation mechanism, as previously observed based on membrane potential and ion permeability measurements [77]. However, in the dPolar dChol sample, it was not possible to observe any water insertion. On the other hand, this sample also had good contrast for detecting AmB insertion and cholesterol removal and gave similar results to the hydrogenous membrane, with 4 ± 2%v/v insertion and less than 2% cholesterol extraction respectively. Also, an upper AmB layer of 32 ± 8Å with less than 1% deuterated cholesterol and a hydration up to 99% v/v, improved the simultaneous fits, while the characteristics of the lipid bilayer itself were not modified by more than uncertainties of the parameters included in the models.

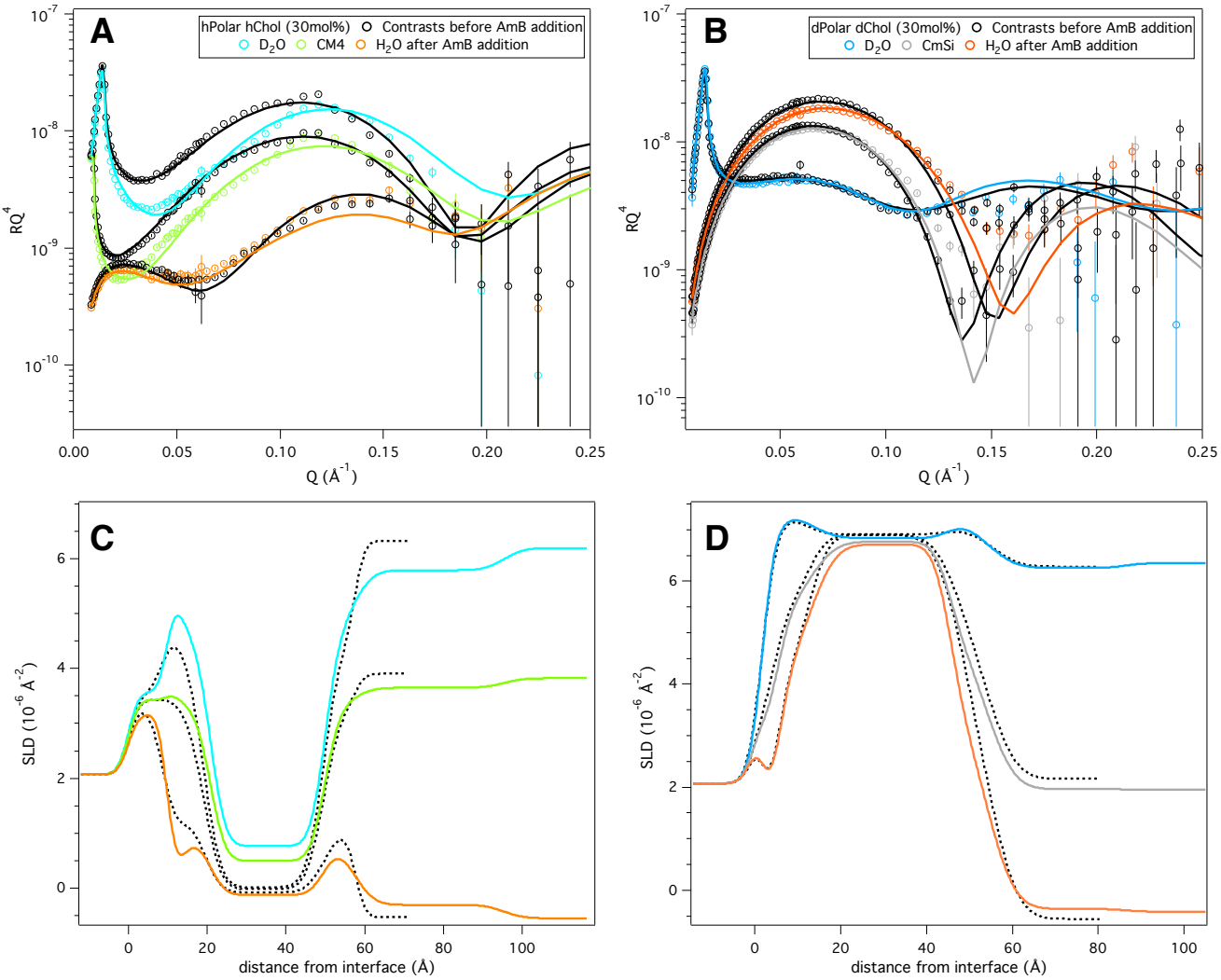

Figure 5.15 : Reflectivity data and fits of hPolar hChol (30 mol%) bilayer before (black) and after AmB addition (light colors) **(A)** and corresponding SLD profiles **(C)**, and reflectivity data and fits of dPolar dChol (30 mol%) bilayer before (black) and after AmB addition (dark colors) **(B)** and corresponding SLD profiles **(D)**.

Samples	hPolar hChol (30 mol%) bilayer after AmB χ^2 = 39.9				dPolar dChol (30 mol%) bilayer after AmB χ^2 = 8.9			
Layers	τ (Å)	ρ (10^{-6} Å^{-2})	ϕ (%)	σ (Å)	τ (Å)	ρ (10^{-6} Å^{-2})	ϕ (%)	σ (Å)
Si	-	2.07	0	2 ± 1	-	2.07	0	2 ± 1
SiO_2	10 ± 1	3.41	6 ± 3	3 ± 2	2 ± 1	3.41	5 ± 5	2 ± 1
Water	2 ± 0.5	Solvent	100	3 ± 2	2 ± 0.5	Solvent	100	3 ± 1
Head (in)	9 ± 2	2.9# ± 0.1	50 ± 12	3 ± 2	9 ± 2	7.9# ± 0.2	40 ± 8	3 ± 2
Chains	29 ± 1	0.12* ± 0.08	11 ± 4	3 ± 2	32 ± 2	6.84**±0.10	2 ± 2	3 ± 2
Head (out)	7 ± 2	2.9# ± 0.1	55 ± 14	4 ± 2	9 ± 2	7.9# ± 0.2	50 ± 10	5 ± 2
AmB layer	38 ± 6	2.87§ ± 0.31	88 ± 6	4 ± 2	32 ± 8	2.90§§	96 ± 3	5 ± 3

Table 5.17 : Fitted parameters of hPolar hChol (30 mol%) and dPolar dChol (30 mol%) bilayers after AmB addition. Parameters were defined in chapter 3 and in table 4.6. #The headgroups SLD varied depending on contrasts and composition; see table 3.2. *in D_2O, 0.10 ± 0.12 10^{-6} Å^{-2} in CM4 and -0.08 ± 0.13 10^{-6} Å^{-2} in H_2O. §in D_2O, 2.4 ± 0.5 10^{-6} Å^{-2} in CM4 and 1.47 ± 0.7 10^{-6} Å^{-2} in H_2O. **in D_2O, 6.83 ± 0.07 10^{-6} Å^{-2} in CM4 and 6.80 ± 0.04 10^{-6} Å^{-2} in H_2O. §§in D_2O, 2.1 10^{-6} Å^{-2} in CMSi and 1.6 10^{-6} Å^{-2} in H_2O. Errors bars are of the same order of magnitude than the SLD values.

The data after AmB addition to hPolar dChol and dPolar hChol, which provide good contrast for detecting cholesterol removal, are shown in figure 5.16 and the parameters corresponding to the fits are detailed in the table 5.18. hPolar dChol was measured in three different water contrasts (D_2O, CM4, and H_2O) whereas dPolar hChol was measured in four different water contrasts (D_2O, CM4, CMSi and H_2O).

The hPol dChol bilayer was difficult to fit and the bilayer after AmB action was even more challenging. It seemed that water was still present in the hydrophobic layer and that an upper layer, very hydrated and with no deuterated cholesterol was observed. The only possibility to fit all the contrasts together with the same model was to modify drastically the SLD of the headgroup, in an asymmetric way. In comparison to the bilayer before AmB, were the headgroup SLD were altered symmetrically by the difficulty to define the separation between heads and chains in presence of cholesterol, with values of 3.5 10^{-6} Å^{-2}, 2.9 10^{-6} Å^{-2} and 2.7 10^{-6} Å^{-2}, for D_2O, CM4 and H_2O, after AmB addition, the inner headgroup layer was unchanged, but the SLDs of the outer headgroup layer were increased with values such as 4.7 10^{-6} Å^{-2}, 3.8 10^{-6} Å^{-2} and 3.4

10^{-6} Å^{-2}, for D_2O, CM4 and H_2O. At the same time, the SLD of the lipid chain dropped from 1.64 ± 0.04 10^{-6} Å^{-2} to 1.54 ± 0.05 10^{-6} Å^{-2} in D_2O. Again, asymmetry in the hydrophobic leaflets, with more cholesterol in the outer leaflet did not constitute an acceptable model. These observations are very unusual, and the strong asymmetry only observed in the headgroups, with high SLD values, is not explained and need further investigation. Thus the differences observed correspond to extraction of 5 ± 2% v/v of cholesterol and large insertion of AmB of 13 ± 3% v/v.

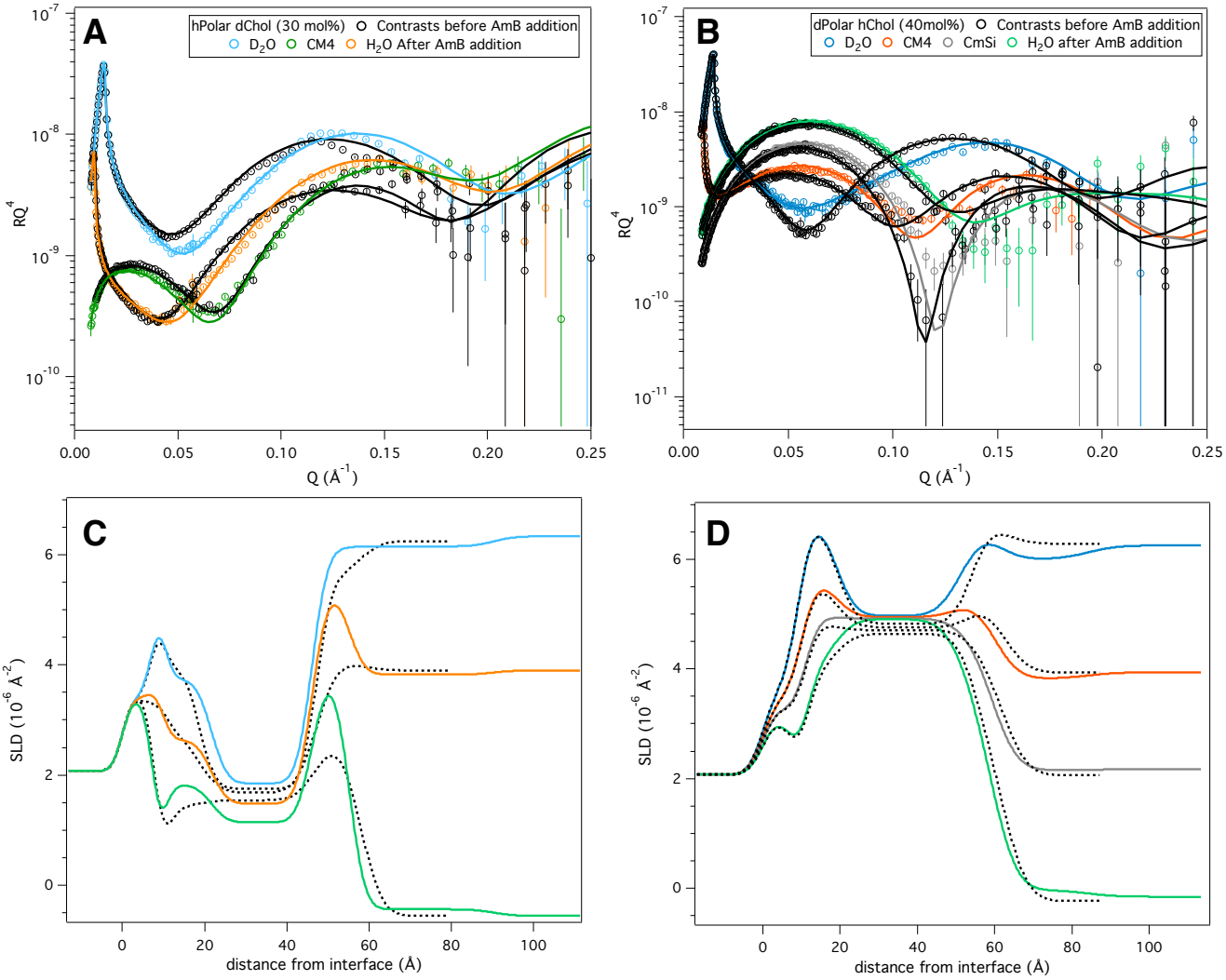

Figure 5.16 : Reflectivity data and fits of hPolar dChol (30 mol%) bilayer before (black) and after AmB addition (light colors) **(A)** and corresponding SLD profiles **(C)**, and reflectivity data and fits of dPolar hChol (40 mol%) bilayer before (black) and after AmB addition (dark colors) **(B)** and corresponding SLD profiles **(D)**.

Samples	hPolar dChol (30 mol%) bilayer after AmB χ^2 = 14				dPolar hChol (40 mol%) bilayer after AmB χ^2 = 3.5			
Layers	τ (Å)	ρ (10^{-6} Å^{-2})	ϕ (%)	σ (Å)	τ (Å)	ρ (10^{-6} Å^{-2})	ϕ (%)	σ (Å)
Si	-	2.07	0	2 ± 2	-	2.07	0	3 ± 1
SiO_2	6 ± 2	3.41	1 ± 1	2 ± 1	9 ± 2	3.41	8 ± 7	2 ± 1
Water	2 ± 0.5	Solvent	100	2 ± 1	2 ± 0.5	Solvent	100	3 ± 2
Head (in)	10 ± 2	3.5# ± 0.2	36 ± 8	3 ± 2	9 ± 2	7.1# ± 0.3	31 ± 11	4 ± 2
Chains	25 ± 2	1.54* ± 0.06	6 ± 2	3 ± 2	33 ± 2	4.97**±0.07	2 ± 2	5 ± 2
Head (out)	14 ± 2	4.7# ± 0.4	27 ± 6	3 ± 2	8 ± 2	7.1# ± 0.3	49 ± 7	5 ± 2
AmB layer	43 ± 5	2.98§ ± 0.63	96 ± 3	4 ± 2	25 ± 9	2.8§§±0.8	93 ± 4	6 ± 2

Table 5.18 : Fitted parameters of hPolar dChol (30 mol%) and dPolar hChol (30 mol%) bilayers after AmB addition. Parameters were defined in chapter 3 and in table 4.6. #The headgroups SLD varied as for the bilayer structural characterization before AmB addition unless for the outer leaflet in hPolar dChol (details in text above). *in D_2O, 1.46 ± 0.06 10^{-6} Å^{-2} in CM4 and 1.43 ± 0.05 10^{-6} Å^{-2} in H_2O. §in D_2O, 2.5 ± 0.6 10^{-6} Å^{-2} in CM4 and 1.6 ± 0.3 10^{-6} Å^{-2} in H_2O. *in D_2O, 4.95 ± 0.05 10^{-6} Å^{-2} in CM4, 4.93 ± 0.06 10^{-6} Å^{-2} in CMSi and 4.91 ± 0.04 10^{-6} Å^{-2} H_2O. §§in D_2O, 2.4 ± 0.9 10^{-6} Å^{-2} in CM4, 2.0 ± 0.9 10^{-6} Å^{-2} in CMSi and 1.5 ± 0.8 10^{-6} Å^{-2} in H_2O.

On the contrary, the reflectivity data for dPolar hChol (40 ± 2mol%) could be fitted correctly with a model that showed no water insertion, 4 ± 3% v/v AmB insertion together with a 6 ± 3% v/v extraction of cholesterol out of the 30 ± 1% in volume initially present in the sample, which was very evident in the D_2O contrasts. The greater cholesterol extraction observed in the 40mol% dPolar hChol than in the 30mol% hPolar hChol and dPolar dChol samples could be directly linked to the difference in composition.

The drug inserted in all cholesterol-containing *P. pastoris* bilayers in a calculated mean value of 5 ± 1% v/v, whereas extraction of cholesterol was very limited, even in the 40 ± 2mol% cholesterol sample. The Amphotericin B upper layer was also observed in all cases and allowed to obtain the best fits. Nevertheless, its hydration level almost always exceeding 90%, the layer was mainly composed of AmB with less than 1% of cholesterol, which is arguably below the detection limit considering the volume fraction uncertainty of solvent (± 4% v/v). Water seemed to insert in the hydrophobic part of the hPolar-containing bilayers, whereas it was not possible to fit the data with such models for the dPolar-containing bilayer. Concerning the mechanism of action of

AmB on cholesterol containing bilayers, it is clear that the AmB removes cholesterol only to a very limited degree if at all from the bilayers and does not form an equally dense extramembraneous layer as it does with ergosterol containing samples. The potential reasons for such behavior and the differences observed between synthetic lipid membranes and natural phospholipids will be discussed in the chapter 5.8.

5.5. Natural phospholipids (*P. pastoris*) Bilayer structural characterization on sapphire substrate

The possibility to use a different supporting material was motivated by both an interest to study the effect of the surface chemistry on the structural characteristics of yeast lipid bilayers and, at the same time, to gain better neutron contrast. Indeed the absence of an additional oxide layer (SiO_2) and the high SLD value of sapphire ($5.74\ 10^{-6}$ $Å^{-2}$) make this material suitable to observe small variations in the lipid bilayers structures. The surface of sapphire also has a less negative charge at neutral pH than silicon, due to its higher isoelectric point, which varies with the surface orientation. Indeed, the crystals used in this work had random orientations and the isoelectric point is expected to be comprised between pH 4.5 and pH 6, the isoelectric point of the different orientations [174].

The sapphire crystals were cleaned as the silicon substrates and the lipid bilayers were prepared in the exact same way as for the deposition on silicon wafers with 30mol% sterol. But it appeared that the composition and structures of the four partially deuterated samples listed in table 5.19 greatly differed from the corresponding bilayers on silica surfaces. Indeed, the models used to fit the data were characterized by an evident asymmetry both in SLD of the headgroups and the chains, and it was found necessary to treat the two membrane leaflets as separate layers. It was assumed that the water content of the leaflets could be constrained to be equal.

Samples	Composition based on chain SLD	Contrasts measured
hPolar dErg	15 ± 3 mol%	D_2O, CM3* and H_2O
dPolar hErg	53 ± 2 mol%	D_2O, CM3 and H_2O
hPolar dChol	32 ± 4 mol%	D_2O, CM3 and H_2O
dPolar hChol	43 ± 5 mol%	D_2O, CM3 and H_2O

Table 5.19 : List of the samples, composition based on SLD and the contrasts measured on FIGARO and D17 at ILL. *CM3 corresponds to 52% D_2O and 48% H_2O for a contrasts match equal to $3\ 10^{-6}$ $Å^{-2}$.

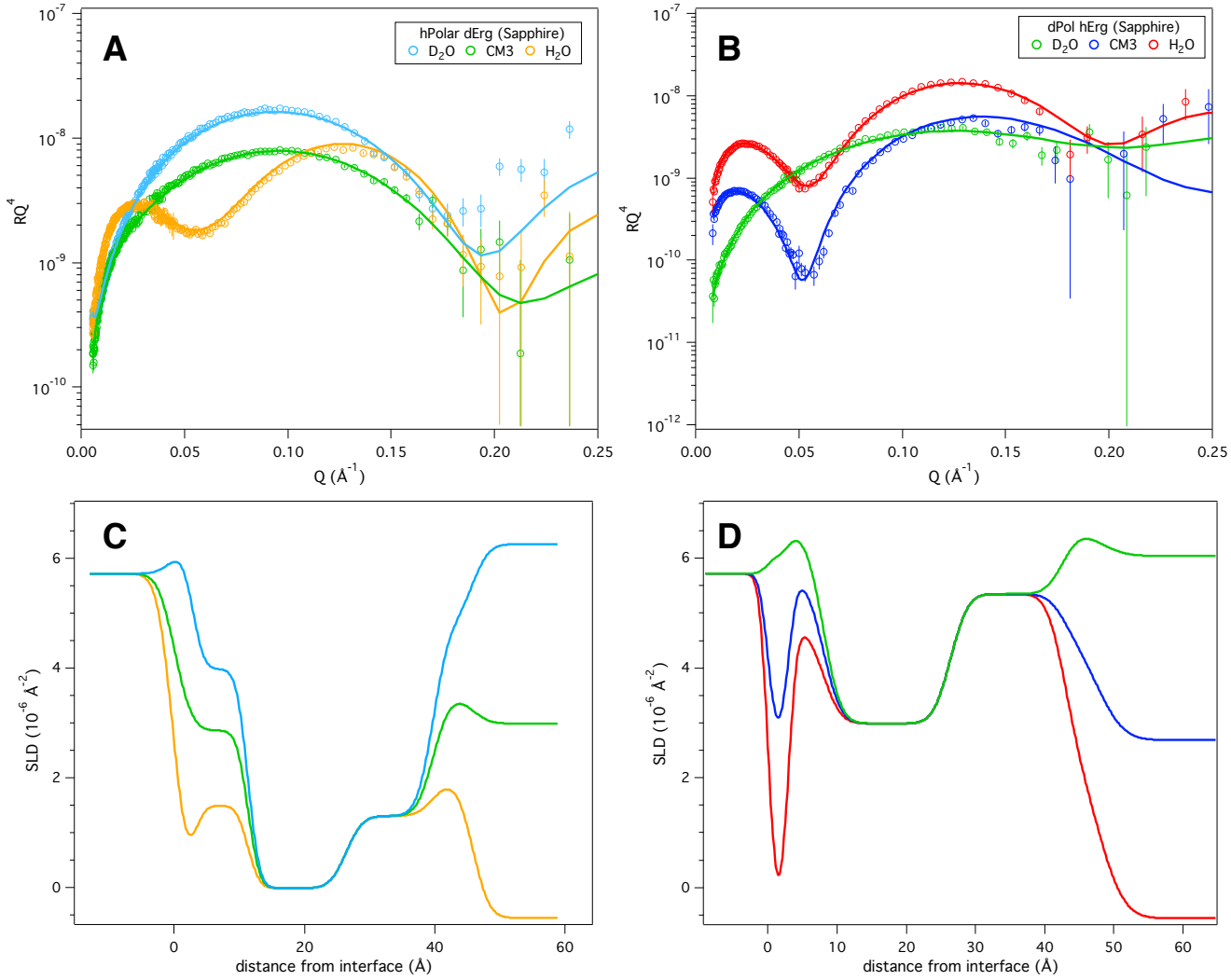

Figure 5.17 : Reflectivity data and fits of hPolar dErg (15 ± 3mol%) bilayer on sapphire **(A)** and corresponding SLD profiles **(C)**, and reflectivity data and fits of dPolar hErg (53 ± 2mol%) bilayer on sapphire **(B)** and corresponding SLD profiles **(D)**.

Samples	**hPolar dErg bilayer (sapphire) χ^2 = 1.7**				**dPolar hErg bilayer (sapphire) χ^2 = 5.3**			
Layers	τ (Å)	ρ (10^{-6} Å^{-2})	ϕ (%)	σ (Å)	τ (Å)	ρ (10^{-6} Å^{-2})	ϕ (%)	σ (Å)
Sapphire	-	5.72	0	2 ± 1	-	5.72	0	2 ± 1
Water	3 ± 1	Solvent	100	2 ± 1	3 ± 1	Solvent	100	2 ± 1
Head (in)	8 ± 2	3.2# ± 0.1	32 ± 7	2 ± 1	5 ± 1	6.3# ± 0.3	20 ± 9	2 ± 1
Chain (in)	15 ± 1	0.01*±0.04	1 ± 1	2 ± 1	19 ± 1	2.99§±0.01	2 ± 2	2 ± 1
Chain (out)	13 ± 1	1.30**±0.1	1 ± 1	2 ± 1	16 ± 1	5.35§§±0.03	2 ± 2	2 ± 1
Head (out)	6 ± 2	3.9# ± 0.1	38 ± 7	3 ± 1	5 ± 2	7.2# ± 0.2	55 ± 12	3 ± 1

Table 5.20 : Fitted parameters of hPol dErg (15 ± 3mol%) and dPol hErg (53 ± 2mol%) bilayers initially prepared with 30mol% ergosterol, deposited on sapphire. Parameters were defined in chapter 3 and in table 4.6. #The headgroups SLD varied differently than calculated as reported in the text below. *Corresponds to 2 ± 2mol% of d-ergosterol. **Corresponds to 28 ± 3mol% of d-ergosterol. §Correspond to 79 ± 1mol% ergosterol. §§Correspond to 28 ± 2mol% ergosterol.

Data obtained in three different water contrasts (D_2O, CM3, and H_2O) for hPolar dErg and dPolar hErg are shown in figure 5.17 and table 5.20. The hPolar dErg bilayer on sapphire had nearly no ergosterol in the inner chain leaflet (less than 3% v/v) and the SLD of the headgroup corresponded to the lipids, whereas the SLD value fitted for the outer leaflet corresponds to 20 ± 1% v/v of deuterated ergosterol. At the same time, the headgroup SLD was found to be 3.9 10^{-6} $Å^{-2}$, 3.8 10^{-6} $Å^{-2}$ and 3.5 10^{-6} $Å^{-2}$ in D_2O, CM3 and H_2O respectively, indicating that, as for the samples on silicon substrate, the separation between the chain and headgroup layers is difficult to define in presence of ergosterol when the contrast between lipid and sterol is enhanced. The overall sample was thus composed of only 15 ± 3mol% deuterated ergosterol with the sterol almost absent in the inner leaflet (2 ± 2mol%) and the equivalent of 28 ± 2mol% present in the outer leaflet. The difference in thickness between the two hydrophobic leaflets was not significant considering the fitting uncertainty even though the sterol concentration was drastically different. The asymmetry of the dPolar hErg sample was even more pronounced. Indeed, the only way found to fit the data implied very high ergosterol content, for with 53 ± 2mol% distributed as 59 ± 1% v/v (79 ± 1mol%) and 21 ± 1% v/v (28 ± 2mol%) in the inner and outer leaflets respectively. This is very different from the 30mol% ergosterol content in vesicles. The SLD of the headgroup was also asymmetric with values of 6.3 10^{-6} $Å^{-2}$, 6.0 10^{-6} $Å^{-2}$ and 5.7 10^{-6} $Å^{-2}$ and 7.2 10^{-6} $Å^{-2}$, 6.9 10^{-6} $Å^{-2}$ and 6.6 10^{-6} $Å^{-2}$ for the inner and outer headgroups in D_2O, CM3 and H_2O respectively, related again to the difficulty to define the layer separation in presence of ergosterol.

Many other alternative models were investigated including ergosterol sequestration in more or less thin layers, at the center of the bilayer, close the headgroups, asymmetric or not, but none of these gave better fits (χ^2 always > 25) than the structures summarized in table 5.20. Multilayer deposition was also not consistent with the data. The ergosterol-containing bilayers were thus asymmetric in both cases but the sterol was predominantly found in the outer leaflet in hPolar dErg sample while predominantly found in the inner leaflet in the dPolar hErg sample. This surprising observation is in agreement with the impossibility to fit both sets of data to an opposite asymmetry. Thus, the large differences in ergosterol content and the polyunsaturation degree may influence this localization.

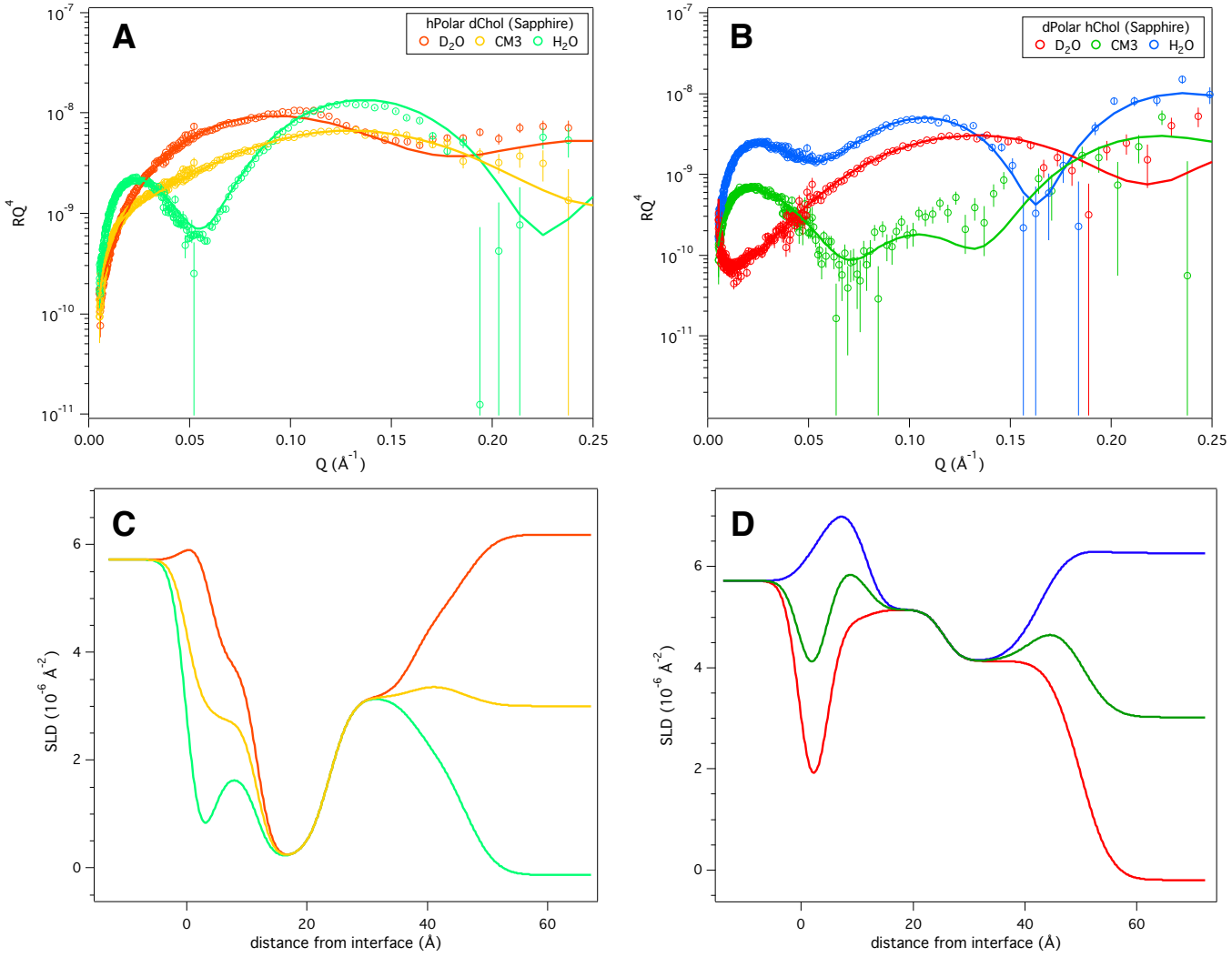

Figure 5.18 : Reflectivity data and fits of hPolar dChol (32 ± 4mol%) bilayer on sapphire **(A)** and corresponding SLD profiles **(C)**, and reflectivity data and fits of dPolar hChol (43 ± 5mol%) bilayer on sapphire **(B)** and corresponding SLD profiles **(D)**.

Samples	**hPolar dChol bilayer (sapphire) χ^2 = 6.1**				**dPolar hChol bilayer (sapphire) χ^2 = 1.7**			
Layers	τ (Å)	ρ (10^{-6} Å^{-2})	ϕ (%)	σ (Å)	τ (Å)	ρ (10^{-6} Å^{-2})	ϕ (%)	σ (Å)
Sapphire	-	5.72	0	2 ± 1	-	5.72	0	2 ± 1
Water	4 ± 1	Solvent	100	2 ± 1	4 ± 1	Solvent	100	2 ± 1
Head (in)	8 ± 2	3.2# ± 0.1	26 ± 9	2 ± 1	8 ± 2	7.5# ± 0.2	30 ± 8	2 ± 1
Chain (in)	12 ± 1	0.2* ± 0.2	2 ± 2	3 ± 1	14 ± 2	5.1§ ± 0.2	2 ± 2	2 ± 1
Chain (out)	14 ± 1	3.4**± 0.1	2 ± 2	3 ± 1	17 ± 2	4.1§§±0.15	2 ± 2	4 ± 2
Head (out)	9 ± 2	4.0# ± 0.1	31 ± 11	3 ± 1	7 ± 2	6.5# ± 0.2	30 ± 15	4 ± 2

Table 5.21 : Fitted parameters of hPol dChol (32 ± 4mol%) and dPol hChol (43 ± 5 mol%) bilayers initially prepared with 30mol% cholesterol, deposited on sapphire. Parameters were defined in chapter 3 and in table 4.6. #The headgroups SLD varied differently than calculated. The values employed are reported in the text below. *Corresponds to 6 ± 4mol% of d-cholesterol. **Corresponds to 58 ± 2mol% of d-cholesterol. §Correspond to 32 ± 4mol% cholesterol. §§Correspond to 54 ± 3mol% cholesterol.

The structures found for cholesterol-containing bilayers were in better agreement with each other, but also showed some differences. The reflectivity curves and scattering length density profiles corresponding to the best fits to the data of hPolar dChol (32 ± 4mol%) and dPolar hChol (43 ± 5mol%) bilayers measured in three different water contrasts (D_2O, CM3 and H_2O) are shown in figure 5.18 and table 5.21. An asymmetry of distribution of cholesterol was also evident and the sterol was mainly sequestrated on the outside of the bilayer, towards the solution. Whereas most of the deuterated cholesterol was found on the solvent side of the hPolar dChol bilayer with 5 ± 2% v/v (6 ± 4 mol%) in the inner hydrophobic leaflet against 42 ± 1% v/v in the outer leaflet (58 ± 2 mol%), the asymmetry was less marked in the dPolar hChol bilayer. Indeed, 24 ± 3% v/v (32 ± 4 mol%) were found in the inner leaflet when 40 ± 2% v/v (54 ± 3 mol %) were necessary to include in the outer leaflet to simultaneously fit the three contrasts. In hPolar dChol, the inner headgroup presented SLD equal to the ones calculated for the lipids, when the outer leaflet displayed higher values; 4.0 10^{-6} $Å^{-2}$, 3.6 10^{-6} $Å^{-2}$ and 3.1 10^{-6} $Å^{-2}$ for D_2O, CM3 and H_2O respectively. A decrease in the SLD of the headgroup of both leaflets was observed in the dPolar hChol sample, whit SLD values of 6.5 10^{-6} $Å^{-2}$, 6.3 10^{-6} $Å^{-2}$ and 6.0 10^{-6} $Å^{-2}$ and 7.5 10^{-6} $Å^{-2}$, 7.3 10^{-6} $Å^{-2}$ and 7.1 10^{-6} $Å^{-2}$ in D_2O, CM3 and H_2O for the outer and the inner leaflet respectively, correlated to the higher amount of cholesterol found in the outer leaflet. This showed again the necessity to include some cholesterol in the headgroup layer in the model used. The thicknesses of the lipid chains were not significantly different, as it was also the case for hPolar dErg. Finally, as seen with the ergosterol-containing bilayers deposited on sapphire (figure 5.17), the sterol concentration was also higher in the cholesterol-containing dPolar membrane than in the hydrogenous hPolar-containing sample.

While the ergosterol-containing samples deposited on sapphire are difficult to compare to their homologous versions on silicon due to important differences in the sterol content, the cholesterol-containing samples displayed a very similar cholesterol content in both cases. And it is possible to observe that the sapphire-deposited bilayer thicknesses are comparable to the ones supported on silicon, with a total bilayer thickness of 48 ± 4 Å and 43 ± 3 Å for hPolar dChol (30 ± 2mol% on silicon and 32 ± 3 mol% on sapphire, respectively) and 52 ± 3 Å and 46 ± 4 Å for dPolar hChol (40 ± 2 mol% on silicon and 44 ± 7 mol% on sapphire, respectively).

Based on these results, it is clear that the surface material and the lipid composition have a significant effect on both the vesicle fusion process of deposition and on the structure of the supported bilayers formed from complex lipid mixtures. This is discussed in chapter 5.8.

5.6. Natural lipids (*C. glabrata* total lipid extracts) - Bilayer structural characterization

As the last step towards modeling the fungal target membranes of AmB, total lipid extracts from the pathogenic yeasts *C. glabrata* were used to reconstitute supported bilayers. The membranes were formed on silica to avoid the unpredictable asymmetry effects observed on sapphire surfaces with *P. pastoris* phospholipid extracts. From the different strains selected, the lipid extracts of the two transformants, differing by their sensitivity towards Amphotericin B and lipid composition, as shown earlier in chapter 4, were characterized with neutrons.

5.6.1. Hydrogenous total extracts

The reflectivity curves and scattering length density profiles corresponding to the best fits to the data for the hydrogenous AmB sensitive C. glabrata (Y2311) total extract and the hydrogenous AmB resistant C. glabrata (Y2310) bilayers measured in four different water contrasts (D_2O, CM4, CMSi and H_2O) are presented in figure 5.19 and the associated parameters are listed in table 5.22.

In both samples, the SLD values of the headgroups, see table 5.22, were in agreement with the calculations performed based on lipid composition when the SLD value of the hydrophobic chains was found slightly higher than calculated (-0.16 10^{-6} Å^{-2} and -0.14 10^{-6} Å^{-2} calculated for Y2311 and Y2310, respectively). The calculation was performed on the basis of fatty acid and ergosterol composition only. But it was shown (figure 4.3) that other constituents were present in the lipid mixture and could explain the small variations observed in the actual SLD. The hydrogenous squalene has an calculated SLD value of 0.13 10^{-6} Å^{-2}, lanosterol a value of 0.26 10^{-6} Å^{-2} and 5,7,24(28)-Ergostatrienol 0.43 10^{-6} Å^{-2}.

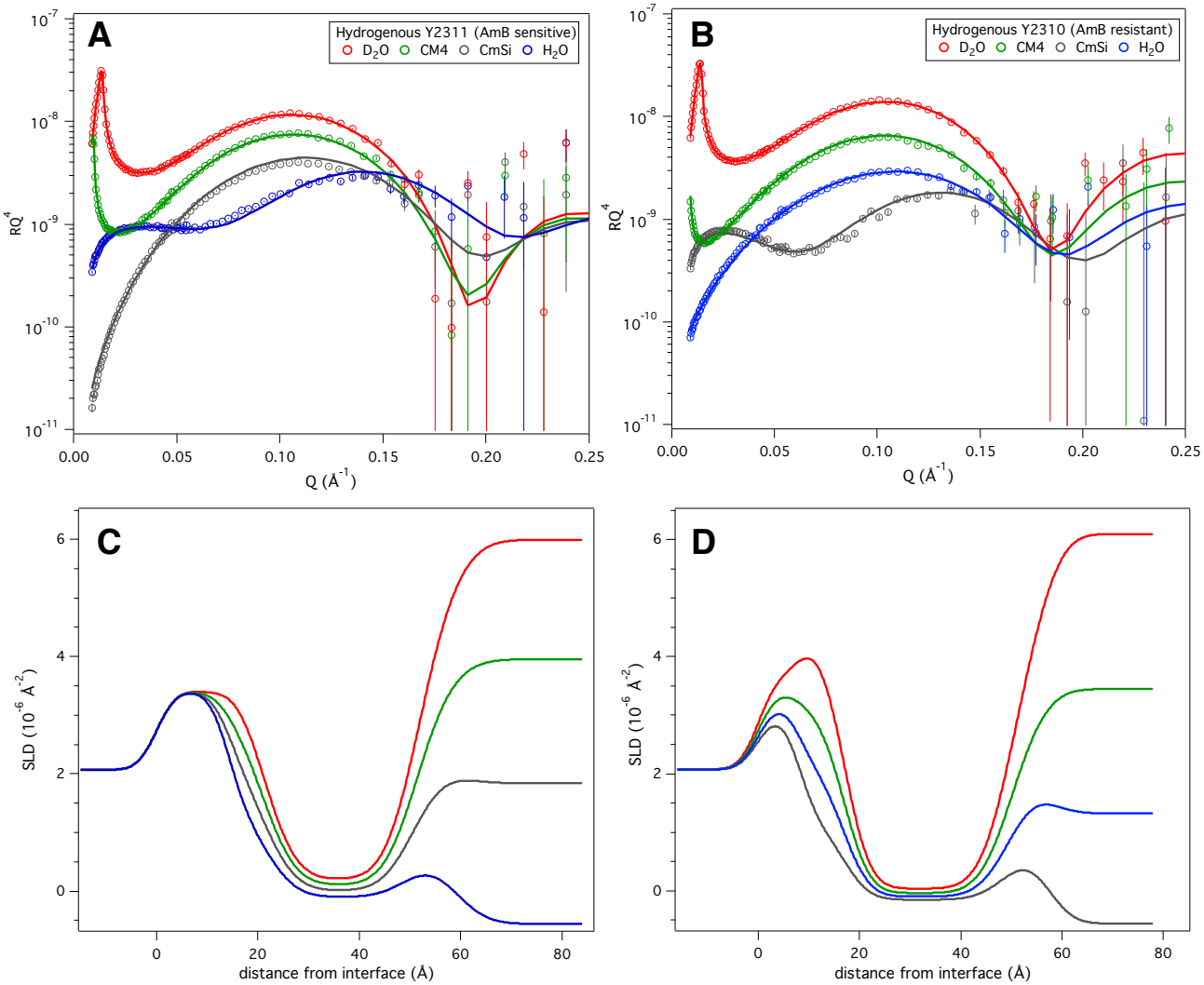

Figure 5.19 : Reflectivity data and fits of hydrogenous Y2311 total lipid extract bilayer **(A)** and corresponding SLD profiles **(C)**, and reflectivity data and fits of hydrogenous Y2310 total lipid extract bilayer **(B)** and corresponding SLD profiles **(D)**.

Samples	**Hydrogenous Y2311 Total extract bilayer χ^2 = 10.4**				**Hydrogenous Y2310 Total extract bilayer χ^2 = 8.0**			
Layers	τ (Å)	ρ (10^{-6} Å^{-2})	ϕ (%)	σ (Å)	τ (Å)	ρ (10^{-6} Å^{-2})	ϕ (%)	σ (Å)
Si	-	2.07	0	3 ± 2	-	2.07	0	3 ± 1
SiO_2	14 ± 1	3.41	1 ± 1	3 ± 2	8 ± 1	3.41	8 ± 5	3 ± 2
Head (in)	7 ± 2	2.9# ± 0.1	27 ± 9	5 ± 1	9 ± 2	3.0# ± 0.2	42 ± 11	3 ± 2
Chains	30 ± 2	-0.09±0.01	6 ± 4	5 ± 2	33 ± 2	-0.12±0.01	3 ± 3	5 ± 2
Head (out)	7 ± 1	2.9# ± 0.1	53 ± 15	5 ± 2	7 ± 2	3.0# ± 0.2	54 ± 15	5 ± 2

Table 5.22 : Fitted parameters of hydrogenous C. glabrata total extracts bilayers. Parameters were defined in chapter 3 and in table 4.6. #The headgroups SLD varied as based on composition; for hydrogenous Y2311, headgroups SLD values were 2.93 10^{-6} Å^{-2} (D_2O), 2.74 10^{-6} Å^{-2} (CM4), 2.58 10^{-6} Å^{-2} (CMSi) and 2.38 10^{-6} Å^{-2} (H_2O). For hydrogenous Y2310, headgroups SLD values were 3.02 10^{-6} Å^{-2} (D_2O), 2.83 10^{-6} Å^{-2} (CM4), 2.67 10^{-6} Å^{-2} (CMSi) and 2.46 10^{-6} Å^{-2} (H_2O).

5.6.2. Deuterated total extracts

The observations made for the hydrogenous extracts correlate well with the structure of the deuterated total extract bilayers. The bilayers were relatively symmetrical, the SLD of headgroup was used as calculated and the chain SLD were lower than calculated due to the additional ergosterol precursors, especially the perdeuterated squalene presenting the lowest SLD value. Indeed the deuterated squalene has an expected SLD value of 5.68 10^{-6} $Å^{-2}$, when lanosterol and 5,7,24(28)-Ergostatrienol have values of 7.65 10^{-6} $Å^{-2}$ and 7.71 10^{-6} $Å^{-2}$, respectively. The water content of the hydrophobic layer was also more important than in the hydrogenous samples as it was also the case for *P. pastoris* deuterated phospholipid bilayers.

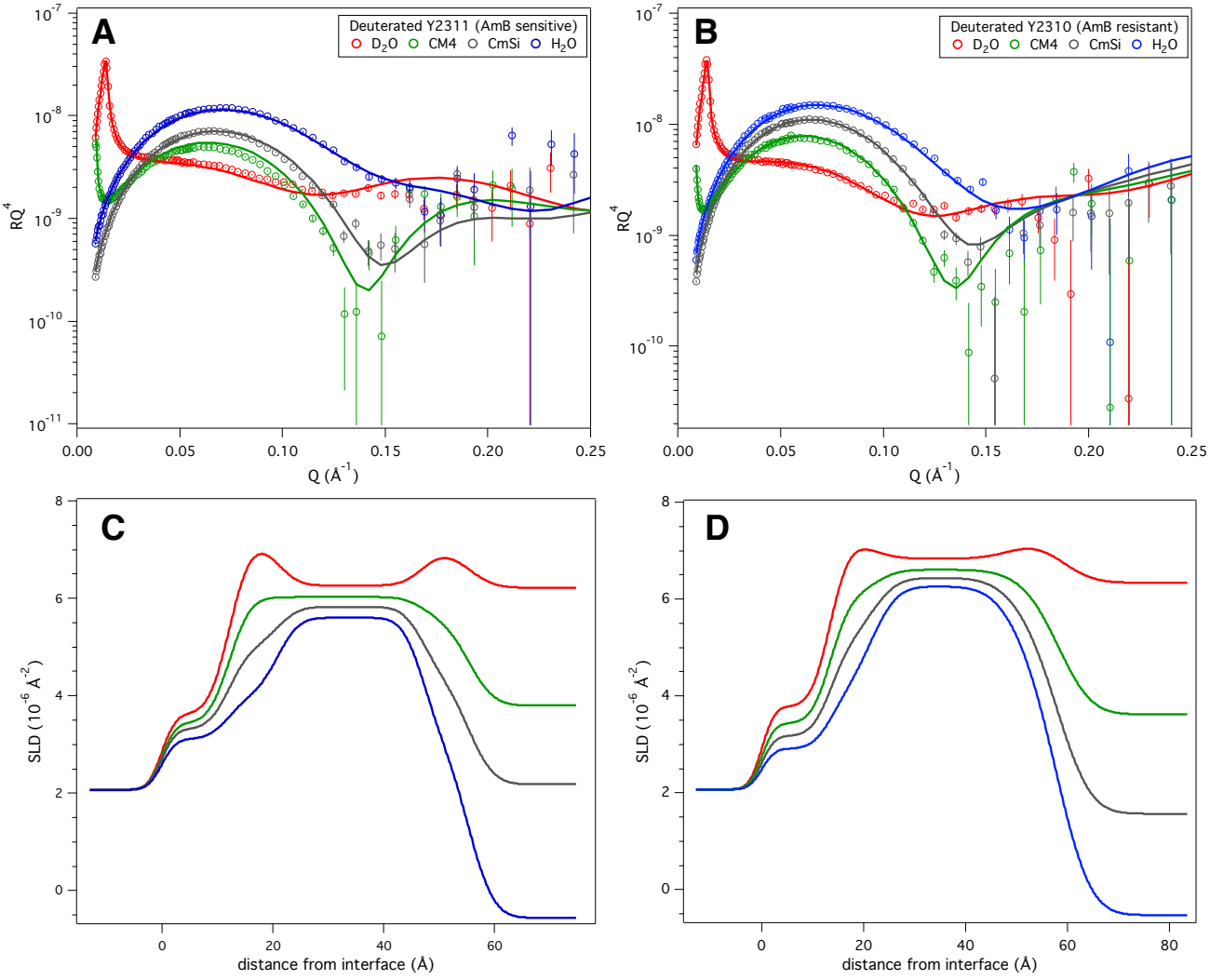

Figure 5.20 : Reflectivity data and fits of deuterated Y2311 total lipid extract bilayer **(A)** and corresponding SLD profiles **(C)**, and reflectivity data and fits of deuterated Y2310 total lipid extract bilayer **(B)** and corresponding SLD profiles **(D)**.

Samples	Deuterated Y2311 Total extract bilayer χ^2 = 18.9				Deuterated Y2310 Total extract bilayer χ^2 = 15.4			
Layers	τ (Å)	ρ (10^{-6} Å^{-2})	ϕ (%)	σ (Å)	τ (Å)	ρ (10^{-6} Å^{-2})	ϕ (%)	σ (Å)
Si	-	2.07	0	3 ± 1	-	2.07	0	3 ± 1
SiO_2	12 ± 2	3.41	7 ± 3	3 ± 2	13 ± 2	3.41	13 ± 4	3 ± 2
Head (in)	9 ± 2	7.8$^{\#}$ ± 0.1	41 ± 7	3 ± 2	8 ± 2	7.8$^{\#}$ ± 0.1	40 ± 8	4 ± 2
Chains	26 ± 2	6.27§± 0.05	9 ± 3	3 ± 2	29 ± 2	6.88§± 0.04	8 ± 3	5 ± 2
Head (out)	8 ± 2	7.8$^{\#}$ ± 0.1	48 ± 12	4 ± 2	8 ± 2	7.8$^{\#}$ ± 0.1	34 ± 11	5 ± 2

Table 5.23 : Fitted parameters of deuterated C. glabrata Total extracts bilayers. Parameters were defined in chapter 3 and in table 4.6. $^{\#}$The headgroups SLD varied as based on composition; for deuterated Y2311, headgroups SLD values were 7.78 10^{-6} Å^{-2} (D_2O), 7.58 10^{-6} Å^{-2} (CM4), 7.42 10^{-6} Å^{-2} (CMSi) and 7.19 10^{-6} Å^{-2} (H_2O). For deuterated Y2310 they were 7.80 10^{-6} Å^{-2} (D_2O), 7.61 10^{-6} Å^{-2} (CM4), 7.46 10^{-6} Å^{-2} (CMSi) and 7.25 10^{-6} Å^{-2} (H_2O). §In both cases, expected value based on fatty acids and ergosterol content was 6.8 10^{-6} Å^{-2}.

It is worth noting that the important differences in apolar lipid composition between the d-Y2311 and d-Y2310 strains (figure 4.3 and table 4.2) did not result in significant structural differences between the bilayers.

The *C glabrata* lipid bilayers contained a few percent of water in the hydrophobic layer and all had an almost symmetrical structure. The structure is actually very similar to the ergosterol-containing POPC or the ergosterol-containing *P. pastoris* lipid membranes. Note also that, as already seen with *P. pastoris* total extract bilayers characterized by neutron reflectometry [16] no water layer was needed between the membrane and the substrate to fit the data properly.

5.7. Natural lipids (*C. glabrata* total lipid extracts) - Amphotericin B effect

5.7.1. Hydrogenous total extracts

The effects of AmB in the hydrogenous total extract lipid bilayers, measured in three water contrasts (D_2O, CM4 and H_2O) are shown in figure 5.21 and the parameters corresponding to the associated fits are detailed in table 5.24.

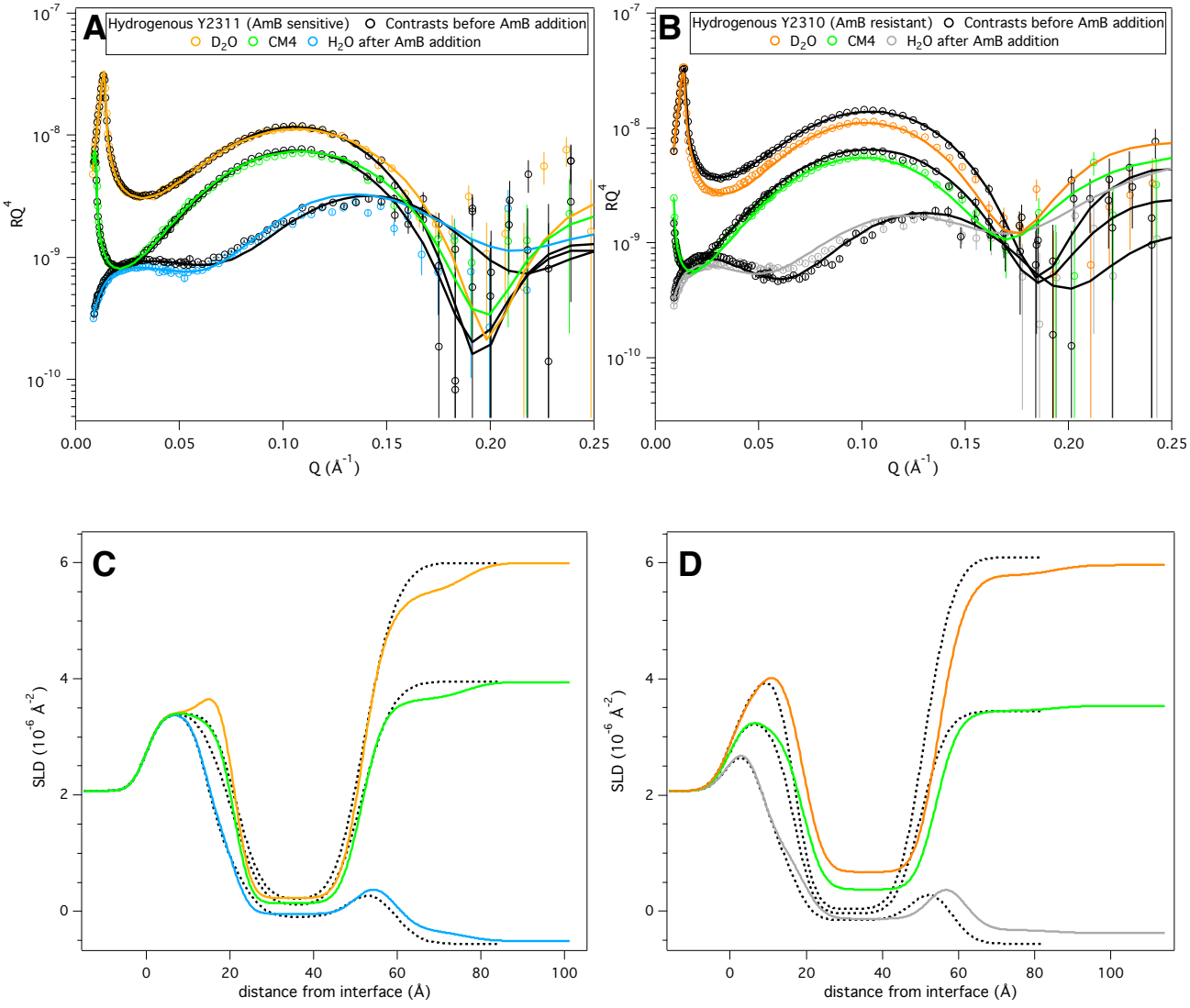

Figure 5.21 : Reflectivity data and fits of hydrogenous Y2311 total lipid extract bilayer before (black) and after AmB addition (colors) **(A)** and corresponding SLD profiles **(C)**, and reflectivity data and fits of hydrogenous Y2310 total lipid extract bilayer before (black) and after AmB addition (colors) **(B)** and corresponding SLD profiles **(D)**.

Samples	Hydrogenous Y2311 Total extract bilayer after AmB addition χ^2 = 7.8				Hydrogenous Y2310 Total extract bilayer after AmB addition χ^2 = 50.1			
Layers	τ (Å)	ρ (10^{-6} Å^{-2})	ϕ (%)	σ (Å)	τ (Å)	ρ (10^{-6} Å^{-2})	ϕ (%)	σ (Å)
Si	-	2.07	0	3 ± 2	-	2.07	0	3 ± 1
SiO_2	14 ± 1	3.41	1 ± 1	3 ± 2	8 ± 1	3.41	8 ± 5	3 ± 2
Head (in)	7 ± 1	2.9# ± 0.1	26 ± 5	3 ± 2	11 ± 2	3.0# ± 0.2	44 ± 6	4 ± 2
Chains	30 ± 2	0.11*±0.04	2 ± 2	3 ± 1	35 ± 1	-0.01**±0.06	12 ± 2	4 ± 2
Head (out)	7± 2	2.9# ± 0.1	45 ± 5	4 ± 2	6 ± 2	3.0# ± 0.2	51 ± 5	4 ± 2
AmB layer	18 ± 3	1.65§±0.62	88 ± 2	5 ± 2	23 ± 7	1.66§§	96 ± 3	5 ± 2

Table 5.24 : Fitted parameters of hydrogenous C. glabrata total extract bilayers after AmB addition. Parameters were defined in chapter 3 and in table 4.6. #The headgroups SLD varied as before AmB addition. *in D_2O, 0.06 ± 0.09 10^{-6} Å^{-2} in CM4 and -0.04 ± 0.10 10^{-6} Å^{-2} in H_2O. **in D_2O, -0.04 ± 0.09 10^{-6} Å^{-2} in CM4 and -0.10 ± 0.10 10^{-6} Å^{-2} in H_2O. §in D_2O, 1.43 ± 0.79 10^{-6} Å^{-2} in CM4 and 0.97 ± 0.83 10^{-6} Å^{-2} in H_2O. §§Error bars are of the same order of magnitude or higher than the parameters.

At first glance, the yeast extract from the AmB sensitive *C. glabrata* strain (Y2311) seemed to not react to AmB while changes can easily be seen for the mixture extracted from the AmB resistant strain. But a closer look into the models and the SLD profiles allowed to define two different scenarios and fit the small changes observed mainly in the H_2O contrast. Since different sterol-like molecules present were found in the *C. glabrata* lipid mixtures, it was not possible to identify the sterols removed. Nevertheless, by fitting the data using a similar model as before, with a lipid mixture of a given SLD equal to the one fitted before AmB addition, which includes theoretically the phospholipids, the ergosterol precursors and the ergosterol, the chain SLD variation in the hydrogenous AmB sensitive Y2311 total lipid extract could be linked to 7 ± 2% v/v removal out of the 9 ± 1% v/v total ergosterol initially present and to AmB insertion of 11 ± 3% v/v of AmB. The SLD values of the 88 ± 2% hydrated AmB upper layer observed, corresponds to a relative volume ratio 1:1 of ergosterol and AmB, similar to what was observed for hPolar hErg. This corresponds to three molecules of ergosterol for two molecules of AmB. The concomitant decrease in the lipid chain water content makes these effects difficult to observe in the reflectivity profiles.

On the contrary, the changes in reflectivity for the hydrogenous extract of the resistant strain Y2310 were clearly related to an increase in hydration of the chains from 3 ± 3% v/v to 12 ± 3% v/v after AmB addition, while the SLD of the hydrophobic layer was modified to a lower extent. Indeed, in the Y2310 total extract bilayer, the SLD changes given in table 5.24 are linked to the removal of 3 ± 2% v/v ergosterol out of the 11 ± 1% v/v originally present and AmB insertion of 5 ± 2% v/v. The uncertainty in the SLD and thickness of the AmB layer is larger due to its high hydration. For the same reason, inclusion of the upper layer did not significantly decrease the χ^2 of the simultaneous fit.

5.7.2. Deuterated total extracts

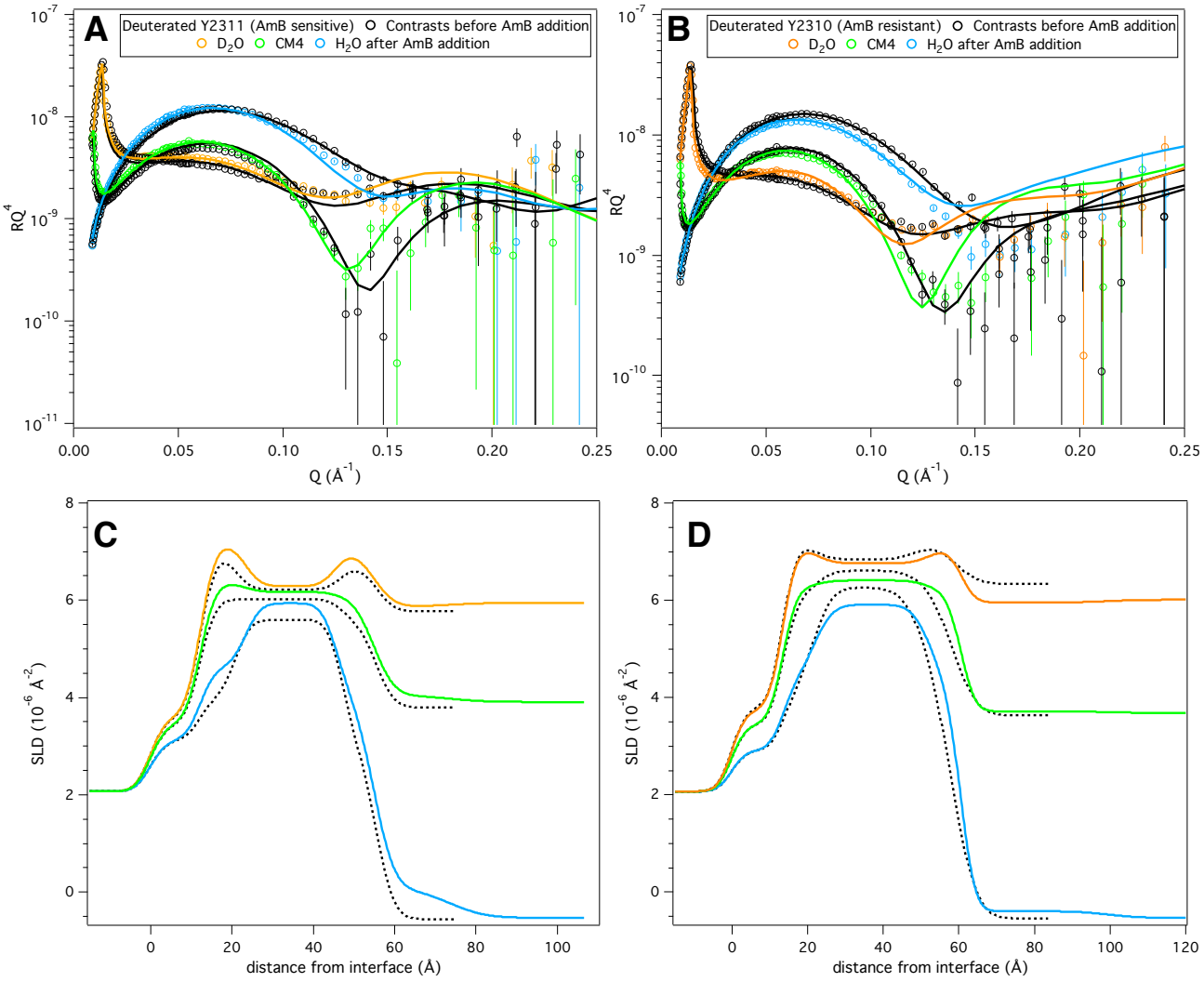

Figure 5.22: Reflectivity data and fits of deuterated Y2311 total lipid extract bilayer before (black) and after AmB addition (colors) **(A)** and corresponding SLD profiles **(C)**, and reflectivity data and fits of deuterated Y2310 total lipid extract bilayer before (black) and after AmB addition (colors) **(B)** and corresponding SLD profiles **(D)**.

Samples	Deuterated Y2311 Total extract bilayer after AmB addition χ^2 = 38.5				Deuterated Y2310 Total extract bilayer after AmB addition χ^2 = 48.0			
Layers	τ (Å)	ρ (10^{-6} Å^{-2})	ϕ (%)	σ (Å)	τ (Å)	ρ (10^{-6} Å^{-2})	ϕ (%)	σ (Å)
Si	-	2.07	0	3 ± 1	-	2.07	0	3 ± 1
SiO_2	12 ± 2	3.41	7 ± 3	3 ± 2	13 ± 2	3.41	13 ± 4	3 ± 2
Head (in)	11 ± 2	7.8$^{\#}$ ± 0.1	32 ± 7	3 ± 2	8 ± 2	7.8$^{\#}$ ± 0.1	37 ± 8	4 ± 2
Chains	22 ± 2	6.30* ± 0.20	3 ± 3	3 ± 2	31 ± 2	6.80**±0.11	11 ± 2	4 ± 2
Head (out)	9 ± 2	7.8$^{\#}$ ± 0.1	38 ± 13	4 ± 2	8 ± 2	7.8$^{\#}$ ± 0.1	43 ± 14	4 ± 2
AmB layer	17 ± 4	5.3§ ± 0.9	90 ± 6	4 ± 2	32 ± 8	3.2§§ ± 1.8	94 ± 4	4 ± 2

Table 5.25 : Fitted parameters of deuterated *C. glabrata* total extract bilayers after AmB addition. Parameters were defined in chapter 3 and in table 4.6. $^{\#}$The headgroups SLD varied as before AmB addition. *in D_2O, 6.25 ± 0.16 10^{-6} Å^{-2} in CM4 and 6.15 ± 0.13 10^{-6} Å^{-2} in H_2O. **in D_2O, 6.79 ± 0.11 10^{-6} Å^{-2} in CM4, and 6.78 ± 0.09 10^{-6} Å^{-2} in H_2O. §in D_2O, 5.05 ± 0.8 10^{-6} Å^{-2} in CM4 and 4.60 ± 0.6 10^{-6} Å^{-2} in H_2O. §§in D_2O, 3.0 10^{-6} Å^{-2} in CM4 and 2.4 10^{-6} Å^{-2} in H_2O. Error bars are of the same order of magnitude than the parameters due to poor contrast in CM4 and H_2O.

Figure 5.22 and table 5.25 shows the reflectivity curves, scattering length density profiles and the parameters of the best fits for the deuterated total lipid extract bilayers from *C. glabrata* measured in three water contrasts (D_2O, CM4 and H_2O).

The reflectivity curves measured after AmB addition on the deuterated total extracts bilayers showed different changes. In the case of the AmB sensitive Y2311 membrane in all the contrasts, particularly in the most sensitive contrasts H_2O and CM4, the reflectivity at low q ($q \leq 0.05$ Å^{-1}) in comparison to the contrasts measured before AmB addition, while for the AmB resistant Y2310 membrane the curves tended to fall below the ones measured before adding AmB, even at low q. These relative changes in contrast can be explained by the same observations made before in the hydrogenous bilayers. In the case of the deuterated AmB sensitive strain Y2311, 8 ± 1% v/v out of the 9 ± 1% v/v ergosterol initially present was removed and 11 ± 2% v/v insertion of AmB was observed, extremely similar to the hydrogenous extract bilayer from Y2311. A similar AmB upper layer in thickness and hydration was found with also a ratio 1:1 of ergosterol:AmB.

The bilayer from the AmB resistant strain Y2310 was altered to a smaller degree with less than 2 ± 1% v/v removal of ergosterol out of the 9 ± 1% v/v initially present and about the same amount of AmB insertion (2 ± 1% v/v) in the hydrophobic chains. Surprisingly, the hydration of the hydrophobic chains remains significantly high. And the upper AmB layer was still very hydrated (94 ± 4% v/v), but its presence was required for a good fit even given the large uncertainties of its SLD values (χ^2 = 48.0 with AmB upper layer against χ^2 = 87.0 without it).

The four samples presented in this final NR study clearly illustrated a difference in the effect of AmB on lipid membranes depending on the phenotype of the yeast of origin and it sensitivity to the antifungal drug. The fatty acid composition of the mixture were very similar, both between the strains and in hydrogenous or deuterated form but the sterol fraction were shown to be different. The effect of AmB on the total extract from the sensitive strain (Y2311) was coupled to a significant removal of ergosterol and formation of an AmB layer composed of 2:3 AmB:ergosterol. This is consistent with the ergosterol-extracting AmB sponge-layer suggested recently as the underlying mechanism to explain the anti fungal activity of AmB [5] as it was observed in all the ergosterol-containing bilayers composed of lipids extracted from both *P. pastoris* too. Finally, the AmB was shown to insert in significant proportions (11 ± 2% v/v).

In the bilayer reconstituted from the total lipid extract of a resistant *C. glabrata* strain, the AmB effect is markedly different. The ergosterol extraction is very limited, the AmB upper layer is very discreet as very hydrated and AmB inserts into the resistant lipid membranes to smaller proportions (5 ± 2% and 2 ± 1% v/v in hydrogenous and deuterated Y2310 total extracts respectively). However, water was also found to insert in the hydrophobic layer after interaction of AmB in the hydrogenous total extract from Y2310. Water present in the chain region was also still observed in the deuterated total extract of Y2310 after AmB addition. This observation suggests the formation of pores as seen in both model and bacterial membranes [74-75]. It can be concluded that the yeast lipid bilayers from *C. glabrata* show promises as candidates for more complex lipid membranes in structural investigation of cell membranes via neutron reflectometry.

5.8. Discussion

5.8.1. Structure of model and yeast lipid bilayers

The different model membranes employed on silicon substrates, from POPC to phospholipids and total extracts from yeasts, are very similar. No structural effects could be ascribed to the deuteration level of the lipids, whereas the effects of lipid composition were significant, with thicker membranes formed from the deuterated phospholipids extracted from *P. pastoris,* due to the presence of less polyunsaturated lipid chains. Whereas at 15mol%, ergosterol and cholesterol exhibited a similar condensing effect on POPC, the structural impact of the 30mol% sterols in the bilayers from *P. pastoris* phospholipids, was more pronounced. Independently of the polyunsaturation degree of the lipids, the hydrophobic chains of the yeast lipid bilayers were found to be thicker in presence of cholesterol than in presence of the same amount of ergosterol, which is consistent with the effect of cholesterol [173] straightening and therefore lengthening the lipid chains of the phospholipids, both saturated and unsaturated to a higher degree than ergosterol does. Nevertheless, the condensing effect of both sterol increase with concentration as seen with the possibility to compensate the differences in thickness due to the polyunsaturation degree of the lipid mixtures by adaptation of the amount of sterol, see hPolar dErg (39 mol%) and dPolar hErg (15 mol%).

The most interesting aspect concerning the structures of the supported bilayers is that an asymmetry in the sterol distribution was observed and necessary to fit the data of the sapphire-supported bilayers, whereas such behavior could not be observed in any of the bilayers on silicon substrates. If lipid asymmetry is stable in biological membranes and important for many cellular processes [175], its maintenance is an active enzymatic process [27]. Such asymmetry is difficult to access in many biophysical studies but recent work with neutron techniques have related a lipid asymmetry to a redistribution of cholesterol in the presence of a ganglioside lipids in floating model bilayers [176] formed with coupled Langmuir–Blodgett and Langmuir–Schaefer techniques. Asymmetric model membranes have been used to study the time resolution of phospholipid flip flop, the spontaneous transfer of one phospholipid molecule from one leaflet to the other, involving an energetically unfavorable step with passage of the

headgroup in the hydrophobic part of the bilayer. And even if experimental astuteness, with the careful deuteration of vesicles in solution on the top of a hydrogenous deposited bilayer allowed some interesting results [11] but it was impossible to keep the asymmetry with lipids in the fluid phase.

As cholesterol is thought to have an important role in the formation of the so-called lipid rafts, many studies have investigated the affinity of cholesterol to lipids with different acyl chains. Indeed, numerous experimental techniques including DSC and NMR [177], fluorescence anisotropy [178], electron paramagnetic resonance (EPR) [179] and also molecular dynamics simulations [180] have shown differences in the interaction between cholesterol and different classes of phospholipids and specific acyl chains. It was shown that cholesterol is preferably surrounded by certain classes like SM, PC and PS due to the its enhanced affinity for C_{14} to C_{18}-long unsaturated acyl chains that are usually found with these classes [181] and that the localization of cholesterol is dependent on the lipid nature. It is likely that similar effects occur for ergosterol, but it is less well documented. Based on the affinity of the sterols for certain lipid molecules, the sterol asymmetry observed in this work could be linked to an asymmetry of the phospholipid composition of the supported bilayers, as there is no existing evidence for the repulsion of only the sterol from the support surface. Indeed, since the sapphire is less negatively charged than the silicon substrate at neutral pH [182], it may promote a different distribution of the lipids in our yeast lipid extracts.

Therefore, the asymmetric distribution of the sterols on sapphire-supported bilayers could arise as a consequence of an asymmetry in lipid composition between the inner and the outer leaflets. In the current work, fully deuterated lipid mixtures were used, and thus the lipid asymmetry cannot be verified from this data, but by separating the lipid classes and reconstituting membranes where specific lipids could be selectively deuterated in turn the reason(s) behind the sterol asymmetry in the leaflets may be further investigated.

Stable lipid bilayer asymmetry has been recently achieved and controlled with Langmuir-Blodgett Langmuir-Schaefer deposition techniques but was limited to few species in the gel phase at the investigated temperatures [11, 176] as mixing usually occurs for fluid samples during the deposition process. Asymmetric bilayers can also be prepared by vesicle fusion [183-184]. Both the support surface and the conditions of

bilayer deposition by vesicle fusion have an effect on the distribution of lipids on surfaces. In the case of charged lipid such as PS and PG, osmotic shock sometimes aids the formation of a continuous membrane, whereas Ca^{2+} can act as a bridge between a negatively charged oxide surface and the lipid negative charge [185]. These effects could be investigated in the future as a means to force bilayer deposition and to modulate the distribution of the different lipids in our yeast lipid mixtures.

The possibility of changing the charge of the sapphire surface with pH [182], and thus control the lipid asymmetry, could be potentially used to probe either physical processes such as flip-flop as well as the effect of a given phospholipid in the first step(s) of an interaction mechanism between an external agent and a lipid membrane, such as in the formation of the AmB upper layer. Developing our yeast lipid extracts as versatile lipid model systems could allow NR to address in the future new biologically relevant processes and mechanisms involving membranes.

5.8.2. The effect of Amphotericin B on model and yeast lipid bilayers

Concerning the action of Amphotericin B, it is clear that the complexity of the lipid membranes, both in terms of lipid classes and acyl chain composition, is of great importance for the detection and interpretation of the mechanisms of action of AmB. AmB was found to lead to several different effects in supported bilayers, including insertion, sterol removal, water penetration and formation of an extramembraneous AmB sponge layer. The effects observed are summarized in table 5.26.

The first aspect to be discussed concerns the presence or absence of an AmB rich layer on the top of the membrane, depending on the lipid model employed. The AmB upper layer is linked to the recently described sponge extraction model [5] in which extramembraneous aggregates of AmB extract the ergosterol from lipid bilayers, and the lack of bioavailable ergosterol is thought to be the main fungicidal effect of the drug. Indeed, in the model membranes composed of POPC, there was no evidence in any of the samples prepared of an upper layer formed of aggregates of AmB only or AmB and sterol molecules. This is perhaps not surprising given the fact such entities were previously only observed in electron microscopy images of dried POPC vesicles, which could lead to artifact [5]. The different protocols with the use of a less concentrated

Samples	AmB insertion (% v/v)	Water in chains after AmB addition (%)	Sterol removal (% of sterol initially present)	AmB layer, τ and ϕ (Å and %)
	POPC bilayers			
hPOPC	4 ± 2	-	NA	None
d_{82}POPC	6 ± 1	-	NA	None
hPOPC hErg (15 mol%)	4 ± 4	-	45 ± 35	None
hPOPC dErg (15 mol%)	4 ± 3	+ 8 ± 3	55 ± 9	None
d_{82}POPC hErg (15 mol%)	21 ± 7	- 9 ± 3	40 ± 40	None
hPOPC hChol (15 mol%)	8 ± 7	-	9 ± 9	None
hPOPC dChol (12 mol%)	6 ± 2	-	10 ± 10	None
d_{82}POPC dChol (15 mol%)	22 ± 2	- 5 ± 2	9 ± 9	None
d_{82}POPC hChol (15 mol%)	12 ± 4	- 6 ± 2	9 ± 9	None
	P. Pastoris phospholipids			
hPolar hErg (30 mol%)	8 ± 2	-	70 ± 20	32 ± 1 Å, 50 ± 5 %
hPolar dErg (39 mol%)	6 ± 4	-	10 ± 8	24 ± 2 Å, 82 ± 9 %
dPolar dErg (30 mol%)	8 ± 2	- 7 ± 2	70 ± 20	27 ± 6 Å, 94 ± 3 %
dPolar hErg (15 mol%)	11 ± 5	-	72 ± 18	25 ± 3 Å, 73 ± 4 %
hPolar hChol (30 mol%)	8 ± 4	+ 10 ± 5	7 ± 7	38 ± 6 Å, 88 ± 6 %
hPolar dChol (30 mol%)[#]	13 ± 3	+ 3 ± 3	23 ± 10	43 ± 5 Å, 96 ± 3 %
dPolar dChol (30 mol%)	4 ± 2	-	5 ± 5	32 ± 8 Å, 96 ± 3 %
dPolar hChol (40 mol%)	4 ± 3	-	20 ± 10	25 ± 9 Å, 93 ± 4 %
	***C. glabrata* total extracts**			
h Y2311 (AmB sensitive)	11 ± 3	-	75 ± 25	18 ± 3 Å, 88 ± 2 %
h Y2310 (AmB resistant)	5 ± 2	+ 9 ± 4	27 ± 19	23 ± 7 Å, 96 ± 3 %
d Y2311 (AmB sensitive)	11 ± 2	- 6 ± 4	85 ± 15	17 ± 4 Å, 90 ± 6 %
d Y2310 (AmB resistant)	2 ± 1	unchanged*	20 ± 10	32 ± 8 Å, 94 ± 4 %

Table 5.26 : Summary of the AmB effects observed in this work. The AmB insertion is expressed in % v/v with respect to the lipids of the bilayer, the sterol removal is expressed as the percentage of the sterol removed over the initial sterol content fitted in the bilayer. - means the water content is below the detection level, usually less than 4%. NA stands for Non Applicable. [#]To be repeated. *No significant changes were observed before and after AmB addition with the water content of the bilayer still elevated at 11 ± 2% hydration.

AmB solution in the present work (1mM against 8.83mM) together with the fact that the neutron measurements were performed in pure water (while HEPES was used in [5]) and the samples were rinsed before the measurements in different water contrasts, are also possible reasons that could explain the absence of such aggregates above the POPC bilayers. However, another possibility is that the aggregates do not bind to the zwitterionic membrane composed of PC but form in the surrounding media which would explain why such large structures where not observed in previous neutron and X-ray reflectivity studies involving synthetic lipid membranes [48, 163]. In other cases, the way in which the samples were formed (with AmB premixed in the lipids) could mean that a free AmB layer cannot form [47, 186].

On the contrary, in all the samples prepared with lipid mixtures extracted from yeasts, a top layer consistent with the presence of AmB was necessary to fit the data. It is unlikely that the formation of this layer was due to the higher sterol content added in the *P. pastoris* lipid bilayers compared to the POPC membranes, because in previous work on total lipid extracts from *P. pastoris* containing 14.5 mol% (hydrogenous extract) and 5.5 mol% (deuterated extract), an AmB upper layer was observed [16]. This suggests that an interaction between AmB with the headgroups is involved in the formation of the AmB layer and perhaps its stability. AmB is zwitterionic at neutral pH [187] and aggregates in aqueous solution were found by molecular dynamics simulation to be mainly driven by hydrophobic interactions [188]. A horizontal interaction of AmB with a lipid bilayer has been suggested on the basis of FTIR and surface pressure measurements [78, 189, 190], and as such, it could be enhanced by hydrogens bonds between the hydrophilic side chain or the mycosamine group of the drug with the different lipid headgroups. However, the methods used to suggest horizontal orientation of AmB lack structural information (surface pressure measurements) or specificity to surface structures (FTIR), whereas our NR data is not sensitive to the molecular orientation of AmB. More precise control of the composition of supported bilayers, by the reconstitution of membranes with specific classes present or missing, could help solve to answer the questions about the role of different headgroups on the AmB layer formation and stability.

The thickness of the AmB upper layers observed in this work varied from 17 ± 4 Å to 43 ± 5 Å and its hydration from 50 ± 5 to 96 ± 3%. Such values are consistent with the previous work performed on *P. Pastoris* lipid extract bilayers [16] in which AmB

thicknesses of 37 ± 2 to 47 ± 2 Å and hydration of 77 ± 1 to 94 ± 1% were found. The thickness and the hydration of the AmB upper layer does not seem to be linked to the degree of sterol extraction, even though in cholesterol-containing membranes, the AmB layers observed were particularly diffuse. In the protocol used, the membranes were left to interact with the AmB solution for 30 minutes before gentle rinsing followed by the measurements. It would be interesting to study a possible time dependence, as potentially suggested in QCM-D measurements with the dissipation and frequencies evolving over large periods of time (see figure 4.12) differently depending on the sterol content of the bilayer. The possibility that most of these effects during the equilibration time are induced by the change of solvent viscosity and the presence of DMSO exists but the complex lipid composition of mixtures extracted from yeast may also affect the interaction of AmB and thus the effect of the equilibration time should be investigated. Also, the possibility of an effect of gravity on the AmB aggregates should be investigated, because the NR experiments of POPC membranes (on Platypus, ANSTO) were not done in the same sample geometry as the yeast experiments (FIGARO, ILL)

Another important aspect to be discussed concerns the insertion of AmB observed in all samples, even in the sterol-free hPOPC and d_{82}POPC bilayers. This is consistent with AmB insertion [16] occurring in both sterol-free and sterol-containing bilayers, although it does not necessarily indicate pore formation [191]. The proportion of AmB inserted seems relatively constant once the initial surface coverage of the bilayers is taken into account. Indeed, an average value of 6 ± 2% v/v AmB insertion is consistent with all samples that had a good lipid surface coverage. The samples with a lower surface coverage (often the deuterated samples) are characterized by a higher proportion of AmB found in the chain region, but also a reduction of the water as shown in table 5.26. Therefore, it is not possible to conclude that lower polyunsaturation or that the ergosterol content of the deuterated samples leads to larger AmB insertion in the hydrophobic chain layer.

The changes of thicknesses of the bilayers were very limited after AmB addition and no clear trend was observed that could be linked to either the sterol or lipid composition. However the fits suggest some differences of the total thicknesses before and after AmB addition. While in most cases (hPolar hErg 30mol%, hPolar dErg 39mol%, dPolar dErg 30mol%, hPolar hChol 30mol%, dPolar hChol 40mol% and dPol dChol 30mol%) the

chain region became thinner upon AmB interaction (From 1 to 5Å), in some cases there seemed to be no thinning or even a slight increase in the thickness (dPol hErg 15mol% and hPol dChol 30mol%). But once taken into account the uncertainties, all changes are below the detection limit of the experiments unless for dPolar dErg and a thinning of 5 ± 4Å. Access to better resolutions may allow to clarify the changes of thicknesses of the bilayers after AmB addition.

However, the structural consequences of AmB addition on lipid bilayers is probably the sum of the effects of the initial lipid composition effect on the structure, the proportion of the AmB insertion, of the sterol removal and of the presence of water in the chains, when it was observed. The water insertion in consequence of AmB addition and related to aqueous pore formation [74-76], was only observed in few cases without evident relationship to lipid composition, isotopic labelling or sterol origin. The only significant difference to previously published data on yeast lipids was the thinning of the deuterated hydrophobic chain layer in dPolar dErg (30 mol%) in contradiction to the previous observation that higher polyunsaturation was linked to greater structural changes induced by AmB [16], whereas our data suggests that the more pronounced changes are related to the nature and amount of sterol present in the membrane.

Indeed, the degree of sterol extraction clearly depends on the nature of the sterol. AmB extracts more ergosterol than cholesterol and no significant differences could be related to the degree of polyunsaturation of the lipid membranes. Nonetheless, two samples behave differently. The hPolar dErg (39 mol%) containing the highest amount of ergosterol displays a lower sterol extraction than the samples containing less ergosterol while the highest cholesterol-content sample (dPolar hChol 40 mol%) seems to induce a bigger effect of AmB through larger cholesterol extraction. This does not correlate with the better AmB resistance of yeasts containing less ergosterol [151-152] and is counter-intuitive in the case of cholesterol. The fact that the membrane fluidity is greatly influenced by higher sterol content may influence the AmB action and this has been hypothesized before [191], but the difference between ergosterol and cholesterol-containing bilayers remains unsolved.

A final observation concerns the bilayers composed of the total extracts of *C. glabrata*. The AmB effects are very different between the lipid mixtures associated to the AmB

sensitive strain (Y2311) and those associated to the AmB resistant strain (Y2310). Indeed, a higher proportion of ergosterol is extracted while a higher insertion of AmB occurs in the bilayer corresponding to the AmB sensitive strain. On the contrary, water seemed to be incorporated to the chain layer when ergosterol extraction and AmB insertion were limited in the bilayer corresponding to the AmB resistant strain. This is consistent in both hydrogenous and deuterated conditions. Since the fatty acid composition is relatively constant in all four samples, they constitute complementary samples to the *P. pastoris* bilayers. However, the sterol fraction was shown to be affected mainly by deuteration, and these preliminary results enlighten the importance of other sterol-like molecules and sterol intermediates, especially lanosterol and squalene, in the resistance or sensitivity towards AmB. Their action on the resistance or sensitivity to AmB is not intensively investigated. Besides one paper that showed a correlation between supplementation of yeasts with squalene and enhanced fungicidal properties of AmB [192], these intermediates are usually only observed in traces amount and were not linked yet to any protecting effect against AmB.

In conclusion, synthetic model membranes are necessary to understand how to develop and handle lipid systems and are useful to determine the main physical parameters involved in more complex systems. However, the constant use of PC bilayers, with the advantage of a precise and controlled model, presents the drawback of being disconnected from the real systems when expected to mimic and be used to investigate certain mechanisms occurring in natural membranes. It was demonstrated in this work that the models developed from lipid mixtures extracted from yeasts are relevant models allowing to access a broader view of the mechanism of action of AmB than in POPC-based membranes only. Cholesterol was shown to be less susceptible than ergosterol to extraction from the lipid bilayer by AmB, while AmB inserts in a membrane independently of its polyunsaturation degree. However, the concentration of sterol(s) may play a role in the modulation of the extraction and/or the insertion of AmB which needs to be further investigated. A better control of the composition of the bilayers, especially concerning the amount of sterol integrated in the membranes, would also allow to clarify many of the observations of this work. The versatility of the model membranes based on yeast extracts is of interest for many biophysical studies and the problems it could address in the future will be significantly extended by separation and purification of the individual lipid components, both in hydrogenous

and deuterated forms. Once fully purified and characterized, a whole library of model membranes will become accessible to studies of membrane-binding drugs such as AmB, which will enable a more detailed view of the molecular effects to be established.

6. NEUTRON DIFFRACTION

Neutron diffraction has been intensively exploited to determine the nanometer-scale structure of lipid multilayers [193-195], principally of mixtures of one to three lipid molecular species. As explained in the Material and Methods earlier in this manuscript, detection of Bragg peaks due to a lipid multilayer architecture allows the determination of the repeat distance between membranes. Also, by contrasts variation, the scattering length density profile can be reconstructed. All the studies performed in the past have enable to investigate the role and impact of the phospholipid classes and/or the unsaturation of lipids on membrane structure and properties [196-197]. Recently, complex mixtures of lipids extracted from natural sources, such as plant lipids or the stratum corneum lipid matrices [124, 198], have been successfully characterized by means of neutron diffraction. The idea of the present work was to demonstrate a proof of concept for the use of the complex lipid mixtures from *P. pastoris* yeast in neutron diffraction studies by comparing the multilamellar organization of different hydrogenous and deuterated lipid mixtures in different humidity conditions. Its use could also represent a more realistic tool for neutron diffraction, as for neutron reflectometry, for life-science related interaction studies. The comparison with the synthetic lipid multilayers (POPC) and the investigation of the relevancy of the use of the perdeuterated cholesterol newly available complemented our study. The results are presented following an increase of complexity of the multilayers studied, from synthetic lipid multilayers, to extracted phospholipid multilayers and finally total extracts multilayers.

6.1. Synthetic lipids - POPC multilayers

The synthetic lipids membranes, i.e. POPC, POPC with cholesterol were investigated as starting point for comparison purpose of both the deposition process and the structural characteristics of natural membranes. Also, hydrogenous and perdeuterated cholesterol, for possible isotope effects, was investigated. Intensity vs 2θ plots for POPC at 60% and 98% Relative Humidity (RH) presented in figure 6.1, showed that the pure POPC multilayer was characterized by the same d-spacing in the two different conditions as already reported previously [50]. D_2O was used as surrounding vapor with hydrogenous samples for better contrast.

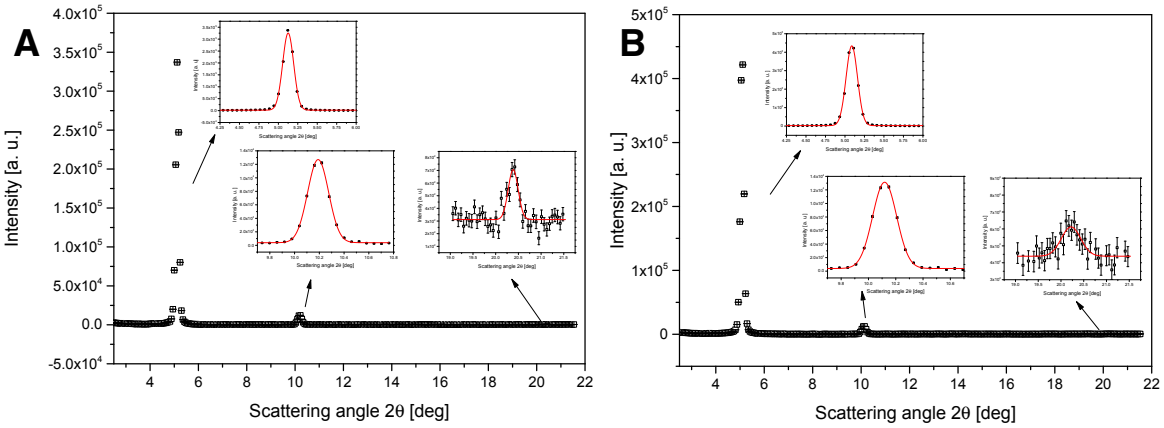

Figure 6.1 : Intensity vs 2θ plot for POPC multilayer at 60% RH **(A)** and 98% RH **(B)**. The inserts illustrate the gaussian fits of the Bragg peaks.

On the other hand, when either h-cholesterol or d-cholesterol (30% w/w) was mixed with POPC, significant differences were observed at both 60% and 98% RH. At 60% RH POPC, POPC hChol (57 mol%) and POPC dChol (54.3 mol%) exhibited a similar d-spacing of 50.9 ± 0.1 Å, 49.7 ± 0.1 Å and 51.4 ± 0.1 Å respectively, but an increase of 5.4 ± 0.2 Å and 3.9 ± 0.6 Å in the d-spacing at 98% RH was only observed when hChol and dChol were respectively added to POPC, see figure 6.2.

The d-spacing values found are closely related to published data, even if a variation was observed depending on RH in the neutron diffraction work of Gawrisch et al., with values of 52.0 ± 0.1 Å at 66% RH and 53.5 ± 0.1 Å at 93% RH at room temperature [199] or the value of 53.2 Å obtained from X-Ray diffraction at 28°C and 83% RH

[200]. Values of 56.3 Å are given for a d_{31}-POPC-cholesterol (30mol%) multilayer at room temperature and 100% RH [47].

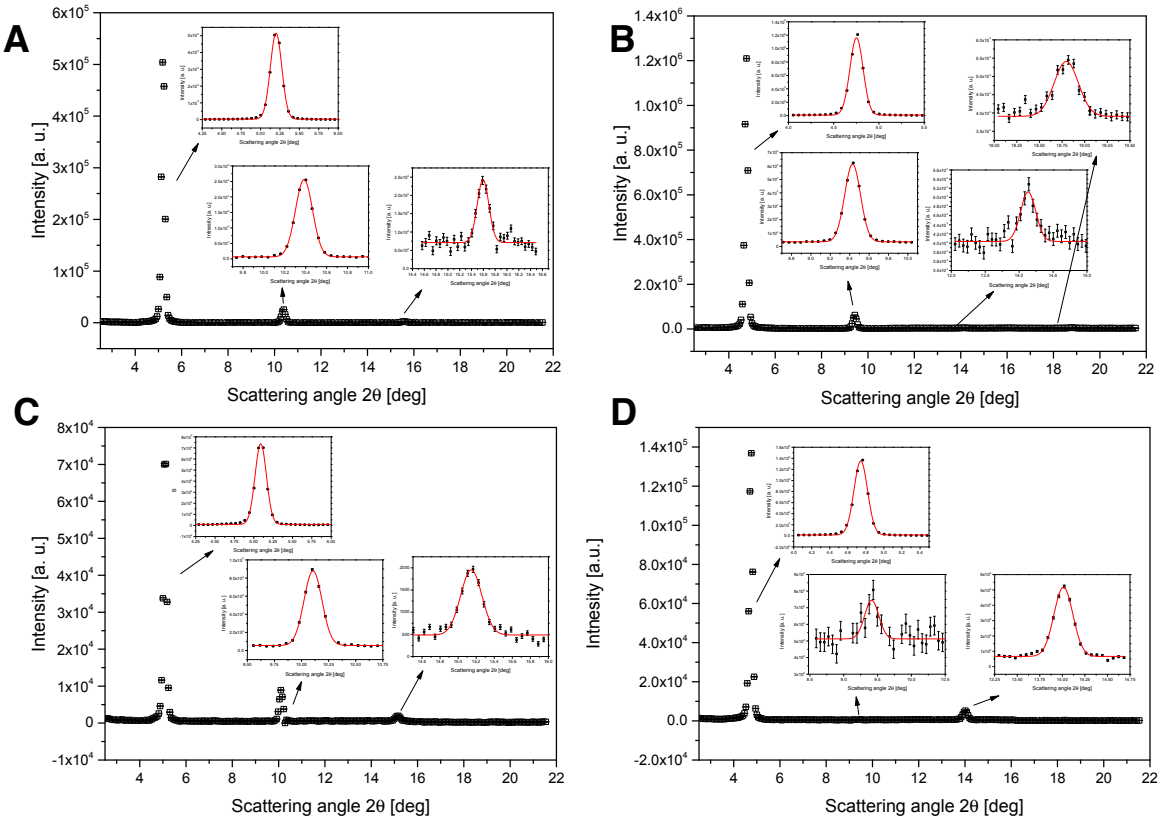

Figure 6.2 : Intensity vs 2θ plot for POPC/hChol multilayer at 60% RH **(A)** and 98% RH **(B)** and Intensity vs 2θ plot for POPC/dChol multilayer at 60% RH **(C)** and 98% RH **(D)**. The inserts illustrate the gaussian fits of the Bragg peaks.

Thus, the results highlight the well-known effect of the cholesterol molecule on the organization of phospholipids [173] and also show a similar effect induced by both the hydrogenous and the perdeuterated cholesterol. Table 6.1 summarizes the d-spacing values obtained.

Samples	d [Å] at 60% RH	d [Å] at 98% RH
POPC	50.9 ± 0.1	51.2 ± 0.1
POPC hChol (57 mol%)	49.7 ± 0.1	55.1 ± 0.1
POPC dChol (54.3 mol%)	51.4 ± 0.1	55.3 ± 0.5

Table 6.1 : Values of d-spacing (d) and the relative error (δ d) calculated from the analysis of the Intensity vs 2θ plot for POPC, POPC hChol and POPC dChol at 60% and 98% RH (D_2O).

6.2. *P. pastoris* phospholipid multilayers

6.2.1. Hydrogenous phospholipid multilayers

Data were then collected from the multilayers prepared with hydrogenous phospholipids extracted from *P. pastoris*. The 3D images recorded for h-phospholipids at 60 and 98 %RH (D_2O) together with the corresponding intensity vs 2θ plots obtained are reported in figure 6.3.

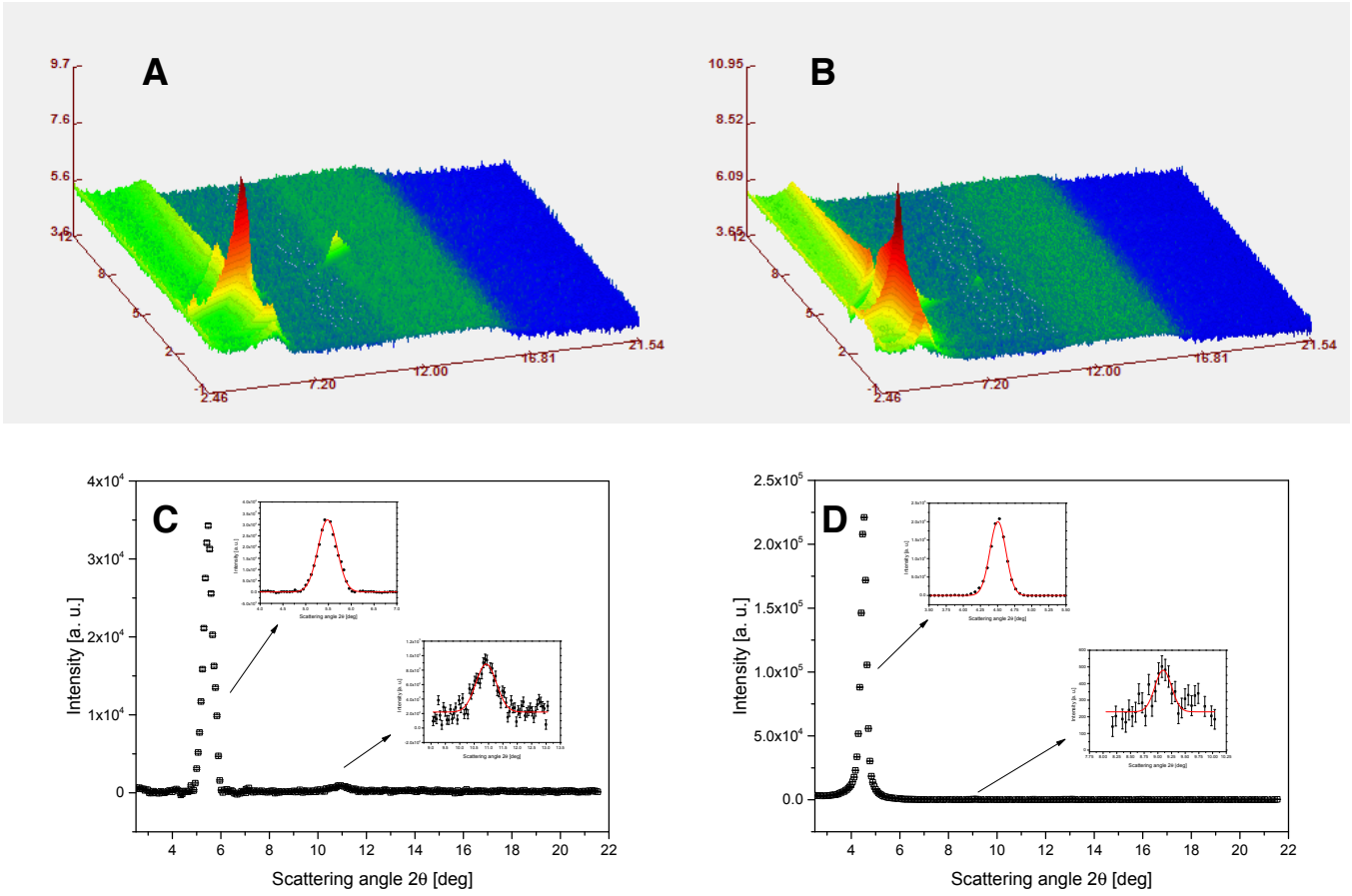

Figure 6.3 : 3D image recorded for h-phospholipids from *P. pastoris* at 60%RH **(A)** and the corresponding Intensity vs 2θ plot **(C)**. 3D image recorded for h-phospholipids at 98%RH **(B)** and the corresponding Intensity vs 2θ plot **(D)**. For 3D images, ω, 2θ and the intensity are reported on the y,x,z axes, respectively. Concerning Intensity vs 2θ plots, the inserts illustrate the fits of the Bragg peaks.

The multilayer exhibited a single lamellar phase, with only two Bragg peaks, at both 60% and 98% RH and the calculated d-spacings were 47.4 ± 0.5 Å and 56.1 ± 0.8 Å respectively. The increasing humidity lowered the intensity of the second Bragg peak observed but the d-spacing increased consequently, by 8.7 ± 0.9Å. This large variation, more significant than the changes linked to the presence of cholesterol in POPC multilayers, is only due to the diversity of the molecular species found in the hydrogenous phospholipid mixture and their rearrangement together with the increasing amount of water molecules between the bilayers. The fact that the d-spacing of the hydrogenous phospholipid mixture is lower at low humidity than in the pure POPC multilayer could be linked to the large polyunsaturation profile of the hydrogenous natural lipids.

6.2.2. Deuterated phospholipid multilayers

Figure 6.4 shows the 3D image recorded for d-phospholipids at 60% RH (H_2O) together with the corresponding intensity vs 2θ plot. As for the hydrogenous phospholipid multilayers, the d-phospholipids exhibited a lamellar structure but the associated d-spacing was calculated as 53.4 ± 0.5 Å. Interestingly, the difference of d-spacing between h and d-phospholipids multilayers of 6.0 ± 0.7 Å coincide with the observation made in NR, due to the differences in fatty acid composition between the two samples (see figure 4.5). The deuterated samples were measured with H_2O vapor in the surrounding for better contrast.

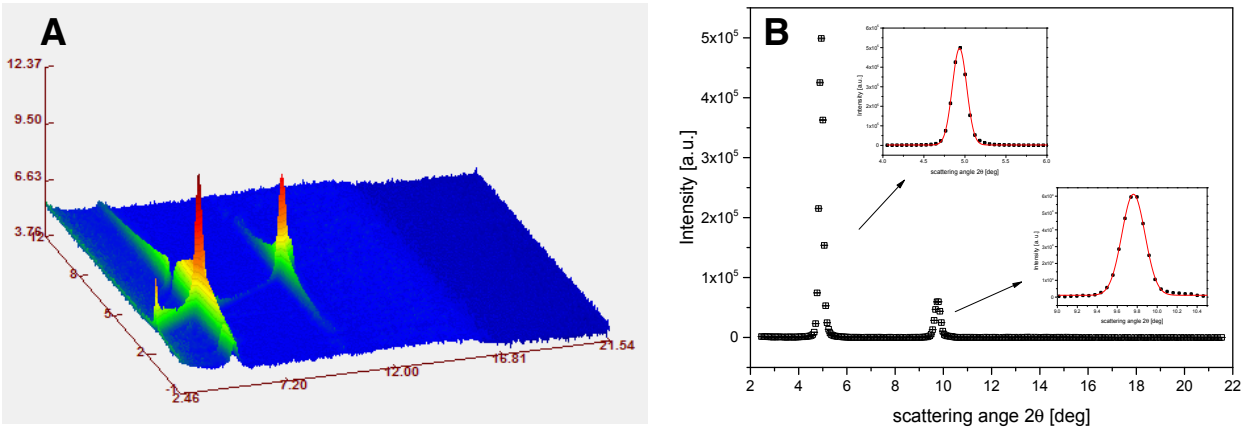

Figure 6.4 : 3D image recorded for d-phospholipid multilayer from *P. pastoris* at 60%RH **(A)** where ω, 2θ and the intensity are reported on the y,x,z axes, respectively and the corresponding Intensity vs 2θ plot **(B)** with the inserts illustrating the fits of the Bragg peaks.

By increasing the humidity to 98% RH the structure of the multilayer composed by the d-phospholipids strongly changed as seen in the 3D image recorder for d-phospholipid multilayer at 98%RH, figure 6.5.

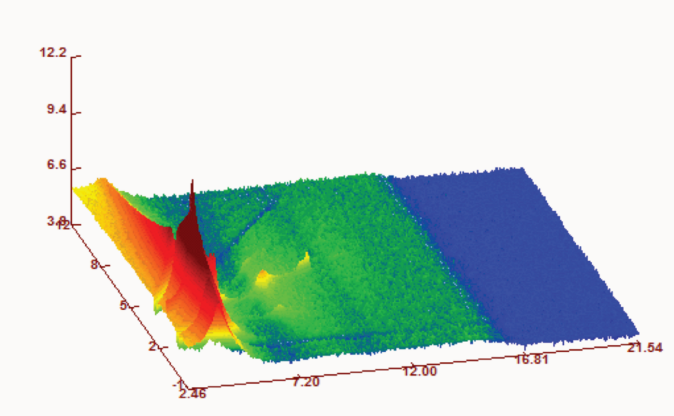

Figure 6.5 : 3D image recorded for d-phospholipid multilayers from *P. pastoris* at 98%RH where ω, 2θ and the intensity are reported on the y,x,z axes, respectively.

Indeed, a more complex pattern of Bragg peaks was observed as Bragg peaks appeared in the direction perpendicular to the surface (along 2θ) as well as in the parallel (along ω) one. This suggests the presence of an in-plane structure together with the lamellar organization of the d-phospholipids. The analysis of the diffraction data thus involved evaluation of the d-spacing along both the perpendicular and parallel direction presented in figure 6.6.

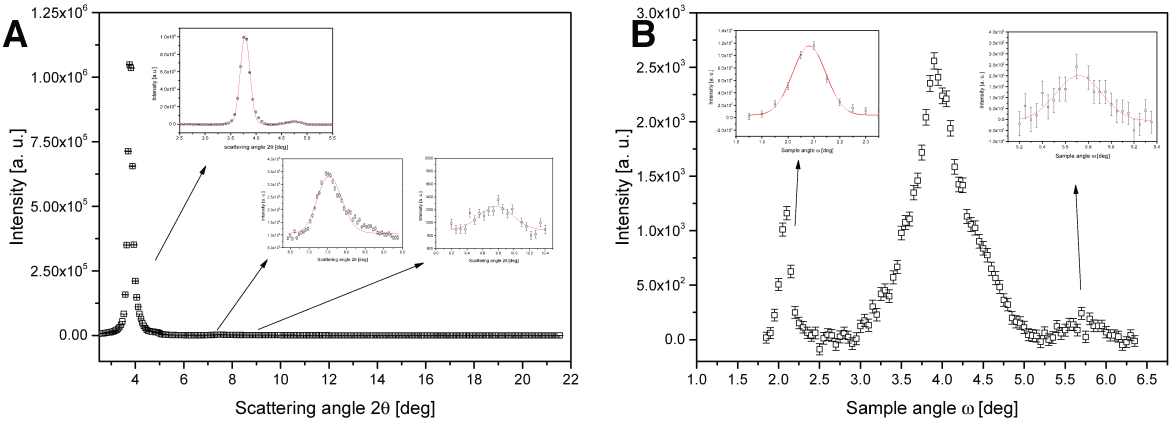

Figure 6.6 : Intensity vs 2θ plot **(A)** and intensity vs **ω** plot **(B)** of the d-phospholipid multilayer from *P. pastoris* at 98% RH. The inserts illustrate the fits of the Bragg peaks.

In the intensity vs 2θ plot, two different sets of diffraction peaks were observed, suggesting that two different lamellar phases coexist within the d-phospholipid multilayer. The calculated d-spacings, 51 ± 1 Å and 68 ± 0.5 Å respectively, indicates that one of the lamellar phases is similar to the one observed at 60% RH, while the other is the product of a rearrangement of some of the phospholipids as the humidity was increased to 98% RH. The lamellar phase with the smaller d-spacing 51 ± 1 Å, also exhibited Bragg peaks in the ω direction, from which a characteristic in-plane distance of 74.8 ± 0.8 Å was calculated.

6.3. Total lipid extracts multilayers from *P. pastoris*

6.3.1. Hydrogenous total lipid extract multilayers

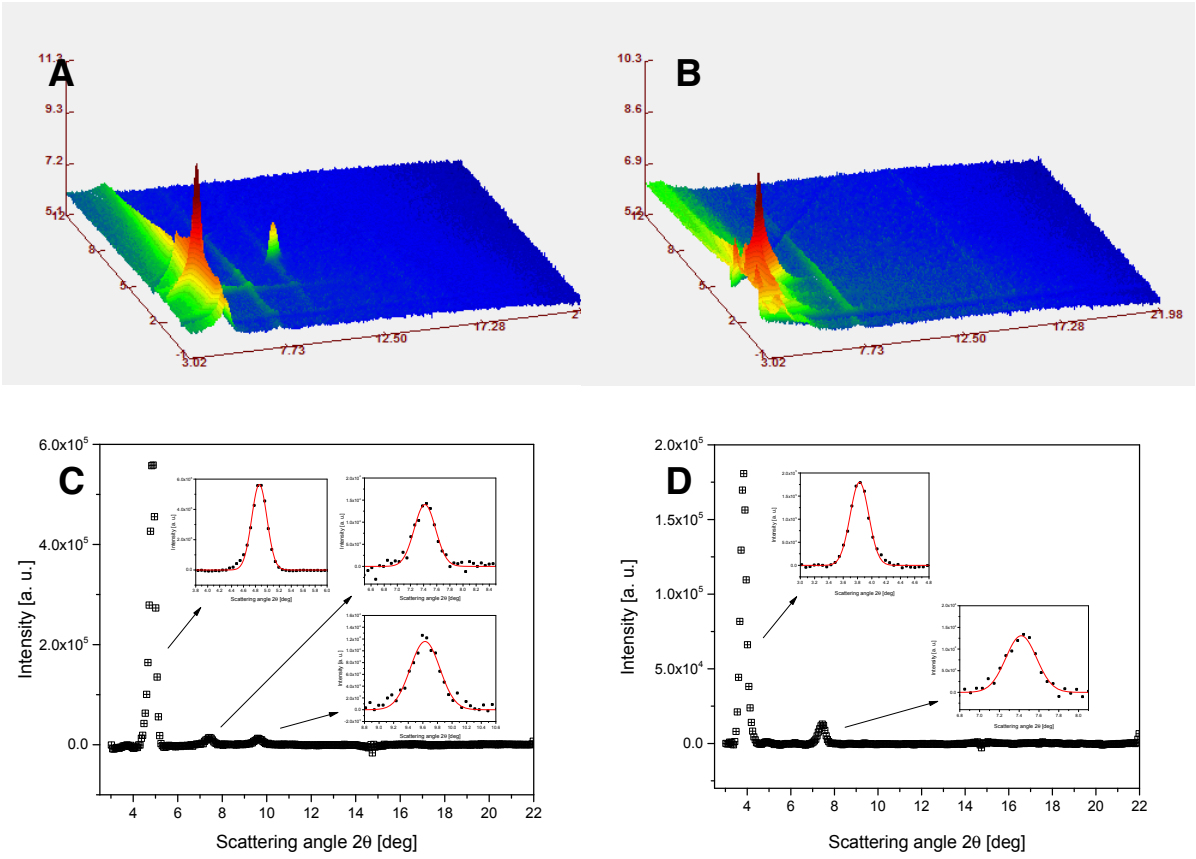

Figure 6.7 : 3D image recorded for h-total lipid extract from *P. pastoris* at 67%RH **(A)** and the corresponding Intensity vs 2θ plot **(C)**. 3D image recorded for h-total lipid extract at 98%RH **(B)** and the corresponding Intensity vs 2θ plot **(D)**. For 3D images, ω, 2θ and the intensity are reported on the y,x,z axes, respectively. Concerning Intensity vs 2θ plots, the inserts illustrate the fits of the Bragg peaks.

The data of the hydrogenous total extracts from *P. pastoris* were collected and the 3D images recorded at 67 and 98% RH (D_2O) together with the corresponding intensity vs $2\boldsymbol{\theta}$ plots obtained are reported in figure 6.7. At 67% RH, the multilayer exhibited a single lamellar phase, with a calculated d-spacing of 54.2 ± 0.4 Å. The increasing humidity had as consequence to make the second Bragg peak disappear whereas one diffuse peak spread over $\boldsymbol{\omega}$ remained unchanged at $2\boldsymbol{\theta}$ = 7.45°. Such diffuse peak probably corresponds to non orientated crystalline ergosterol, shown to be co-extracted with other lipids in the total extracts and earlier quantified (see table 4.5) and often observed for cholesterol in diffraction experiments [201-203]. The structural information lost with the increase in relative humidity as shown in figure 6.8, displaying the Intensity vs $2\boldsymbol{\theta}$ plots depending on RH, from 67% RH (30/22.7) to 98% RH, (30/29.11). The values in parenthesis (T_1/T_2) correspond to the controlled temperatures values of the sample T_1 and of the water reservoir T_2 of the D16 humidity chamber and related to the RH via equation **(48)**. The peak attributed to the sterol crystalline phase is very stable over the range of humidity measured (peak at $2\boldsymbol{\theta}$ = 7.45°).

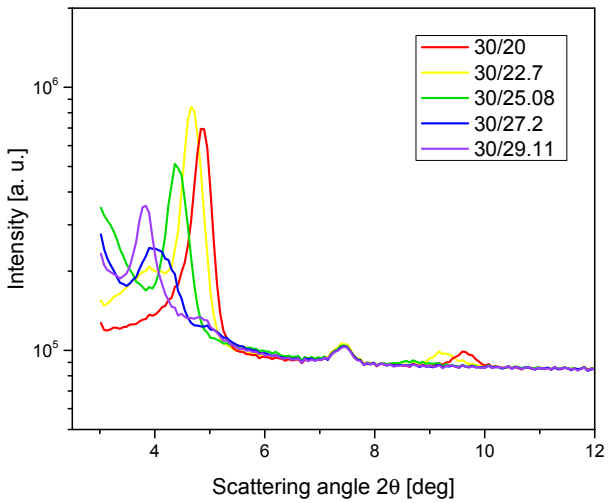

Figure 6.8 : Intensity vs $2\boldsymbol{\theta}$ plot of h-total lipid extract multilayer from *P. pastoris* at various RH, from 55% RH (30/20) to 98% RH (30/29.11). The values in parenthesis (T_1/T_2) correspond to the controlled temperatures values of the sample T_1 and of the water reservoir T_2 of the D16 humidity chamber to define RH.

6.3.2. Deuterated total lipid extract multilayers

As opposed to the results obtained with the hydrogenous total extracts, the multilayers formed with the deuterated total extract lipids were characterized by the absence of a diffuse ergosterol peak and the second Bragg peak, was still present, even though at lower intensity, after increasing of the relative humidity. Figure 6.9 shows the 3D images and the corresponding intensity vs 2θ plots at 67 and 98% RH of the d-total lipid extract multilayers measured with surrounding vapor of H_2O for better contrast.

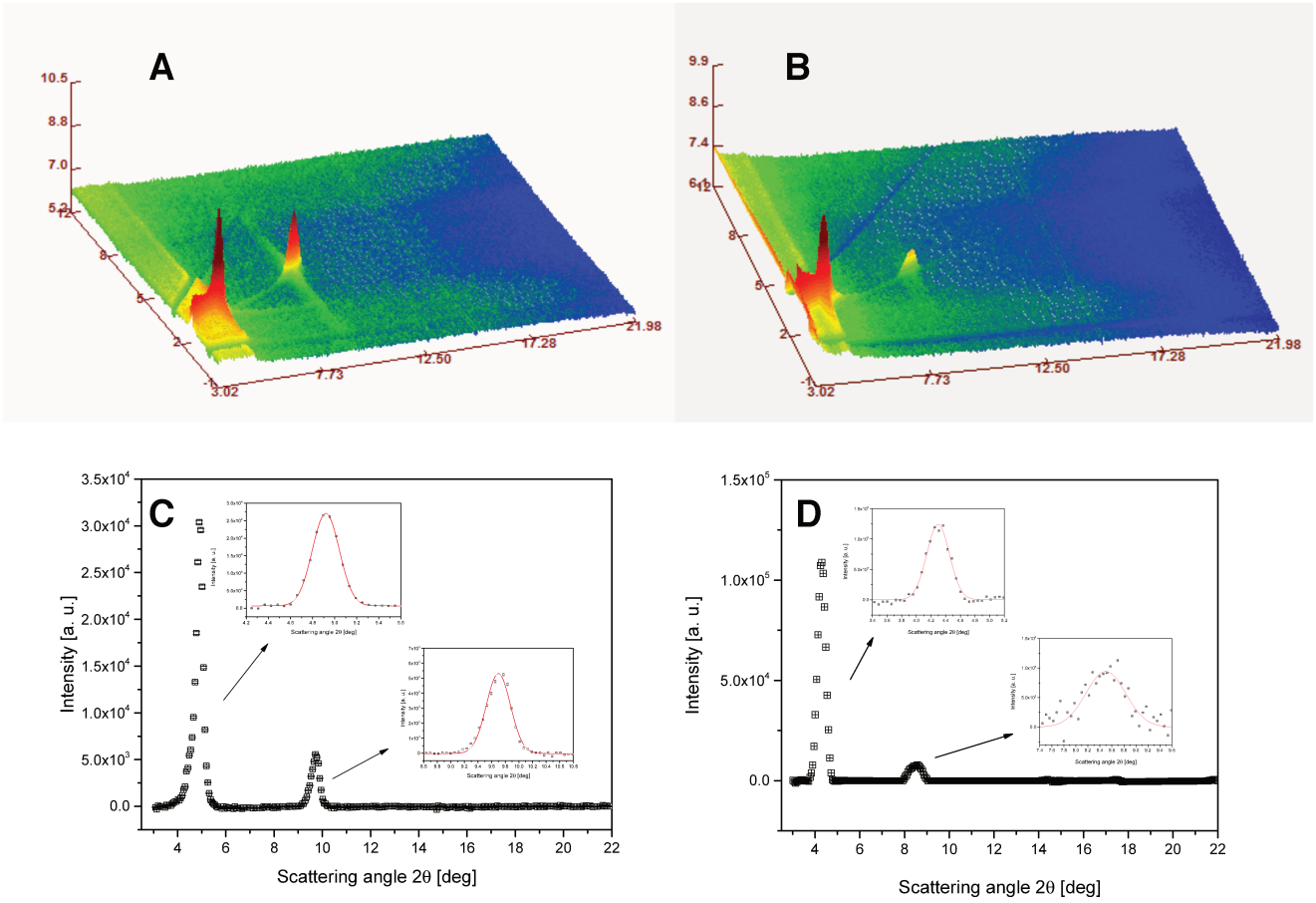

Figure 6.9 : 3D image recorded for d-total lipid extract from *P. pastoris* at 67%RH **(A)** and the corresponding Intensity vs 2θ plot **(C)**. 3D image recorded for d-total lipid extract at 98%RH **(B)** and the corresponding Intensity vs 2θ plot **(D)**. For 3D images, ω, 2θ and the intensity are reported on the y,x,z axes, respectively. Concerning Intensity vs 2θ plots, the inserts illustrate the fits of the Bragg peaks.

Indeed, data collected for the d-total extract multilayer at 67% RH (figure 6.9 A and C) shows two Bragg peaks produced by the lamellar organization of the deuterated lipids. The position of the peaks can be quantitatively evaluated in the Intensity vs 2θ plot, as described before, and the characteristic d-spacing was calculated to be 56.8 ± 0.4 Å, higher than the value obtained with the hydrogenous total extract. The dependence of the multilayer structure on humidity was also investigated by collecting data RH values in the range 40%-98%. The diffraction patterns were all characterized by the presence of two Bragg peaks and the d-spacing value increased with RH, from 54.5 ± 0.5 Å to 62 ± 0.1 Å between 55 and 98% RH as shown in figure 6.10.

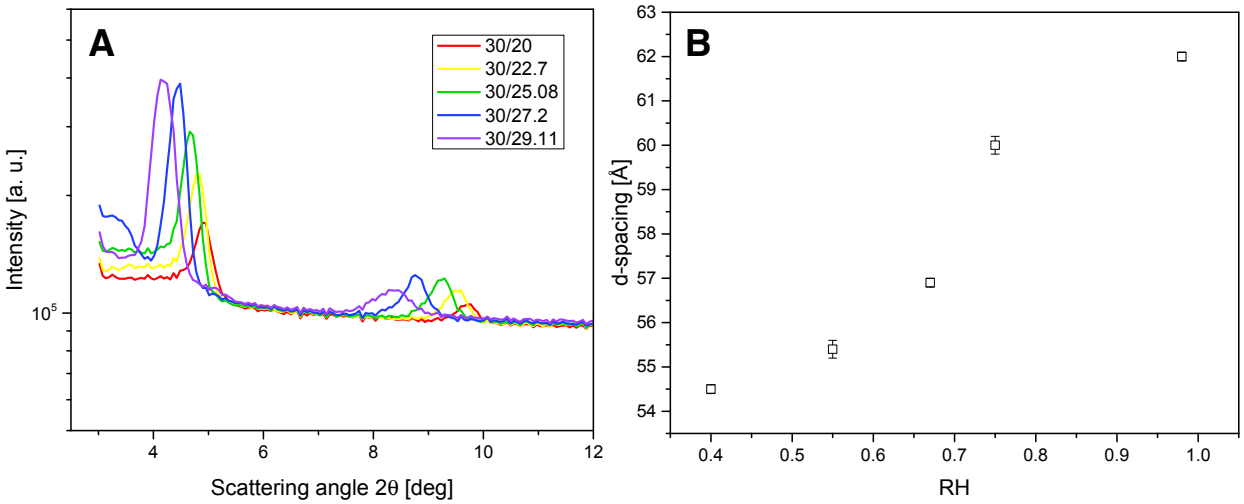

Figure 6.10 : Intensity vs 2θ plot for d-total extract from *P. pastoris* at different RH **(A)** and d-spacing calculated from the diffraction data referring to the d-total extract as function of the applied relative humidity (RH) **(B)**. See figure 6.8 for the values in parenthesis.

The multilayer systems prepared with lipids extracted from yeast were successfully deposited with the rock'n'roll technique even if it would be desirable to obtain more ordered multilayers leading to a higher number of observed Bragg peaks. The presence of a diffuse peak due to isotropic crystalline ergosterol in the hydrogenous total extract multilayer also needs to be further investigated. It was also shown that the deuterated cholesterol produced by the Deuteration laboratory at ILL could be used for biophysical studies as it appeared to give similar results to the hydrogenous one.

The structural parameters obtained from the preliminary neutron diffraction experiments are summarized in table 6.2.

Samples	d [Å] at 60% RH	d [Å] at 98% RH
POPC	50.9 ± 0.1	51.2 ± 0.1
POPC hChol (57 mol%)	49.7 ± 0.1	55.1 ± 0.1
POPC dChol (54.3 mol%)	51.4 ± 0.1	55.3 ± 0.5
hPolar	47.4 ± 0.5	56.1 ± 0.8
dPolar	53.4 ± 0.5	68.5 ± 0.5
h-total extract	54.2 ± 0.4*	-
d-total extract	56.8 ± 0.4*	62.0 ± 0.1
d-total extract (d_{II} [Å])	-	74.8 ± 0.8

Table 6.2 : Values of d-spacing (d) and the relative error (δd) calculated from the analysis of the Intensity vs 2θ plots and of d-spacing (d_{II}) and the relative error (δd_{II}) calculated from the analysis of the Intensity vs ω plots collected for all the investigated lipid systems. *Data corresponding to the total extracts refers to 67%RH

6.4 Discussion

We have characterized natural lipid multilayers composed of the hydrogenous and deuterated total extract or of the corresponding phospholipids. Those samples were compared with the synthetic lipid multilayer POPC and the newly available deuterated cholesterol (d_{46}) was compared to the hydrogenous one in POPC multilayers (POPC hChol and POPC dChol, respectively) to check for deuterium isotope effects. Neutron diffraction data were collected at different humidity conditions, specifically 60% RH and 98% RH. All the investigated samples exhibited a single lamellar phase at 60% RH, although with different d-spacing as reported in table 6.2. Upon increasing the humidity at 98% RH (around 12h equilibration time) different results were observed. In most of the analyzed samples the high humidity produced an increase in the lamellar d-spacing, however, the case of the deuterated phospholipid multilayer is particularly interesting. In this specific case, different sets of Bragg peaks were observed in both the

perpendicular and parallel direction with respect to the surface. It has already been shown that complex lipid mixtures, as d-phospholipids, can produce coexistence of different lamellar phases [204-205]. These lamellar phases can be detected by the presence of Bragg peaks belonging to different sets, i.e. different Δq spacing. If at least two diffraction orders are measured per each set, the nature of different phases as well as their relative d-spacing can be validated based on q and intensities. In the case of the d-phospholipid multilayer, we have observed the presence of Bragg peaks at $2\boldsymbol{\theta}$ 3.7 and 7.5, as well as at $2\boldsymbol{\theta}$ 4.7 and 9.5, which correspond to the expected positions for a first and a second order peak of two different lamellar phases. The structure proposed for the d-phospholipid multilayer involves the organization of the phospholipid species in two different lamellar phases which exhibit an in-plane periodicity of 74.8 ± 0.8 Å, as calculated from the diffraction peaks in the direction parallel to the lamellar surface.

On the other hand, the h-phospholipid extract exhibited a homogenous organization in a single lamellar phase at both the investigated RH. Already at 60% RH, the d-phospholipids exhibited a larger d-spacing with respect to the h-phospholipids; the difference in the calculated d-spacing values is of 2.6 ± 0.6 Å. The different organization of d- and h-natural phospholipids was even more evident at 98% RH. The difference between the h- and d-phospholipid multilayers can be justified by recalling the different chemical composition of the two samples. The fatty acid compositions correspond to the figure 4.5 and the class distribution was as referenced in previous work [50]. The two extracts are both predominantly composed by C_{18} acyl chains with 0-3 double bonds and have a high content of PC and PE polar headgroups. The d-phospholipid extract contains a higher fraction of mono-unsaturated 18:1 carbon-atom chains (60% vs 36% in the h-extract) as well as a higher amount of lipids with phosphoinositol (PI) headgroups (15% vs 11% in the h-extract). In particular, mixtures of saturated and unsaturated phospholipids are known to form separated lamellar phases when mixed together [206-208] as a result of the positive interaction between the hydrocarbon chains which brings closely packed lipids with similar tail structure [209]. Hence the higher content of $C_{18:1}$ chains in the d-phospholipid extract can drive the organization of the multilayer in different lamellar phases.

Surprisingly this difference is not observed anymore in h- and d-total lipid extract multilayers detailed in this work. The synthetic lipid multilayers exhibited more ordered organization with respect to the natural lipids; this resulted in a higher number of Bragg reflections. We observed that while the POPC multilayer was unaffected by the increase in humidity [210], both POPC hChol and POPC dChol mixtures presented an average increase of the d-spacing of 4.6 ± 0.6 Å as the humidity was increased to 98% RH. Interestingly, similar values of the d-spacing were observed for both deuterated and hydrogenous cholesterol suggesting no effects from the deuteration of the sterol at least at the explored 70/30 w/w ratio.

As for NR, future diffraction experiments will aim at separating different lipid species from yeast cells. This will tell us if the structural differences observed in the h- and d-phospholipid bilayers are actually driven by the presence of molecular species at different percentages (e. g. unsaturated C_{18} chains and PI headgroups) or if it is related to isotope effects only.

7. CONCLUSION

The present work recounts a multidisciplinary project aiming to develop relevant model membranes designed for neutron scattering techniques, sourced from yeast biomass. This involved the deuteration of different yeasts, performed to access a large variety of perdeuterated lipid molecules that are non-commercially available. The limitations for the production of specific deuterated lipid molecules from biomass reside in the relatively limited knowledge of the mechanisms that govern the changes observed in the lipid composition upon deuteration. In addition, the production of polyunsaturated phospholipids seems to be challenged by the isotopic effects that result from deuteration of the growth medium.

The composition of the obtained lipid mixtures was analyzed in order to gain an understanding of the effects of deuteration on the lipidome of the yeasts. Further purification and pre-characterization were performed on the phospholipid extracts in order to form either a single lipid bilayer deposited on a solid surface and probed with neutron reflectometry, or a stack of multilayers, investigated via neutron diffraction. The different models designed from yeast extracts were compared to synthetically prepared hydrogenous and perdeuterated (d_{82}) POPC membranes. The polyunsaturation degree was shown to decrease the thickness of the hydrophobic chains while the lateral condensing effect of cholesterol was superior to the condensing effect of ergosterol in all the investigated fluid membranes, containing the same proportions of sterol. The single lipid bilayers were further placed in contact with AmB to investigate its fungicidal mechanism as well as a possible mechanism responsible of its toxic side effect on mammalian cells, modeled by cholesterol-containing membranes. The differences observed, depending on the lipid models employed, demonstrate the importance of developing new model membranes with a complex composition mimicking cell

membranes, relevant to investigating biochemical processes in cells. It also highlighted differences between ergosterol and cholesterol-containing bilayers, while pointing in the direction of some sterol intermediates that could help to understand additional aspects of the AmB mechanism. The use of the newly available perdeuterated cholesterol as well as the search for a multilayer deposition protocol was also detailed.

The advantages of the systems developed are their complex compositions and their relevance for interaction studies mimicking natural systems. But theses advantages also represent a drawback as the system is rendered more difficult to handle and the structures more difficult to characterize in detail. With further investigations and more precisely controlled deposition parameters, the system will be able to help solving new questions in the field of lipid and membrane science due to the versatility of the models. With access to larger quantities of the deuterated lipid species not commercially available, and by developing chromatographic purification routes, it could also profit to other communities, for NMR and IR experiments for example. Theoretically, the production of all the molecular species the different yeasts can offer is possible. And an access to the largest lipid collections, both hydrogenous and deuterated, in sufficient quantities, will enable, when the neutron beam intensities will be enhanced in the near future, to screen and investigate more complex lipid bilayers or multilayers on a time scale still not accessible today. Thus, efforts should continue towards this direction, with the production and the characterization of the largest possible number of lipid systems.

BIBLIOGRAPHY

[1] Wickner, W., & Rizo, J. (2017). A cascade of multiple proteins and lipids catalyzes membrane fusion. Molecular Biology of the Cell, 28(6), 707–711. http://doi.org/10.1091/mbc.E16-07-0517

[2] Genheden, S., Essex, J. W., & Lee, A. G. (2017). G protein coupled receptor interactions with cholesterol deep in the membrane. BBA - Biomembranes, 1859(2), 268–281. http://doi.org/10.1016/j.bbamem.2016.12.001

[3] Chierico, L., Joseph, A. S., Lewis, A. L., & Battaglia, G. (2014). Live cell imaging of membrane / cytoskeleton interactions and membrane topology. Scientific Reports, 4(1), 82–10. http://doi.org/10.1038/srep06056

[4] Nel, A. E., Mädler, L., Velegol, D., Xia, T., Hoek, E. M. V., Somasundaran, P., et al. (2009). Understanding biophysicochemical interactions at the nano–bio interface. Nature Publishing Group, 8(7), 543–557. http://doi.org/10.1038/nmat2442

[5] Anderson, T. M., Clay, M. C., Cioffi, A. G., Diaz, K. A., Hisao, G. S., Tuttle, M. D., et al. (2014). Amphotericin forms an extramembranous and fungicidal sterol sponge. Nature Chemical Biology, 10(5), 400–406. http://doi.org/10.1038/nchembio.1496

[6] Hooke, R. (1665). Micrographia, or, Some physiological descriptions of minute bodies made by magnifying glasses: With observations and inquiries thereupon. London: Printed by J. Martyn and J. Allestry.

[7] Overton, E. (1895) Ueber die osmotischen Eigenschaften der lebenden Pflanzen- und Tierzelle.

[8] Gorter, E., & Grendel, F. (1925). On bimolecular layers of lipoids on the chromocytes of the blood. The Journal of Experimental Medicine, 41(4), 439–443.

[9] Singer, S. J., & Nicolson, G. L. (1972). The Fluid Mosaic Model of the Structure of Cell Membranes. Science, 175(4023), 720–731. http://doi.org/10.1126/science.175.4023.720

[10] OpenStax, Concepts of Biology. OpenStax CNX. 6 févr. 2017 http://cnx.org/contents/b3c1e1d2-839c-42b0-a314-e119a8aafbdd@9.21.

[11] Gerelli, Y., Porcar, L., Lombardi, L., & Fragneto, G. (2013). Lipid Exchange and Flip-Flop in Solid Supported Bilayers. Langmuir, 29(41), 12762–12769. http://doi.org/10.1021/la402708u

[12] Engelman, D. M. (2005). Membranes are more mosaic than fluid. Nature, 438(7068), 578–580. http://doi.org/10.1038/nature04394

[13] Goñi, F. M. (2014). The basic structure and dynamics of cell membranes: An update of the Singer–Nicolson model. BBA - Biomembranes, 1838(6), 1467–1476. http://doi.org/10.1016/j.bbamem.2014.01.006

[14] Crowder, C. M. (2001). Enantiospecificity of Cholesterol Function in Vivo. Journal of Biological Chemistry, 276(48), 44369–44372. http://doi.org/10.1074/jbc.C100535200

[15] Perozo, E., Kloda, A., Cortes, D. M., & Martinac, B. (2002). Physical principles underlying the transduction of bilayer deformation forces during mechanosensitive channel gating. Nature Structural Biology, 9(9), 696–703. http://doi.org/10.1038/nsb827

[16] de Ghellinck, A., Fragneto, G., Laux, V., Haertlein, M., Jouhet, J., Sferrazza, M., & Wacklin, H. (2015). Lipid polyunsaturation determines the extent of membrane structural changes induced by Amphotericin B in Pichia pastoris yeast. BBA - Biomembranes, 1848(PA), 2317–2325. http://doi.org/10.1016/j.bbamem.2015.06.006

[17] Chan, D. I., & Vogel, H. J. (2010). Current understanding of fatty acid biosynthesis and the acyl carrier protein. Biochemical Journal, 430(1), 1–19. http://doi.org/10.1042/BJ20100462

[18] Denning, E. J., & Beckstein, O. (2013). Influence of lipids on protein-mediated transmembrane transport. Chemistry and Physics of Lipids, 169, 57–71. http://doi.org/10.1016/j.chemphyslip.2013.02.007

[19] Bloch, K. (1965). The Biological Synthesis of Cholesterol. Science, 150(3692), 19–28. http://doi.org/10.1126/science.150.3692.19

[20] McLean, K. J., Hans, M., & Munro, A. W. (2012). Cholesterol, an essential molecule: diverse roles involving cytochrome P450 enzymes. Biochemical Society Transactions, 40(3), 587–593. http://doi.org/10.1042/BST20120077

[21] Ourisson, G., & Nakatani, Y. (1994). The terpenoid theory of the origin of cellular life: the evolution of terpenoids to cholesterol. Chemistry & Biology, 1(1), 11–23. http://doi.org/10.1016/1074-5521(94)90036-1

[22] Galea, A. M., & Brown, A. J. (2009). Special relationship between sterols and oxygen: Were sterols an adaptation to aerobic life? Free Radical Biology and Medicine, 47(6), 880–889. http://doi.org/10.1016/j.freeradbiomed.2009.06.027

[23] Deamer, D. (2017). The Role of Lipid Membranes in Life's Origin. Life, 7(1), 5–17. http://doi.org/10.3390/life7010005

[24] Simons, K., & Ikonen, E. (1997). Functional rafts in cell membranes, 387(6633), 569–572. http://doi.org/10.1038/42408

[25] Róg, T., Pasenkiewicz-Gierula, M., Vattulainen, I., & Karttunen, M. (2009). Ordering effects of cholesterol and its analogues. BBA - Biomembranes, 1788(1), 97–121. http://doi.org/10.1016/j.bbamem.2008.08.022

[26] Levental, I., & Veatch, S. L. (2016). The Continuing Mystery of Lipid Rafts. Journal of Molecular Biology, 428(Part A), 4749–4764. http://doi.org/10.1016/j.jmb.2016.08.022

[27] van Meer, G., Voelker, D. R., & Feigenson, G. W. (2008). Membrane lipids: where they are and how they behave. Nature Reviews Molecular Cell Biology, 9(2), 112–124. http://doi.org/10.1038/nrm2330

[28] Stefaniu, C., & Brezesinski, G. (2014). X-ray investigation of monolayers formed at the soft air/water interface. Current Opinion in Colloid & Interface Science, 19(3), 216–227. http://doi.org/10.1016/j.cocis.2014.01.004

[29] Als-Nielsen, J., Jacquemain, D., Kjaer, K., Leveiller, F., Lahav, M., & Leiserowitz, L. (1994). Principles and applications of grazing incidence X-ray and neutron scattering from ordered molecular monolayers at the air-water interface. Physics Reports, 246(5), 251–313. http://doi.org/10.1016/0370-1573(94)90046-9

[30] Pérez-Morales, M., Pedrosa, J. M., Muñoz, E., Martín-Romero, M. T., Möbius, D., & Camacho, L. (2005). Ellipsometric study of a phospholipid monolayer at the air–water interface in presence of large organic counter ions. Thin Solid Films, 488(1-2), 247–253. http://doi.org/10.1016/j.tsf.2005.04.080

[31] Wu, F., Gericke, A., Flach, C. R., Mealy, T. R., Seaton, B. A., & Mendelsohn, R. (1998). Domain Structure and Molecular Conformation in Annexin V/1,2-Dimyristoyl-sn-Glycero-3-Phosphate/Ca2+ Aqueous Monolayers: A Brewster Angle Microscopy/Infrared Reflection-Absorption Spectroscopy Study. Biophysical Journal, 74(6), 3273–3281. http://doi.org/10.1016/S0006-3495(98)78034-8

[32] Stottrup, B. L., & Keller, S. L. (2006). Phase Behavior of Lipid Monolayers Containing DPPC and Cholesterol Analogs. Biophysical Journal, 90(9), 3176–3183. http://doi.org/10.1529/biophysj.105.072959

[33] Papahadjopoulos, D., Jacobson, K., Nir, S., & Isac, I. (1973). Phase transitions in phospholipid vesicles Fluorescence polarization and permeability measurements concerning the effect of temperature and cholesterol. Journal of Bacteriology, 311(3), 330–348. http://doi.org/10.1016/0005-2736(73)90314-3

[34] Tanaka, T., & Yamazaki, M. (2004). Membrane Fusion of Giant Unilamellar Vesicles of Neutral Phospholipid Membranes Induced by La 3. Langmuir, 20(13), 5160–5164. http://doi.org/10.1021/la049681s

[35] Bernard, A. L., Guedeau-Boudeville, M. A., Jullien, L., & di Meglio, J. M. (2000). Strong Adhesion of Giant Vesicles on Surfaces: Dynamics and Permeability. Langmuir, 16(17), 6809–6820. http://doi.org/10.1021/la991341x

[36] Sackmann, E. (1996). Supported Membranes: Scientific and Practical Applications. Science, 271(5245), 43–48. http://doi.org/10.1126/science.271.5245.43

[37] Wacklin, H. P. (2010). Neutron reflection from supported lipid membranes. Current Opinion in Colloid & Interface Science, 15(6), 445–454. http://doi.org/10.1016/j.cocis.2010.05.008

[38] Montis, C., Gerelli, Y., Fragneto, G., Nylander, T., Baglioni, P., & Berti, D. (2015). Nucleolipid bilayers: A quartz crystal microbalance and neutron reflectometry study, 1–11. http://doi.org/10.1016/j.colsurfb.2015.07.039

[39] Alessandrini, A., & Facci, P. (2014). Phase transitions in supported lipid bilayers studied by AFM. Soft Matter, 10, 7145–7164. http://doi.org/10.1039/C4SM01104J

[40] West, J. D., Zhu, Y., Saem, S., Moran-Mirabal, J., & Hitchcock, A. P. (2017). X-ray Absorption Spectroscopy and Spectromicroscopy of Supported Lipid Bilayers. The Journal of Physical Chemistry B, 121(17), 4492–4501. http://doi.org/10.1021/acs.jpcb.7b02646

[41] Tamm, L. K., & McConnell, H. M. (1985). Supported phospholipid bilayers. Biophysical Journal, 47(1), 105–113. http://doi.org/10.1016/S0006-3495(85)83882-0

[42] Vacklin, H. P., Tiberg, F., & Thomas, R. K. (2005). Formation of supported phospholipid bilayers via co-adsorption with β-d-dodecyl maltoside. Journal of Bacteriology, 1668(1), 17–24. http://doi.org/10.1016/j.bbamem.2004.11.001

[43] Richter, R. P., Bérat, R., & Brisson, A. R. (2006). Formation of Solid-Supported Lipid Bilayers: An Integrated View. Langmuir, 22(8), 3497–3505. http://doi.org/10.1021/la052687c

[44] Maccarini, M., Watkins, E. B., Stidder, B., Alcaraz, J.-P., Cornell, B. A., & Martin, D. K. (2016). Nanostructural determination of a lipid bilayer tethered to a gold substrate. The European Physical Journal E, 39(12), 580–8. http://doi.org/10.1140/epje/i2016-16123-5

[45] Junghans, A., Watkins, E. B., Majewski, J., Miranker, A., & Stroe, I. (2016). Influence of the Human and Rat Islet Amyloid Polypeptides on Structure of Phospholipid Bilayers: Neutron Reflectometry and Fluorescence Microscopy Studies. Langmuir, 32(17), 4382–4391. http://doi.org/10.1021/acs.langmuir.6b00825

[46] Luchini, A., Gerelli, Y., Fragneto, G., Nylander, T., Pálsson, G. K., Appavou, M.-S., & Paduano, L. (2017). Neutron Reflectometry reveals the interaction between functionalized SPIONs and the surface of lipid bilayers. Colloids and Surfaces B: Biointerfaces, 151, 76–87. http://doi.org/10.1016/j.colsurfb.2016.12.005

[47] Foglia, F., Lawrence, M. J., Demeė, B., Fragneto, G., & Barlow, D. (2012). Neutron diffraction studies of the interaction between amphotericin B and lipid-sterol model membranes. Scientific Reports, 2, 1–6. http://doi.org/10.1038/srep00778

[48] Foglia, F., Fragneto, G., Clifton, L. A., Lawrence, M. J., & Barlow, D. J. (2014). Interaction of Amphotericin B with Lipid Monolayers. Langmuir, 30(30), 9147–9156. http://doi.org/10.1021/la501835p

[49] Yepuri, N. R., Darwish, T. A., Krause-Heuer, A. M., Leung, A. E., Delhom, R., Wacklin, H. P., & Holden, P. J. (2016). Synthesis of Perdeuterated 1-Palmitoyl-2-oleoyl- sn-glycero-3-phosphocholine ([D 82]POPC) and Characterisation of Its Lipid Bilayer Membrane Structure by Neutron Reflectometry. ChemPlusChem, 81(3), 315–321. http://doi.org/10.1002/cplu.201500452

[50] de Ghellinck, A., Schaller, H., Laux, V., Haertlein, M., Sferrazza, M., Maréchal, E., et al. (2014). Production and Analysis of Perdeuterated Lipids from Pichia pastoris Cells. PLoS ONE, 9(4), e92999–9. http://doi.org/10.1371/journal.pone.0092999

[51] Richards, O. W. (1934). The Effect of Deuterium on the Growth of Yeast. Journal of Bacteriology, 28(3), 289–294.

[52] Mosin, O., & Ignatov, I. (2014). Phenomenon of Biological Adaptation to Heavy Water. Journal of Health, Medicine and Nursing, 6(0), 73–110–39.

[53] Paz Ramos, A., & Lafleur, M. (2015). Chain Length of Free Fatty Acids Influences the Phase Behavior of Stratum Corneum Model Membranes. Langmuir, 31(42), 11621–11629. http://doi.org/10.1021/acs.langmuir.5b03271

[54] Berbée, J. F. P., Mol, I. M., Milne, G. L., Pollock, E., Hoeke, G., Lütjohann, D., et al. (2017). Deuterium-reinforced polyunsaturated fatty acids protect against atherosclerosis by lowering lipid peroxidation and hypercholesterolemia. Atherosclerosis, 1–8. http://doi.org/10.1016/j.atherosclerosis.2017.06.916

[55] Guard-Friar, D., Chen, C. H., & Engle, A. S. (1985). Deuterium isotope effect on the stability of molecules: phospholipids. The Journal of Physical Chemistry, 89, 1810-1813.

[56] Madrid, E., & Horswell, S. L. (2015). Effect of Deuteration on Phase Behavior of Supported Phospholipid Bilayers: A Spectroelectrochemical Study. Langmuir, 31(45), 12544–12551. http://doi.org/10.1021/acs.langmuir.5b02765

[57] Matsuki, H., Okuno, H., Sakano, F., Kusube, M., & Kaneshina, S. (2005). Effect of deuterium oxide on the thermodynamic quantities associated with phase transitions of phosphatidylcholine bilayer membranes. Journal of Bacteriology, 1712(1), 92–100. http://doi.org/10.1016/j.bbamem.2005.03.005

[58] Alba-Lois, L. & Segal-Kischinevzky, C. (2010) Beer & Wine Makers. Nature Education 3(9): 17

[59] Mattanovich, D., Sauer, M., & Gasser, B. (2014). Yeast biotechnology: teaching the old dog new tricks. Microbial Cell Factories, 13(1), 1–5. http://doi.org/10.1186/1475-2859-13-34

[60] Papanikolaou, S., Rontou, M., Belka, A., Athenaki, M., Gardeli, C., Mallouchos, A., et al. (2016). Conversion of biodiesel-derived glycerol into biotechnological products of industrial significance by yeast and fungal strains. Engineering in Life Sciences, 17(3), 262–281. http://doi.org/10.1002/elsc.201500191

[61] Lind, T. K., Wacklin, H., Schiller, J., Moulin, M., Haertlein, M., Pomorski, T. G., & Cárdenas, M. (2015). Formation and Characterization of Supported Lipid Bilayers Composed of Hydrogenated and Deuterated Escherichia coli Lipids. PLoS ONE, 10(12), e0144671–16. http://doi.org/10.1371/journal.pone.0144671

[62] Brown, G. D., Denning, D. W., & Levitz, S. M. (2012). Tackling Human Fungal Infections. Science, 336(6082), 647–647. http://doi.org/10.1126/science.1222236

[63] Fidel, P. L., Vazquez, J. A., & Sobel, J. D. (1999). Candida glabrata: Review of Epidemiology, Pathogenesis, and Clinical Disease with Comparison to C. albicans. Clinical Microbiology Reviews, 12(1), 80–96.

[64] Geber, A., Hitchcock, C. A., Swartz, J. E., Pullen, F. S., Marsden, K. E., Kwon-Chung, K. J., & Bennett, J. E. (1995). Deletion of the Candida glabrata ERG3 and ERG11 genes: effect on cell viability, cell growth, sterol composition, and antifungal susceptibility. Antimicrobial Agents and Chemotherapy, 39(12), 2708–2717. http://doi.org/10.1128/AAC.39.12.2708

[65] Khadija Mohamed Ahmad, Genome dynamics and virulence in the human pathogen Candida glabrata; Doctoral thesis 2014, Lund University (ISBN978-91-7473-865-0). https://lup.lub.lu.se/search/publication/4331909

[66] Ishchuk OP, Ahmad KM, Koruza K, Bojanovič K, Kasper L, Brunke S, Hube B, Säll T, Hellmark T, Gullstrand B, Brion C, Freel K, Schacherer J, Regenberg B, Knecht W, Piškur J. RNAi as a tool to study virulence genes in the yeast *Candida glabrata*. *Manuscript in preparation*.

[67] Caffrey, P., Lynch, S., Flood, E., Finnan, S., & Oliynyk, M. (2001). Amphotericin biosynthesis in Streptomyces nodosus: deductions from analysis of polyketide synthase and late genes. Chemistry & Biology, 8(7), 713–723. http://doi.org/10.1016/S1074-5521(01)00046-1

[68] Mesa-Arango, A. C., Scorzoni, L., & Zaragoza, O. (2012). It only takes one to do many jobs: Amphotericin B as antifungal and immunomodulatory drug. Frontiers in Microbiology, 3, 1–10. http://doi.org/10.3389/fmicb.2012.00286

[69] Hamill, R.J. (2013) Amphotericin B Formulations: A Comparative Review of Efficacy and Toxicity. Drugs 73: 919. http://doi.org/10.1007/s40265-013-0069-4

[70] Gabrielska, J., Gago, M., Gubernator, J., & Gruszecki, W. A. I. (2006). Binding of antibiotic amphotericin B to lipid membranes: A 1H NMR study. FEBS Letters, 580(11), 2677–2685. http://doi.org/10.1016/j.febslet.2006.04.021

[71] Gray, K. C., Palacios, D. S., Dailey, I., Endo, M. M., Uno, B. E., Wilcock, B. C., & Burke, M. D. (2012). Amphotericin primarily kills yeast by simply binding ergosterol. Proceedings of the National Academy of Sciences, 109(7), 2234–2239. http://doi.org/10.1073/pnas.1117280109

[72] Ciesielski, F., Griffin, D. C., Loraine, J., Rittig, M., Delves-Broughton, J., & Bonev, B. B. (2016). Recognition of Membrane Sterols by Polyene Antifungals Amphotericin B and Natamycin, A 13C MAS NMR Study. Frontiers in Cell and Developmental Biology, 4, 253–12. http://doi.org/10.3389/fcell.2016.00057

[73] Matsumori, N., Tahara, K., Yamamoto, H., Morooka, A., Doi, M., Oishi, T., & Murata, M. (2009). Direct Interaction between Amphotericin B and Ergosterol in Lipid Bilayers As Revealed by 2H NMR Spectroscopy. Journal of the American Chemical Society, 131(33), 11855–11860. http://doi.org/10.1021/ja9033473

[74] Huang, W., Zhang, Z., Han, X., Tang, J., Wang, J., Dong, S., & Wang, E. (2002). Ion Channel Behavior of Amphotericin B in Sterol-Free and Cholesterol- or Ergosterol-Containing Supported Phosphatidylcholine Bilayer Model Membranes Investigated by Electrochemistry and Spectroscopy. Biophysical Journal, 83(6), 3245–3255. http://doi.org/10.1016/S0006-3495(02)75326-5

[75] Venegas, B., n, J. G. L.-D., Celis, H., & Ortega-Blake, I. N. (2003). Amphotericin B Channels in the Bacterial Membrane: Role of Sterol and Temperature. Biophysical Journal, 85(4), 2323–2332. http://doi.org/10.1016/S0006-3495(03)74656-6

[76] Matsuoka, S., & Murata, M. (2003). Membrane permeabilizing activity of amphotericin B is affected by chain length of phosphatidylcholine added as minor constituent. Journal of Bacteriology, 1617(1-2), 109–115. http://doi.org/10.1016/j.bbamem.2003.09.010

[77] Romero, E. A., Valdivieso, E., & Cohen, B. E. (2009). Formation of Two Different Types of Ion Channels by Amphotericin B in Human Erythrocyte Membranes. Journal of Membrane Biology, 230(2), 69–81. http://doi.org/10.1007/s00232-009-9187-z

[78] Gagoś, M., Gabrielska, J., Dalla Serra, M., & Gruszecki, W. I. (2005). Binding of antibiotic amphotericin B to lipid membranes: monomolecular layer technique and linear dichroism-FTIR studies. Molecular Membrane Biology, 22(5), 433–442. http://doi.org/10.1080/09687860500287832

[79] Chudzik, B., Koselski, M., Czuryło, A., Trębacz, K., & Gagoś, M. (2015). A new look at the antibiotic amphotericin B effect on Candida albicans plasma membrane permeability and cell viability functions. European Biophysics Journal, 44(1-2), 77–90. http://doi.org/10.1007/s00249-014-1003-8

[80] Falcón-González, J. M., Jiménez-Domínguez, G., Ortega-Blake, I., & Carrillo-Tripp, M. (2017). Multi-Phase Solvation Model for Biological Membranes: Molecular Action Mechanism

of Amphotericin B. Journal of Chemical Theory and Computation, acs.jctc.7b00337–10. http://doi.org/10.1021/acs.jctc.7b00337

[81] Dufourc, E. J. (2008). Sterols and membrane dynamics. Journal of Chemical Biology, 1(1-4), 63–77. http://doi.org/10.1007/s12154-008-0010-6

[82] De Ghellinck D'Elseghem, A. (2013). Natural and model membranes: structure and interaction with bio-active molecules via neutron reflection (Unpublished doctoral dissertation). Université libre de Bruxelles, Faculté des Sciences – Chimie, Bruxelles.

[83] Sauerbrey G. (1959) Verwendung von Schwingquarzen zur wägung dünner schichten und zur mikrowägung. Z Phys; 155: 206–222.

[84] Nomura, T., & Hattori, O. (1980). Determination of micromolar concentrations of cyanide in solution with a piezoelectric detector. Analytica Chimica Acta, 115, 323–326. http://doi.org/10.1016/S0003-2670(01)93171-X

[85] Rodahl, M., Höök, F., Fredriksson, C., Keller, C. A., Krozer, A., Brzezinski, P., ... & Kasemo, B. (1997). Simultaneous frequency and dissipation factor QCM measurements of biomolecular adsorption and cell adhesion. Faraday Discussions, 107, 229-246.

[86] Voinova, M. V., Jonson, M., & Kasemo, B. (2002). "Missing mass" effect in biosensor's QCM applications. Biosensors and Bioelectronics, 17(10), 835–841. http://doi.org/10.1016/S0956-5663(02)00050-7

[87] Chadwick, J. (1932). Possible existence of a neutron. Nature, 129(3252), 312.

[88] Picture uploaded from http://pd.chem.ucl.ac.uk/pdnn/inst3/neutrons.htm

[89] Ankner, J. F., Heller, W. T., Herwig, K. W., Meilleur, F. and Myles, D. A. (2013). Neutron Scattering Techniques and Applications in Structural Biology. Current Protocols in Protein Science. 72:17.16:17.16.1–17.16.34.

[90] Fragneto-Cusani, G. (2001). Neutron reflectivity at the solid/liquid interface: examples of applications in biophysics. Journal of Physics: Condensed Matter, 13(21), 4973–17. http://doi.org/10.1088/0953-8984/13/21/322

[91] Born, M., Wolf, E., Bhatia, A., Clemmow, P., Gabor, D., Stokes, A., . . . Wilcock, W. (1999). Principles of Optics: Electromagnetic Theory of Propagation, Interference and Diffraction of Light. Cambridge: Cambridge University Press. http://doi.org/10.1017/CBO9781139644181

[92] Wlodawer, A., Walter, J., Huber, R., & Sjölin, L. (1984). Structure of bovine pancreatic trypsin inhibitor. Journal of Molecular Biology, 180(2), 301–329. http://doi.org/10.1016/S0022-2836(84)80006-6

[93] Koynova, R. and Tenchov, B. (2008). Lipids: Phase Transitions. Wiley Encyclopedia of Chemical Biology. 1–15.

[94] Seddon, J. M. (1990). Structure of the inverted hexagonal (HII) phase, and non-lamellar phase transitions of lipids. Biochimica Et Biophysica Acta (BBA)-Reviews on Biomembranes, 1031(1), 1–69.

[95] Moulin, M. Strohmeier, G.A, Hirz, M. Thompson, K. Pichler, H., Forsyth V.T. and M.Haertlein, Perdeuteration of cholesterol for neutron scattering applications using recombinant Pichia pastoris. 2017, submitted.

[96] Dunne, O., Weidenhaupt, M., Callow, P., Martel, A., Moulin, M., Perkins, S. J., et al. (2016). Matchout deuterium labelling of proteins for small–angle neutron scattering studies using prokaryotic and eukaryotic expression systems and high cell–density cultures. European Biophysics Journal, 46(5), 425–432. http://doi.org/10.1007/s00249-016-1186-2

[97] Hirz, M., Richter, G., Leitner, E., Wriessnegger, T., & Pichler, H. (2013). A novel cholesterol-producing Pichia pastoris strain is an ideal host for functional expression of human Na,K-ATPase α3β1 isoform. Applied Microbiology and Biotechnology, 97(21), 9465–9478. http://doi.org/10.1007/s00253-013-5156-7

[98] Shabalina, S. A., & Koonin, E. V. (2008). Origins and evolution of eukaryotic RNA interference. Trends in ecology & evolution, 23(10), 578-587.

[99] Drinnenberg, I. A., Weinberg, D. E., Xie, K. T., Mower, J. P., Wolfe, K. H., Fink, G. R., & Bartel, D. P. (2009). RNAi in Budding Yeast. Science, 326(5952), 544–550. http://doi.org/10.1126/science.1176945

[100] Ahmad, K. M. Doctoral thesis (2014). Genome dynamics and virulence in the human pathogen Candida glabrata. Lund University (ISBN978-91-7473-865-0) https://lup.lub.lu.se/search/publication/4331909

[101] Cormack, B. P., & Falkow, S. (1999). Efficient Homologous and Illegitimate Recombination in the Opportunistic Yeast Pathogen Candida glabrata. Genetics, 151(3), 979–987. http://doi.org/10.1016/0378-1119(88)90185-0

[102] Fidel Jr, P. L., Cutright, J. L., Tait, L., & Sobel, J. D. (1996). A murine model of Candida glabrata vaginitis. Journal of Infectious Diseases, 173(2), 425-431.

[103] Ishchuk, O. P., Ahmad, K. M., Koruza, K., Bojanovič, K., Kasper, L., Brunke, S., Hube, B., Säll, T., Hellmark, T., Gullstrand, B., Brion, C., Freel, K., Schacherer, J., Regenberg, B., Knecht, W., Piškur, J. RNAi as a tool to study virulence genes in the yeast Candida glabrata. *Manuscript in preparation*.

[104] Folch, J., Lees, M., & Sloane-Stanley, G. H. (1957). A simple method for the isolation and purification of total lipids from animal tissues. J Biol Chem.

[105] Singh, A., Prasad, T., Kapoor, K., Mandal, A., Roth, M., Welti, R., & Prasad, R. (2010). Phospholipidome of Candida: Each Species of CandidaHas Distinctive Phospholipid Molecular

Species. OMICS: a Journal of Integrative Biology, 14(6), 665–677. http://doi.org/10.1089/omi.2010.0041

[106] Reis, A., & Spickett, C. M. (2012). Chemistry of phospholipid oxidation. BBA - Biomembranes, 1818(10), 2374–2387. http://doi.org/10.1016/j.bbamem.2012.02.002

[107] Christie, W.W. and Han, X. (2010) Lipid Analysis - Isolation, Separation, Identification and Lipidomic Analysis http://doi.org/10.1533/9780857097866.55

[108] Rondelli, V., Brocca, P., Motta, S., Messa, M., Colombo, L., Salmona, M., et al. (2016). Amyloidβ Peptides in interaction with raft-mime model membranes: a neutron reflectivity insight. Scientific Reports, 6(1), 708–11. http://doi.org/10.1038/srep20997

[109] Lind, T. K., & Cárdenas, M. (2016). Understanding the formation of supported lipid bilayers via vesicle fusion—A case that exemplifies the need for the complementary method approach (Review). Biointerphases, 11(2), 020801–13. http://doi.org/10.1116/1.4944830

[110] Campbell, R. A., Watkins, E. B., Jagalski, V., Åkesson-Runnsjö, A., & Cárdenas, M. (2014). Key Factors Regulating the Mass Delivery of Macromolecules to Model Cell Membranes: Gravity and Electrostatics. ACS Macro Letters, 3(2), 121–125. http://doi.org/10.1021/mz400551h

[111] Tristram-Nagle, S. A. (2007). Preparation of Oriented, Fully Hydrated Lipid Samples for Structure Determination Using X-Ray Scattering. In A. M. Dopico (Ed.), Methods in Membrane Lipids (Vol. 400, pp. 63–75). Totowa, NJ: Humana Press. http://doi.org/10.1007/978-1-59745-519-0_5

[112] James, M., Nelson, A., Holt, S. A., Saerbeck, T., Hamilton, W. A., & Klose, F. (2011). The multipurpose time-of-flight neutron reflectometer "Platypus" at Australia's OPAL reactor. Nuclear Inst. and Methods in Physics Research, A, 632(1), 112–123. http://doi.org/10.1016/j.nima.2010.12.075

[113] Nelson, A. (2006). Co-refinement of multiple-contrast neutron/X-ray reflectivity data using MOTOFIT. Journal of Applied Crystallography, 39(2), 273–276. http://doi.org/10.1107/S0021889806005073

[114] Campbell, R. A., Wacklin, H. P., Sutton, I., Cubitt, R., & Fragneto, G. (2011). FIGARO: The new horizontal neutron reflectometer at the ILL. The European Physical Journal Plus, 126(11), 329–22. http://doi.org/10.1140/epjp/i2011-11107-8

[115] Cubitt, R., & Fragneto, G. (2002). D17: the new reflectometer at the ILL. Applied Physics a: Materials Science & Processing, 74(0), s329–s331. http://doi.org/10.1007/s003390201611

[116] Cristiglio, V., Giroud, B., Didier, L., & Demé, B. (2015). D16 is back to business: more neutrons, more space, more fun. Neutron News, 26(3), 22–24. http://doi.org/10.1080/10448632.2015.1057051

[117] https://www.ill.eu/en/instruments-support/sample-environment/equipment/soft-matter/humidity-chambers/

[118] Petrache, H. I., Feller, S. E., & Nagle, J. F. (1997). Determination of component volumes of lipid bilayers from simulations. Biophysical Journal, 72(5), 2237–2242. http://doi.org/10.1016/S0006-3495(97)78867-2

[119] Nagle, J. F., & Tristram-Nagle, S. (2000). Structure of lipid bilayers. Biochimica Et Biophysica Acta (BBA)-Reviews, 1469(3), 159–195. http://doi.org/10.1016/S0304-4157(00)00016-2

[120] Mukhopadhyay, P., Monticelli, L., & Tieleman, D. P. (2004). Molecular Dynamics Simulation of a Palmitoyl-Oleoyl Phosphatidylserine Bilayer with Na+ Counterions and NaCl. Biophysical Journal, 86(3), 1601–1609. http://doi.org/10.1016/S0006-3495(04)74227-7

[121] Pan, J., Cheng, X., Sharp, M., Ho, C.-S., Khadka, N., & Katsaras, J. (2014). Structural and mechanical properties of cardiolipin lipid bilayers determined using neutron spin echo, small angle neutron and X-ray scattering, and molecular dynamics simulations. Soft Matter, 11, 130–138. http://doi.org/10.1039/C4SM02227K

[122] Kučerka, N., van Oosten, B., Pan, J., Heberle, F. A., Harroun, T. A., & Katsaras, J. (2015). Molecular Structures of Fluid Phosphatidylethanolamine Bilayers Obtained from Simulation-to-Experiment Comparisons and Experimental Scattering Density Profiles. The Journal of Physical Chemistry B, 119(5), 1947–1956. http://doi.org/10.1021/jp511159q

[123] Greenwood, A. I., Tristram-Nagle, S., & Nagle, J. F. (2006). Partial molecular volumes of lipids and cholesterol. Chemistry and Physics of Lipids, 143(1-2), 1–10. http://doi.org/10.1016/j.chemphyslip.2006.04.002

[124] Deme, B., Cataye, C., Block, M. A., Marechal, E., & Jouhet, J. (2014). Contribution of galactoglycerolipids to the 3-dimensional architecture of thylakoids. The FASEB Journal, 28(8), 3373–3383. http://doi.org/10.1096/fj.13-247395

[125] Xie, X., & Zubarev, R. A. (2017). On the Effect of Planetary Stable Isotope Compositions on Growth and Survival of Terrestrial Organisms. PLoS ONE, 12(1), e0169296–9. http://doi.org/10.1371/journal.pone.0169296

[126] Itoh, T., Waki, H., & Kaneko, H. (2014). Changes of Lipid Composition with Growth Phase of Cryptococcus neoformans. Agricultural and Biological Chemistry, 39(12), 2365–2371. http://doi.org/10.1080/00021369.1975.10861966

[127] Carnicer, M., Baumann, K., Töplitz, I., Sánchez-Ferrando, F., Mattanovich, D., Ferrer, P., & Albiol, J. (2009). Macromolecular and elemental composition analysis and extracellular metabolite balances of Pichia pastoris growing at different oxygen levels. Microbial Cell Factories, 8(1), 65–14. http://doi.org/10.1186/1475-2859-8-65

[128] Grob, R. L. (2004). Theory of Gas Chromatography. In Modern Practice of Gas Chromatography (pp. 23–63). Hoboken, NJ, USA: John Wiley & Sons, Inc. http://doi.org/10.1002/0471651141.ch2

[129] Onyewu, C., Blankenship, J. R., Del Poeta, M., & Heitman, J. (2003). Ergosterol Biosynthesis Inhibitors Become Fungicidal when Combined with Calcineurin Inhibitors against Candida albicans, Candida glabrata, and Candida krusei. Antimicrobial Agents and Chemotherapy, 47(3), 956–964. http://doi.org/10.1128/AAC.47.3.956-964.2003

[130] S.E. Stein, "Mass Spectra" dans le WebBook de Chimie NIST, Base de Données Standard de référence NIST numéro 69, Eds. P.J. Linstrom and W.G. Mallard, National Institute of Standards and Technology, Gaithersburg MD, 20899, http://doi.org/10.18434/T4D303

[131] Rood, D. (2007). Appendix D: Column Bleed Mass Spectra. In The Troubleshooting and Maintenance Guide for Gas Chromatographers (pp. 267–272). Weinheim, Germany: Wiley-VCH Verlag GmbH & Co. KGaA. http://doi.org/10.1002/9783527611300.app4

[132] Carman, G. M., & Han, G.-S. (2009). Regulation of phospholipid synthesis in yeast. Journal of Lipid Research, 50(Supplement), S69–S73. http://doi.org/10.1194/jlr.R800043-JLR200

[133] de Kroon, A. I. P. M., Rijken, P. J., & De Smet, C. H. (2013). Checks and balances in membrane phospholipid class and acyl chain homeostasis, the yeast perspective. Progress in Lipid Research, 52(4), 374–394. http://doi.org/10.1016/j.plipres.2013.04.006

[134] Tehlivets, O., Scheuringer, K., & Kohlwein, S. D. (2007). Fatty acid synthesis and elongation in yeast. Biochimica Et Biophysica Acta (BBA) - Molecular and Cell Biology of Lipids, 1771(3), 255–270. http://doi.org/10.1016/j.bbalip.2006.07.004

[135] Buist, P. H., & Behrouzian, B. (1998). Deciphering the Cryptoregiochemistry of Oleate Δ12 Desaturase: A Kinetic Isotope Effect Study. Journal of the American Chemical Society, 120(5), 871–876. http://doi.org/10.1021/ja971362i

[136] Martin, C. E., Oh, C.-S., & Jiang, Y. (2007). Regulation of long chain unsaturated fatty acid synthesis in yeast. Biochimica Et Biophysica Acta (BBA) - Molecular and Cell Biology of Lipids, 1771(3), 271–285. http://doi.org/10.1016/j.bbalip.2006.06.010

[137] Santomartino, R. (2017). Three, two, one yeast fatty acid desaturases: regulation and function. World Journal of Microbiology and Biotechnology, 33(5), 1–12. http://doi.org/10.1007/s11274-017-2257-y

[138] Wiberg, K. B. (1955). The Deuterium Isotope Effect. Chemical Reviews, 55(4), 713–743. http://doi.org/10.1021/cr50004a004

[139] Behrouzian, B., & Buist, P. H. (2002). Fatty acid desaturation: variations on an oxidative theme. Current Opinion in Chemical Biology, 6(5), 577–582. http://doi.org/10.1016/S1367-5931(02)00365-4

[140] Anthony, C. (1982) The Biochemistry of Methylotrophs, Academic press, London.

[141] Huffer, S., Clark, M. E., Ning, J. C., Blanch, H. W., & Clark, D. S. (2011). Role of Alcohols in Growth, Lipid Composition, and Membrane Fluidity of Yeasts, Bacteria, and Archaea. Applied and Environmental Microbiology, 77(18), 6400–6408. http://doi.org/10.1128/AEM.00694-11

[142] Wriessnegger, T., Gubitz, G., Leitner, E., Ingolic, E., Cregg, J., Delacruz, B., & Daum, G. (2007). Lipid composition of peroxisomes from the yeast Pichia pastoris grown on different carbon sources. Biochimica Et Biophysica Acta (BBA) - Molecular and Cell Biology of Lipids, 1771(4), 455–461. http://doi.org/10.1016/j.bbalip.2007.01.004

[143] Vanz, A. L., nsdorf, H. L., Adnan, A., Nimtz, M., Gurramkonda, C., Khanna, N., & Rinas, U. (2012). Physiological response of Pichia pastoris GS115 to methanol-induced high level production of the Hepatitis B surface antigen: catabolic adaptation, stress responses, and autophagic processes. Microbial Cell Factories, 11(1), 1–1. http://doi.org/10.1186/1475-2859-11-103

[144] Kaganer, V. M., Möhwald, H., & Dutta, P. (1999). Structure and phase transitions in Langmuir monolayers. Reviews of Modern Physics, 71(3), 779–41. http://doi.org/10.1103/RevModPhys.71.779

[145] Ladha, S., Mackie, A. R., Harvey, L. J., Clark, D. C., Lea, E. J., Brullemans, M., & Duclohier, H. (1996). Lateral diffusion in planar lipid bilayers: a fluorescence recovery after photobleaching investigation of its modulation by lipid composition, cholesterol, or alamethicin content and divalent cations. Biophysical Journal, 71(3), 1364–1373. http://doi.org/10.1016/S0006-3495(96)79339-6

[146] Bartucci, R., Erilov, D. A., Guzzi, R., Sportelli, L., Dzuba, S. A., & Marsh, D. (2006). Time-resolved electron spin resonance studies of spin-labelled lipids in membranes. Chemistry and Physics of Lipids, 141(1-2), 142–157. http://doi.org/10.1016/j.chemphyslip.2006.02.009

[147] Miñones, J., Jr, Pais, S., Miñones, J., Conde, O., & Dynarowicz-Łątka, P. (2009). Interactions between membrane sterols and phospholipids in model mammalian and fungi cellular membranes — A Langmuir monolayer study. Biophysical Chemistry, 140(1-3), 69–77. http://doi.org/10.1016/j.bpc.2008.11.011

[148] Sinensky, M. (1974). Homeoviscous Adaptation—A Homeostatic Process that Regulates the Viscosity of Membrane Lipids in Escherichia coli. Proceedings of the National Academy of Sciences, 71(2), 522–525.

[149] Beney, L., Gervais, P. (2001). Influence of the fluidity of the membrane on the response of microorganisms to environmental stresses. Applied Microbiology and Biotechnology, 57(1-2), 34–42. http://doi.org/10.1007/s002530100754

[150] Stanley, D., Bandara, A., Fraser, S., Chambers, P. J., & Stanley, G. A. (2010). The ethanol stress response and ethanol tolerance of Saccharomyces cerevisiae. Journal of Applied Microbiology, 110, 34–12. http://doi.org/10.1111/j.1365-2672.2009.04657.x

[151] Hull, C. M., Parker, J. E., Bader, O., Weig, M., Gross, U., Warrilow, A. G. S., et al. (2012). Facultative Sterol Uptake in an Ergosterol-Deficient Clinical Isolate of Candida glabrata Harboring a Missense Mutation in ERG11 and Exhibiting Cross-Resistance to Azoles and Amphotericin B. Antimicrobial Agents and Chemotherapy, 56(8), 4223–4232. http://doi.org/10.1128/AAC.06253-11

[152] Vandeputte, P., Tronchin, G., Berges, T., Hennequin, C., Chabasse, D., & Bouchara, J. P. (2007). Reduced Susceptibility to Polyenes Associated with a Missense Mutation in the ERG6 Gene in a Clinical Isolate of Candida glabrata with Pseudohyphal Growth. Antimicrobial Agents and Chemotherapy, 51(3), 982–990. http://doi.org/10.1128/AAC.01510-06

[153] Richter, R., Mukhopadhyay, A., & Brisson, A. (2003). Pathways of Lipid Vesicle Deposition on Solid Surfaces: A Combined QCM-D and AFM Study. Biophysical Journal, 85(5), 3035–3047. http://doi.org/10.1016/S0006-3495(03)74722-5

[154] Jing, Y., Trefna, H., Persson, M., Kasemo, B., & Svedhem, S. (2014). Formation of supported lipid bilayers on silica: relation to lipid phase transition temperature and liposome size. Soft Matter, 10(1), 187–195. http://doi.org/10.1039/C3SM50947H

[155] Chong, C. S., & Colbow, K. (1976). Light scattering and turbidity measurements on lipid vesicles. Journal of Bacteriology, 436(2), 260–282. http://doi.org/10.1016/0005-2736(76)90192-9

[156] Campbell, R. A., Yanez Arteta, M., Angus-Smyth, A., Nylander, T., & Varga, I. (2012). Multilayers at Interfaces of an Oppositely Charged Polyelectrolyte/Surfactant System Resulting from the Transport of Bulk Aggregates under Gravity. The Journal of Physical Chemistry B, 116(27), 7981–7990. http://doi.org/10.1021/jp304564x

[157] Kučerka, N., Nieh, M.-P., & Katsaras, J. (2011). Fluid phase lipid areas and bilayer thicknesses of commonly used phosphatidylcholines as a function of temperature. BBA - Biomembranes, 1808(11), 2761–2771. http://doi.org/10.1016/j.bbamem.2011.07.022

[158] Mouritsen, O. G. (2004). Life - As a Matter of Fat: The Emerging Science of Lipidomics. Springer Berlin Heidelberg.

[159] Smondyrev, A. M., & Berkowitz, M. L. (2001). Molecular Dynamics Simulation of the Structure of Dimyristoylphosphatidylcholine Bilayers with Cholesterol, Ergosterol, and Lanosterol. Biophysical Journal, 80(4), 1649–1658. http://doi.org/10.1016/S0006-3495(01)76137-1

[160] Róg, T., Pasenkiewicz-Gierula, M., Vattulainen, I., & Karttunen, M. (2009). Ordering effects of cholesterol and its analogues. BBA - Biomembranes, 1788(1), 97–121. http://doi.org/10.1016/j.bbamem.2008.08.022

[161] Urbina, J. A., Pekerar, S., Le, H.-B., Patterson, J., Montez, B., & Oldfield, E. (1995). Molecular order and dynamics of phosphatidylcholine bilayer membranes in the presence of cholesterol, ergosterol and lanosterol: a comparative study using 2H-, 13C- and 31P-NMR spectroscopy. Journal of Bacteriology, 1238(2), 163–176. http://doi.org/10.1016/0005-2736(95)00117-L

[162] Smaby, J. M., Momsen, M. M., Brockman, H. L., & Brown, R. E. (1997). Phosphatidylcholine acyl unsaturation modulates the decrease in interfacial elasticity induced by cholesterol. Biophysical Journal, 73(3), 1492–1505. http://doi.org/10.1016/S0006-3495(97)78181-5

[163] Kamiński, D. M., Czernel, G., Murphy, B., Runge, B., Magnussen, O. M., & Gagoś, M. (2014). Effect of cholesterol and ergosterol on the antibiotic amphotericin B interactions with dipalmitoylphosphatidylcholine monolayers: X-ray reflectivity study. BBA - Biomembranes, 1–7. http://doi.org/10.1016/j.bbamem.2014.08.004

[164] Smondyrev, A. M., & Berkowitz, M. L. (1999). Structure of Dipalmitoylphosphatidylcholine/Cholesterol Bilayer at Low and High Cholesterol Concentrations: Molecular Dynamics Simulation. Biophysical Journal, 77(4), 2075–2089. http://doi.org/10.1016/S0006-3495(99)77049-9

[165] Readio, J. D., & Bittman, R. (1982). Equilibrium binding of amphotericin B and its methyl ester and borate complex to sterols. Journal of Bacteriology, 685(2), 219–224. http://doi.org/10.1016/0005-2736(82)90103-1

[166] Barwicz, J., & Tancrède, P. (1997). The effect of aggregation state of amphotericin-B on its interactions with cholesterol- or ergosterol-containing phosphatidylcholine monolayers. Chemistry and Physics of Lipids, 85(2), 145–155. http://doi.org/10.1016/S0009-3084(96)02652-7

[167] Jacquier, N., & Schneiter, R. (2012). Mechanisms of sterol uptake and transport in yeast. Journal of Steroid Biochemistry and Molecular Biology, 129(1-2), 70–78. http://doi.org/10.1016/j.jsbmb.2010.11.014

[168] van Meer, G., & de Kroon, A. I. P. M. (2010). Lipid map of the mammalian cell. Journal of Cell Science, 124(1), 5–8. http://doi.org/10.1242/jcs.071233

[169] Callow, P., Fragneto, G., Cubitt, R., Barlow, D. J., Lawrence, M. J., & Timmins, P. (2005). Interaction of Cationic Lipid Vesicles with Model Cell MembranesAs Determined by Neutron Reflectivity. Langmuir, 21(17), 7912–7920. http://doi.org/10.1021/la050957l

[170] Soranzo, T., Martin, D. K., Lenormand, J.-L., & Watkins, E. B. (2017). Coupling neutron re ectivity with cell-free protein synthesis to probe membrane protein structure in supported bilayers OPEN. Scientific Reports, 1–10. http://doi.org/10.1038/s41598-017-03472-8

[171] Tero, R. (2012). Substrate Effects on the Formation Process, Structure and Physicochemical Properties of Supported Lipid Bilayers. Materials, 5(12), 2658–2680. http://doi.org/10.3390/ma5122658

[172] Åkesson, A., Lind, T., Ehrlich, N., Stamou, D., Wacklin, H., & Cárdenas, M. (2012). Composition and structure of mixed phospholipid supported bilayers formed by POPC and DPPC. Soft Matter, 8(20), 5658–8. http://doi.org/10.1039/c2sm00013j

[173] Hung, W.-C., Lee, M.-T., Chung, H., Sun, Y.-T., Chen, H., Charron, N. E., & Huang, H. W. (2016). Comparative Study of the Condensing Effects of Ergosterol and Cholesterol. Biophysical Journal, 110(9), 2026–2033. http://doi.org/10.1016/j.bpj.2016.04.003

[174] Franks, G. V., & Meagher, L. (2003). The isoelectric points of sapphire crystals and alpha-alumina powder. Colloids and Surfaces a: Physicochemical and Engineering Aspects, 214(1-3), 99–110. http://doi.org/10.1016/S0927-7757(02)00366-7

[175] Fadeel, B., & Xue, D. (2009). The ins and outs of phospholipid asymmetry in the plasma membrane: roles in health and disease. Critical Reviews in Biochemistry and Molecular Biology, 44(5), 264–277. http://doi.org/10.1080/10409230903193307

[176] Rondelli, V., Fragneto, G., Motta, S., Del Favero, E., Brocca, P., Sonnino, S., & Cantù, L. (2012). Ganglioside GM1 forces the redistribution of cholesterol in a biomimetic membrane. BBA - Biomembranes, 1818(11), 2860–2867. http://doi.org/10.1016/j.bbamem.2012.07.010

[177] Engberg, O., Hautala, V., Yasuda, T., Dehio, H., Murata, M., Slotte, J. P., & Nyholm, T. K. M. (2016). The Affinity of Cholesterol for Different Phospholipids Affects Lateral Segregation in Bilayers. Biophysical Journal, 111(3), 546–556. http://doi.org/10.1016/j.bpj.2016.06.036

[178] Halling, K. K., Ramstedt, B., Nyström, J. H., Slotte, J. P., & Nyholm, T. K. M. (2008). Cholesterol Interactions with Fluid-Phase Phospholipids: Effect on the Lateral Organization of the Bilayer. Biophysical Journal, 95(8), 3861–3871. http://doi.org/10.1529/biophysj.108.133744

[179] Williams, J. A., Wassall, C. D., Kemple, M. D., & Wassall, S. R. (2013). An Electron Paramagnetic Resonance Method for Measuring the Affinity of a Spin-Labeled Analog of Cholesterol for Phospholipids. The Journal of Membrane Biology, 246(9), 689–696.

[180] Martinez-Seara, H., Róg, T., Pasenkiewicz-Gierula, M., Vattulainen, I., Karttunen, M., & Reigada, R. (2008). Interplay of Unsaturated Phospholipids and Cholesterol in Membranes: Effect of the Double-Bond Position. Biophysical Journal, 95(7), 3295–3305. http://doi.org/10.1529/biophysj.108.138123

[181] Ohvo-Rekila, H. (2002). Cholesterol interactions with phospholipids in membranes. Progress in Lipid Research, 41(1), 66–97. http://doi.org/10.1016/S0163-7827(01)00020-0

[182] Li, N., Thomas, R. K., & Rennie, A. R. (2012). Effect of pH, surface charge and counter-ions on the adsorption of sodium dodecyl sulfate to the sapphire/solution interface. Journal of Colloid and Interface Science, 378(1), 152–158. http://doi.org/10.1016/j.jcis.2012.04.026

[183] Wacklin, H. P., & Thomas, R. K. (2007). Spontaneous Formation of Asymmetric Lipid Bilayers by Adsorption of Vesicles. Langmuir, 23(14), 7644–7651. http://doi.org/10.1021/la063476q

[184] Wacklin, H. P. (2011). Composition and Asymmetry in Supported Membranes Formed by Vesicle Fusion. Langmuir, 27(12), 7698–7707. http://doi.org/10.1021/la200683e

[185] Stanglmaier, S., Hertrich, S., Fritz, K., Moulin, J. F., Haese-Seiller, M., Rädler, J. O., & Nickel, B. (2012). Asymmetric Distribution of Anionic Phospholipids in Supported Lipid Bilayers. Langmuir, 28(29), 10818–10821. http://doi.org/10.1021/la3019887

[186] Foglia, F., Drake, A. F., Terry, A. E., Rogers, S. E., Lawrence, M. J., & Barlow, D. J. (2011). Small-angle neutron scattering studies of the effects of amphotericin B on phospholipid and phospholipid–sterol membrane structure. BBA - Biomembranes, 1808(6), 1574–1580. http://doi.org/10.1016/j.bbamem.2011.02.012

[187] Gagoś, M., Hereć, M., Arczewska, M., Czernel, G., Dalla Serra, M., & Gruszecki, W. I. (2008). Anomalously high aggregation level of the polyene antibiotic amphotericin B in acidic medium: Implications for the biological action. Biophysical Chemistry, 136(1), 44–49. http://doi.org/10.1016/j.bpc.2008.04.005

[188] Zielińska, J., Wieczór, M., Bączek, T., Gruszecki, M., & Czub, J. (2016). Thermodynamics and kinetics of amphotericin B self-association in aqueous solution characterized in molecular detail. Scientific Reports, 1–11. http://doi.org/10.1038/srep19109

[189] Miñones, J., Conde, O., Rodriguez Patino, J. M., & Dynarowicz-Latka, P. (2002). Mixed Monolayers of Amphotericin B–Dipalmitoyl Phosphatidyl Choline: Study of Complex Formation. Langmuir, 18(7), 2817–2827. http://doi.org/10.1021/la011378t

[190] Miñones, J., Rodriguez Patino, J. M., Conde, O., & Iribarnegaray, E. (2003). Miscibility of Amphotericin B–Dipalmitoyl Phosphatidyl Serine Mixed Monolayers Spread on the Air/Water Interface. The Journal of Physical Chemistry B, 107(17), 4189–4195. http://doi.org/10.1021/jp0207275

[191] V Cotero, B., Rebolledo-Antúnez, S., & Ortega-Blake, I. (1998). On the role of sterol in the formation of the amphotericin B channel. Journal of Bacteriology, 1375(1-2), 43–51. http://doi.org/10.1016/S0005-2736(98)00134-5

[192] Masuda, A., Akiyama, S.-I., Kuwano, M., & Ikekawa, N. (1982). Potentiation of antifungal effect of amphotericin B by squalene, an intermediate for sterol biosynthesis. The Journal of Antibiotics, 35(2), 230–234. http://doi.org/10.7164/antibiotics.35.230

[193] Kanduč, M., Schlaich, A., de Vries, A. H., Jouhet, J., chal, E. M. E., eacute, B. D., Netz, R. R., et al. (2017). Tight cohesion between glycolipid membranes results from balanced water/headgroup interactions. Nature Communications, 8, 1–9. http://doi.org/10.1038/ncomms14899

[194] Zaccai, G., Bagyan, I., Combet, J., Cuello, G. J., Demé, B., Fichou, Y., et al. (2016). Neutrons describe ectoine effects on water H-bonding and hydration around a soluble protein and a cell membrane. Scientific Reports, 1–12. http://doi.org/10.1038/srep31434

[195] Narayanan, T., Wacklin, H., Konovalov, O., & Lund, R. (2017). Recent applications of synchrotron radiation and neutrons in the study of soft matter. Crystallography Reviews, 23(3), 160–226. http://doi.org/10.1080/0889311X.2016.1277212

[196] Kučerka, N., Pencer, J., Sachs, J. N., Nagle, J. F., & Katsaras, J. (2007). Curvature Effect on the Structure of Phospholipid Bilayers. Langmuir, 23(3), 1292–1299. http://doi.org/10.1021/la062455t

[197] Pan, J., Cheng, X., Monticelli, L., Heberle, F. A., Kučerka, N., Tieleman, D. P., & Katsaras, J. (2014). The molecular structure of a phosphatidylserine bilayer determined by scattering and molecular dynamics simulations. Soft Matter, 10(21), 3716–10. http://doi.org/10.1039/c4sm00066h

[198] Mueller, J., Schroeter, A., Steitz, R., Trapp, M., & Neubert, R. H. H. (2016). Preparation of a New Oligolamellar Stratum Corneum Lipid Model. Langmuir, 32(18), 4673–4680. http://doi.org/10.1021/acs.langmuir.6b00655

[199] Gawrisch, K., Gaede, H. C., Mihailescu, M., & White, S. H. (2007). Hydration of POPC bilayers studied by 1H-PFG-MAS-NOESY and neutron diffraction. European Biophysics Journal, 36(4-5), 281–291. http://doi.org/10.1007/s00249-007-0142-6

[200] Cathcart, K., Patel, A., Dies, H., Rheinstädter, M., & Fradin, C. (2015). Effect of Cholesterol on the Structure of a Five-Component Mitochondria-Like Phospholipid Membrane. Membranes, 5(4), 664–684. http://doi.org/10.3390/membranes5040664

[201] Mojumdar, E. H., Gooris, G. S., Groen, D., Barlow, D. J., Lawrence, M. J., Deme, B., & Bouwstra, J. A. (2016). Stratum corneum lipid matrix: Location of acyl ceramide and cholesterol in the unit cell of the long periodicity phase. BBA - Biomembranes, 1858(8), 1926–1934. http://doi.org/10.1016/j.bbamem.2016.05.006

[202] Mojumdar, E. H., Gooris, G. S., Barlow, D. J., Lawrence, M. J., Demé, B., & Bouwstra, J. A. (2015). Skin Lipids: Localization of Ceramide and Fatty Acid in the Unit Cell of the Long Periodicity Phase. Biophysical Journal, 108(11), 2670–2679. http://doi.org/10.1016/j.bpj.2015.04.030

[203] Groen, D., Gooris, G. S., Barlow, D. J., Lawrence, M. J., van Mechelen, J. B., Deme, B., & Bouwstra, J. A. (2011). Disposition of Ceramide in Model Lipid Membranes Determined by Neutron & Diffraction. Biophysical Journal, 100(6), 1481–1489. http://doi.org/10.1016/j.bpj.2011.02.001

[204] Bouwstra, J. A., Gooris, G. S., van der Spek, J. A., & Bras, W. (1991). Structural Investigations of Human Stratum Corneum by Small-Angle X-Ray Scattering. Journal of Investigative Dermatology, 97(6), 1005–1012. http://doi.org/10.1111/1523-1747.ep12492217

[205] Bouwstra, J. A., Gooris, G. S., Dubbelaar, F., Weerheim, A. M., Ijzerman, A. P., & Ponec, M. (1998). Role of ceramide 1 in the molecular organization of the stratum corneum lipids. Journal of Lipid Research, 39(1), 186–196.

[206] Benesch, M. G. K., Lewis, R. N. A. H., & McElhaney, R. N. (2016). A calorimetric and spectroscopic comparison of the effects of cholesterol and its sulfur-containing analogs thiocholesterol and cholesterol sulfate on the thermotropic phase behavior and organization of dipalmitoylphosphatidylcholine bilayer membranes. BBA - Biomembranes, 1858(2), 168–180. http://doi.org/10.1016/j.bbamem.2015.11.006

[207] García-Arribas, A. B., Busto, J. V., Alonso, A., & Goñi, F. M. (2015). Atomic Force Microscopy Characterization of Palmitoylceramide and Cholesterol Effects on Phospholipid Bilayers: A Topographic and Nanomechanical Study. Langmuir, 31(10), 3135–3145. http://doi.org/10.1021/la504047n

[208] Bagatolli, L. A., & Gratton, E. (2000). A Correlation between Lipid Domain Shape and Binary Phospholipid Mixture Composition in Free Standing Bilayers: A Two-Photon Fluorescence Microscopy Study. Biophysical Journal, 79(1), 434–447. http://doi.org/10.1016/S0006-3495(00)76305-3

[209] Svetlovics, J. A., Wheaten, S. A., & Almeida, P. F. (2012). Phase Separation and Fluctuations in Mixtures of a Saturated and an Unsaturated Phospholipid. Biophysical Journal, 102(11), 2526–2535. http://doi.org/10.1016/j.bpj.2012.04.017

[210] Katsaras, J., Jeffrey, K. R., Yang, D. S. C., & Epand, R. M. (2002). Direct evidence for the partial dehydration of phosphatidylethanolamine bilayers on approaching the hexagonal phase. Biochemistry, 32(40), 10700–10707. http://doi.org/10.1021/bi00091a021

ABSTRACT

The formation and structural investigation of planar bilayers from synthetic lipids and natural extracts is described. The bilayers were used as model membrane systems for the investigation and quantification of the molecular mechanisms of the membrane-binding antifungal drug Amphotericin B, primarily by neutron reflectometry. Different membrane models of increasing complexity were investigated, with ergosterol or cholesterol included to mimic fungal and mammalian cell membranes, respectively. The extraction, chemical analysis and preparation of hydrogenous and deuterated lipid mixtures from yeasts are presented together with the optimization of the deposition process of supported lipid bilayers on silicon substrates using Quartz Crystal Microbalance with Dissipation monitoring to create relevant natural model membranes for the neutron scattering experiments. The effects of deuteration on the lipid composition in two different yeasts, the methylotrophic *Pichia pastoris* and the pathogenic *Candida glabrata* are detailed and is shown to be useful for understanding the modulation of the lipids accessible from these microorganisms. Model membranes from the synthetic lipid 1-palmitoyl-2-oleoyl-sn-glycero-3-phosphocholine were initially characterized and compared to those formed by the phospholipids or the total lipids extracted from the yeasts, mainly using neutron reflectometry but also membrane diffraction. Finally, the relationship between the lipid composition and the response to Amphotericin B was investigated. Although different behavior of the drug is observed in fungal and mammal membrane mimics, the composition and degree of complexity of the model systems employed were shown to affect the findings and the interpretation of the mechanisms involved in the interaction of the drug with the membranes. The differences found between synthetic and natural lipid systems demonstrate the relevance of the newly developed model membranes from lipids extracted from biomass.

RÉSUMÉ

La formation et l'étude structurale de bicouches planes formées à partir de lipides synthétiques et d'extraits lipidiques naturels sont décrites. Les bicouches ont été utilisées comme modèles membranaires pour étudier et quantifier les mécanismes d'action du médicament antifongique Amphotéricine B, principalement par réflectométrie des neutrons. Différents modèles membranaires de complexités croissantes, qui intègrent de l'ergostérol ou du cholestérol afin d'imiter respectivement des systèmes fongiques ou mammifères, ont été étudiés. L'extraction, l'analyse chimique et la préparation des mélanges de lipides hydrogénés et deutérés issus de levures sont présentés en même temps que l'optimisation du procédé de déposition sur des substrats de silicium, initialement contrôlés avec une microbalance à quartz et mesure de la dissipation, qui permet d'accéder à des modèles de membranes naturelles pertinentes pour les techniques de diffusion neutronique. Les effets de la deutération sur la composition lipidique de la levure méthylotrophe *Pichia pastoris* ou de la levure pathogène *Candida glabrata*, sont détaillés et utiles pour comprendre la modulation des lipides obtenus de ces micro-organismes. Les modèles membranaires basés sur le lipide synthétique 1-palmitoyl-2-oléoyl-sn-glycéro-3-phosphocholine ont d'abord été caractérisés et comparés à ceux formés des phospholipides ou des lipides totaux extraits des levures, principalement par réflectométrie des neutrons, mais aussi par diffraction de membrane. Enfin, la relation entre la composition lipidique et les réponses des modèles à l'Amphotéricine B ont été étudiées. Bien que différents comportements soient observés pour les systèmes fongiques et mammifères, les différents degrés de complexité des modèles utilisés a montré une incidence sur les résultats et l'interprétation des mécanismes impliqués lors de l'interaction du médicament avec les membranes. Les différences observées entre les systèmes lipidiques synthétiques et naturels démontrent la pertinence des modèles membranaires nouvellement développés à partir des lipides extraits de biomasse.